INFLUENCES OF SURFACE QUALITY ON THE ROLLING CONTACT FATIGUE BEHAVIOUR OF CERAMICS

An Investigation into the Relationship between the Finishing Process, Surface Quality and Failure Modes of Advanced Si_3N_4 Rolling Elements

JINSHENG KANG

A thesis submitted in partial fulfilment of the requirement of Bournemouth University for the degree of Doctor of Philosophy

July 2001

Bournemouth University
In collaboration with SKF
Engineering & Research Centre

This copy of the thesis has been supplied on condition that anyone who consults it is understood to recognise that its copyright rests with its author and that no quotation from the thesis and no information derived from it may be published without the author's prior consent.

Dedicated to my father Jianhua Kang, who past away on 14th March 2001

AUTHOR'S DECLARATION

This thesis is submitted for the degree of Doctor of Philosophy in the School of Design, Engineering & Computing, Bournemouth University. I am responsible for the work submitted in this thesis. The submitted work is original, except where references have been made to others. The research was carried out by myself in the period from October 1997 to July 2001 under the supervision of Professor Mark Hadfield in the School of Design, Engineering & Computing, Bournemouth University.

No part of this thesis, or any other work similar to it, has been, or is currently being submitted for any degree or any other qualification. This thesis is less than 40,000 words.

Jinsheng Kang

School of Design, Engineering & Computing,
Bournemouth University
UK

ABSTRACT

A novel eccentric lapping machine was designed by the author and manufactured in-house, to serve as a test bench to investigate the finishing process parameters in relation to surface quality, as well as the feasibility of accelerating the finishing process of HIPed silicon nitride balls. The kinematics of the eccentric lapping were analysed and discussed. Taguchi Methods were used to optimise the finishing parameters to achieve maximum material removal rate in lapping and to achieve minimum surface roughness value R_a in polishing. Two kinds of HIPed silicon nitride ball blanks were finished by this machine. A finishing rate of 68 μm/hour was achieved which is 15 times higher than the conventional concentric lapping (normally 3~4μm/hour). The surface roughness and roundness of the polished ball were above grade 5, close to grade 3 precision bearing ball specification. The upper limits of lapping load and lapping speed were determined by aggressive lapping tests. The effects of various finishing parameters on the surface quality generated were studied by detailed surface analysis, including X-ray diffraction residual stress measurement. As a result, the relationship between the finishing process and surface quality has been established.

Accelerated rolling contact fatigue tests were performed both under a standard 4-ball and a modified 5-ball rolling configuration, with a ceramic ball as the upper ball and steel balls as lower balls. The tests were conducted at high speed and lubricated conditions under different loads and were run for up to 135~200 million stress cycles. Tests were conducted on commercially finished balls with different surface roughness and with different surface integrity (heterogeneous porosity, star defect, grinding defect and C-cracks). Tests were also conducted on self-finished balls with different finishing parameters and with different surface roughness. After tests, the rolling tracks and failure areas were examined by detailed surface analysis. The residual stresses on the rolling tracks were measured. Finite Element Approaches were also employed to describe the contact stress status. Failure modes in relation to surface quality were discussed. The research has provided an understanding of the finishing process, surface quality and rolling contact fatigue behaviour of HIPed silicon nitride balls.

PUBLICATIONS RESULTING FROM THESIS

1. Kang, J. and Hadfield, M., "A novel eccentric lapping machine for finishing advanced ceramic balls" *Journal of Engineering Manufacture, Proceedings of Institution of Mechanical Engineers, Part B,* Vol. 215, No. B6, 2001, pp. 781-795.
2. Kang, J. and Hadfield, M., "Parameter optimization by Taguchi Methods for finishing advanced ceramic balls using a novel eccentric lapping machine" *Journal of Engineering Manufacture, Proceedings of Institution of Mechanical Engineers, Part B,* Vol. 215, No. B1, 2001, pp. 69-78.
3. Kang, J. and Hadfield, M., "The Influence of Heterogeneous Porosity on Silicon Nitride/Steel Failure in Lubricated Rolling Contact", *Ceramics International,* Vol. 26, No. 3, 2000, pp. 315-324.
4. Kang, J., Hadfield, M. and Cundill, R. "Rolling contact fatigue performance of HIPed Si_3N_4 with different surface roughness", *Ceramics International,* Vol. 27, No. 7, 2001, pp. 781-794.
5. Kang, J. , Cundill, R. and Hadfield, M., "The consequences of aggressive lapping processes on the surface integrity of HIPed silicon nitride bearing balls", *Tribology in Environmental Design 2000,* Professional Engineering Publishing Ltd., London, pp. 227-234. ISBN: 1-86058-266-4
6. Kang, J. and Hadfield, M., "Finishing Advanced Ceramic Balls Using an Eccentric Lapping Machine", The 9th International Manufacturing Conference in China, Hong Kong, 16-17 August 2000.
7. Kang, J. and Hadfield, M., "A study on the lapping of ceramic balls", *Surface treatment IV — computer methods and experimental measurements,* Computational Mechanics Publications, Southampton, 1999, pp. 389-399, ISBN: 1-85312-697-7
8. Kang, J. and Hadfield, M, "Rolling Contact Failure Modes of Lubricated Silicon Nitride in Relation to Surface Defects", *Advances in Science and Technology, Vol. 13, Ceramics: Getting into the 2000's, Part A,* TECHNA, 1999, pp. 533-540, ISBN 88-86538-14-6

ACKNOWLEDGEMENTS

The author wishes to acknowledge the help, support and encouragement received whilst undertaking the PhD research.

My supervisor, Professor Mark Hadfield has provided a constant source of inspiration, strength and encouragement. Every step in the progress of my work reflects his solid support and patient help.

The financial support of the project from SKF Engineering & Research Centre B. V. in the Netherlands, in particular the technical advice from Dr Robin Cundill.

The financial support from the School of Design, Engineering & Computing, Bournemouth University, and the support and help from the staff, especially Mrs Christine Thwaites.

Professor Shogo Tobe, Dr Yasutaka Ando and Professor Fumio Inaba in Ashikaga Institute of Technology, Japan, for help with measuring residual stresses and atomic force microscopy of the balls.

Dr Rahan Ahmed in Heroit-Watt University (UK), Department of Mechanical and Chemical Engineering, for help with measuring the 3D topography of the balls.

F. J. Engineering in Milford on Sea, Hampshire (UK), for manufacturing the eccentric lapping machine. Taymar Precision Grinding in Poole, Dorset (UK), for manufacturing the 5-ball cup and cage. ProMinent Fluid Control (UK) Ltd, for contributing a Gamma/4 diaphragm-type metering pump.

Last but not least, the encouragement and support from my parents, my sister and my brother, my wife and my daughter.

LIST OF CONTENTS

LIST OF TABLES

LIST OF ILLUSTRATIONS

SYMBOLS

The following symbols are used in Section 2.1.2 Eccentric Lapping Kinematics Analysis:

R_b	ball radius
R_g	circular V-groove radius
R_i	radius from centre of circular V-groove to ball/V-groove inner contact point
R_o	radius from centre of circular V-groove to ball/V-groove outer contact point
r_i	radius from rotating axis of lower lapping plate to ball/V-groove inner contact point
r_o	radius from rotating axis of lower lapping plate to ball/V-groove outer contact point
E	Eccentricity (the distance between rotating axis and centre of circular V-groove)
V_{ip}	lower plate linear speed at ball /V-groove inner contact point perpendicular to the radial plane through centre of circular V-groove.
V_{op}	lower plate linear speed at ball /V-groove outer contact point perpendicular to the radial plane through centre of circular V-groove.
β	ball spin angle
θ	V-groove half-angle
Ω_p	lower lapping plate angular speed
ω_b	ball spin angular speed
ω_c	ball circulation around circular V-groove angular speed

The following symbols are used in Section 4.2 Taguchi Method:

GTSS	grand total sum of squares of Signal-to-Noise ratio
MSD	mean square deviation
n_{Ai}	number of tests conducted at level i of parameter A
S/N	Signal-to-Noise ratio
S/N_{LTB}	Signal-to-Noise ratio (larger-the-better)
$\overline{S/N}$	overall mean of Signal-to-Noise ratios
$\overline{S/N}_{Ai}$	the level average S/N of parameter A at level i
SS_A	the sum of the squares of the S/N variation induced by parameter A around overall mean.
SS_B	the sum of the squares of the S/N variation induced by parameter B around overall mean.
SS_C	the sum of the squares of the S/N variation induced by parameter C around overall mean.
SS_D	the sum of the squares of the S/N variation induced by parameter D around overall mean.
SS_{mean}	the sum of the squares due to overall mean of S/N
$SS_{variation}$	the sum of the squares due to variation around overall mean of S/N
y_i	the individually measured response value at measurement *I*
σ_T^2	the total sum of the squares of the standard deviation
σ_A^2	square of the standard deviation caused by parameter A
σ_B^2	square of the standard deviation caused by parameter B
σ_C^2	square of the standard deviation caused by parameter C
σ_D^2	square of the standard deviation caused by parameter D

ABBREVIATIONS

ANOVA	Analysis of Variance
AFM	Atomic Force Microscopy
BBA	Ball Blank A
BBB	Ball Blank B
EDX	Energy Dispersive X-Ray Spectroscopy
EHD	Elastohydrodynamic
ERC	SKF Engineering and Research Centre, B. V., Nieuwegein, The Netherlands.
FEA	Finite Element Analysis
GPS	Gas Pressure Sintered
HP	Hot Pressed
HIPed	Hot Isostatically Pressed
HV	High Viscosity
LV	Low Viscosity
MFG	Magnetic Fluid Grinding, Magnetic Float Grinding
OA	Orthogonal Array
RMS	Root Mean Square (surface roughness, R_q)
rms	root mean square (surface roughness, R_q)
SEM	Scanning Electron Microscopy
SRB	Sintered Reaction Bounded
TCP	Tribochemical Polishing
UV	Ultra-Violet

1.0 INTRODUCTION

1.1 General Background

Current demands on load bearing contacts in all kinds of machinery are leading to developments aimed at running them at high speeds, hostile environments, increased unit loads and restricted lubrication. The design and manufacture of such contacts are at the limit of established technology. At present, the most promising designs able to cope with such extreme demands are believed to be in the area of ceramic/ceramic, ceramic/coated metal or ceramic/metal combinations (Hadfield et al. 1993a).

Hybrid precision ball-bearings (with ceramic balls as the rolling elements and steel inner and outer rings) give substantial performance advantages in many applications. Silicon nitride is a ceramic material with the optimum combination of properties for use in rolling bearings. Technologies of powder manufacture and material densification have advanced to the stage that fully dense Hot Isostatically Pressed (HIPed) silicon nitride components are readily available (Cundill 1992a). The rolling contact fatigue life of HIPed silicon nitride is superior to that of bearing steels. The material properties — low density, high elastic modulus, corrosion resistance, and temperature resistance — give significant performance advantages in hybrid bearings and all-ceramic bearings (Cundill 1992b). Hybrid precision bearings with HIPed silicon nitride balls as the rolling elements are used extensively in machine tools and other applications involving high speeds or extreme operating conditions.

The application of hybrid precision bearings also has some positive environmental impacts in the sense that these bearings are less noisy, save energy and have longer service life. The only disadvantage in environmental terms is that the ceramic balls are difficult to recycle after service, but they produce no pollution when

discarded. With more widespread use of hybrid bearings, it will be possible to re-process used balls by lapping them down to a smaller size after use. The overall influences of the application of hybrid precision bearings on the environment are therefore positive. The only restriction is the relatively high manufacturing cost of HIPed silicon nitride balls compared to steel balls. It is estimated that the finishing of HIPed silicon nitride balls and associated inspection constitutes up to half of the total manufacturing cost. Therefore, finishing balls to high levels of dimensional accuracy and surface quality in a cost effective manner is critical to their widespread application.

The requirement to accelerate finishing times on technical ceramic surfaces is an area under intensive study. It is well known that the surface quality generated from final finishing processes will be directly related to the fatigue failure modes and life. It is not known what effects the finishing process parameters, finishing rate or the surface roughness have on the fatigue failure mode and life of HIPed silicon nitride. This research will aim to resolve these uncertainties.

1.2 Literature Review

1.2.1 Manufacturing Processes for Engineering Ceramics

The manufacturing processes of engineering ceramic elements can be classified into four stages, stage 1 – powder and fibre manufacture, stage 2 – green body forming, stage 3 – transformation to final shape, stage 4 – surface finishing (McColm and Clark 1988). Ceramic balls at stage 3 are made from processes either Sinter + HIP (Hot Isostatically Pressed), or GPS (Gas Pressure Sintered), or Direct HIP, or SRB (Sintered Reaction Bounded), or HP (Hot Pressed) (Cundill 1997). In all cases, a final surface finishing process is needed for the balls to achieve the required surface quality and geometric accuracy for precision ball bearing application.

Ceramics are brittle materials. The finishing methods of ceramics can be categorised as: abrasion machining, which involves abrasive particles either on the cutting tools (diamond saw or grinding wheel) or in slurry or paste (lapping,

polishing) mechanically scratching or wearing against the workpiece to remove stock; and abrasionless machining including hydrodynamic machining, chemical milling, electric discharge machining, electron beam machining, laser beam machining and ion beam machining etc. (Firestone 1978). Whether or not these abrasionless machining methods could be applied to ceramic balls needed to be studied. For abrasion machining methods, Imanaka and Okutomi (1978) summarised the novel lapping/polishing apparatus used in Japan on the ultra-fine finishing of ceramics. The abrasion machining methods for engineering ceramics were also compiled in a recent book by Marinescu et al (2000).

1.2.2 Finishing Methods Applied to Advanced Ceramic Balls

1.2.2.1 Different finishing methods for advanced ceramic balls

In industry, ceramic balls are typically finished by concentric lapping, through several operations by gradually changing the load, plates and diamond grits sizes in the slurry or suspension. The surface skin of the ceramic ball produced in previous manufacturing stages is compositionally and microstructurally different from the core of the ball and has to be removed during the final finishing stage (Stolarski and Tobe 1997). For a 12.7 mm ball, 500-800 μm stock in diameter has to be removed from the ball surface. It takes weeks to finish a batch of ceramic balls.

Obviously, the conventional finishing processes of ceramic balls need to be advanced. Some research has been conducted on the finishing methods of ceramic balls. Magnetic Fluid Grinding (MFG), also called Magnetic Float Grinding (Polishing), was first developed by Tani and Kawata (1984) and improved significantly using a float by Umehara and Kato (1988). Three research groups involved in Magnetic Fluid Grinding of ceramic balls are Kato (Umehara and Kato 1996), Childs (Childs et al. 1995) and Komanduri (Jiang and Komanduri 1998). Stolarski et al (Stolarski and Jisheng 1998, Jisheng et al.1996), studied the grinding wear of silicon nitride in diamond slurry at a relatively high speed (3,000 rpm or so), using a 4-ball rolling fatigue test machine as the grinding machine by replacing the upper ball with a stainless cone and the lower balls with 9 silicon nitride 6.5 mm

diameter balls. Hah and Fischer (1998) studied the tribochemical polishing (TCP) of silicon nitride which is based on the friction-stimulated dissolution of material in a liquid with no abrasive particles. These researches provided some innovative ideas on finishing methods for ceramic balls. It is not yet known whether these laboratory test results could be applied in large scale, low cost production or whether the ball roundness generated by these methods has reached the requirement for precision bearing balls. In industry, the two-plate lapping method is still common practice for finishing advanced ceramic balls. It is recognised that the fundamental mechanism of the loose abrasive process in the two-plate lapping method has received less attention and there is still great potential for this method.

1.2.2.2 Comparison of different two-plate lapping mechanisms

a) Two flat surfaces lapping

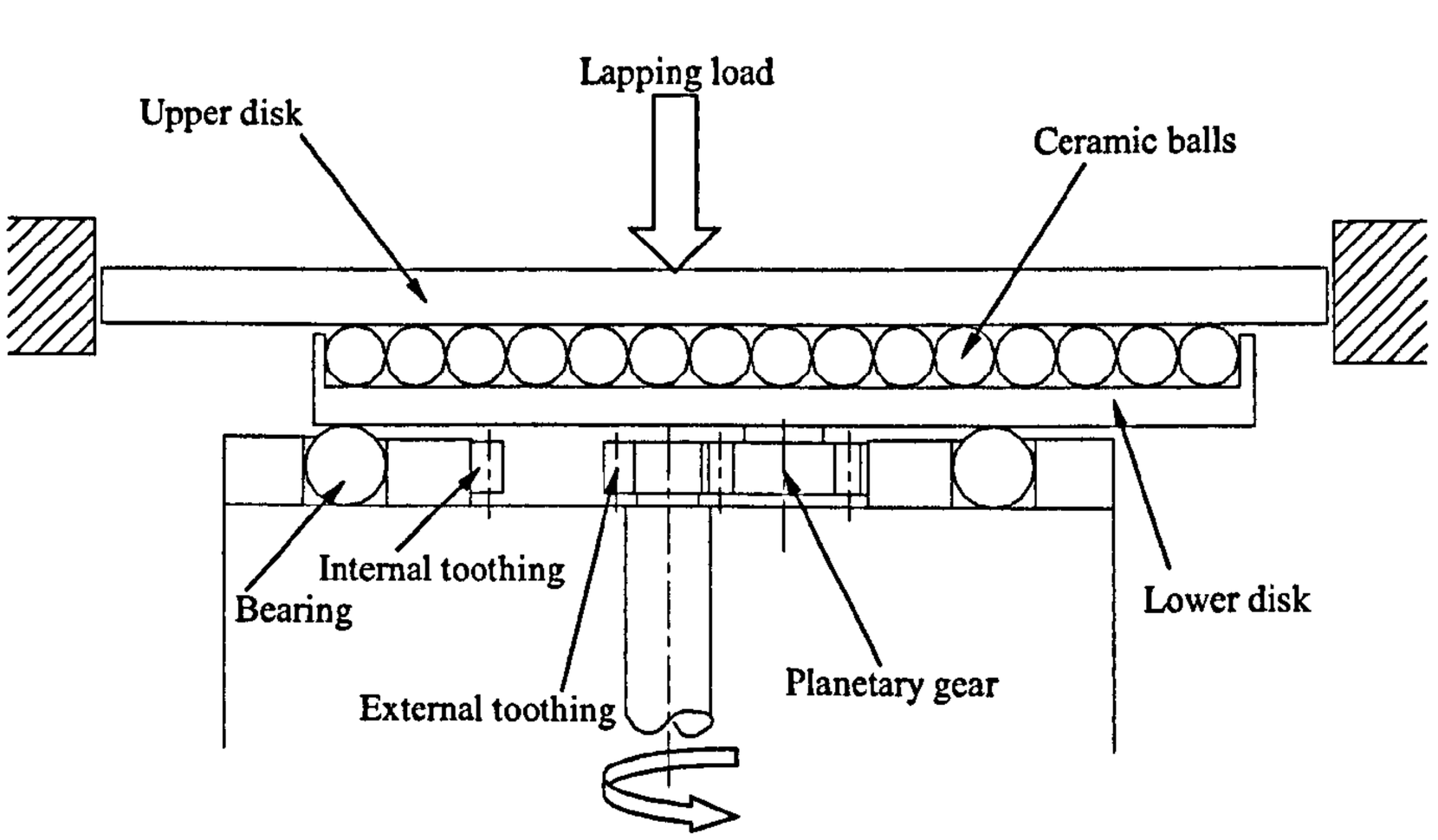

Fig. 1-1 Two flat surfaces lapping

Fig. 1-1 shows the mechanism of two flat surfaces lapping (Ichikawa et al. 1993). Balls being lapped are placed in between two flat lapping surfaces (upper disk and lower disk) with no carrier to separate the balls from each other. The upper disk is

stationary while the lower disk is mounted on a planetary gear. Its motion thus consists of both its own rotation and the revolution around the spindle. The balls being lapped are rolling and skidding in between two plates, and their positions are changing at random. This mechanism can only be used for rough lapping.

b) One flat surface, loading tools and carrier lapping

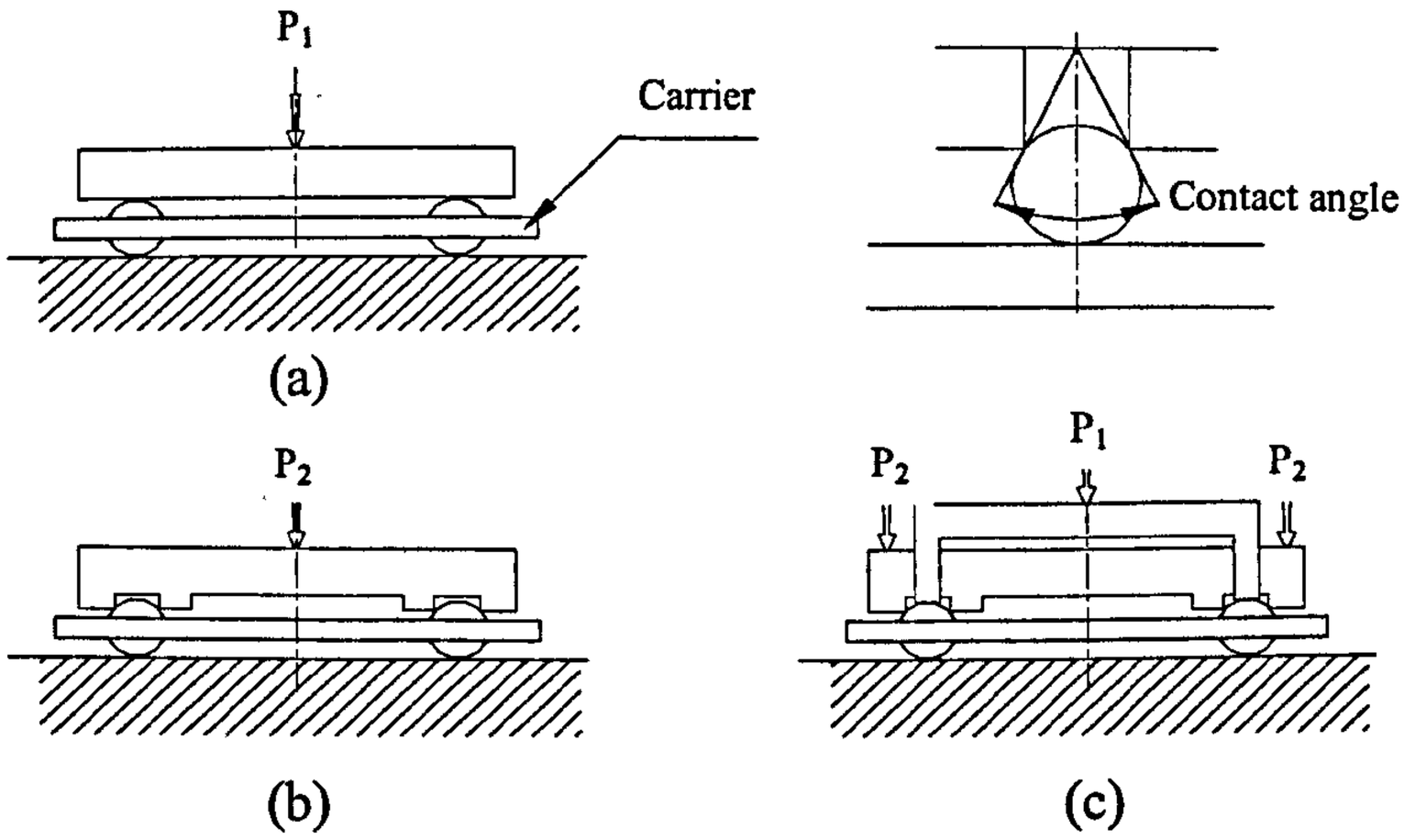

Fig. 1-2 One flat surface, loading tools and carrier lapping

Fig. 1-2 shows the mechanism of one flat surface, loading tools and carrier lapping (Ichikawa et al. 1993). The lower lapping plate is a flat disk, while the upper ones are called "tools", rotating and applying lapping pressure. Balls are separated by carriers. If using a single tool, it will make a two-point or three-point contact with the ball according to the contact angle of the tool. Fig. 1-2 (a) is a two-point contact (contact angle = 180°), Fig. 1-2 (b) is a three-point contact. If two upper tools are used, that will make a four-point contact (Fig 1-2 (c)), two tools can apply load independently.

c) One flat surface, one concentric v-groove lapping

Fig. 1-3 depicts the mechanism of one flat surface and one concentric V-groove lapping. The top lapping plate is a flat surface whilst the bottom plate has a circular V-groove. The centre of the circular V-groove is the rotational axis of the plate. Both

top and bottom plates rotate independently along the same axis (Fig 1-3 upper). Balls being lapped are placed in the circular V-groove. Kurobe et al. (1996) modified the lapping apparatus by separating the two sides of a V-groove into two parts (Fig 1-3 lower, B and C), which can rotate independently. They designed a lapping apparatus

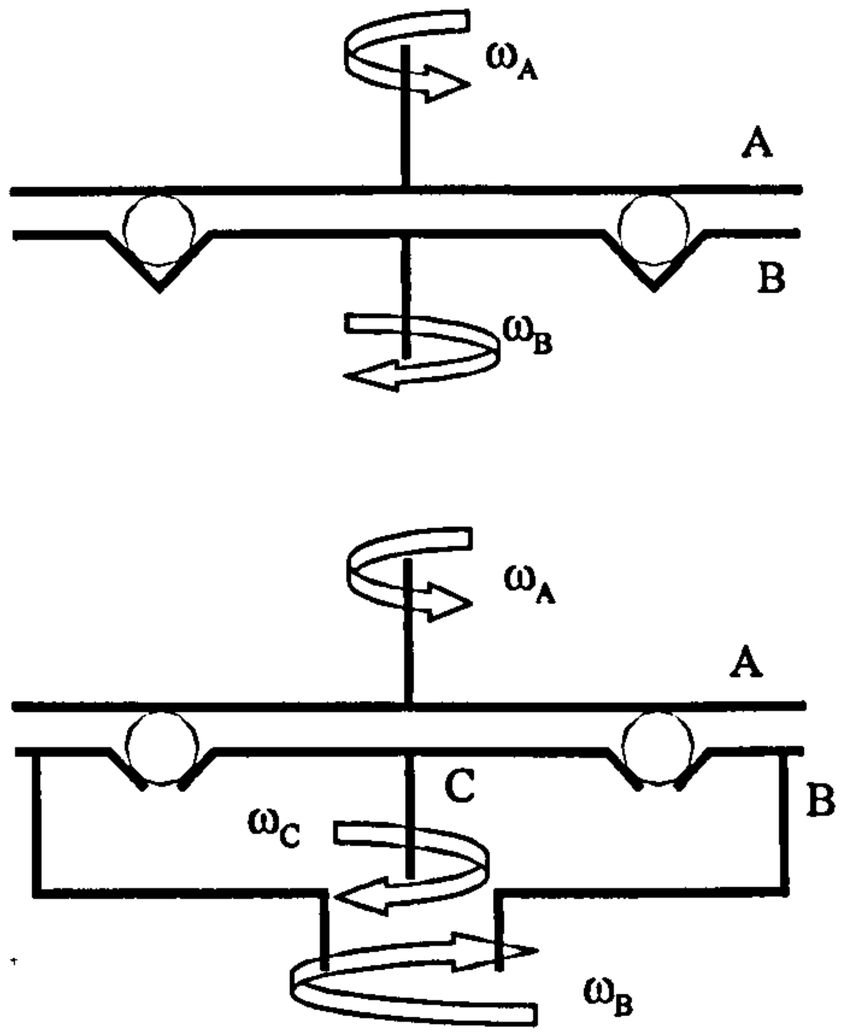

Fig. 1-3 One flat surface, one concentric V-groove lapping

in which the spin angle (β) of the finishing balls is controlled by changing the angular velocities of upper flat, outer V-groove and inner V-groove lapping plates (three plates can rotate independently). This lapping apparatus enables the ball spin angle (β) to vary from 0° to 90°. It was found from the experiments that the ball spin angle (β) has a significant influence on lapping (Kurobe et al., 1997).

d) Two concentric circular grooves lapping

Fig. 1-4 shows two concentric circular grooves lapping. With two lapping plates, normally one is rotating and one is stationary. Both have a circular V-groove or a round curve groove (conforming to the balls being lapped). The centre of the circular

groove is the rotating axis. This mechanism is the one most commonly used by industry to finish advanced ceramic balls.

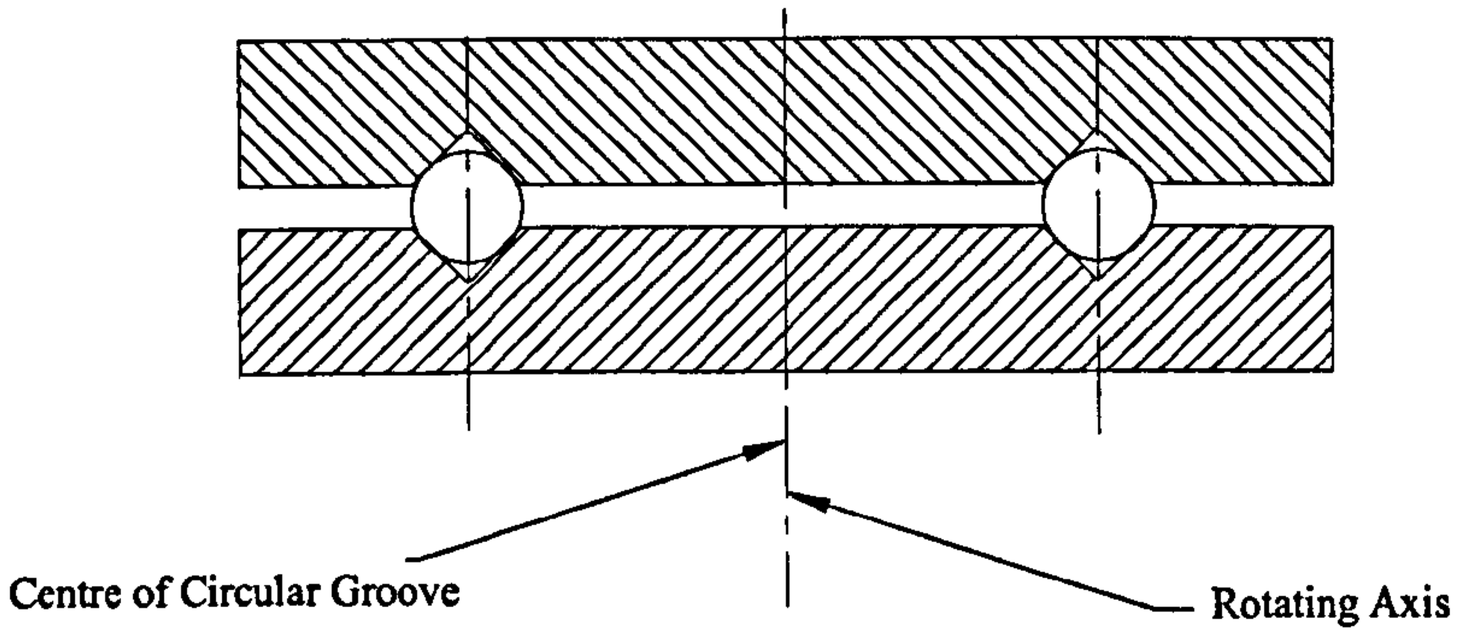

Fig. 1-4 Two concentric circular grooves lapping

1.2.3 Surface Quality of Engineering Ceramics in Relation to Finishing Parameters

Surface quality can be defined as surface topography (such as surface roughness and surface waviness) and surface integrity (surface microstructural variations and defects) (Field and Kahles 1971). The distribution and magnitude of residual stresses are also an integral part of surface quality. Since lapping, polishing and grinding are the most commonly used methods for finishing ceramic balls, the focus of the literature review is concentrated on these methods. In order to recognise the influences of finishing process parameters on the surface qualities produced, the mechanism of material removal during finishing must be fully understood.

1.2.3.1 The Mechanism of Material Removal during Finishing

The material removal processes in grinding, lapping and polishing of ceramics can be considered as two-body or three-body wear. The mechanical action of the abrasive can be thought of as the repeated application of relatively sharp sliding indenters to the surface. Under these conditions, a small number of mechanisms dominate the

material removal process. These are brittle fracture due to crack systems oriented both parallel (lateral) and perpendicular (radial/median) to the surface, ductile cutting with the formation of thin ribbon-like chips and chemically assisted wear in the presence of a reactant that is enhanced by the mechanical action (tribochemical reaction). The relative role of each of these mechanisms in a particular finishing process can be related to the load applied to an abrasive particle, the sliding speed of the particle, and the presence of a chemical reactant. These wear mechanisms also cause damage to the near surface in the form of microcracking, residual stress, plastic deformation and surface roughness which together determine the strength and performance of the finished component (Chandrasekar and Farris 1997).

A model was built by Buijs and Korpelvanhouten (1993a; 1993b) for three-body abrasion of brittle materials which is based on material removal by rolling abrasive particles. The particles indent the workpiece surface and remove material by lateral cracking. Median cracking introduces subsurface damage. The model leads to expressions for removal (or wear) rate, surface roughness, subsurface damage and load per particle as a function of particle shape, particle size, material parameters of workpiece and lapping plate, applied pressure and relative velocity between plate and workpiece. The model was found to give a good description of the experimental results, allowing among other things the calculation of removal rate, surface roughness or damage penetration from the measurement of either one of these parameters. An indentation model for the lapping of ceramics was also proposed by Ahn and Park (1997) to predict surface roughness R_a and R_t. Bulsara et al. (1998) developed a model to determine the number and sizes of abrasive particles involved in material removal by polishing, and the forces acting on these particles.

Gardos and Hardisty (1993) first reported that the abrasive or polishing wear rate of silicon nitride balls is dependant on fracture toughness K_{IC} and hardness H_V. Later Dill, Gardos and Hardisty (1997) reported that the grinding wear of individual silicon nitride balls increased at different rates as a function of load and no simple relationship between hardness, fracture toughness and grinding rate could be found.

Chromium oxide (Cr_2O_3) was found to be an excellent abrasive for polishing silicon nitride and chemical analysis showed that Cr_2O_3 participated in the

chemomechanical polishing of silicon nitride to form chromium nitride and chromium silicate (Bhagavatula and Komanduri 1996).

Water can accelerate the abrasive ratio by tribochemical reaction with silicon nitride. M. Woydt and U. Effner studied the wear of ceramics under water lubrication. The materials SiC, ZrO_2 and Si_3N_4-TiN are not applicable since water accelerates the pitting formation. Only HIP-Si_3N_4 can be used as it demonstrates a wear rate a hundred times higher than paraffinic oil (Effner and Woydt 1995, Woydt and Effner 1996a). This confirms the findings of Fischer etc. (Hah and Fischer, 1998) and Stolarski (Stolarski and Jisheng 1998).

1.2.3.2 Surface Topography

It was observed that the lapping pressure has less effect on surface roughness R_a and R_t and that surface roughness decreases with decreasing abrasive particle size (Ahn and Park 1997, Chen and Inasaki 1991). Reduced surface roughness could be attained by using a softer lapping plate (Chen and Inasaki 1991; Gardos and Hardisty 1993). Surface roughness increases when the abrasive concentration in the slurry is increased. (Ahn and Park 1997). It was shown that lapping with softer abrasives and smaller particles reduces surface roughness (Chandrasekar et al. 1990). Somakumar et al. (1994) found that the minimum surface roughness of Y_2O_3-ZrO_2 and CeO_2-ZrO_2 was reached earlier at lower lapping speeds compared with higher lapping speeds.

1.2.3.3 Surface Integrity

Lapping and polishing processes introduce damage on the near surface of ceramic material because of the nature of the material removal action (Marshall et al. 1983, Chandrasekar et al. 1987). This damage is usually in the form of microcracking and dislocations. Prominent among these effects are the changes in mechanical strength and hardness, alterations in near surface permeability, electrical and thermal conductivity and refractive index (Stokes 1972). Fig 1-5 shows the different deformed layers near a finished ceramic surface (Chandrasekar et al. 1988).

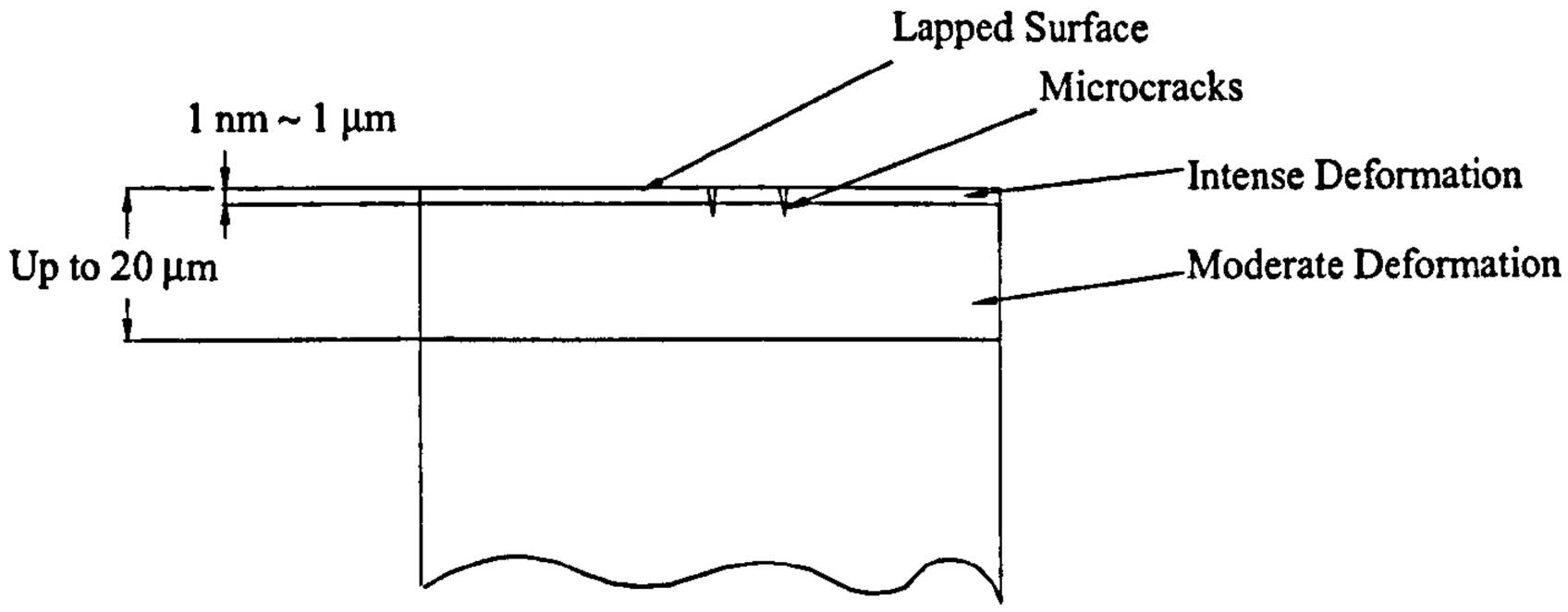

Fig. 1-5 Deformed layers after lapping

1.2.3.4 Residual Stresses

It was found that the surface residual stresses in silicon nitride induced by grinding were compressive. They were higher in the direction perpendicular to the lay than parallel to the lay(Zanoria 1998, Pfeiffer and Hollstein 1997). The compressive stresses within a 0.6 μm depth of finely ground surface (by 320 grit wheel) were lower than those of a coarsely ground surface (by an 80 grit wheel) by 25% and by 41.4% respectively at directions perpendicular and parallel to the lay (Zanoria 1998). It was recognised that increasing the grinding speed reduced the residual stresses. The samples ground at the maximum speed no longer showed significant residual stresses and the microstrain state had reached the low level of bulk material (Pfeiffer and Hollstein 1997).

Feng (1993) studied the phase transformation induced by surface grinding and residual stresses in Al_2O_3-ZrO_2 composite. It was found that ZrO_2 transformation increased with the severity of the grinding conditions. The magnitude of the residual stresses was primarily controlled by the volume fraction of tetragonal ZrO_2 that transformed to monoclinic during surface grinding.

Chandrasekar et al (1988, 1990) studied the effects of abrasive-particle properties and lapping process parameters on surface residual stresses during the

lapping of ceramics. It was shown that the maximum compressive stress as well as the depth of the compressively stressed zone increases with increasing lapping pressure; lapping with softer abrasives and smaller particles results in lower compressive residual stresses near the surface; A larger grit size will result in larger residual stresses.

Stolarski and Tobe (1997) studied the effect of accelerated material removal on the residual stresses of 6.5mm diameter HIPed silicon nitride balls. It indicated that the residual compressive stress decreases as the amount of material removed grows. Initially, the rate of residual stress decrease is fairly high but this lessens as the removal of material progresses. This could be attributed to the fact that the outermost layer of material with highest residual stresses (generated during HIP process) was removed.

1.2.4 Surface Quality in Relation to Rolling Contact Fatigue Failure Modes

Surface topography was recognised very early as being crucial to surface contact. The number of contact areas, their size and spacing will affect the contact resistance or the local temperature caused by frictional heating during sliding (Holm 1946, Bowden and Tabor 1950). It is assumed that an increase in contact load increases both the number and size of the contact areas. (Archard 1953).

The functional behaviour of surface from a mechanical aspect was reviewed by R. Van Hasselt (1969). For metal, it was summarised that surface quality affects fatigue-strength in three ways: (1) the roughness of surface presents a pattern of irregularities and scratches, each being a potential starting point for a fatigue crack. (2) residual surface stresses may be beneficial if compressive, or detrimental if tensile. (3) heat introduced into a surface by machining has a detrimental effect on fatigue-strength.

The surface quality of ceramics generated from machining and finishing has been a concern of academia and industry since the 1970's. The National Bureau of Standards, USA held two symposiums on the machining and surface finishing of ceramics in 1972 and 1978 (Rice and Schneider 1972, Hockey et al. 1979).

Besides the surface quality, the synthesis of ceramic powder, crystal structures and consolidation techniques also play an important part in relation to rolling contact performance. L. Y. Chao et al (1995) reviewed the manufacturing processes (apart from surface finishing), rolling contact fatigue and wear test techniques, failure modes and mechanisms of silicon nitride for bearing application. This could complement the current literature review, which focuses only on surface finishing related topics. In that literature review, it is also highlighted that as the fatigue life has improved in recent years due to expensive processes such as hot–isostatic-pressing, wear has become a more important issue in silicon nitride bearing elements.

1.2.4.1 Effect of Material Removal Rate During Finishing

In the late 1970's, it was reported that with hot-pressed silicon nitride, coarser grinding media introduced larger flaws and reduced strength (Andersson and Bratton 1979), while finer grit sizes resulted in higher ground strengths (Wu and McKinney 1979). Regarding the effect of lapping on surface strength alteration, Guha and Chatterjee (1980) observed, using an Instrom strength measuring instrument, that the decrease in strength was only marginal on polishing sintered alumina ceramic. Tomlinson and Newton (1990) reported that lapping increases the strength of ground specimens (fully dense sintered reaction-bounded silicon nitride) by about 10%. But the Weibull statistics results from Ovri and Davies' (1987) investigation showed that the mean flexural strength values for the diamond-lapped silicon nitride are lower than in the as-sintered condition.

Recently, Woydt and Effner, using a twin-disk wear tester, studied the influences of material removal and surface roughness on slip-rolling wear in paraffinic oil and water (Effner and Woydt 1995, Effner and Woydt 1998, Woydt and Effner 1996b, Woydt and Effner 1997). The ceramic materials investigated were HIP-Si_3N_4 , HIP-ZrO_2, S-SiC and GPS-Si_3N_4-TiN. Each sample was machined to cylindrical and spherical shapes by both "fine" and "rough" grinding; honing; lapping and polishing, resulting in different surface roughness. They defined a specific wear coefficient $K_V=W_V/F_NS$ (mm^3/Nm), where W_V is the wear volume (mm^3), F_N is the normal force (N), and S is the sliding distance (m). For HIP-Si_3N_4,

HIP-ZrO_2 and GPS-Si_3N_4-TiN, a lesser material removal rate in the machining process resulted in a lower wear coefficient later in the slip-rolling wear test in paraffinic oil. The wear coefficient of spherical HIP-Si_3N_4 samples was proportional to the material removal rate during machining, whereas for cylindrical HIP-Si_3N_4, spherical and cylindrical GPS-Si_3N_4-TiN, HIP-ZrO_2 samples, below a material removal rate of 0.02 mm^3/s, a strong low-wear/high-wear transition occurred. Surprisingly, for S-SiC, a material removal rate below 0.005 mm^3/s increased the wear coefficient.

1.2.4.2 Effect of Surface Topography

Surface topography includes roughness, waviness, form, lay etc.. Since ceramic balls are usually finished by lapping or polishing, there is no obvious lay direction (machining pattern) generated by grinding wheels. Form is the general surface shape as it deviates from the desired shape. This can be controlled by a variation in the ball diameter, which is tight for grade 3 or grade 5 balls. Ball waviness affects vibration and noise in high frequency bands in ball bearings (Cundill 1992a).

There are many parameters to describe surface roughness, for example, R_a (roughness average), R_q, also called RMS (rms) (root-mean-square roughness), R_t (maximum peak to valley height) and R_{sk} (skewness). Among those, R_a is most commonly used to represent surface roughness and R_q is generally considered most important in wear because it defines the composite surface roughness, which determines the lambda (λ) ratio (under EHD lubrication). With steel, it was reported that surface fatigue depended greatly on R_q (Liu 1994). A data-fitted rolling bearing life prediction model revealed that the compiled steel full rolling-bearing life tests showed a consistent downward trend as the composite RMS roughness height increased. This indicated the mathematical life prediction model, which took the surface roughness into account, underestimated the life-shortening effect of a rougher surface (Tallian 1996).

Recently, Lakshminarayanan and Chao studied the lubricated rolling contact of steel/silicon nitride using a ball-on-rod rolling-contact-fatigue (RCF) tester. The as-ground silicon nitride rods (R_a 0.18μ) exhibited neither wear nor spalling in the

RCF tests, while the ground-and-lapped silicon nitride rods (R_a 0.08μ) showed no wear but occasional spalling failure (Lakshminarayanan et al. 1997). Silicon nitride balls on silicon nitride rods rolling contact fatigue tests showed the bearing-grade balls (R_a 0.005μ) rolling on as-ground (R_a 0.18μ) rods produced a high initial wear rate in both elements that decreased exponentially with time or number of loading cycles. Improving the surface finish on the rods by lapping (R_a 0.05μ) produced delayed wear in both elements, i.e., the wear rate was initially zero during an incubation period, then increased and finally decreased (Chao et al. 1998).

Woydt and Effner conducted slip-rolling tests on a twin-disk tribometer and found the spherical samples of Si_3N_4 and Si_3N_4-TiN showed a minimum in the wear coefficient for surface roughness values R_{VK} (reduced valley depth) (NLG 1990) in the range of 0.5 μm ≤ R_{VK} ≤ 0.9 μm. For the cylindrical Si_3N_4 and Si_3N_4-TiN samples, wear coefficient is proportional to R_{VK}. (Effner and Woydt 1995, Effner and Woydt 1998, Woydt and Effner 1996b, Woydt and Effner 1997). It was found that for HIP-Si_3N_4 and Si_3N_4-TiN with initial roughness R_z≥0.5μm, running-in can act as a cost-free "surface finishing" process. It was found also that under conditions of slip-rolling in oil for the ceramic couples at room temperature there was no correlation between wear coefficient and the machining process or initial surface roughness (Effner and Woydt 1995, Woydt and Effner 1996b).

Westkaemper and Hoffmeister (1996) did a similar test. They also found that for S-SiC if R_{VK} was below 0.3 μm the rolling wear increased considerably. The upper limit for R_{VK} was 2 μm, above that the rolling wear rose strongly again. During rolling contact, the initial roughness peaks were very quickly removed in the running-in period and thus had little influence on the rolling wear. The shape of the valleys in surface topography will have the greatest effect on rolling contact fatigue life. A wear model for HIP-Si_3N_4 in rolling contact was established and a new rolling wear relevant surface characteristic value "valley sharpness R_S" proposed. Rolling wear test results showed a better correlation with valley sharpness R_S than the conventional roughness parameter "average roughness height R_{zDIN}". It was found that different materials may need different surface characteristic values, for HIP-Si_3N_4-TiN and

HIP-Y-PSZ-A, unfiltered reduced valley depth P_{VK} showed a good correlation with rolling wear (Westkaemper and Hoffmeister 1997).

1.2.4.3 Effect of Surface Integrity

Surface integrity includes surface microstructural variations and defects. Surface defects are classified as 'C' cracks (ring cracks), pressing defects, grinding defects, star defects (point defects) etc. (Cundill 1992a). Surface integrity (surface microstructural variations and defects) of a ceramic ball will have a definite effect on its rolling contact performance. The question is to what extent and by which mechanism the surface integrity influences the rolling contact behaviour.

The microstructural variation is a significant factor in the fatigue failure of ceramics. In a theoretic review of the mechanism of fatigue process by Evans (1980), the fact that fatigue degradation is dependent upon microstructural details was emphasized. To test "bearing-quality" silicon nitride, 11 candidate monolithic and 2 silicon carbide whisker-reinforced silicon nitride materials were evaluated with respect to their rolling-contact fatigue performance using a ball-on-rod machine. When they were tested at a maximum Hertzian contact pressure of 5.930 GPa, with steel loading balls and SAE-20 mineral oil lubricant, the materials exhibited life differences of several orders of magnitude. Attempts to correlate the fatigue performance with such properties as density, hardness and elastic moduli were generally unsuccessful. However, the microstructural features such as porosity, second-phase distribution and, in particular, the crystal size and morphology showed a good qualitative relationship to the fatigue life and failure mode. Under these relatively high-stress conditions, fatigue durability increased dramatically as the microstructure tended toward finer, more equiaxed grains and a uniform, minimum distribution of second phases (Burrier 1996).

The intrinsic microstructure in addition to the matrix of silicon nitride (or sialon) and glassy grain boundary phases, can contain porosity, metallic phases and ceramic second phases and inclusions. Pronounced microstructural variations are not considered suitable for use in high performance bearing application. A porosity content of 0.1 % volume would be regarded as high. Areas of ceramic second phases

or metallic appearing phases or a combination of both types greater in extent than 25 μm are considered as inclusions (Cundill 1992b). The presence of ceramic phase is considered to have relatively little effect on fatigue performance. In the case of metallic phase, the composition of the phase is important with hybrid bearings. In normal operation, the rolling elements are separated from the rings by a thin film of lubricant, but some direct contact may occur at low speeds or where lubrication is poor. Some types of metallic phase have a high welding affinity to steel bearing races which results in material being pulled out of the ceramic rolling elements (Cundill 1992b).

The porosity and wear performance of silicon nitride was investigated in the early 1970's (Burke et al. 1974, 1978). A full literature on the formation and effects of porosity in engineering ceramics was compiled by Rice (1998). It is generally recognised that there is a progressive decrease in elastic modulus, thermal conductivity and flexural strength with any increasing amount of porosity in the microstructure; however this decrease can be kept to a minimum by controlling the size and shape of porosity content (Divakar 1994). The effects of porosity size and distribution on rolling contact fatigue performance were studied on a disc-on-rod machine (Hadfield and Stolarski 1995b). Silicon nitride rods containing micro-porosity performed better than steel rods, whereas with silicon nitride rods with high porosity (pore size reaches 10 μm in length), the fatigue performance was reduced by an order of magnitude compared to those containing micro-porosity.

Rolling contact fatigue tests were conducted on HIPed silicon nitride balls with artificially pre-cracked radial and lateral cracks by Vickers pyramid heads. After testing, in some cases no radial crack propagation was observed but lateral crack propagation was evident (Hadfield et al. 1993b). In some cases both radial crack propagation and lateral crack propagation were observed, and the observation of subsurface cracks provided evidence of lubricant driven delamination fatigue failure (Hadfield and Stolarski 1995a).

Rolling contact fatigue tests were also conducted on HIPed silicon nitride balls with artificially pre-cracked ring cracks (C-cracks) by blunt impact loads. Ring cracks (C-cracks) failed by spalling after testing in a non-catastrophic mode during all

tests. The fatigue failure process was classified into three stages: first stage—beginning of material removal, second stage—incipent spall, and third stage—severe material removal and secondary damage (Hadfield et al. 1993b, Hadfield et al. 1993c).

Although natural C-cracks (formed during the ball handling and finishing process) have been observed on balls above 10mm diameter, their effect on the performance of hybrid bearings is generally not considered to be significant due to the higher intrinsic strength of small balls (Cundill 1997). A recent rolling contact fatigue test on 12.7 mm silicon nitride balls with surface C-cracks showed that fatigue failure under rolling contact loading is markedly sensitive to the location of the C-crack on the rolling track. Only a few locations on the rolling track can lead to fatigue failure at the maximum Hertz contact pressure of 5.58 GPa (Wang 2000a, Wang 2000b).

1.2.4.4 Effect of Residual Stresses

It was considered that in mechanical and structural ceramics such as silicon nitride and zirconia, where the mechanical strength properties are of interest, the presence of a deep zone of surface finishing residual compressive stresses can be beneficial in improving the finished ceramics. A requirement, in this case, is to maximize the surface residual stress zone depth and minimize the finishing induced crack size, so as to ensure that the crack is embedded well inside the residual compressive stress layer (Chandrasekar et al. 1988).

Residual stresses do exist in finished bearing quality ceramic balls due to previous manufacturing processes and surface finishing operations. A survey of HIPed 12.7 mm silicon nitride balls from 7 different manufacturers showed that the residual stresses are all compressive and range from 54MPa to 111MPa (Hadfield and Tobe 1998).

The residual stresses around the wear track of an upper ball of silicon nitride/silicon nitride contact after a rolling 4-ball test under maximum contact stress of 7.6GPa for 150 million stress cycles were measured. It was shown that at the centre of the wear track along the rolling direction, residual stress is 296 MPa

compressive and perpendicular to the rolling direction 111 MPa compressive; near the edges of the wear track, perpendicular to the rolling direction, upper side 200 MPa compressive, lower side 308 MPa compressive. (Hadfield and Tobe 1998). In an earlier study on the residual stresses in the delamination area using different measurement parameter settings, the correlation of compressive residual stresses with failure depth suggested a shear stress type of failure (Hadfield et al. 1993a, Hadfield et al. 1993b).

Studies have shown that there is a dormant period between each successive crack advancement during which the residual stress and a plastic component are each built up in a cumulative manner leading to eventual failure. During fatigue, $\sigma_{(p)}$, (plastic) and $\sigma_{(r)}$, (residual stress) components are predominant for ductile metals and brittle glass/ceramics respectively (Sarkar 1995).

The dynamic relationship between residual stress development and fatigue fracture formation under cyclic loading was investigated by Pruitt and Suresh (1993). Direct and in situ measurements of cyclic stress fields ahead of fatigue flaws in a model amorphous solid subjected to far-field cyclic compression loading, photoelasticity and laser interferometry experiments were conducted on single-edged-notched plates of a photoelastic resin. This was to determine the residual stresses within the near-tip damage zone during the inception and subcritical growth of the fatigue flaw from the stress concentration. Transmission electron microscopy observations were presented for a rubber-toughened polystyrene to illustrate how the residual tensile stresses developing within the cyclic damage zone cause crazes to form along the plane of the fatigue crack in the direction normal to the far-field compression axis.

Residual stresses resulting from crystallization of the boundary glass phase in ceramics are expected to play a significant role in determining the abrasive wear resistance. A comparison of the surface and bulk microstructures of two 96% aluminas indicates that the residual stresses arising from thermal expansion mismatch created by crystallization of the amorphous boundary phase, when combined with stresses created during grinding, can lead to excessive pullout of the

alumina grains. However, neither source of residual stress is, by itself, sufficient to cause such pullout (PowellDogan et al. 1991).

A study on the repeated impact wear of silicon nitride showed that the higher residual compressive stresses in the coarsely ground surface impedes the rate of microcrack propagation and causes lower wear (Zanoria 1998). However, a dynamic fatigue study on a Li_2O-Al_2O_3-SiO_2 glass ceramic showed that the material strength and lifetime was seen to increase due to the removal of residual stress through grinding and polishing (Gent and Tucker 1995).

1.2.5 State of the Art from Literature Review

HIPed Si_3N_4 rolling elements give substantial performance advantages in hybrid and all ceramic bearings and also have positive environmental impact. The only restriction preventing the widespread application is the high manufacturing cost, especially in the finishing process. Current finishing methods for HIPed Si_3N_4 rolling elements need to be advanced, although limited research has already been conducted. Both theoretical and experimental studies are needed to explore the potential of the two-plate lapping method further. From a short-term view point, varying the two-plate lapping kinematics and the V-groove angle or the groove curve shape, adding water to oil-based slurry, using tribochemically assisted abrasive grits such as Cr_2O_3, optimising lapping operation parameters (such as load, speed, grits size), or combining these measures are most promising. From a mid-term view point, improving or inventing new, efficient lapping and polishing apparatus for ceramic balls, for example, by adding vibration to the top flat lapping plate, rotating the top flat lapping plate with embedded abrasive grits, or ultrasonic assisted lapping, are expected to show positive results. From a long-term view point, the applicability of abrasionless machining described by Firestone (1978) to the finishing of advanced ceramic balls is worth exploring. It is clear, however, if a finishing method can only be realised in a laboratory at great expense, it is useless. Efforts must be concentrated to develop finishing methods which have potential industrial value.

The surface quality produced by using different finishing methods on different ball blanks (different manufacturers use different material powder, additives and

processes resulting in different microstructure and properties) needs to be further investigated both experimentally and theoretically and directly related to rolling contact fatigue performance. Theoretical analysis of the finishing process will provide both guidelines for efficient finishing and the basis for surface failure analysis under rolling contact. Rolling contact failure modes of ceramics have been studied extensively but less directly related to surface quality. Extensive experimental studies are needed to quantitatively find out the relationship between finishing parameters, surface quality and rolling contact failure modes.

1.3 Outline of Research Work

1.3.1 Research Objective and Scope

The primary objective of this research is to investigate experimentally the influences of surface quality on the rolling contact fatigue life and failure modes of HIPed silicon nitride. Since the surface quality is directly related to the finishing process, a systematic study of the finishing process of HIPed silicon nitride balls has been carried out.

The specific objectives are:

(1) to design and manufacture a lapping machine as the test bench to study the finishing process of HIPed Si_3N_4 rolling elements, to modify the current two-plate lapping mechanism in order to achieve maximum finishing rate while maintaining a satisfactory surface quality and to further explore the potential and find out the upper limits of load and speed in two-plate lapping.

(2) to investigate experimentally the influences of finishing parameters, namely, load, speed, diamond particle size and paste concentration, on the material removal rate and surface quality of HIPed Si_3N_4, and using Taguchi Methods to optimise the finishing parameters.

(3) to investigate experimentally the influences of surface roughness, surface heterogeneous porosity, surface defects (star defects, grinding defects and

C-crack defects), surface finishing parameters and surface residual stresses on the RCF life and failure modes of HIPed Si_3N_4 under lubricated conditions by using the TE92/HS Rotary Tribometer configured as 4-ball and 5-ball RCF test apparatus.

The logical links between finishing parameters, surface quality and RCF performance are illustrated in Fig 1-6.

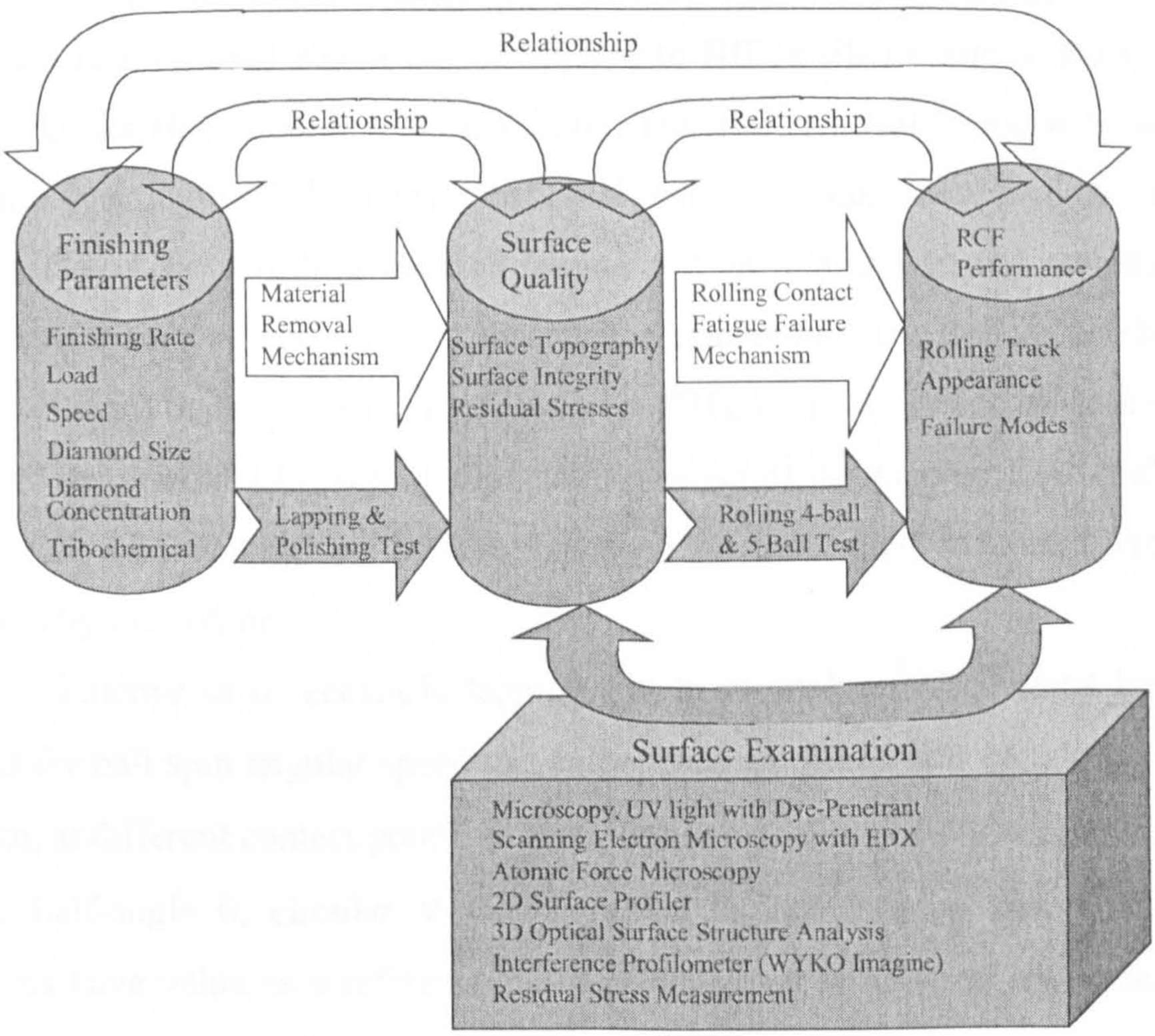

Fig. 1-6 Research Scope

1.3.2 Research Findings and Implications

A novel eccentric lapping machine was designed and manufactured. Two kinds of HIPed silicon nitride ball blanks were finished on this machine. A finishing rate of 68

μm/hour was achieved, which is 15 times higher than conventional concentric lapping (normally 3~4μm/hour). The polished ball surface roughness value R_a is 0.003 μm, and ball roundness is 0.08~0.09μm which is above grade 5, close to grade 3 precision bearing ball specification. This novel eccentric lapping method can be used by industrial manufacturers; the potential savings on the finishing time and cost are huge.

This research has identified the lapping load as the most influential parameter on the finishing rate. The finishing rate is almost proportional to the lapping load. The maximum lapping load which can be applied to HIPed silicon nitride balls is 42.87 N/ball. Under this condition the maximum material removal rate can be achieved without subjecting the ball to any substantial surface or subsurface damage. This has been validated by a rolling contact fatigue test in addition to the residual stress measurement and ball surface and subsurface examination. This finding also has great industrial value because currently in industry HIPed silicon nitride balls are lapped under a load around 19.6 N/ball. One-fold increase of the lapping load could cause the increase of finishing rate by one fold even for traditional concentric lapping as predicted by the author.

The kinematics of eccentric lapping has been analysed. Equations have been derived for ball spin angular speed ω_b, ball spin angle β and ball circulation angular speed ω_c at different contact points on the V-groove as functions of eccentricity E, V-groove half-angle θ, circular V-groove radius R_g and lapping speed Ω_p. These equations have value as a reference point in designing large-scale eccentric lapping machines for industrial application.

It was found through rolling contact fatigue tests that the surface roughness values R_a and R_q (rms) are still the most influential parameters to RCF behaviour. The effect of other parameters such as the shape of the valley, R_{sk} and R_{ku} are not obvious. With an initial roughness value R_a from 0.016 to 0.094 μm, the surface became smoother after the RCF test and surface pitting (10~20μm) occurred. No typical surface fatigue spall occurred in association with different surface roughness values. In contrast, the surface defects such as C-cracks, star defects, grinding defects and heterogeneous porosity proved to be detrimental to RCF performance.

It was also found through experiment that the residual stress change due to the finishing processes remained within 130 MPa, even under extreme high lapping load. This will not greatly affect the contact stress distribution according to FEA modelling.

1.4 Structure of Thesis

Chapter 1 presents the general background of the research, the current literature on the finishing methods of advanced ceramic balls, the finishing parameters in relation to surface quality and the surface quality in relation to rolling contact fatigue performance. The outline of the research and the thesis structure are also briefly described in this chapter.

The design of a novel eccentric lapping machine and 5-ball rolling contact fatigue test, together with the eccentric lapping kinematics analysis are described in Chapter 2. The experimental and analytical methodology including the sample preparation and inspection, finishing test, rolling 4-ball and rolling 5-ball test, surface microscopy study and surface topography measurement, residual stress measurement, etc., are described in Chapter 3.

The experimental results and discussions on the finishing processes are presented in Chapter 4. The investigations of different lapping parameters on material removal rate are reported in section 1. The application of the Taguchi Method to optimise lapping parameters for maximum material removal rate is described in section 2. The effects of aggressive lapping on ball surface integrity are covered in section 3. The influencing factors at the final polishing stage together with a small L4 Arrays two-level Taguchi Method investigation are described in section 4. Residual stresses induced by the finishing process are investigated and discussed in section 5. The material removal mechanism during lapping is explored in section 6.

Experimental results and discussions on the rolling contact fatigue test are presented in Chapter 5. The effects of the surface roughness parameter on rolling contact fatigue performance are discussed first, followed by the influences of surface

heterogeneous porosity. The influences of surface defects, namely, star defects, grinding defects and C-cracks, and the finishing rate on RCF life, the comparison of 4-ball and 5-ball rolling tests and the changes in residual stresses during RCF tests are also discussed in this chapter.

The conclusions and recommended further research topics resulting from this thesis are outlined in Chapter 6. The detailed calculations on contact mechanics and EHD analysis as well as FEA modelling, the technical drawings for the eccentric lapping machine and the 5-ball rolling test are contained in the Appendices.

2.0 DESIGN OF A NOVEL ECCENTRIC LAPPING MACHINE & 5-BALL ROLLING CONTACT FATIGUE TEST

This chapter presents the design of a novel eccentric lapping machine. The purpose for designing such a machine is to modify the current two-plate lapping method, aiming to increase productivity. This machine is also used to conduct all lapping and polishing tests. The design of a 5-ball rolling contact fatigue test is also presented in this chapter. It was envisaged that the 5-ball rolling configuration would introduce more traction on the upper ball, and might thus change the fatigue behaviour. The eccentric lapping machine and 5-ball rolling contact fatigue test were designed by the author. The non-standard mechanical parts were manufactured by local industry, the standard mechanical parts and electronic components were purchased, and assembled by the author.

2.1 Design of A Novel Eccentric Lapping Machine

2.1.1 Basic Idea of Eccentric Lapping

The urgent need to advance the finishing process of advanced ceramic balls and a comparison of different two-plate lapping mechanisms were described in the Literature Review in Chapter 1. In an attempt to accelerate the finishing process by modifying current two-plate lapping mechanisms, a novel eccentric lapping machine was designed by the author. Fig. 2-1 illustrates the two-plate eccentric lapping mechanism.

The basic idea of the eccentric lapping mechanism is that while the upper plate with a flat lapping surface is stationary, the lower plate with an eccentric circular V-groove rotates. The distance between the centre of the circular V-groove and the rotating axis is the eccentricity. Because of the eccentricity, it is anticipated that there will be an increase and decrease of ball circulation velocity. The balls will skid between lapping plates and the ball spin angle will change continuously. This could be advantageous in achieving fast finishing of advanced ceramic balls.

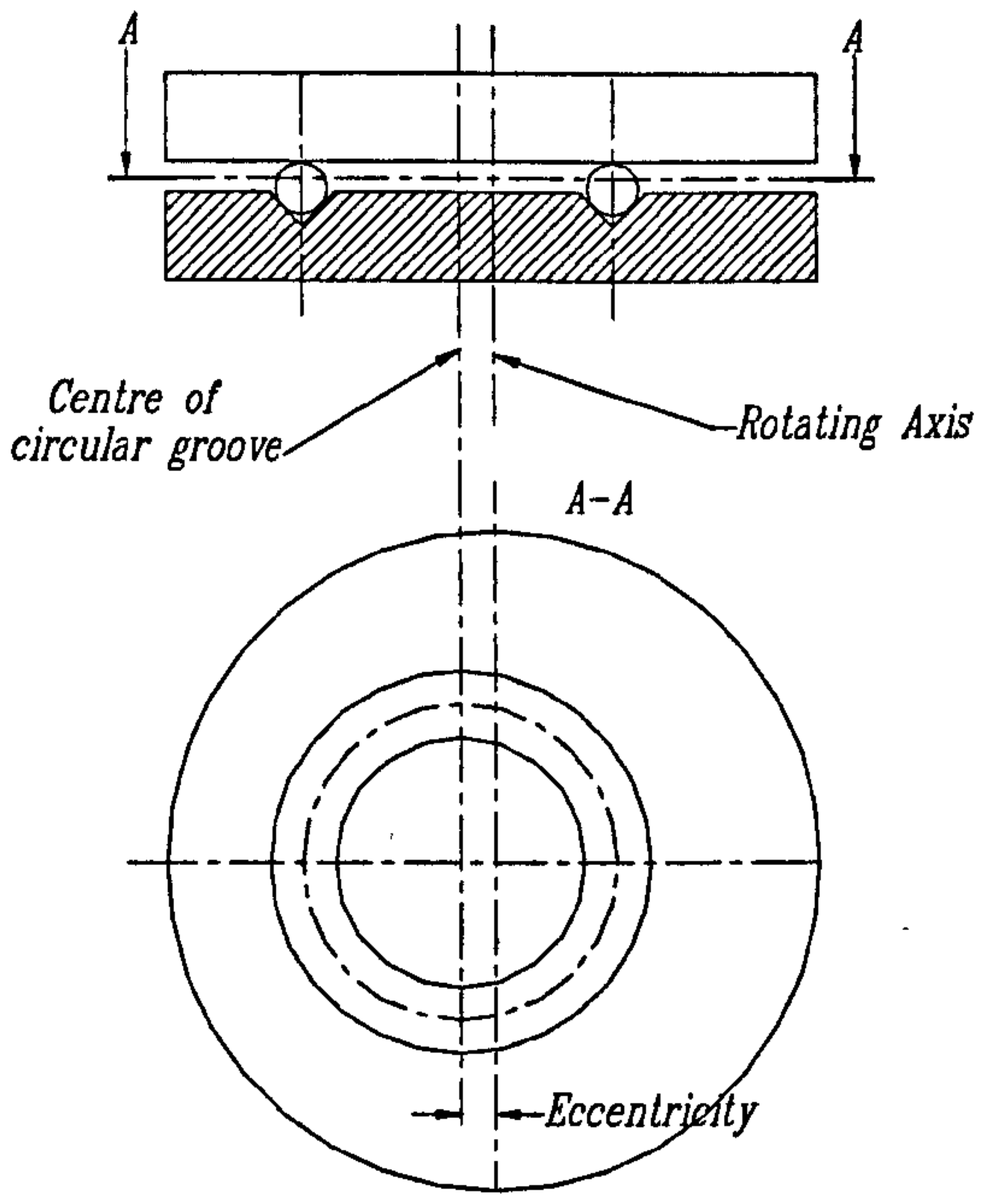

Fig. 2-1 Two-plates eccentric lapping mechanism

2.1.2 Design of Lapping Machine System

A small-scale eccentric lapping machine was designed by the author which allows finishing of 13.4 mm diameter ball blanks in small batches (15 balls). This machine was intentionally designed for small batches in order to carry out various lapping and polishing tests using a minimum number of ball blanks. This machine provides a platform to verify the basic eccentric lapping idea and also enables the investigating of the loose abrasive process and the effects of different lapping parameters on the

finishing of advanced ceramic balls. This section outlines the whole eccentric lapping machine system. The lapping load, lapping speed and kinematics of this eccentric lapping machine will be described in the following sections. The general assembly drawing of this machine and all technical drawings for each of the non-standard mechanical parts are listed in Appendix 1. This machine system can be seen in Fig 2-2. A labelled diagram is given in Fig 2-3.

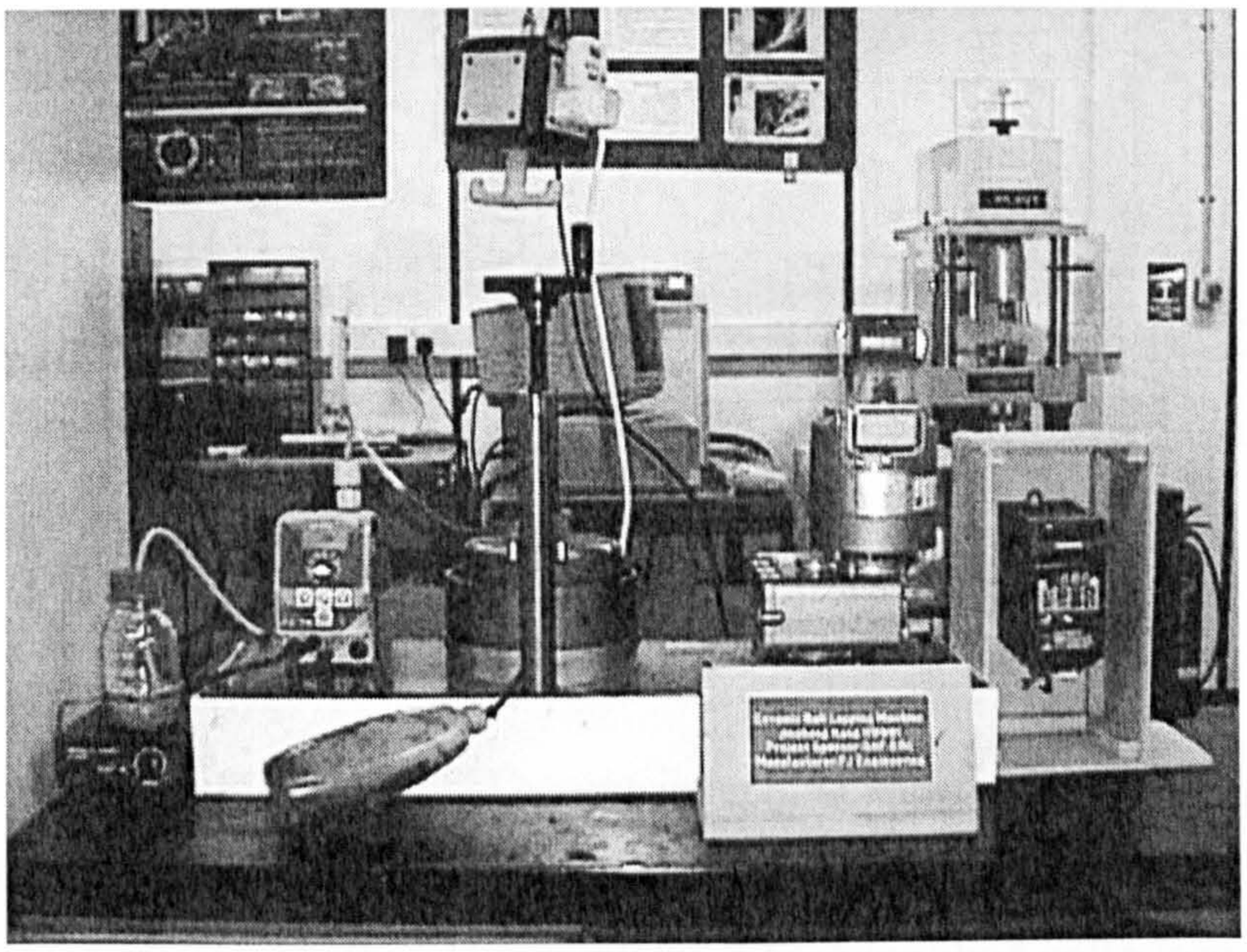

Fig. 2-2 Overview of the novel eccentric lapping machine system

A three-phase AC motor and gearbox combination (1) drives a flange shaft (3) through pulleys and belt (2) to rotate at a pre-set speed. The speed of the AC motor is determined by the output current frequency of a MicroMaster inverter (15). The input current frequency of the inverter is 50 Hz, while the output current frequency of the inverter can be set to 0.1 Hz ~ 400 Hz, which is the input of the AC motor. Because the input current frequency is proportional to the rotating speed of the AC motor, the rotating speed of the flange shaft can be set from 0.54 rpm to 2160 rpm. The lower plate (4) which has an eccentric V groove is mounted on the flange shaft. The upper plate (6) which has a flat surface is stationary. Ceramic balls (5) are lapped between the upper plate and the V groove of the lower plate.

The lapping fluid outside the V groove circle on the lower lapping plate will

flow to the hub of the flange shaft under centrifugal force and drip through a hole to the lapping fluid tray (8) underneath the flange shaft. From there, the fluid goes through a pipe to a lapping fluid collection tank (7). Lapping fluid is pumped by a ProMinent gamma/4 diaphragm-type metering pump (11) at a pre-set stroke through

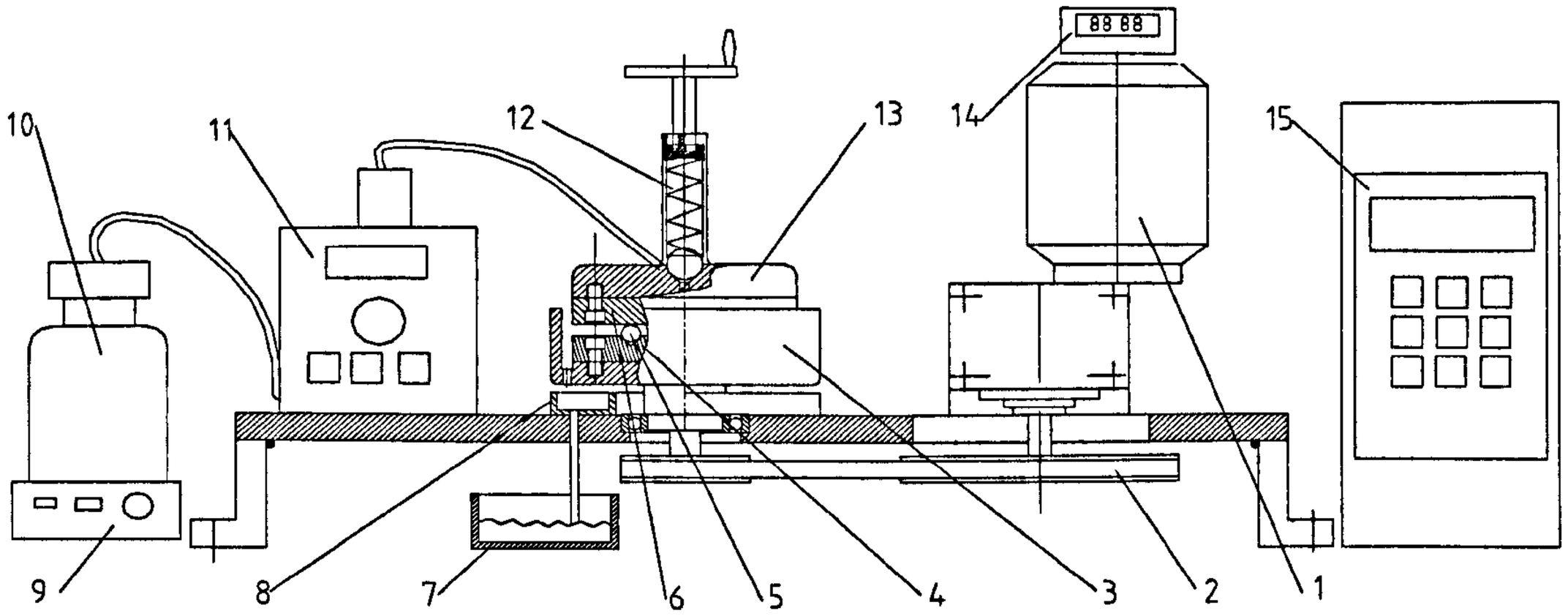

Fig. 2-3 Novel eccentric lapping apparatus

1 AC motor and gearbox combination 2 Pulleys and belt 3 Flange shaft
4 Lower plate 5 Ceramic ball 6 Upper plate 7 Lapping fluid collection tank
8 Lapping fluid tray 9 Magnetic stirrer 10 Lapping fluid container 11 Pump
12 Spring-loading Unit 13 Backing plate 14 Time counter 15 MicroMaster inverter

a pipeline to the centre of the upper lapping plate. The lapping fluid is a mixture of diamond paste and lapping fluid. It is in a container (10) and is mixed and maintained in equal concentration by a magnetic stirrer (9). The amount of lapping fluid applied is controlled by the pre-set stroke number/minutes of the pump and a timer. The duration of the application (i.e. 5 minutes) and time interval (i.e. every 3 hours) are controlled by this timer. When the timer is at "ON" period, the pump and magnetic stirrer will activate simultaneously. The load (lapping pressure) is applied to the upper lapping plate by the spring-loading unit (12). To ensure the lapping pressure is evenly distributed across the upper plate, the spring load is applied through a

spherical element to the cone surface of a blind countersink on the top centre of the backing plate (13). A digital time counter (14) is connected to the voltage input of the AC motor so that the actual lapping time can be counted.

Both upper and lower lapping plates can be easily removed from the backing plate and flange shaft for change or trim purposes. The lapping plates are made in pairs using different materials (cast iron, steel, and aluminium). The eccentricity and angle of the V-groove also varies.

2.1.3 Lapping Load

The lapping load is applied to the upper plate by a spring-loading unit (see Fig 2-3, also Appendix A1.9 Spring Assembly) through a hand wheel and an M16 screw bar. The end of the screw bar is connected to the spring by a joint, to enable rapid changing of the spring. To ensure the lapping pressure is evenly distributed on the upper plate without any bending moment, the other end of the spring load is applied through a spherical element to the cone surface of a blind countersink on the top centre of the backing plate. Three different loading springs have been used. Two were supplied by SpringMasters with a loading rate 8.16N/mm (D23340) and a loading rate of 47.8N/mm (D13800). Another spring was procured from SouthernSprings, with a loading rate of 12.9N/mm calibrated by the manufacturer. The upper plate and backing plate together weigh 68.6N.

Because of the eccentricity, the lapping load on the individual balls is not equal. That is, when a ball is closer to the geometric centre of the upper plate, it will bear more lapping load; and when it is further from the geometric centre of the upper plate, it will bear less lapping load. This is because the lapping load is applied to the geometric centre of the upper plate, but not the centre of the circular V-groove. The precise solution for the load on each of the balls is achievable by considering the upper plate as a simply supported circular plate without a hole and carrying only one eccentric load (Timoshenko and Woinowsky-Krieger 1981), but this is beyond the scope of this PhD study.

A rough estimation has been made to assess the eccentric loading effect. Most of the lapping tests were conducted using a lapping plate with 8 mm eccentricity and a circular V-groove of 65 mm diameter. Assume in this case only three balls bearing the entire lapping load from the upper plate, evenly distributed at 0°, 120° and 240° to the centre of the circular V-groove, with the centre of the upper plate at 0° to 180° axis and 8 mm closer to Ball 1 at 0° (Fig 2-4). In this case, Ball 2 at 120° and Ball 3

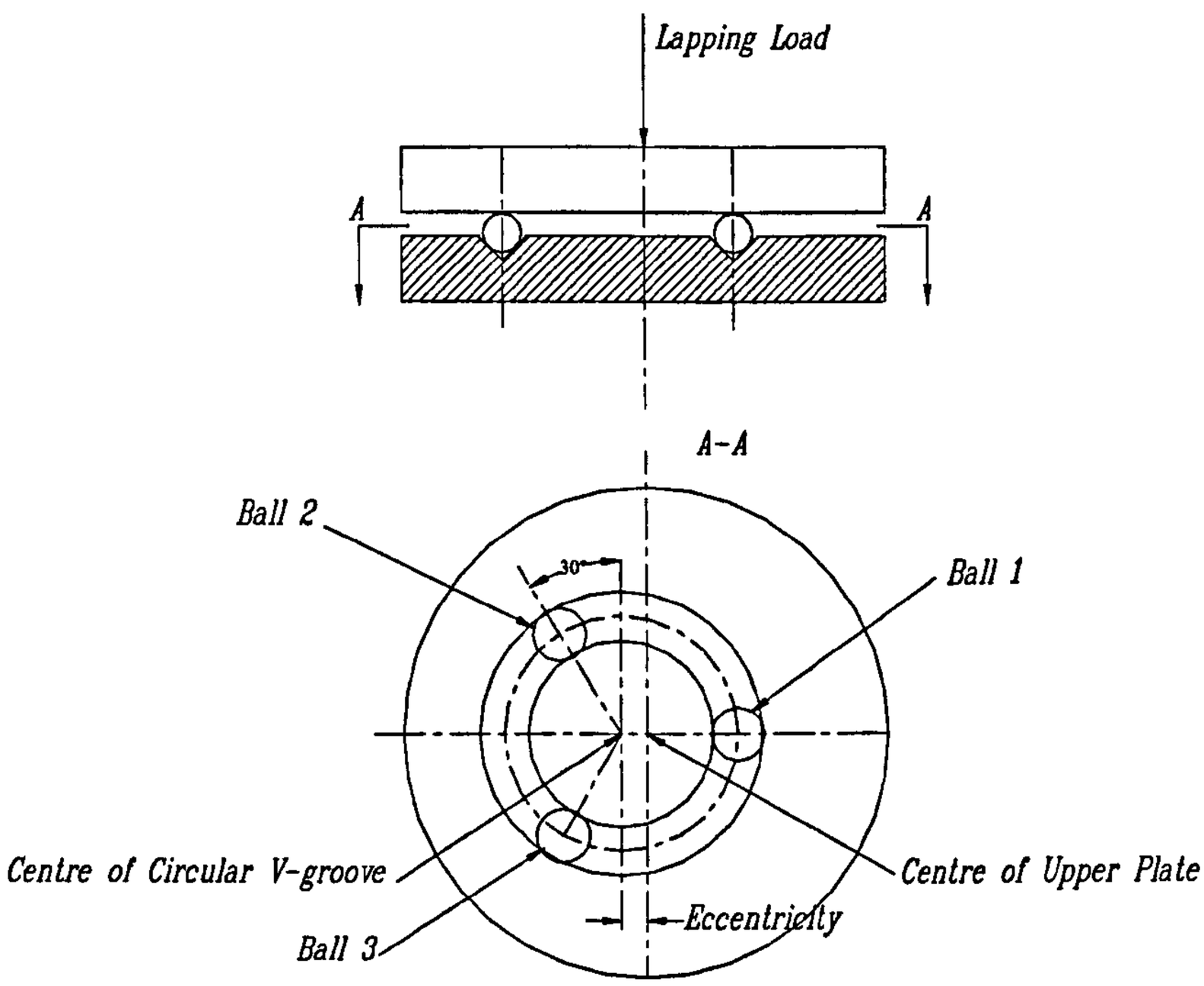

Fig 2-4 Rough estimation of eccentric loading effect

at 240° each carry 0.286 of the entire lapping load, Ball 1 at 0° carries 0.427 of the entire lapping load. The maximum lapping load on a ball (0.427) is 28% higher than the nominal load on a ball (0.333), which is simply the entire lapping load divided by the number of balls bearing lapping load. If only two balls bear the entire lapping load, at 0° and 180°, one would be 0.623 and the other 0.377. The maximum lapping load on a ball (0.623) is 25% higher than the nominal load in this case. From these

two rough estimations, it is concluded that the maximum lapping load on a ball could be 25% ~ 30% higher than the nominal load because of the eccentric loading effect.

In the lapping process (first step of finishing), diamond particles (in the size of 6μ ~ 60μ and below) are distributed between the balls and the lapping plates. In any instance, there may be only a few balls (certainly less than 15) which bear the entire lapping load. Consider an extreme condition where only three balls bear the entire lapping load. In this extreme condition, Ball 1 in Fig 2-4 carries 0.427 of the entire lapping load. The nominal lapping load which is simply the entire lapping load divided by 15 balls, is only 0.0667 of the entire lapping load. So under an extreme condition the maximum lapping load on a ball could be 6.4 times higher than the nominal load. The contact stresses between the upper plate and the balls, between the balls and the V-groove are calculated using classical Hertz elastic contact stress formulae, and are listed in Appendix 4.

2.1.4 Lapping Speed

The change of lapping speed is achieved mechanically by using different combinations of pulleys and by changing the output current frequency of a MicroMaster Inverter. The input current frequency of this inverter is 50 Hz, while the output current frequency of this inverter can be set to 0.1 Hz ~ 400 Hz, which is the input of the AC motor. Because the input current frequency is proportional to the rotating speed of the AC motor, the rotating speed of the flange shaft can be set to 0.54 rpm ~ 2160 rpm. To ensure the rotating speed of the lower plate is correctly set, a tachometer (SPM TAC10) is used to take non-contact measurements, and the actual speed (r.p.m.) of the flange shaft is read digitally.

2.1.5 Eccentric Lapping Kinematics Analysis

In order to understand thoroughly the eccentric lapping process, analysis of the ball kinematics is essential. In this section, some of the computations of symbolic expressions were carried out by Maple 6 software.

2.1.5.1 Derivation of formulae for ball kinematics variables ω_b, β and ω_c

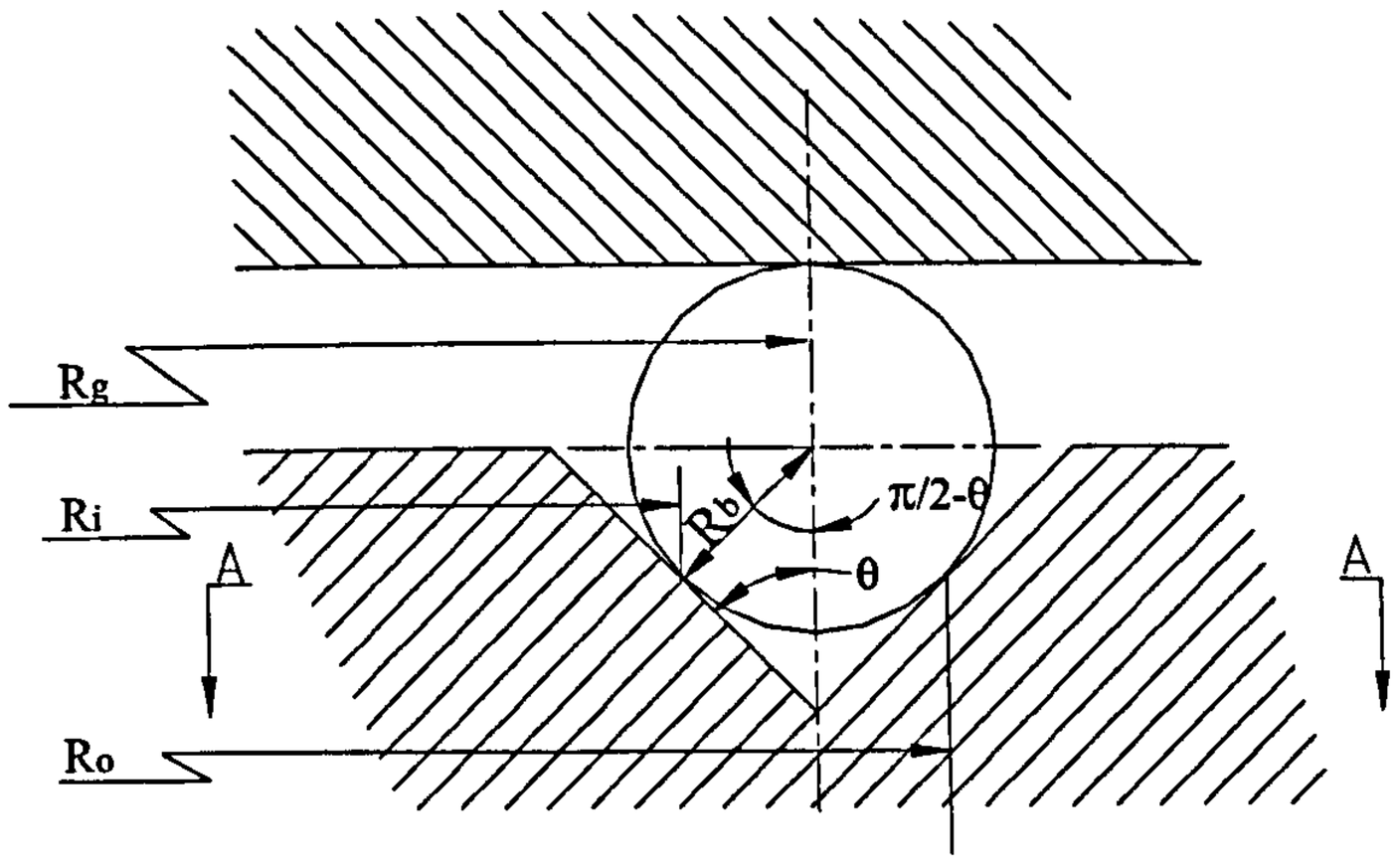

Fig. 2-5 Ball/V-groove inner and outer contact points

Fig. 2-5 shows the contact between a ball and the V-groove in the lower plate. The radius from the centre of the circular V-groove to the ball/V-groove inner contact point, $R_{i,}$, is

$$R_i = R_g - R_b \sin(\frac{\pi}{2} - \theta) = R_g - R_b \cos\theta \tag{2-1}$$

The radius from the centre of the circular V-groove to the ball/V-groove outer contact point, R_o, is

$$R_o = R_g + R_b \sin(\frac{\pi}{2} - \theta) = R_g + R_b \cos\theta \tag{2-2}$$

Fig. 2-6 gives the geometric relationship between the ball/V-groove inner contact point, the ball/V-groove outer contact point and the lower plate rotation angle, which is in the section A-A of Fig. 2-5. If it is assumed that at time t=0, $r_i = R_i - E$, $r_o = R_o - E$, at the instant of time t, the centre of the circular V-groove, the ball/V-groove inner contact point and the centre of the rotating axis form the triangle $R_i\ r_i\ E$, and according to the Cosine Rule from the triangle $R_i\ r_i\ E$,

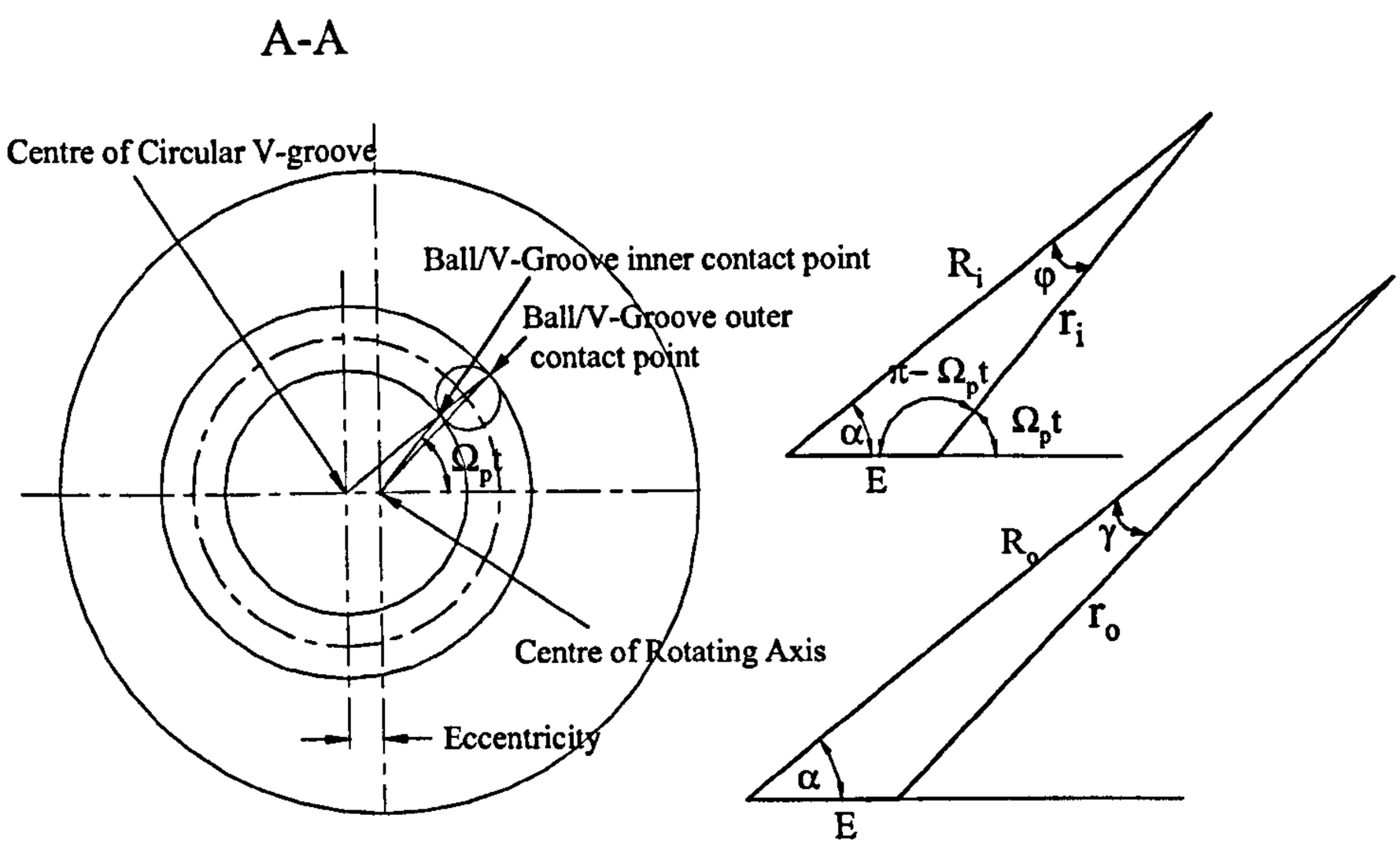

Fig. 2-6 Rotating speeds of lower plate at ball/V-groove inner and outer contact points

$$R_i^2 = E^2 + r_i^2 - 2Er_i\cos(\pi - \Omega_p t) = E^2 + r_i^2 + 2Er_i\cos(\Omega_p t) \qquad (2\text{-}3)$$

Equation (2-3) is a quadratic equation in r_i, and can be solved as

$$r_{i1}, r_{i2} = -E\cos(\Omega_p t) \pm \sqrt{(E^2\cos(\Omega_p t)^2 + R_i^2 - E^2}$$

At $\Omega_p t = 0$, $r_i = R_i - E$, and at $\Omega_p t = \pi$, $r_i = R_i + E$. The real root is

$$r_i = -E\cos(\Omega_p t) + \sqrt{(E^2\cos(\Omega_p t)^2 + R_i^2 - E^2} \qquad (2\text{-}4)$$

According to the Sine Rule from the triangle R_i r_i E,

$$\frac{r_i}{\sin\alpha} = \frac{R_i}{\sin(\pi - \Omega_p t)} = \frac{E}{\sin\varphi}$$

$$\frac{r_i}{\sin\alpha} = \frac{R_i}{\sin(\Omega_p t)} = \frac{E}{\sin\varphi}$$

$$\sin\alpha = \frac{r_i}{R_i}\sin(\Omega_p t)$$

$$\alpha = \arcsin((\frac{r_i}{R_i}\sin(\Omega_p t)) \tag{2-5}$$

$$\sin\varphi = \frac{E}{R_i}\sin(\Omega_p t)$$

$$\varphi = \arcsin((\frac{E}{R_i}\sin(\Omega_p t)) \tag{2-6}$$

At time t, the centre of the circular V-groove, the ball/V-groove outer contact point, and the centre of the rotating axis form the triangle R_o r_o E, and according to the Cosine Rule from the triangle R_o r_o E,

$$r_o^2 = R_o^2 + E^2 - 2ER_o\cos\alpha$$

$$r_o = \sqrt{R_o^2 + E^2 - 2ER_o\cos\alpha} \tag{2-7}$$

substituting α into equation (2-7) from equation (2-5) gives

$$r_o = \sqrt{R_o^2 + E^2 - 2ER_o\sqrt{\frac{R_i^2 - r_i^2 + r_i^2\cos(\Omega_p t)^2}{R_i^2}}} \tag{2-8}$$

According to the Sine Rule from the triangle R_o r_o E,

$$\frac{r_o}{\sin\alpha} = \frac{E}{\sin\gamma}$$

$$\sin\gamma = \frac{E}{r_o}\sin\alpha = \frac{E}{r_o}\sin(\arcsin((\frac{r_i}{R_i}\sin(\Omega_p t))) = \frac{E}{r_o}\frac{r_i}{R_i}\sin(\Omega_p t)$$

$$\gamma = \arcsin(\frac{E}{r_o}\frac{r_i}{R_i}\sin(\Omega_p t)) \tag{2-9}$$

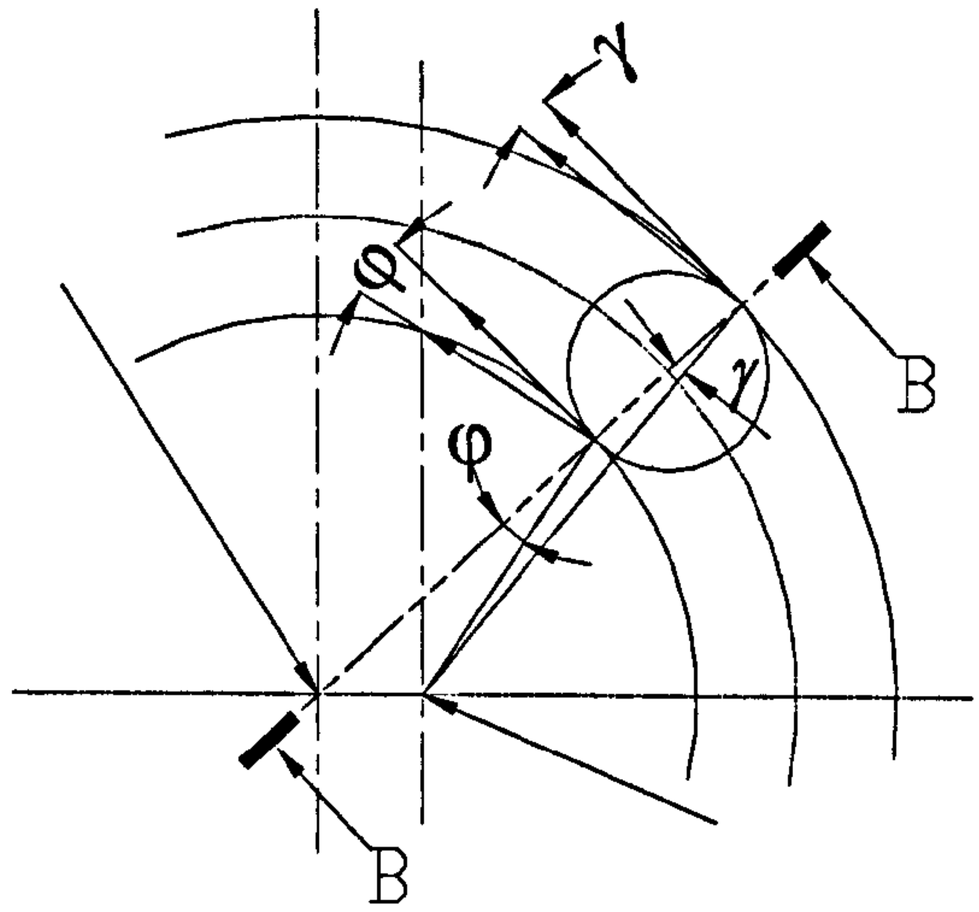

Fig. 2-7 Linear velocities at ball/V-groove inner and outer contact points projected perpendicular to the B-B plane

Fig. 2-7 shows how the linear velocities on the lower plate at the ball/V-groove inner and outer contact points project perpendicularly to the B-B plane (the radial plane through the centre of the circular V-groove). The linear speed at the ball /V-groove inner contact point on the lower plate perpendicular to the B-B plane, V_{ip}, is given by:

$$V_{ip} = r_i \Omega_p \cos\varphi = \Omega_p(-E\cos(\Omega_p t) + \sqrt{(E^2\cos(\Omega_p t)^2 + \mathrm{R_i}^2 - \mathrm{E}^2}\,)\cos(\arcsin(\frac{E}{R_i}\sin(\Omega_p t)))$$

$$= \Omega_p(-E\cos(\Omega_p t) + \sqrt{(E^2\cos(\Omega_p t)^2 + \mathrm{R_i}^2 - \mathrm{E}^2}\,)\sqrt{1 - \frac{E^2\sin(\Omega_p t)^2}{\mathrm{R_i}^2}} \qquad (2\text{-}10)$$

The linear speed at the ball /V-groove outer contact point on the lower plate perpendicular to the B-B plane, $V_{op,}$ is

$$V_{op} = r_o \Omega_p \cos\gamma = \Omega_p \sqrt{R_o^2 + E^2 - 2ER_o\sqrt{\frac{R_i^2 - r_i^2 + r_i^2\cos(\Omega_p t)^2}{R_i^2}}}\ \cos(\arcsin(\frac{E}{r_o}\frac{r_i}{R_i}\sin(\Omega_p t)))$$

$$= \Omega_p \sqrt{R_o^2 + E^2 - 2ER_o\sqrt{\frac{R_i^2 - r_i^2 + r_i^2\cos(\Omega_p t)^2}{R_i^2}}}\ \sqrt{1 - \frac{E^2 r_i^2\sin(\Omega_p t)^2}{R_i^2 r_o^2}} \qquad (2\text{-}11)$$

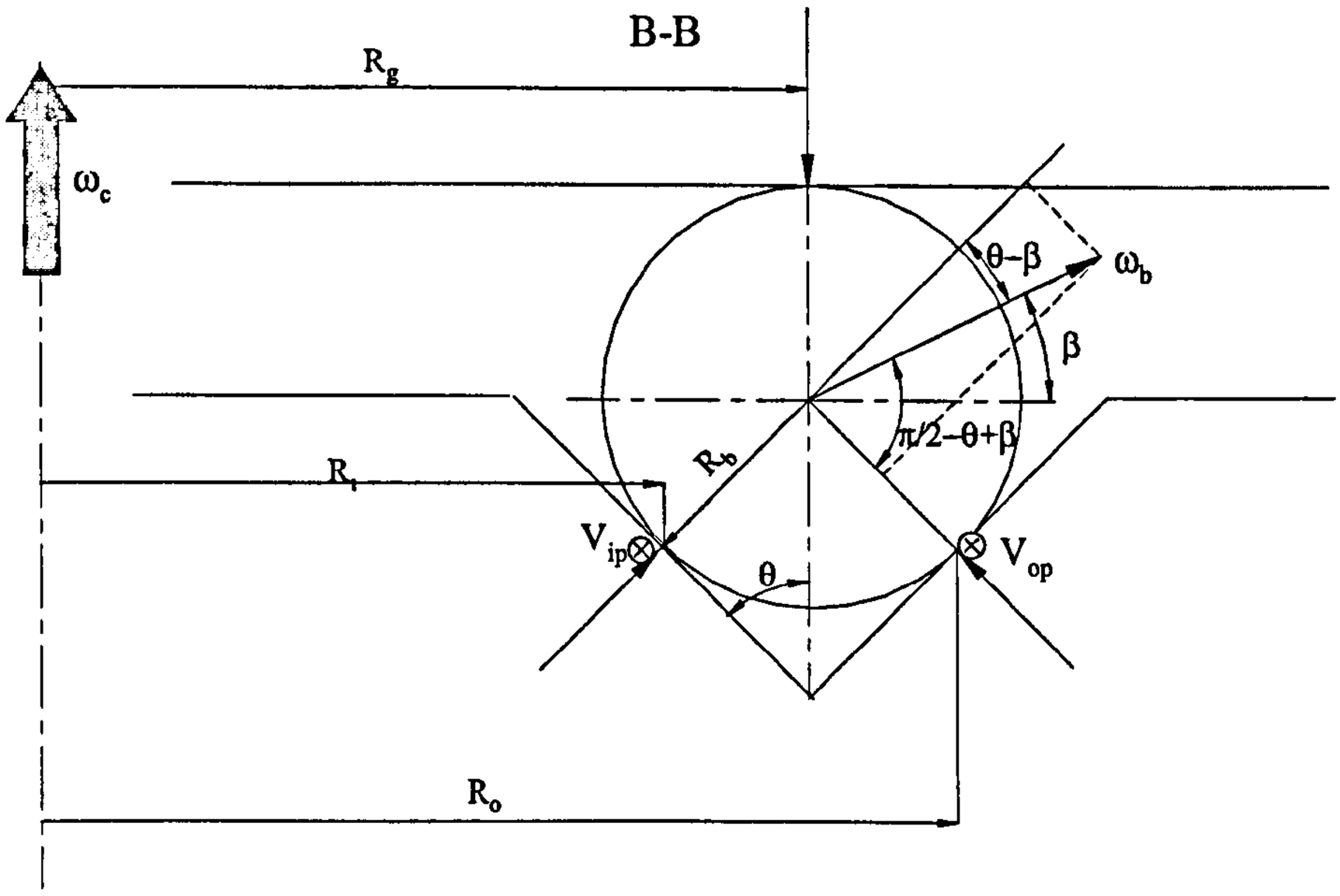

Fig. 2-8 Definition for ball kinematics variables

Fig. 2-8, which is in the section B-B of Fig. 2-7, introduces the ball/V-groove and ball/upper plate contact geometry and defines the independent ball kinematics variables: ball spin angular speed ω_b, ball spin angle β and ball circulation angular speed ω_c. In the analysis of ball kinematics, the following simplification has been made: (1) there is no sliding between ball and plates; (2) the influence of occasional ball to ball contact is not included; (3) ball spin component normal to the plane of Fig. 2-8 is ignored which is equivalent to ignoring the gyroscopic effects and estimated to be small (Childs et al. 1994). In this case, at the ball/V-groove inner contact point,

$$V_{ip} = R_b\omega_b \cos(\frac{\pi}{2} - \theta + \beta) + R_g\omega_c \tag{2-12}$$

at the ball/V-groove outer contact point,

$$V_{op} = R_b\omega_b \cos(\theta - \beta) + R_g\omega_c \tag{2-13}$$

at the ball/upper plate contact point,

$$0 = R_b\omega_b \cos\beta - R_g\omega_c \tag{2-14}$$

The three equations (2-12) to (2-14) with three unknown variables ω_b, ω_c and β, can be solved by eliminating ω_b, ω_c and β.

Subtract equation (2-13) from equation (2-12):

$$V_{ip} - V_{op} = R_b\omega_b \sin(\theta-\beta) - R_b\omega_b \cos(\theta-\beta) = R_b\omega_b(\sin(\theta-\beta) - \cos(\theta-\beta))$$

$$\omega_b = \frac{V_{ip} - V_{op}}{R_b(\sin(\theta-\beta) - \cos(\theta-\beta))} \tag{2-15}$$

From equation (2-14),

$$R_g\omega_c = R_b\omega_b \cos\beta \tag{2-14-1}$$

Substitute (2-14-1) to equation (2-12):

$$V_{ip} = R_b\omega_b \cos(\frac{\pi}{2} - \theta + \beta) + R_b\omega_b \cos\beta = R_b\omega_b(\sin(\theta-\beta) + \cos\beta) \tag{2-12-1}$$

Substitute ω_b into equation (2-12-1) with equation (2-15), equation (2-12-1) then becomes

$$V_{ip} = \frac{(\sin(\theta-\beta) + \cos\beta)(V_{ip} - V_{op})}{\sin(\theta-\beta) + \cos(\theta-\beta)} \tag{2-12-2}$$

β can be derived from equation (2-12-2) as

$$\beta = -\arctan\left[\frac{-V_{op} - V_{op}\sin(\theta) + \cos(\theta)V_{ip} + V_{ip}}{\cos(\theta)V_{op} + \sin(\theta)V_{ip}}\right] \tag{2-16}$$

Substitute β with equation (2-16), ω_b in equation (2-15) can be expressed as function of $\Omega_p t$.

From equation (2-14-1), substitute ω_b with equation (2-15):

$$\omega_c = \frac{R_b\omega_b \cos\beta}{R_g} = \frac{\cos\beta(V_{ip} - V_{op})}{R_g(\sin(\theta-\beta) - \cos(\theta-\beta))}$$

$$= \frac{V_{ip}\sin(\theta) + V_{op}\cos(\theta)}{R_g(1 + \cos(\theta) + \sin(\theta))} \tag{2-17}$$

2.1.5.2 The variations of ω_b, β and ω_c at different contact points on the V-groove

Fig. 2-9 shows the variations in ball spin angular speed ω_b, ball spin angle β and ball circulation angular speed ω_c at different contact points on the V-groove (designated as rotation angle of the lower plate $\Omega_p t$) during a 360° rotation of the lower plate. This is under a typical lapping condition, R_b=6.5 mm, R_g=32.5 mm, θ=45°, Ω_p=169 rpm=17.7 rad/s. The three curves are symmetric to 180°, which is consistent with the eccentric V-groove geometry.

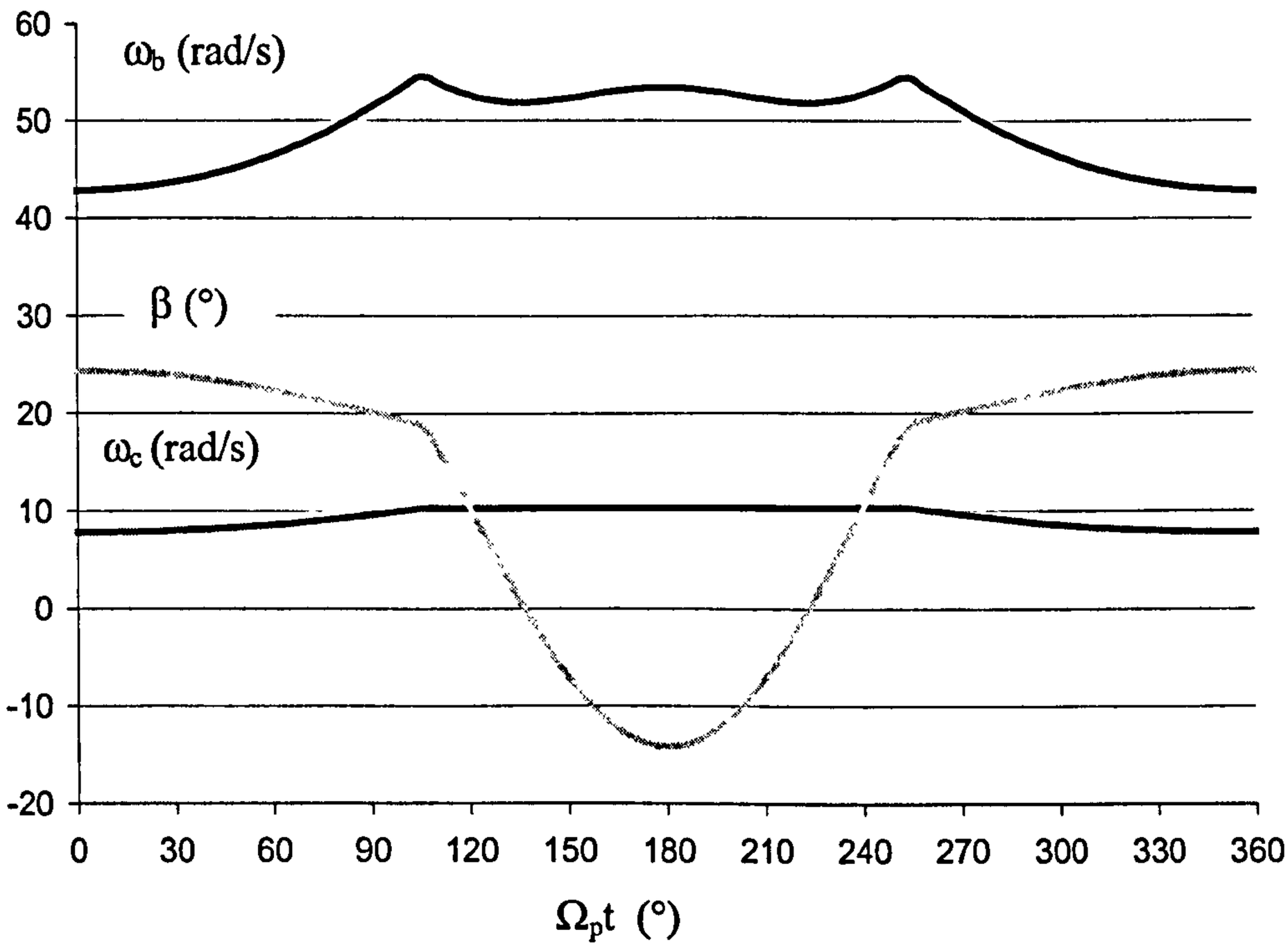

Fig. 2-9 Variations of ball spin angular speed ω_b, ball spin angle β and ball circulation angular speed ω_c during a 360° rotation of the lower plate under a typical lapping condition.

The ball spin angular speed ω_b ranges between 42.9~54.4 rad/s. At first it increases from the lowest to the highest as the lower plate rotation angle increases from 0° to 105°. Then it starts to decrease and maintains a relatively stable value at

around 51.8~53.4 rad/s and increases again as the lower plate rotation angle rises from 105° to 255°. Finally it decreases from the highest to the lowest as the lower plate rotates from 255°to 360°.

The ball spin angle β changes from 24.4°to –14.2°, a range of nearly 40°. This ball spin angle change is considered to be beneficial to ball roundness as well as to material removal rate. The ball spin angle changes gradually as the lower plate rotation angle increases from 0° to 105°. From 105° to 180°, the ball spin angle change is sharp, and at 180° the direction is changed smoothly. From 180° to 360°, the ball spin angle change is symmetric with 180°~0°.

The ball circulation angular speed ω_c is in the range of 7.8~10.4 rad/s, and the ball circulation direction is the same as the rotating direction of the lower plate. The value of ω_c increases gradually from 7.8~10.4 rad/s as the lower plate rotates from 0° to 105°. It maintains 10.4 rad/s unchanged from 105° to 255° and decreases gradually to 7.8 rad/s from 255° to 360°.

The lower plate rotation angles 105° and 255° are transition points for the ball spin angular speed ω_b, the ball spin angle β and the ball circulation angular speed ω_c. It is anticipated that at around these two points, micro-slip will occur which will also be beneficial to ball roundness as well as to the material removal rate. The ball circulation angular speed ω_c is 44%~59% of the lower plate angular speed Ω_p, depending on the relative location of the ball to the lower plate. For a specific ball, its location relative to the lower plate changes by 56%~41% of a full 360° rotation during each complete rotation of the lower plate, but this change could be different from one rotation to another. The ball spin angular speed ω_b and the ball spin angle β is changing all the time, which, with the micro-slip between the ball and the plate at the transition points, as well as the ball-plate contact, actually defines a Hertzian circular area contact, so that all of the ball surface is lapped, and ball roundness is achieved.

2.1.5.3 The influences of eccentricity (E)

Fig. 2-10 demonstrates the influences of different eccentricity values (E =2, 4, 8, 12mm) on ball spin angular speed ω_b, ball spin angle β and ball circulation angular speed ω_c. All the other parameters remain unchanged as in Fig. 2-9, with R_b=6.5 mm, R_g=32.5 mm, θ=45°, and Ω_p=169 rpm =17.7 rad/s. As the eccentricity increases, the changing amplitudes of ω_b, β and ω_c also rise. Among the three variables, the extension of the changing amplitude of β is the most significant. At E=2mm, the changing amplitude of β is only about 10°, while at E=12 mm, the changing amplitude of β becomes 55°. The increase of the changing amplitude of ω_c is least significant. At E=2 mm, for example, the ball circulation angular speed ω_c is almost a constant at the value ω_c=10.4 rad/s, while at E=12 mm, ω_c is changing from 7.2 rad/s to 10.4 rad/s. The increase of the changing amplitude of the ball spin angular speed ω_b is associated with the sharper changes at the transition points. It also indicates that as the eccentricity increases, the transition points for ω_b, β and ω_c shift.

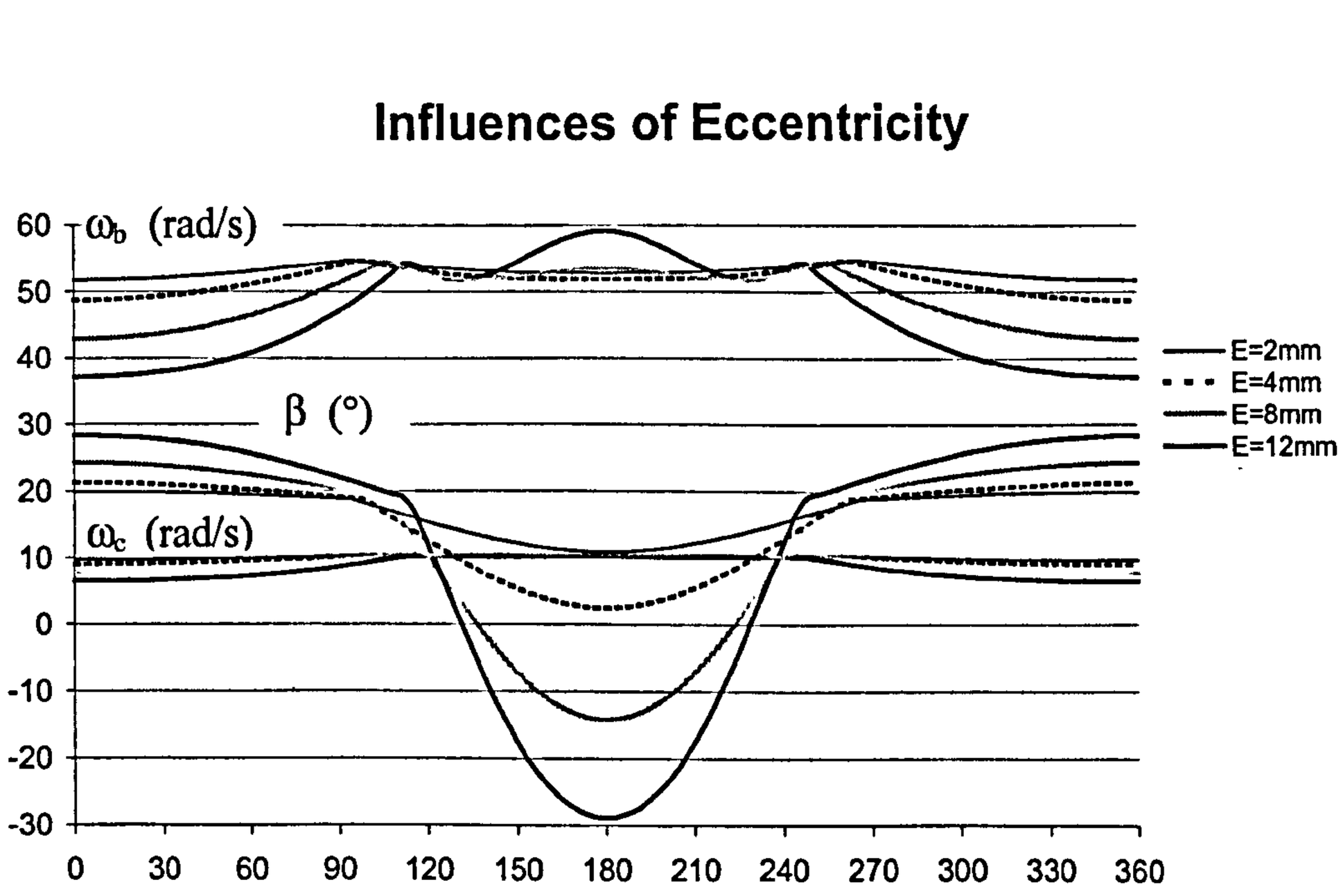

Fig. 2-10 Influences of eccentricity E on ball spin angular speed ω_b, ball spin angle β and ball circulation angular speed ω_c

2.1.5.4 The influences of V-groove half-angle θ

Fig. 2-11 illustrates the influence of V-groove half-angle θ (as specified in Fig. 2-5), on ball spin angular speed ω_b, ball spin angle β and ball circulation angular speed ω_c. The other parameters are set to be the same as in Fig. 2-9, i.e., R_b=6.5 mm, R_g=32.5 mm, E=8 mm, Ω_p=169 rpm =17.7 rad/s. The V-groove half-angle θ does not affect ω_b and ω_c very much, with only a little sharpening at the transition points of ω_b as θ increases. The changing amplitude of β does not vary, although there is a shift in angle β.

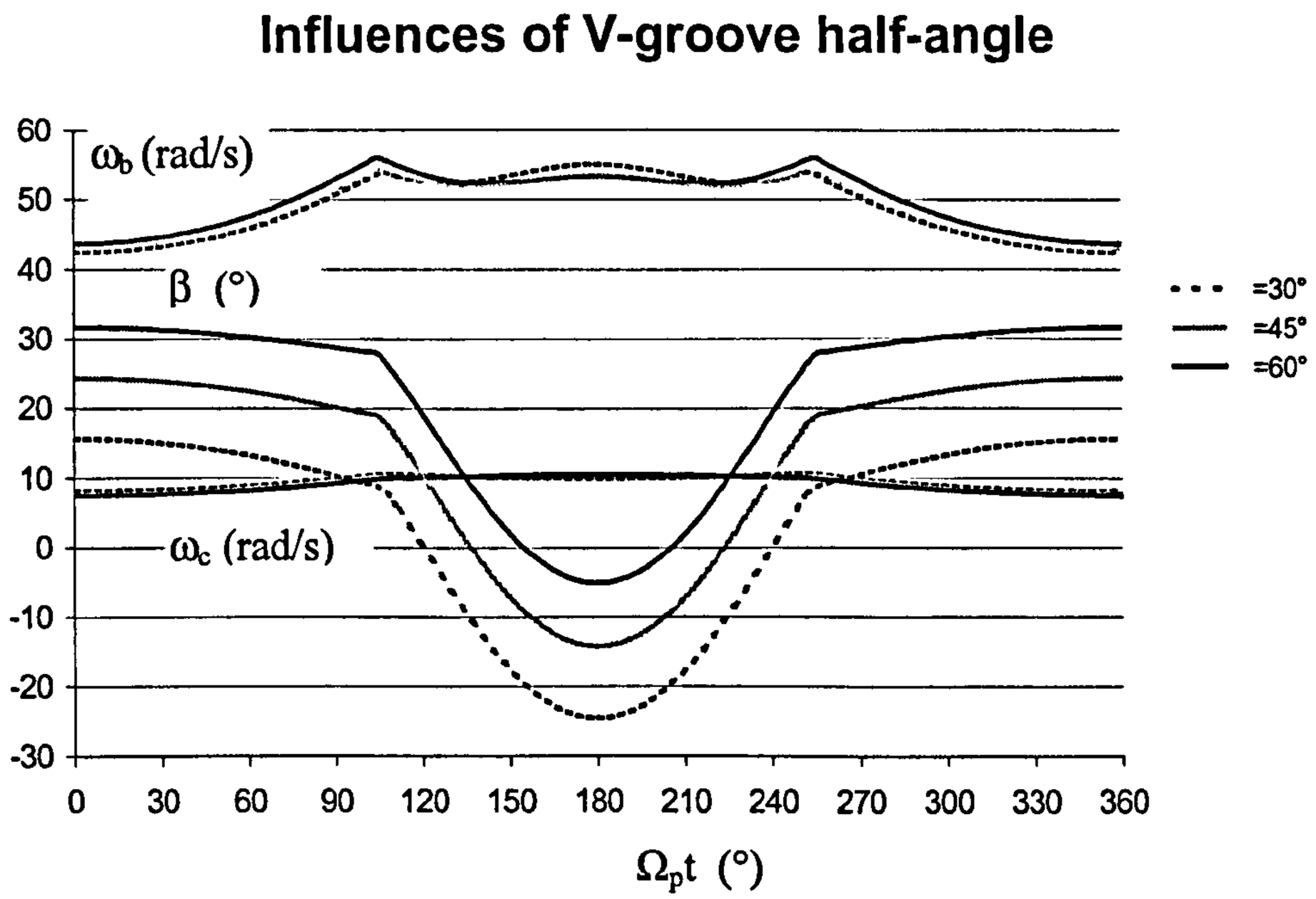

Fig. 2-11 Influences of V-groove half-angle θ on ball spin angular speed ω_b, ball spin angle β and ball circulation angular speed ω_c

2.1.5.5 The influences of lapping speed Ω_p

Fig. 2-12 presents the influences of lapping speed, Ω_p (specified as rpm for straightforward understanding), on ball spin angular speed ω_b, ball spin angle β and ball circulation angular speed ω_c. All other parameters are the same as in Fig. 2-9, i.e.,

R_b=6.5 mm, R_g=32.5 mm, E=8 mm, θ=45°. The lapping speed has no effect on β, as the β value for all different lapping speeds is the same (the curves for β overlapped in Fig. 2-12). As the lapping speed increases, the ball spin angular speed ω_b rises and the change at the transition points becomes sharper. The ball circulation angular speed ω_c rises proportionally as the lapping speed increases.

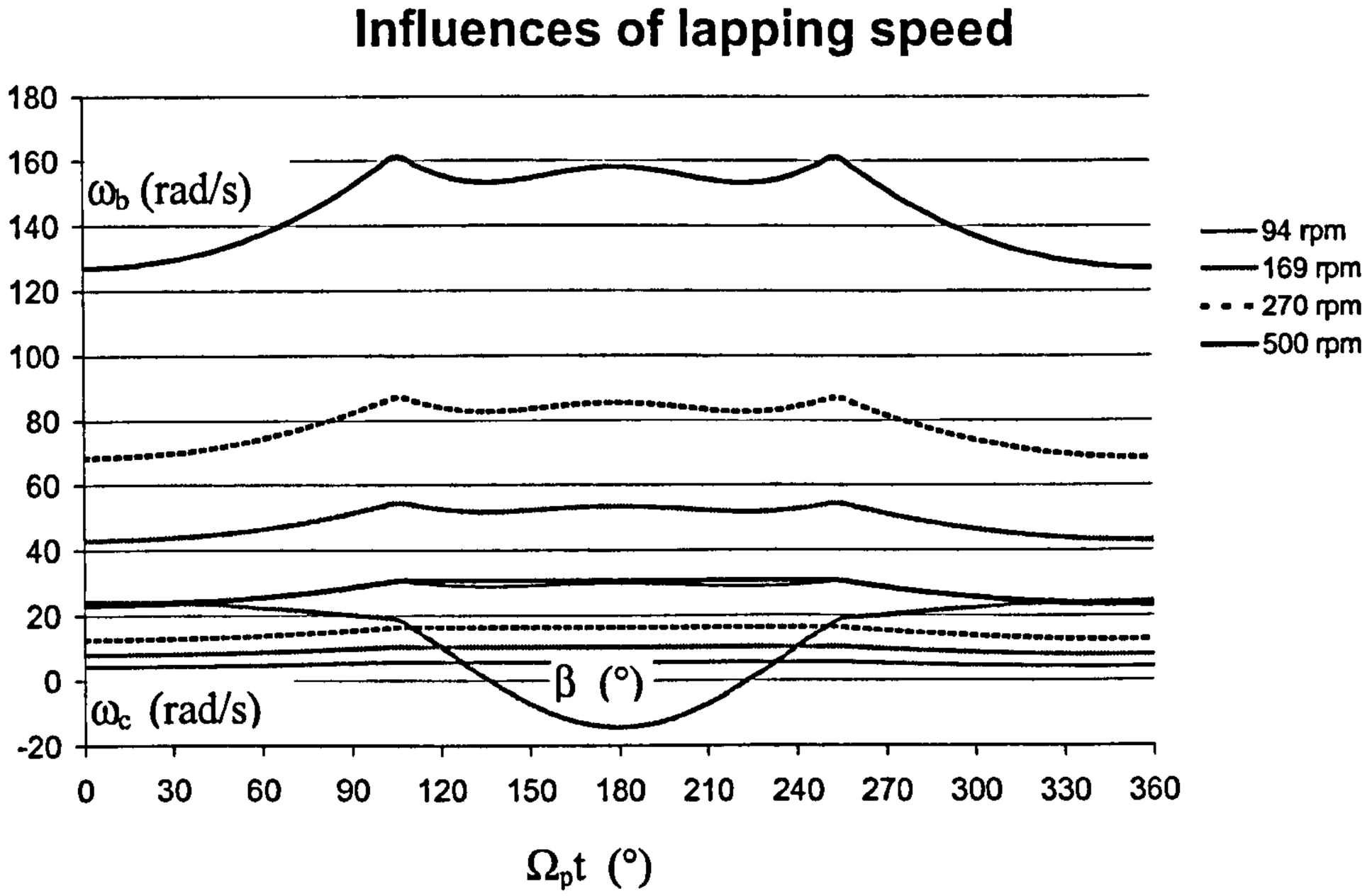

Fig. 2-12 Influences of lapping speed on ball spin angular speed ω_b, ball spin angle β and ball circulation angular speed ω_c

2.1.5.6 The influences of the circular V-groove radius R_g

Fig. 2-13 reveals the influences of the circular V-groove radius, R_g, on ball spin angular speed ω_b, ball spin angle β and ball circulation angular speed ω_c. All other parameters are the same as in Fig. 2-9, R_b=6.5 mm, E=8 mm, θ=45°, Ω_p=169 rpm =17.7 rad/s. Comparing Fig. 2-13 with Fig. 2-10, for β and ω_c, the effects of increasing R_g are similar to those of decreasing E. The ball spin angular speed ω_b will rise proportionally as R_g increases. Therefore, if R_g and E increase at the same time, β and ω_c will probably remain unchanged, but ω_b will rise. The increase in ball

spin angular speed ω_b will be beneficial in achieving better material removal rate and ball roundness, implying that even better lapping and polishing results could be achieved on a large scale eccentric lapping machine.

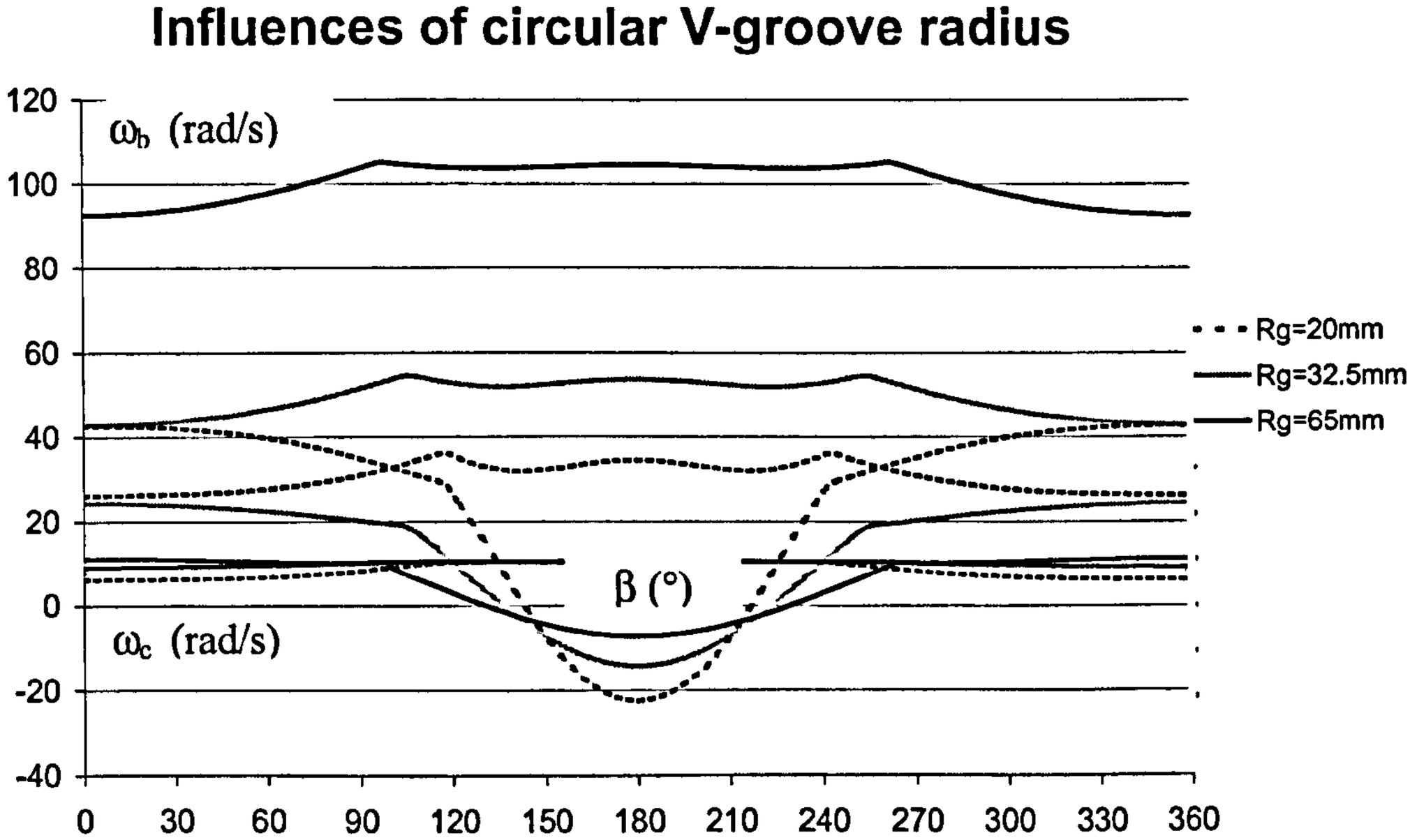

Fig. 2-13 Influences of circular V-groove radius R_g on ball spin angular speed ω_b, ball spin angle β and ball circulation angular speed ω_c

2.1.5.7 Conclusions from kinematics analysis

Kinematics analysis reveals that the most influential parameter is the eccentricity E. The changing amplitudes of the ball spin angular speed ω_b, the ball spin angle β and the ball circulation angular speed ω_c increase as E increases. The V-groove half-angle θ has little effect. With an increase in lapping speed, ω_b and ω_c rise proportionally but β remains unchanged. The effects of increasing circular V-groove radius R_g on β and ω_c are similar to decreasing E, but ω_b rises proportionally with the increase of R_g. This information can be used in designing a large scale eccentric lapping machine for production.

2.2 Design of 5-Ball Rolling Contact Fatigue Test

The design of a 5-ball rolling contact fatigue test incorporated modifications to the cup of the 4-ball test in the TE92/HS Rotary Tribometer, making reference to the 5-Ball Fatigue Tester used in NASA, USA, reported by Paker and Zaretsky (1975). It is anticipated that there will be more traction in the contact zone for the upper ball in the 5-ball test. The purpose of running a 5-ball test was to make a comparison with a 4-ball test to see if there was any difference in the rolling contact fatigue performance for the upper silicon nitride samples.

2.2.1 Design of 5-ball Rolling Cup

The design of the 5-ball rolling cup made modifications to Plint TE92/HS Rotary Tribometer's 4-ball cup to accommodate four lower balls in the cup instead of three. The race maintained the same radius as the 4-ball cup with a maximum size of 7.62 mm and minimum size of 7.59 mm. The only change was the distance between the two centres of the radius of the race in a section. This measured 13.21±0.02 mm for the 4-ball cup and was increased to 18.20±0.02 mm for the 5-ball cup. All the other technical specifications and dimensions for the 5-ball cup are the same as the 4-ball cup in the Plint TE92/HS Rotary Tribometer. The technical drawing for the 5-ball cup is illustrated in Appendix 2.

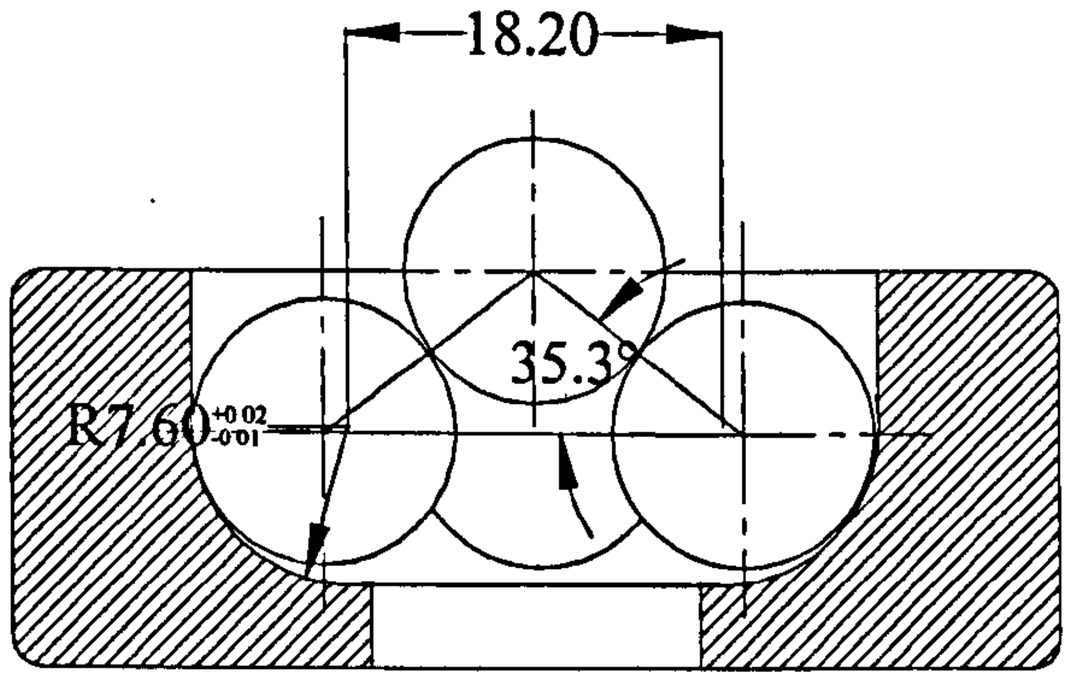

Fig. 2-14 Contact angle design of 5-ball rolling cup

The distance between the two centres of the radius of the race in a section, 18.20 mm, is derived from the contact angle design. The diameters for one upper ball and four lower balls are both 12.7 mm. Fig. 2-14 shows the contact angle design. For a contact angle of 35.3°, the distance between the central axis of the cup and the centre of one lower ball is

$$12.7\cos 35.3° = 10.37$$

The distance between the centre of one lower ball and the centre of the radius of the race is

$$7.62 - 6.35 = 1.27$$

Thus the distance between the two centres of the radius of the race in a section is

$$(10.37 - 1.27) \times 2 = 18.2$$

The tolerance for the dimension 18.2 mm is ±0.02 mm, and the radius of the race may vary from 7.62 mm to 7.59 mm. Taking a minimum dimension of 18.2 mm, and the radius of the race also at the minimum size of 7.59 mm, the maximum contact angle is then achieved. The maximum contact angle is

$$(9.1 - 0.01) + (7.59 - 6.35) = 10.33$$

$$\alpha = \arcsin(10.33/12.7)$$

$$\alpha = 35.5°$$

As the dimension 18.2 mm is taken as the maximum size and the radius of the race is also at the maximum size of 7.62, the minimum contact angle is achieved. The minimum contact angle is

$$(9.1 + 0.01) + (7.62 - 6.35) = 10.38$$

$$\alpha = \arccos(10.38/12.7)$$

$$\alpha = 35.2°$$

2.2.2 Design of Cage

A cage was designed to separate the lower balls in the 5-ball cup. Fig. 2-15 depicts the 3D solid model for the cage. In selecting the appropriate material for manufacture of the cage consideration was given to the mass of the material, wear and temperature resistance, low coefficient of thermal expansion, strength and flexibility within temperature ranges, compatibility with lubricants, etc.. The selection of the material for the cage made reference to "Rolling Bearing Analysis (Third Edition)" (Harris 1990). Reinforced phenolic resin was chosen. This material has been used for many years in high speed bearings. The density of this material is only 15% that of steel. The maximum temperature limit for this material is 100 °C. Tests with 4-ball rolling showed temperatures were usually below 70 °C. The technical drawing for the cage can be seen in Appendix 2.

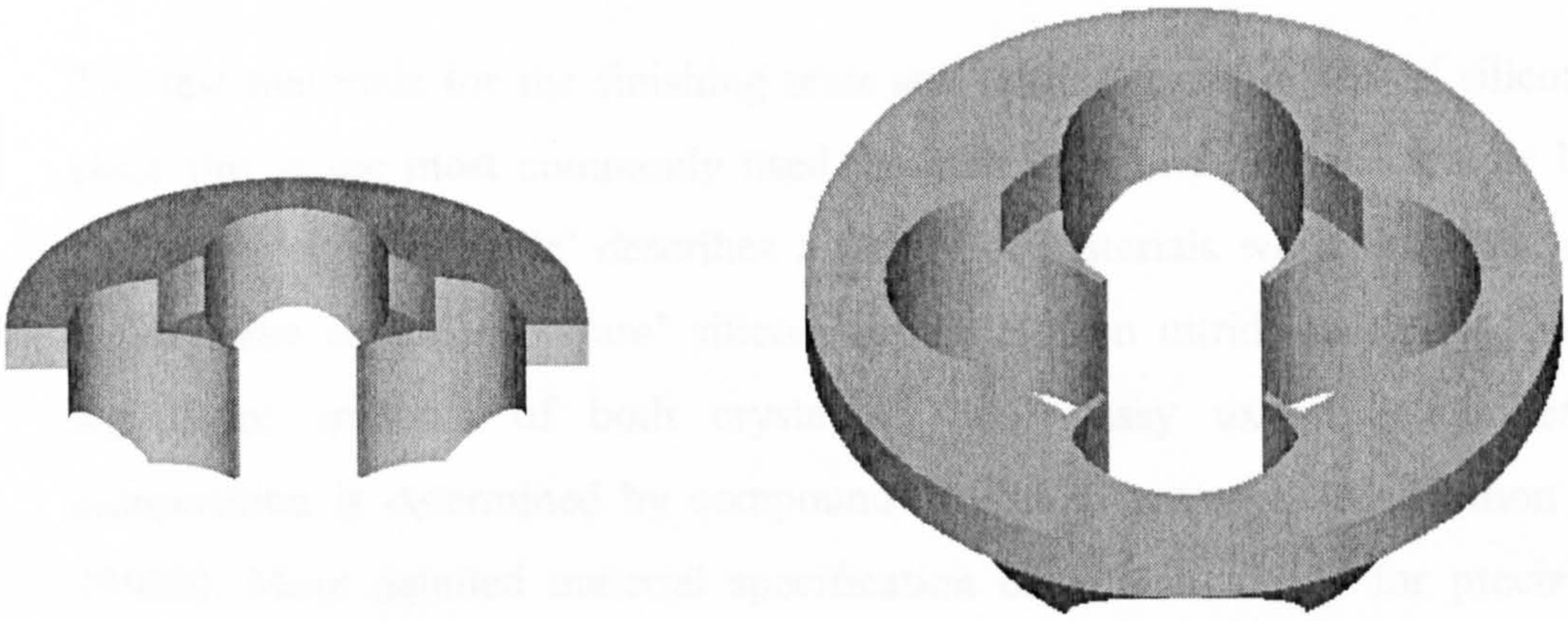

Fig. 2-15 3D solid model for the cage

3.0 EXPERIMENTAL AND ANALYTICAL METHODOLOGY

This chapter presents the experimental and analytical methodology employed in this research. The sample specifications, finishing and fatigue test procedures, surface examination techniques including SEM with EDX, AFM, 2D and 3D topography analysis and residual stress measurement are described. The FEA modelling of the contact stress field with imposed residual stresses is also described.

3.1 Test Materials

The test materials for the finishing tests and fatigue tests are HIPed silicon nitride since this is the most commonly used material in hybrid and all ceramic bearings. The term 'silicon nitride' describes a family of materials which includes alpha- or beta-sialons as well as 'pure' silicon nitride. Silicon nitride materials can contain significant amounts of both crystalline and glassy oxynitride phases whose composition is determined by compounds added to promote densification (Cundill 1992b). More detailed material specification on silicon nitride for precision ball-bearings can be found in references (Cundill 1983, Cundill 1992a, Cundill 1992b).

3.1.1 Sample Balls for Finishing Tests

Sample balls used for finishing tests were two kinds of ball blanks purchased directly from the manufacturers. The individual manufacturing processes and measured characteristics of the two kinds of ball blanks are listed in Table 3-1. Fig. 3-1 shows the 3D topographic images of the two kinds of ball blanks.

	BBA (Ball Blank from manufacturer B)	BBB (Ball Blank from manufacturer B)
Manufacturing Process	Directly HIPed, then rough-ground	Sinter + HIPed
Density (kg/m^3)	3160	3237
Ball Diameter (mm)	13.255	13.46 ~ 13.50
Ball Roundness Variation (mm)	0.001	0.030 ~0.075
Surface Roughness R_a (μm)	0.202	2.645
Surface Hardness (Vikers Hardness Number, VH10)	1682	1532

Table 3-1 Some characteristics of the two kinds of HIPed silicon nitride ball blanks

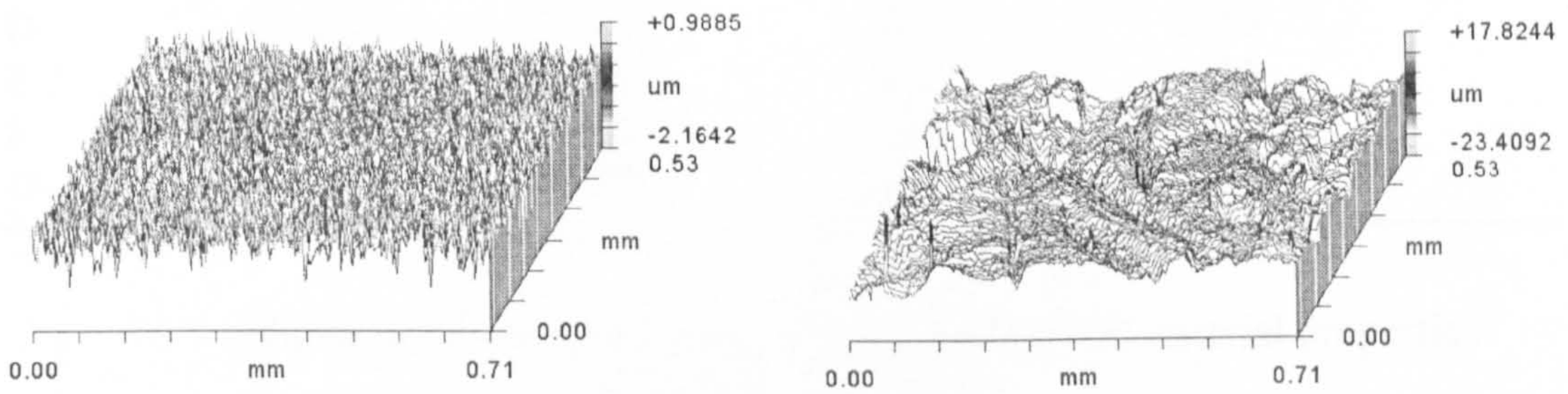

(a) (b)

Fig. 3-1 3D topographic images of ball blanks before finishing,
(a) BBA, (b) BBB

3.1.2 Sample Balls for Fatigue Tests

3.1.2.1 Sample balls with no detectable surface defects

Rolling contact fatigue tests were conducted on balls with no detectable surface defects to investigate the influence of surface roughness and finishing parameters and to compare the 4-ball and 5-ball rolling tests. Sample balls with no detectable surface defects were procured directly from manufacturers A1, B1, C1 and D1 as finished

bearing balls. Self-lapped and polished balls at different loads and speeds from the BBA and BBB were also used.

Table 3-2 shows the measured characteristics of sample balls for fatigue tests to investigate the influences of surface roughness. The 3D topographic images and microscopy observations of these sample balls are shown in Fig. 3-2 and Fig. 3-3 with denotations A for the A1 ball, B for the B1 ball, C for the C1 ball, D for the D1 ball, E for a self-rough-lapped ball from BBB, F for a self-rough-lapped ball from BBA and G for a self-rough-lapped then polished ball from BBA.

Samples	Diameter mm	Surface roughness Ra μm (3D)	Density (kg/m^3)	Surface Hardness (Vickers Hardness Number)
A	12.7004	0.005	3214	1505
B	12.7007	0.016	3238	1560
C	12.6994	0.003	3226	1478
D	12.6998	0.002	3166	1619
E	12.701	0.094	3338	1532
F	12.698	0.08	3160	1682
G	12.703	0.008	3160	1682

Table 3-2 Some of the measured geometric and material properties of fatigue test samples

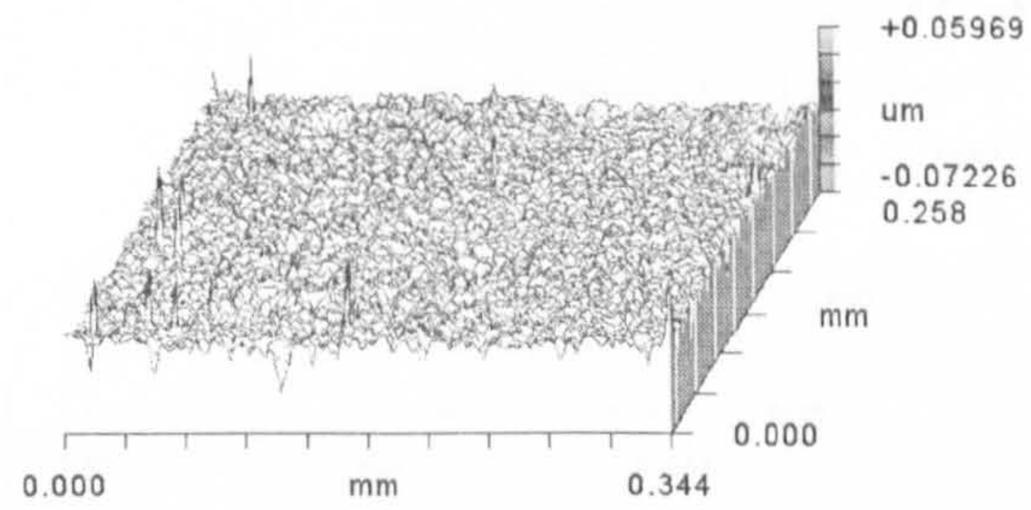

PV	0.132	um	Rku	8.487	
rms	0.007	um	Rsk	-1.380	
Ra	0.005	um	Rz	108.35	nm
Size X	0.34	mm	R3z	106.21	nm
Size Y	0.26	mm	RadCrv	1.23E+011	nm

A

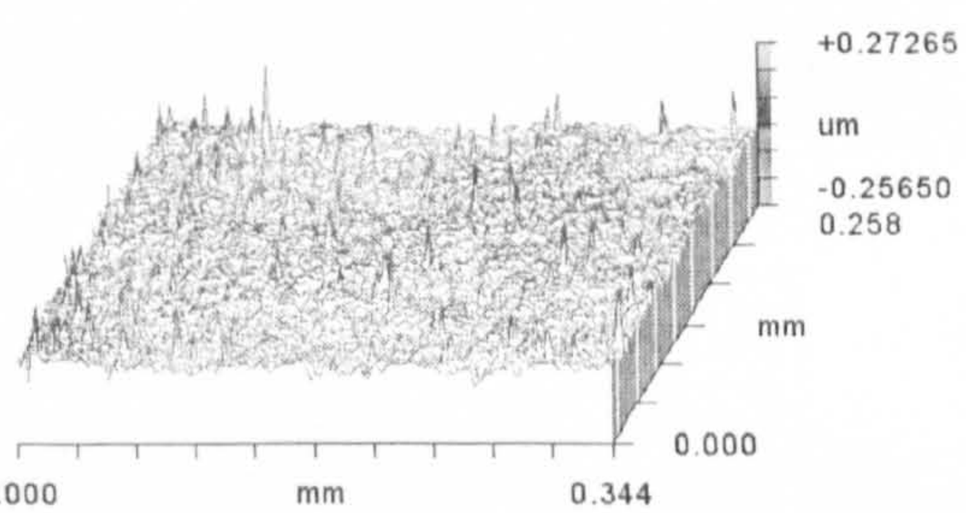

PV	0.529	um	Rku	10.008	
rms	0.021	um	Rsk	0.077	
Ra	0.016	um	Rz	403.54	nm
Size X	0.34	mm	R3z	346.45	nm
Size Y	0.26	mm	RadCrv	-6.34E+009	nm

B

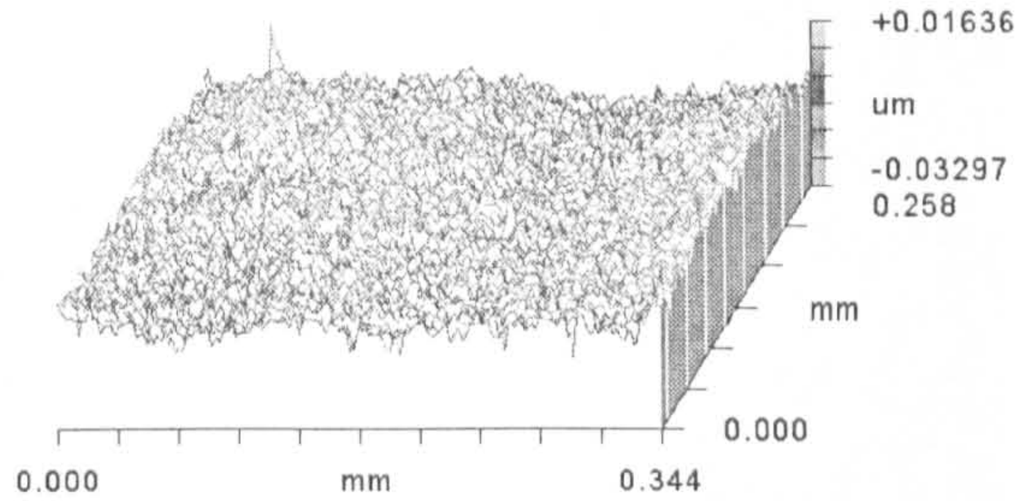

PV	0.049	um	Rku	4.307	
rms	0.004	um	Rsk	-0.597	
Ra	0.003	um	Rz	36.08	nm
Size X	0.34	mm	R3z	36.83	nm
Size Y	0.26	mm	RadCrv	-8.89E+011	nm

C

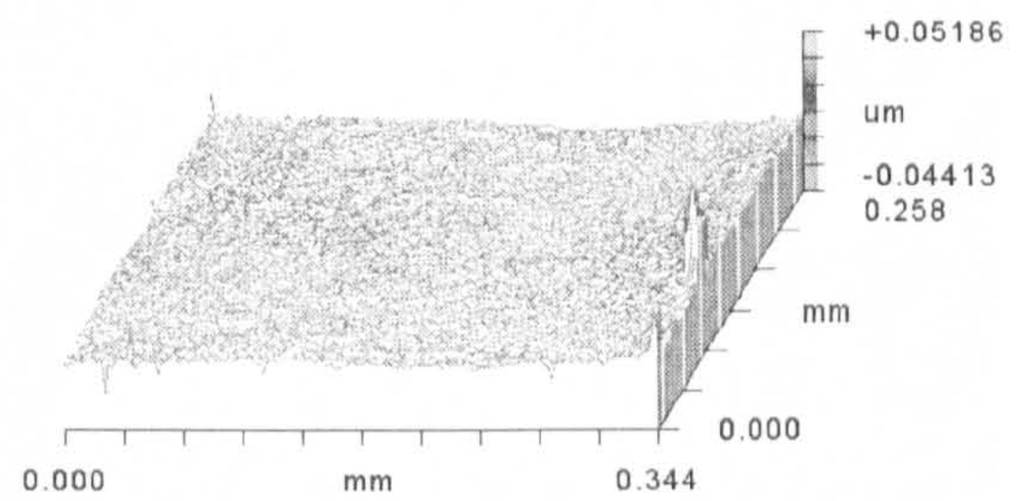

PV	0.096	um	Rku	47.798	
rms	0.003	um	Rsk	2.640	
Ra	0.002	um	Rz	54.56	nm
Size X	0.34	mm	R3z	50.23	nm
Size Y	0.26	mm	RadCrv	-4.14E+011	nm

D

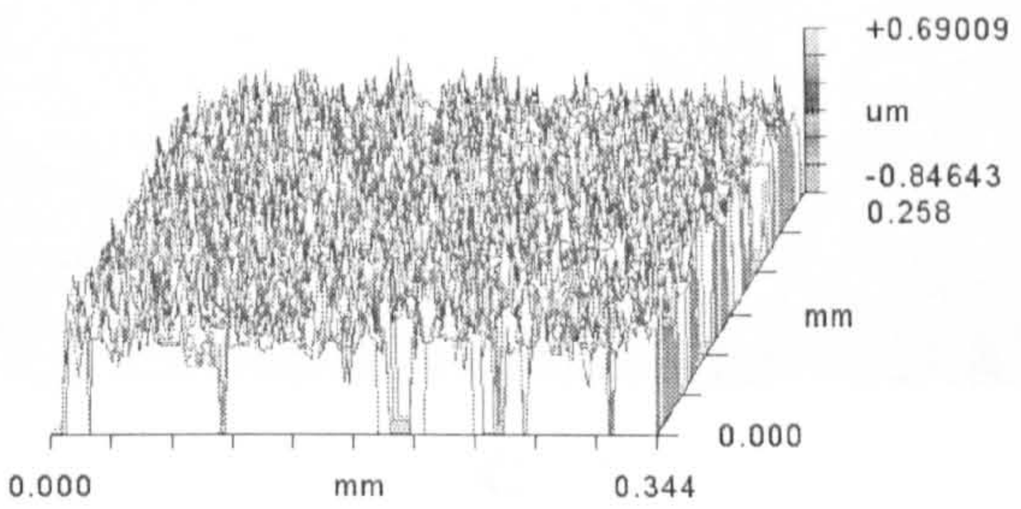

PV	1.537	um
rms	0.132	um
Ra	0.094	um
Size X	0.34	mm
Size Y	0.26	mm

E

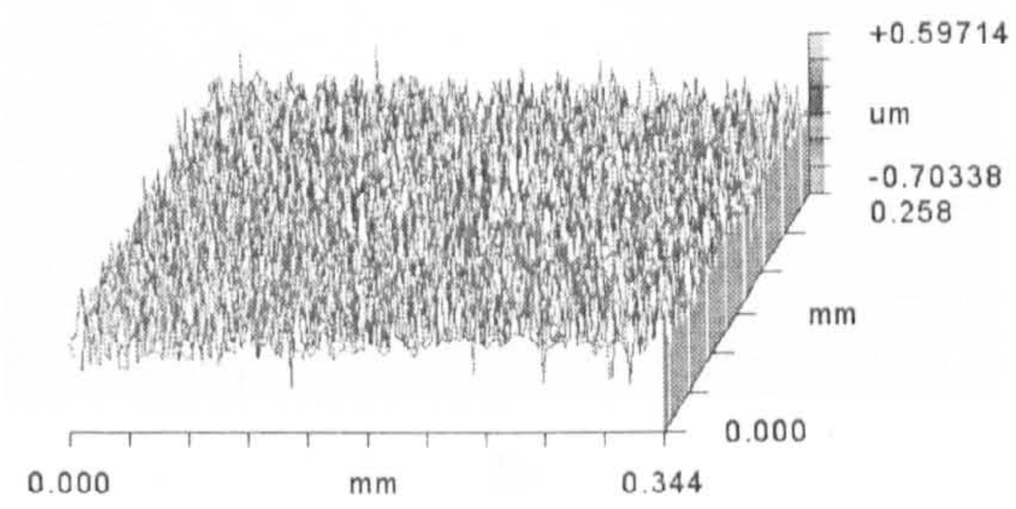

PV	1.301	um	Rku	5.279	
rms	0.118	um	Rsk	0.328	
Ra	0.080	um	Rz	1187.63	nm
Size X	0.34	mm	R3z	1166.10	nm
Size Y	0.26	mm	RadCrv	-5.97E+010	nm

F

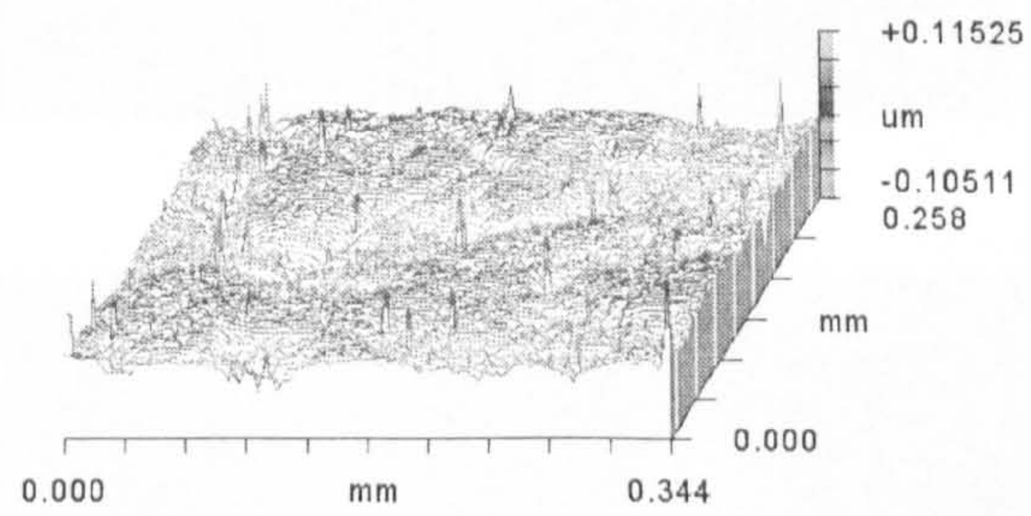

PV	0.220	um	Rku	7.155	
rms	0.010	um	Rsk	-0.868	
Ra	0.008	um	Rz	167.91	nm
Size X	0.34	mm	R3z	161.84	nm
Size Y	0.26	mm	RadCrv	-3.27E+011	nm

G

Fig. 3-2 3D surface topography details of samples A to G

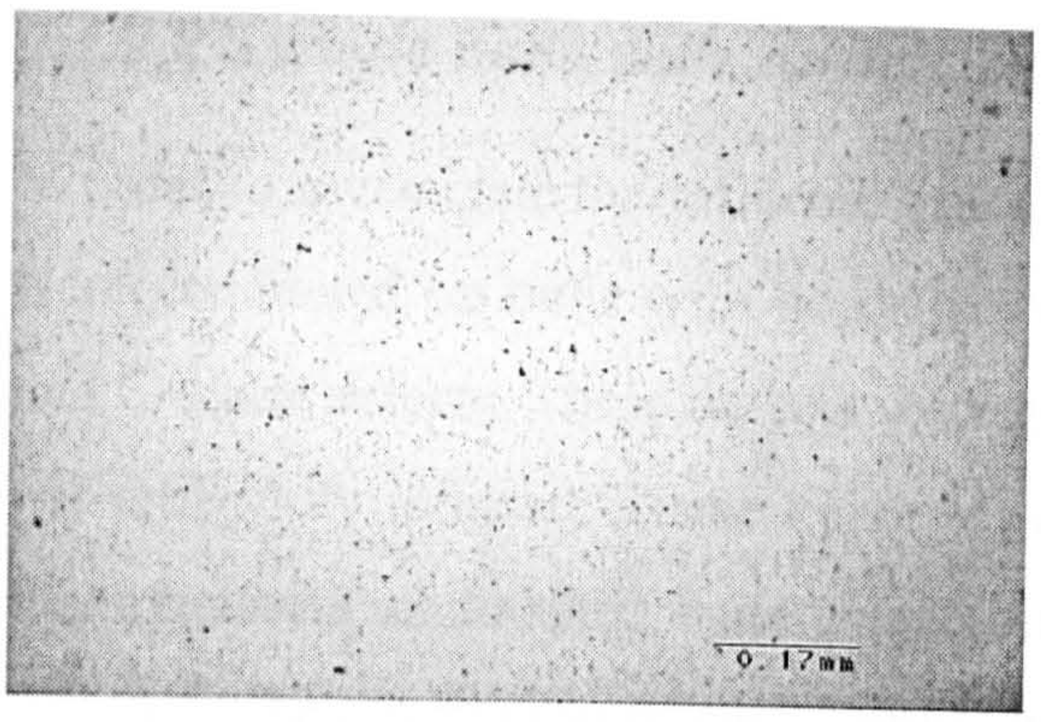

A

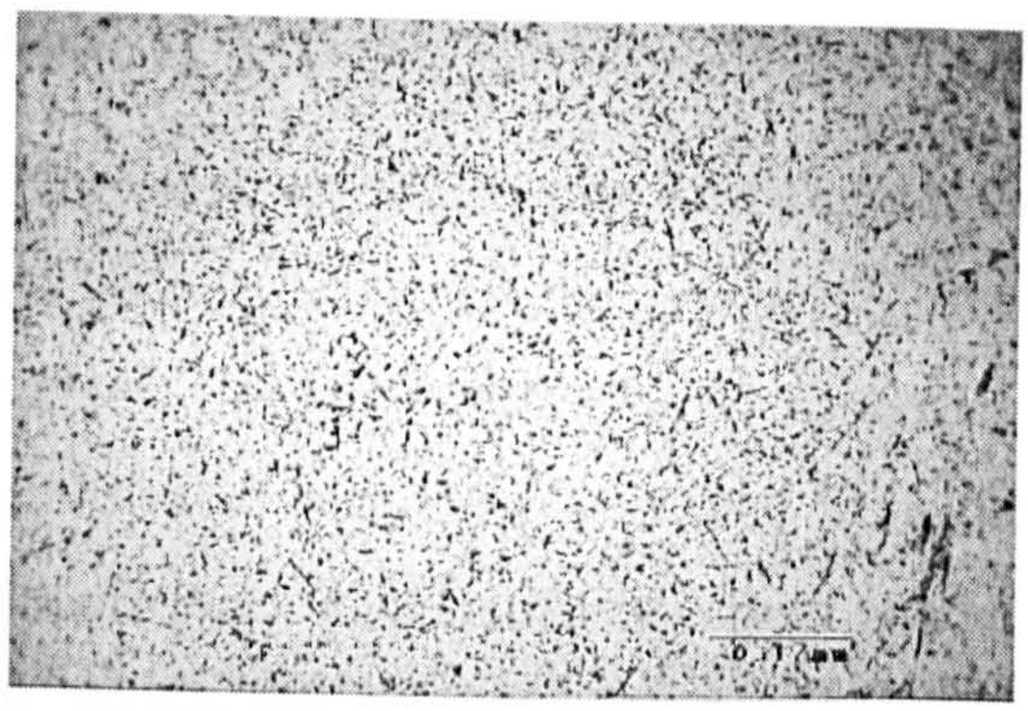

B

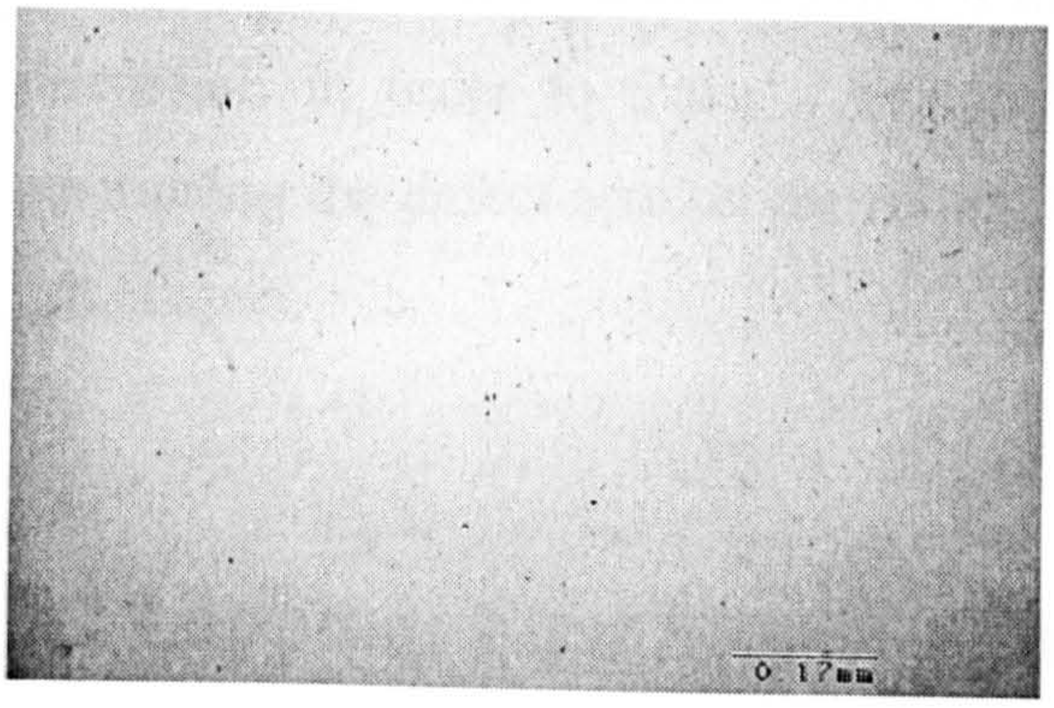

C

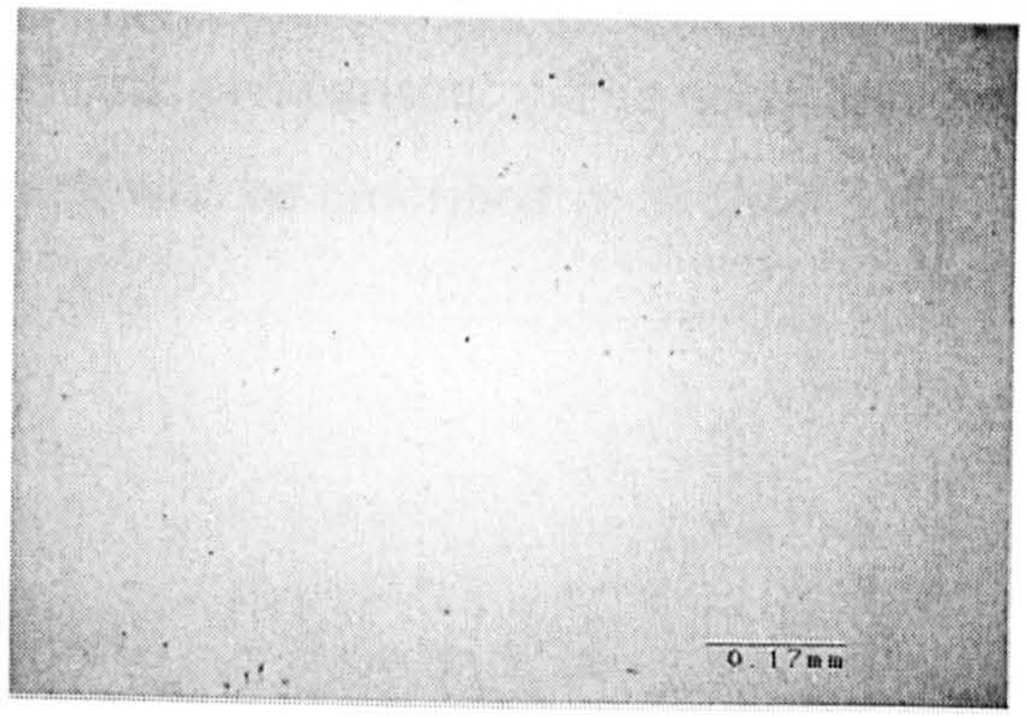

D

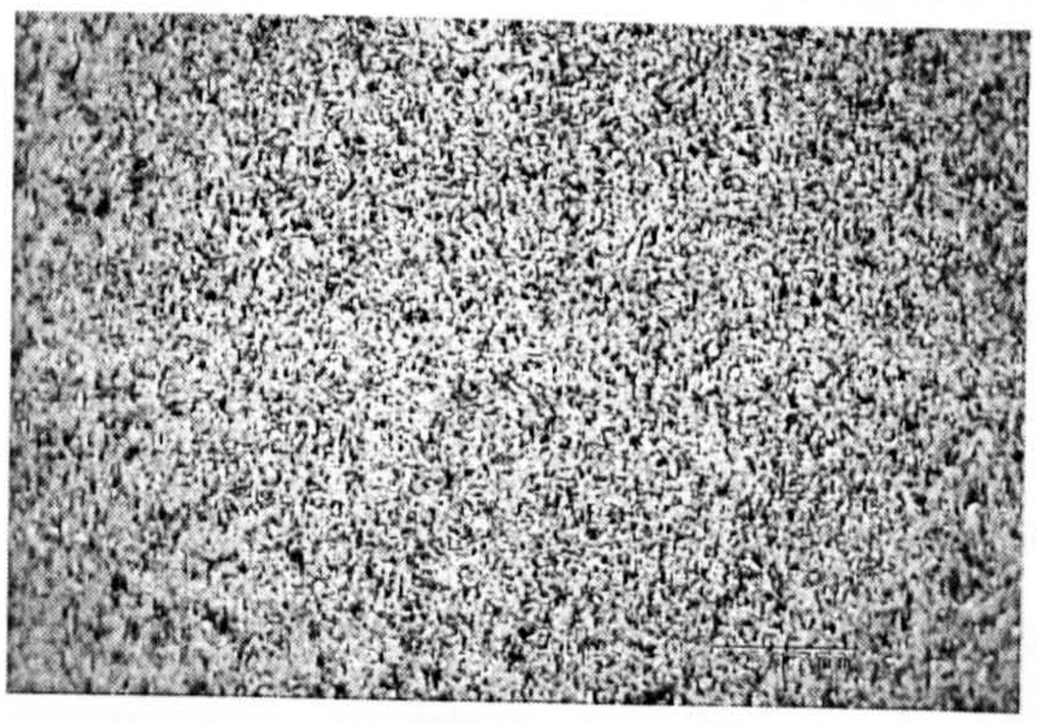

E

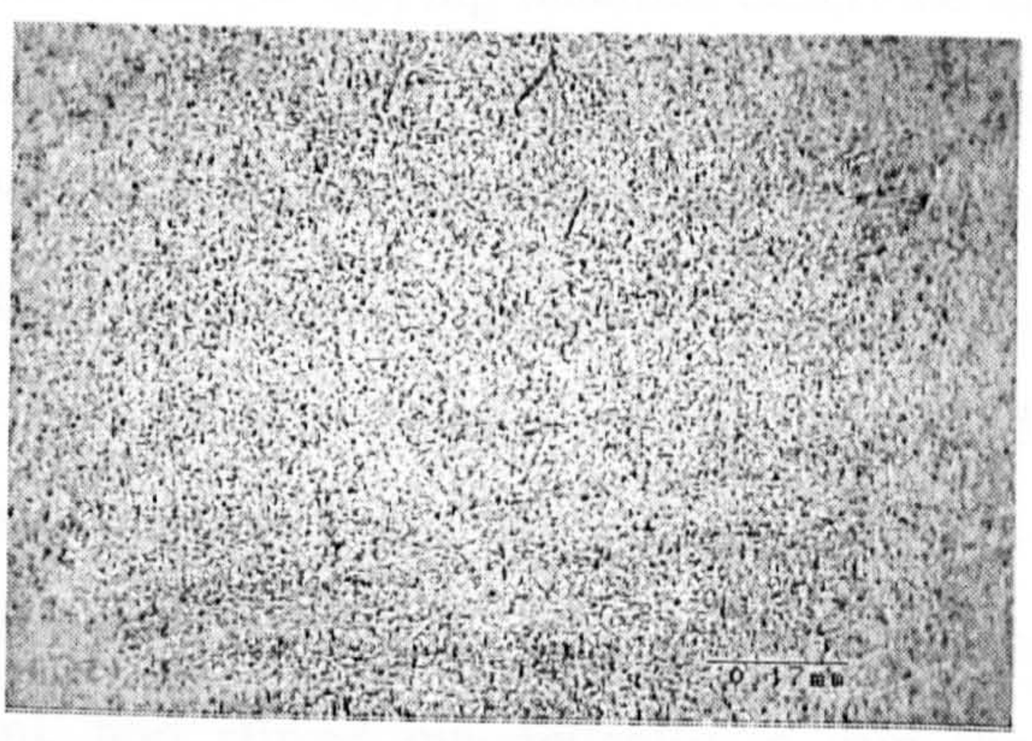

F

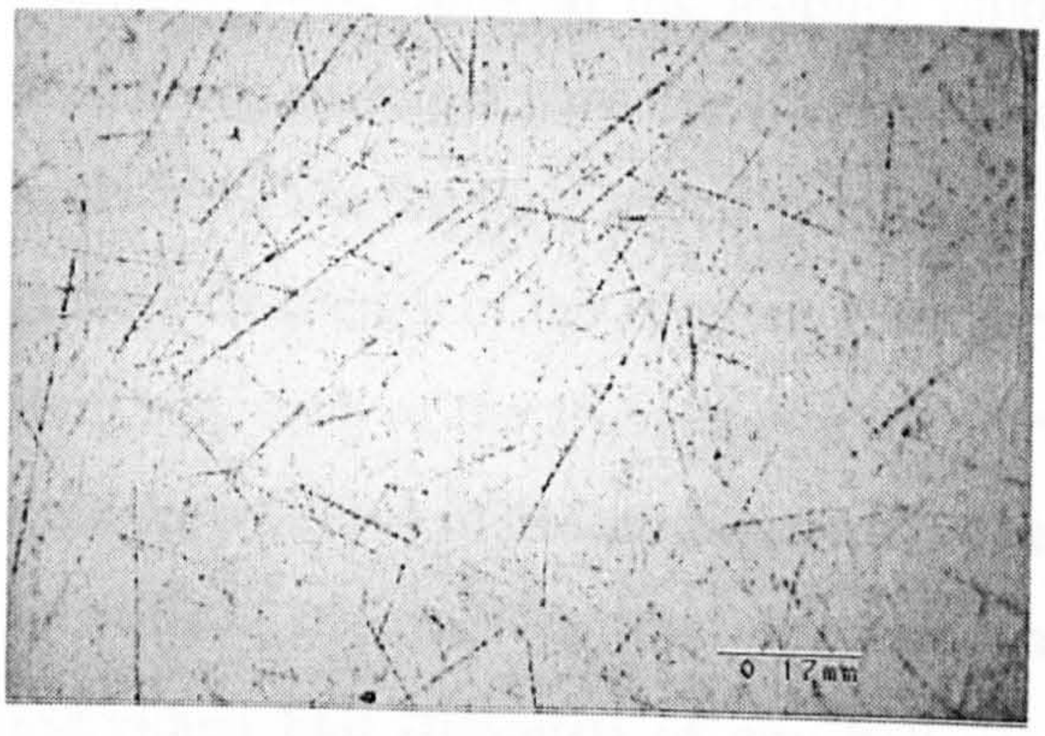

G

Fig. 3-3 Photomicrographs of the surfaces of samples A ~ G before testing

3.1.2.2 Sample balls with surface defects

In order to investigate the influences of surface integrity, rolling contact fatigue tests were conducted on balls with heterogeneous porosity, star defects, grinding defects and C-crack defects. These defects were generated from the manufacturing processes, not artificially induced. These kinds of sample balls were either procured from the manufacturers as finished balls or self-finished. Since each individual case is very different, the description of each sample ball and pre-test surface examination will be presented in Sections 5.2 and 5.3 of this thesis together with experimental results and discussion in order to make a straightforward comparison. The techniques of positioning the defect area on the rolling track will be described in Section 3.4.4 of this chapter.

3.2 Lapping: First Step of Finishing

Lapping tests were conducted using the novel eccentric lapping machine described in Section 2-1. Table 3-3 summarises the lapping materials. Before and after each lapping test run, balls and lapping plates were cleaned using an ultrasonic bath, each ball diameter was measured to ± 1 μm and the total weight of the batch (15 balls) was measured to ± 1 mg. Microscope observations of ball surfaces were also conducted after each lapping test run to monitor any exceptional ball surface damage. The diamond paste and lapping fluid were mixed according to paste concentration parameters, 1g:30ml, 1g:60ml or 1g:120ml, and stirred magnetically to mix the diamond paste fully in the lapping fluid. A quantity of 5ml of this fluid mixture containing diamond particles was spread onto the V-groove of the lower plate before each test. The lapping speed parameter was set by means of choosing the output current frequency of the inverter. Each lapping test was run for 1 hour duration. After each test, each of the 15 balls was measured and the ball diameters were documented on a spreadsheet in descending order. The individual balls within the batch were not identified. Changes to the diameter (measured material removal rate on each individual ball (μ/hour)) of any ball was deduced from two adjacent rows in the

spreadsheet (assuming that the descending order of diameters of the 15 balls was not changed after each test run). This is an acceptable method as the batch diameter scatter after each test is normally very small (1~2 μm), and the individual ball roundness error (ovality) generated from this eccentric lapping is only 0.4~1.1μm. The average weight lost per ball per hour was deduced from the whole batch (15 balls) after each test run purely for monitoring purposes. STDEVP (standard deviation based on the entire population) was also calculated for each test run to monitor the ball diameter scatter.

Lapping plates	material: grey cast iron (grade 12) upper plate flat lower plate with eccentric V-groove V-groove angle 90° symmetric axis parallel to rotating axis diameter of circular V-groove 65 mm eccentricity (distance between centre of circular V-groove and rotating axis) 8 mm
Diamond Paste	Kemet diamond compound Metadi II diamond paste Diamond particle sizes: 6μ ,15μ, 30μ, 45μ ,60μ, 90μ
Lapping Fluid	Metadi fluid (water based) 40-6064UK

Table 3-3 Summary of lapping materials

3.3 Polishing: Second Step of Finishing

Polishing tests were also conducted on the novel eccentric-lapping machine described in Section 2-1. Table 3-4 summarises the polishing materials. Before and after each polishing test run, balls and lapping plates were cleaned using an ultrasonic bath, each ball diameter was measured to ± 1 μm and the total weight of the batch (15

balls) was measured to ± 1 mg. Microscope observations, SEM, ball roundness measurement and 3D topographic measurements were also conducted after each polishing test.

Lapping plates	material: EN1A mild steel upper plate flat, lower plate with eccentric V-groove V-groove angle 90° symmetric axis parallel to rotating axis diameter of circular V-groove 65 mm eccentricity (distance between centre of circular V-groove and rotating axis) 8 mm
Diamond Paste	Metadi II diamond paste, ¼ μ, 1μ
Lapping Fluid	Metadi fluid (water based) 40-6064UK

Table 3-4 Summary of polishing materials

Each polishing test lasted 24 hours. The lapping fluid was pumped at intervals, through a tube to the centre of upper lapping plate by means of the ProMinent gamma/4 diaphragm-type metering pump at pre-set stroke. The lapping fluid was a mixture of diamond paste and lubricating fluid at a concentration of 1g:100ml. This was mixed and maintained in equal concentrations by a magnetic stirrer. The amount of lapping fluid applied was controlled by the pre-set stroke number/min of the pump plus a timer. The application time was for 5 minutes every 4 hours, set by the timer's ON and OFF periods. The pump and magnetic stirrer activated simultaneously with the timer's ON period. Thus, every 4 hours, an amount of 5ml of lapping fluid mixture was added to the lapping plates through the pipe at the centre of the upper plate.

3.4 Rolling Contact Fatigue Test

3.4.1 Test Machine

Fig. 3-4 TE92/HS Microprocessor Controlled Rotary Tribometer

Rolling contact fatigue tests were conducted on a Plint TE92/HS 10,000 rev/min Microprocessor Controlled Rotary Tribometer (Fig 3-4). This tribometer is suitable for a variety of tribology test procedures. In this research, it was configured to run 4-ball or 5-ball rolling contact fatigue tests, which will be described in the following sections. Through a computer interface, the test speed, load, temperature, etc. were controlled by editing values, ramps and steps in the menu of a computer file. The load is applied by a pneumatic actuator from a supply pressure of 8 bars. The contact region between the upper ball and lower balls is immersed in lubricating oil during each test. The test was stopped after a pre-set number of revolutions of the driving-shaft as measured by a counter. A vibration sensor automatically stopped the test at a pre-determined potentiometer adjustment sensitivity (818) and light emitting diode duration. If the upper ball or the lower balls failed during testing the machine would

vibrate. When the machine vibrates such that the diode remains in the ON mode for more than one second, the driving motor will be cut out and the machine will stop. This machine can test materials and lubricants at shaft speeds between 100 and 10,000 rev/min. Most of the present tests were conducted at a shaft speed of 10,000 rev/min.

In this study, the upper ball is the specimen ball and the lower balls are standard steel testing balls (specification: 0.5″ ball Reference RB12.7/310995A, material: AISI 52100 bearing steel). The measured geometric and physical properties of the steel test balls are listed in Table 3-5. The lubricant oil for most tests is Shell Talpa 20 with kinematic viscosity (cSt) 94.6 at 40 °C and 8.8 at 100 °C.

Diameter	12.699 mm
Density	7789 (kg/m^3)
Surface roughness R_a	0.024 μm
Surface roughness R_q	0.037 μm
Surface Hardness	907 (Vickers Hardness Number, HV10)
Surface Hardness	65.2 HRC-150kgf

Table 3-5 Measured geometric and material properties of steel test balls

3.4.2 Rolling Contact 4-Ball Test

The TE92/HS Rotary Tribometer was configured as a modified 4-ball machine according to the Institute of Petroleum (UK) IP 300 rolling test procedure. Fig 3-5 shows the modified 4-ball rolling configuration. The upper ball (3) was held in the collet (2) and rotated at the spindle (1) speed. The retainer cup (7) had a race with slightly bigger radius than a ½″ ball to accommodate three lower balls (4). The cup was filled with oil before the test, and during the test period oil could be added through a hole in the cup cover (8) to ensure the test was conducted under fully

lubricated condition. A heater pad (5) was connected to a thermocouple to ensure the temperature remained above the specified level. Whenever the temperature falls below this specified level the heater pad will be on.

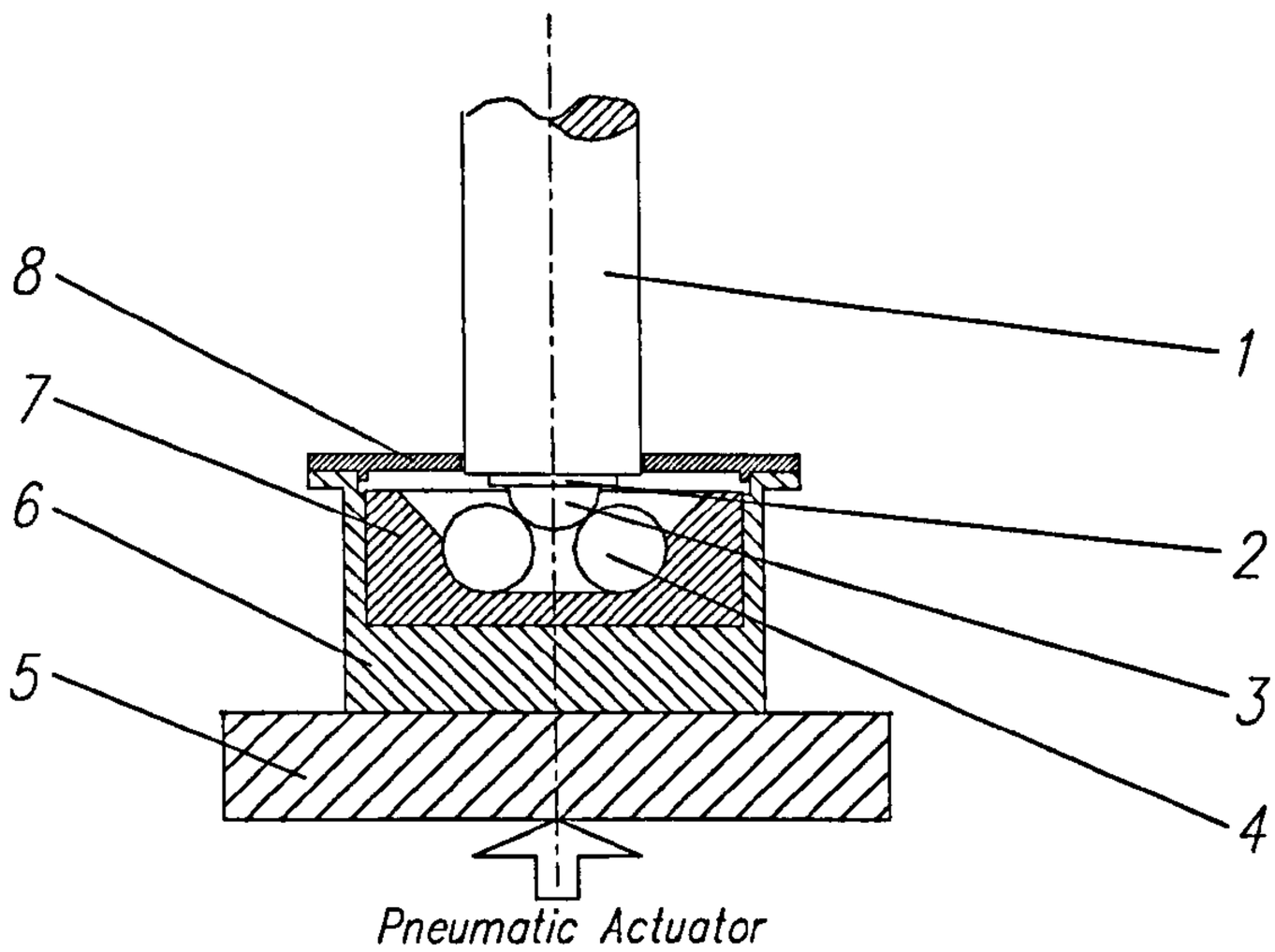

Fig 3-5 Modified 4-ball rolling configuration

Four-ball rolling kinematics was described by Kruger and Bartz in Chapter 10 of reference (Tourret and Wright 1977). The current configuration was categorised as a type II machine. The upper ball stress cycle factor L is:

$$L = Z\left[\frac{R_u + 2R_l}{2(R_u + R_l)}\right] \tag{3-1}$$

Where Z is the number of lower balls, R_u is the upper ball radius, and R_l is the lower ball radius. In this case, $R_u = R_l = 6.35$mm, Z=3. Substitute these figures into equation (3-1), L=2.25. This means that when the spindle rotates one revolution, the upper ball will undergo 2.25 stress cycles.

Before each test, the sample ball was cleaned in an ultrasonic bath by acetone. Surface roughness and surface hardness of the sample ball were examined,

microscopy inspection was conducted. Lubricant oil was added every 24 hours during the test to ensure the silicon nitride/steel rolling contact was in a fully lubricated state. During the test, the load, speed and temperature etc. were recorded in a computer file at a pre-set sampling rate. The load was applied by a pneumatic actuator. A typical load for 4-ball rolling test is 1.96 kN and speed is 10,000 rpm. In all tests, the temperature setting was 50 °C. Therefore when a new test started, the heater pad was on until the temperature reached 50 °C.

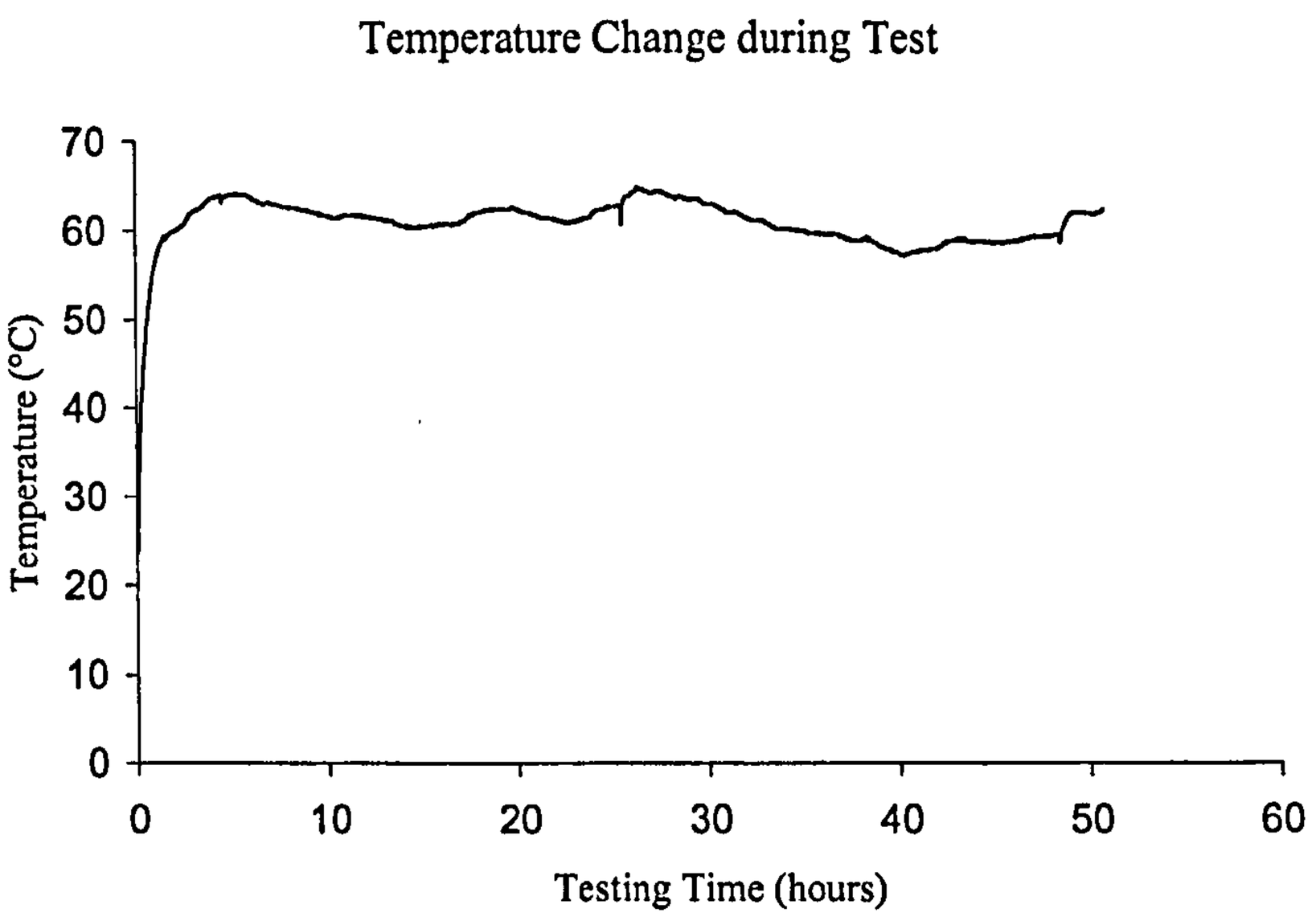

Fig. 3-6 Typical temperature change during the test period

A typical temperature change during the test period is shown in Fig. 3-6. Since the simultaneous measurement of the temperature at the upper/lower balls contact region is not available, the actual temperature measured is the bulk lubricant oil temperature. The temperature is influenced by ambient temperature, which is lower at night. Adding lubricant oil will immediately reduce the temperature, but it rises quickly to the previous level. This is shown in Fig. 3-6 where the temperature dropped at time 4 hours, 26 hours and 49 hours, corresponding to the additions of lubricant oil. The test may have to be stopped before reaching the set time due to the

failure of one of the lower steel balls. In this case the retainer cup assembly is taken out and cleaned. Three new steel balls are then fitted, new oil is added, and the test is continued. The failure of the lower steel ball is normally due to a fatigue spall on the rolling track. By changing the lower steel balls, the rolling contact stress cycles for the upper silicon nitride ball is assured. After each test, the upper silicon nitride ball was cleaned in an ultrasonic bath by acetone, microscopy, SEM, WYKO, 3D topographic and atomic force microscope analyses were conducted.

3.4.3 Rolling Contact 5-Ball Test

The rolling contact 5-ball test is similar to the 4-ball test described above, except that the retainer cup is changed to a 5-ball cup with four lower balls as described in Section 2.2 (technical drawing see Appendix 2). The upper ball stress cycle factor L can also be calculated from equation (3-1). In this case, $R_u = R_l = 6.35mm$, Z=4. Substituting these figures into equation (3-1), L=3 shows that when the spindle rotates one revolution, the upper ball will undergo 3 stress cycles.

In order to distinguish the traction effect of the 5-ball test, the contact stress cycles in unit time and the contact load are set exactly as for the 4-ball test. To ensure that the upper ball undergoes as the same stress cycles over the same time interval as in the 4-ball test, the speed of the 5-ball test was set to 7,500 rpm. This meant that the upper ball would undergo 22500 stress cycles per minute, the same as in the 4-ball test.

For the 4-ball test, the load applied by the pneumatic actuator of the Plint machine $P_{machine}$ is 1.96 kN, the contact load $P_{contact4}$ is:

$$P_{contact4} = \frac{P_{machine}}{3\cos(35.3°)} = \frac{1960N}{3\cos(35.3°)} = 800N \qquad (3\text{-}2)$$

For the 5-ball test, to maintain the contact load $P_{contact5}$ as 800N

$$P_{contact5} = 800N = \frac{P_{machine}}{4\cos(54.7°)} \qquad (3\text{-}3)$$

$$P_{machine} = 800N \times 4\cos(54.7°) = 1.85kN \quad (3\text{-}4)$$

Therefore in the rolling contact 5-ball test, the load was set to 1.85kN, speed was set to 7,500 rpm. All the other settings and the test procedure were exactly the same as for the 4-ball test.

3.4.4 Positioning the Defect Area on the Rolling Track

In order to evaluate the influences of surface integrity on the rolling contact fatigue performance, the defect area must be positioned on the rolling track. Fig 3-7 illustrates how this is achieved.

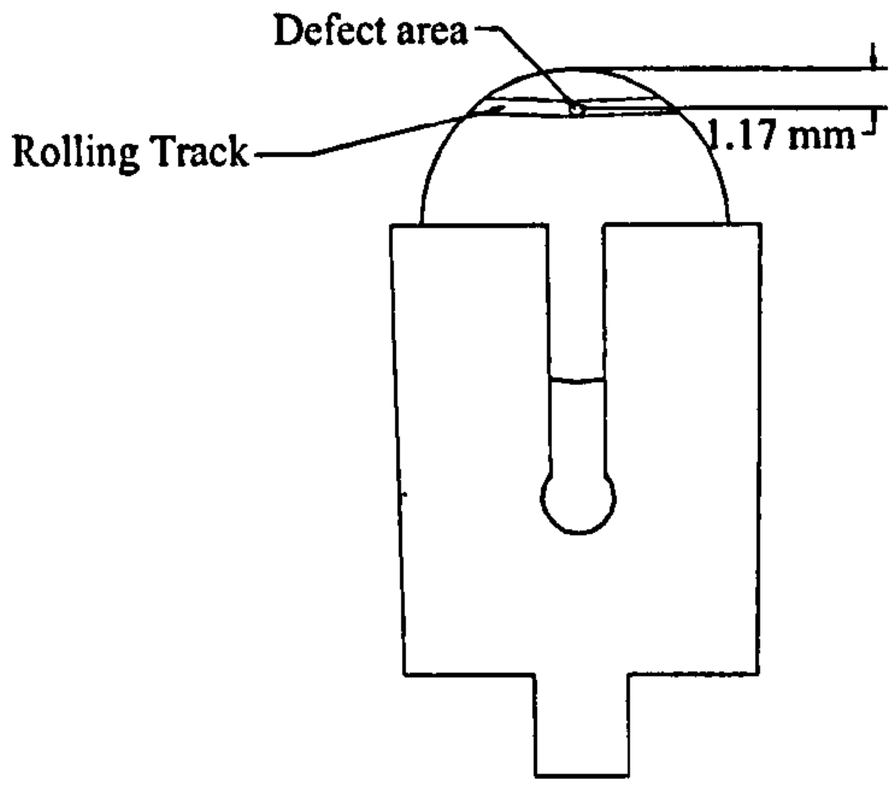

Fig 3-7 Positioning the defect area on the rolling track

According to the contact geometry of the modified 4-ball rolling test, it was calculated that the distance from the centre of the rolling track to the top of the ball was 1.17 mm. The defect area on the ball was marked under UV light microscope beforehand. The sample ball with defect area was loosely fitted into the collet. The collet was fitted onto a specially designed jig, which was placed on a surface table. A vernier height gauge with readings to 0.01mm was used to measure the distance from the centre of the defect area to the top of the ball. The sample ball was gently rotated on the collet until the measurement of 1.17mm was achieved. It was then pressed into the collet. The measurement was re-checked once the ball was pressed into the collet.

When the distance was assured, the collet with the ball in position was mounted onto the spindle of the Plint machine and the rolling test was run for about 20 minutes. Then the collet with the ball was removed, put into a specially designed apparatus for microscopy inspection. At this stage the ball had a rolling track mark, and the position of the defect area on the rolling track could be clearly seen under UV light and white light inspection. If the position of the defect area on the rolling track was as expected, the collet with the ball was put back onto the spindle and the rolling test continued.

3.5 Surface Microscopy Study

3.5.1 Microscopy Inspection, UV light with Dye-Penetrant

The advantage of microscopy inspection is its convenience with no sample preparation being required. Surface cracks and certain defects can be detected with dye-penetrant treatment under UV light. The main disadvantage is the low magnification (maximum 1000×) and the short depth of focus. The microscopy inspection was conducted on an Olympus BX60 Microscope at Bournemouth University. This microscope has three light sources, Bright-field, Dark-field and UV light. The objective lenses range from ×5 to ×100, the maximum magnification is about 1000×. This microscope also features a Video Text Overlay which enables the measurement and characterisation of surface features on the screen. This Microscope is shown in Appendix 3, A3.1.

The dye-penetrant treatment of the ball samples was conducted at SKF ERC. The sample balls were thoroughly cleaned first in an ultrasonic bath by acetone, then soaked in a fluorescent dye-penetrant for a period. After draining, the sample balls were then soaked in a dye remover for a short time in order to remove any dye from the ball surface. Finally, the sample balls were washed thoroughly and dried carefully. Because of the fluorescent dye-penetrant left inside the cracks, any surface or subsurface damage can be revealed under UV light. Some microscopy UV light inspection was also conducted at SKF ERC.

As small cracks or other defects can collect lapping fluid and debris particles which then hinder the penetration of the fluorescent chemical, some of the sample balls were treated in a furnace to 500 °C for one hour then cooled in air in order to 'burn out' residues in any small surface defects.

3.5.2 Scanning Electron Microscope with EDX

SEM gives higher magnification (10× ~300,000×) and wider depth of focus which allows detailed observation of the sample surfaces. The scanning electron microscope inspection was conducted on a Philips SEM 505 machine at Bournemouth University. Since the ceramic ball samples are not conductive, sample preparation is vital in order to obtain satisfactory images. The sample balls were thoroughly cleaned first in an ultrasonic bath of acetone to ensure the ball surface was free of any grease or debris, then dried carefully leaving no marks on the ball. The sample ball was then coated with gold using an Agar Auto-Sputter Coater. To increase conductivity two or three lines of silver paint were applied from near the sample surface area under observation to the conductive adhesive on the metallic stub. The Philips SEM 505 Scanning Electron Microscope with EDX is shown in Appendix 3, A3.2. Some SEM inspections were also conducted at the Experimental Techniques Centre (ETC) at Brunel University.

3.5.3 Atomic Force Microscope

Although the SEM provides higher magnification and greater depth of focus, it is difficult to observe details at high magnification on polished ceramic surfaces without a defect, failure or other feature. In such cases, the Atomic Force Microscope (AFM) is used. The AFM inspection was conducted at the Ashikaga Institute of Technology, Japan. The AFM measures the ultra-small forces between the AFM tip mounted on a very flexible cantilever beam and the sample surface. Relying on a scanning technique, the AFM provides very high resolution, three-dimensional image of the sample surface. However, care is needed with the interpretation of AFM images where the size of features on the surface approaches the AFM tip radius (normally

about 10 nm) (Gee and McCormick 1996). The SPA 35 AFM machine at the Ashikaga Institute of Technology, Japan and a typical output is shown in Appendix 3, A3.3.

3.5.4 Surface Micro-Hardness Measurement

It was reported that the finishing rate of Si_3N_4 balls is dependent on fracture toughness and hardness (Gardos and Hardisty 1993). The surface hardness could also be influential in rolling contact performance. Surface hardness of the sample balls was measured using a Buehler machine at Bournemouth University at load 10 kgf, loading speed 100 μm/sec., load time 10 sec.. Because of the curvature of the ball surface, a special ball holder was manufactured (Appendix 3, A3.4). The concentricity and countersinking of the ball holder shaft ensures that the top area of the ball is subjected to pressure from the diamond pyramid. A tight, accurate fit between the shaft of the ball holder and the bush in the machine is thus essential. Since the diagonal impression made by the hardness test on steel and ceramic is between 100~200 μm, it is assumed that the curvature of a 12.7mm diameter ball at this length is approximately equal to a straight line. To ensure this, the following calculation has been made:

The height of the arc h can be calculated from:

$$h = r - \frac{1}{2}\sqrt{4r^2 - c^2} \tag{3-5}$$

Where r is the radius of the ball, r=6.35mm; c is the length of the arc, in the range of 0.1~0.2 mm, taking c=0.2mm. Substituting these values into (3-5), then h=0.78745μm. This is well below the indentation depth indicating this approximation is acceptable.

The Buehler Hardness Indenter machine and sample ball holder are shown in Appendix 3, A3.4.

3.6 Surface Topography Measurement

3.6.1 2D Surface Profiler

The 2D surface profiler is a stylus instrument, which gives the surface topographic parameters on a length-based measurement. The 2D topographic measurement was carried out at SKF ERC by a Talysurf 2D surface profiler, with a 2CR-ISO filter, cut-off: 0.8mm. The typical measurement outputs are shown in Appendix 3, A3.5.

3.6.2 3D Optical Surface Structure Analyser

The 3D surface structure analyser gives the surface topographic parameters on an area-based measurement and the 3D overview of the measured surface area. The 3D topography of the ball surfaces was measured by a Zygo New View three-dimensional imaging surface structure analyser, at Cambridge University. This New View system uses scanning white light interferometry to image and measure test surfaces and provide surface structure analysis with no actual surface contact, taking measurement depths up to 100 μm, and with 0.1 nm resolution and 0.4 nm RMS repeatability. The Zygo New View three-dimensional imaging surface structure analyser and a typical output are shown in Appendix 3, A3.6.

3.6.3 Interference Profilometer (WYKO Image)

The Interference Profilometer is a scanning laser profilometer, which gives a better 3D topographic overview on a larger area. The Interference Profilometer (WYKO image) observation on the ball surfaces was conducted at SKF ERC. Appendix 3 A3.7 shows typical outputs from the Interference Profilometer (WYKO image) at SKF ERC.

3.6.4 Ball Roundness Measurement

The ball roundness was measured at SKF ERC by an MWA 1605B Roundness machine and at the Ashikaga Institute of Technology, Japan, using a Taylor-Hobson

Talyrond 73 Roundness Profiler. Appendix 3 A3.8a and A3.8b show the typical outputs from these two machines respectively.

3.7 Surface and Subsurface Residual Stress Measurement

The residual stresses induced by the finishing process and the residual stress change occurring during the RCF test were measured by the X-ray diffraction method, since this is the only practical and non-destructive method for ceramic materials. The principle of the X-ray diffraction method is that when a stress is applied to a material, the inter-atomic distance in the crystal will be extended or compressed within the elastic limit of the material in proportion to the stress. The X-ray diffraction method measures the variation of the inter-planar spacing in the crystal from the variation of the X-ray diffraction angle. By using Bragg's equation, strain is calculated, and then stress is calculated from strain. A detailed description of the X-ray diffraction method can be found in reference (Cullity 1996).

In order to gain hands-on experience of residual stress measurement by the X-ray diffraction method the author went to Japan to carry out the measurements himself.

3.7.1 Measuring Equipment

The residual stress measurement of the ball was conducted at the Ashikaga Institute of Technology, Japan, using a Rigaku Rint 2000 X-Ray Diffractormeter. Appendix A3.9a shows the machine, and Appendix A3.9b shows the ball holder inside the machine with a jig to move and rotate the ball holder along three co-ordinate axes.

3.7.2 Measurement Procedure

The sample balls were cleaned in an ultrasonic bath by acetone. The three sample balls to be measured were then put into the three countersink holes in the ball holder (Fig 3-8), with the area intended to be measured on the top and centre of each hole.

The ball diameter was 12.7mm while the hole diameter was 13 mm. The small gap between the sample ball and the hole was sealed with tape around the edge of the hole, in order to eliminate any clamping force applied to the sample ball. The ball holder with three sample balls was fitted vertically into the jig (Appendix 3 A3.9b) and fastened. This jig can be moved along X, Y, Z axes and rotated around X, Y, Z axes. Adjustment of the two knobs on the jig moved it along X and Y axes to bring the area to be measured under the cross of a detachable microscope. Another knob moving the jig along Z-axis adjusted the focus. When this had been completed, the sample was correctly installed.

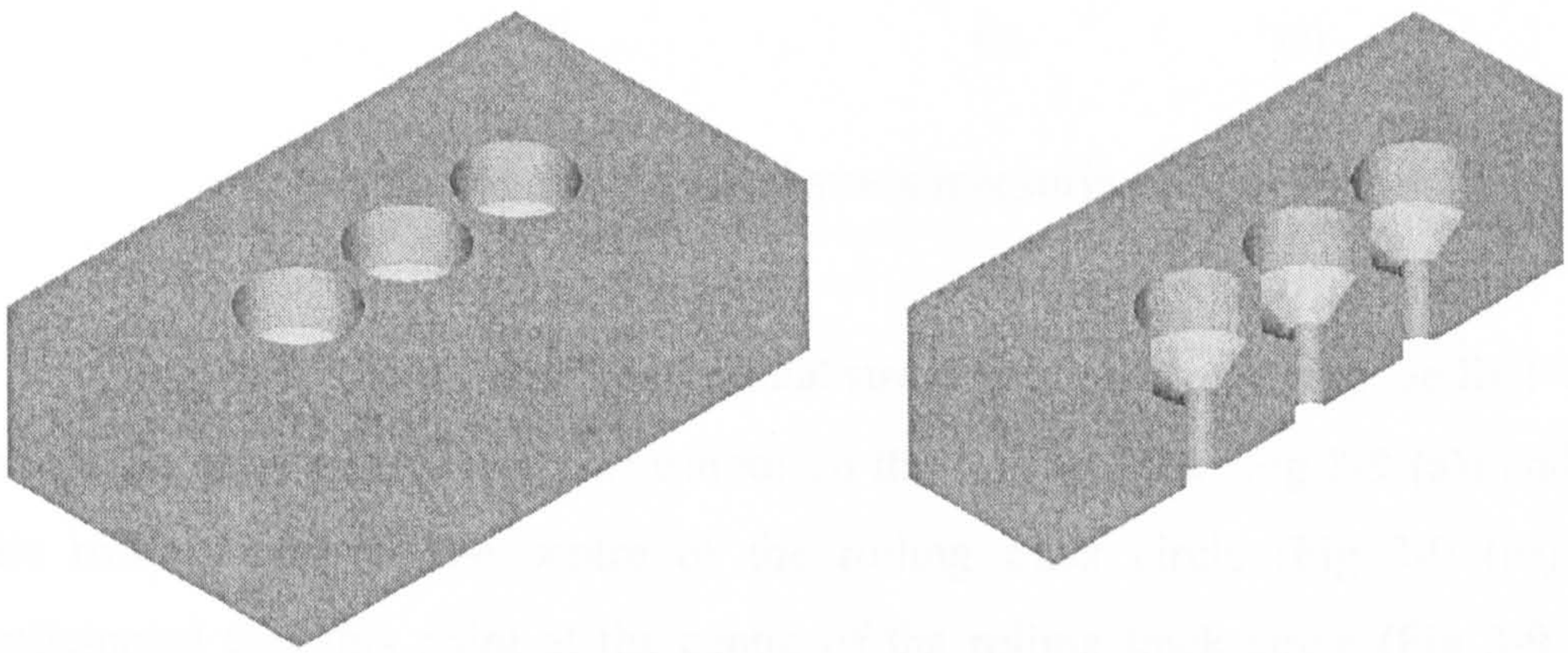

Fig. 3-8 3D solid model for ball holder

The parameter setting of the Rigaku Rint 2000 X-Ray Diffractormeter is listed in Table 3-6.

X-ray source: Cr Kα1 at 40 kV and 250 mA
Collimator: 1.0 mm
Scan range: 123°~127°,
Sampling time: 100 sec.
Step angle: 0.002°
Young's modulus: 310000 Mpa
Poisson's ratio: 0.26

Table 3-6 Parameter setting for residual stress measurement

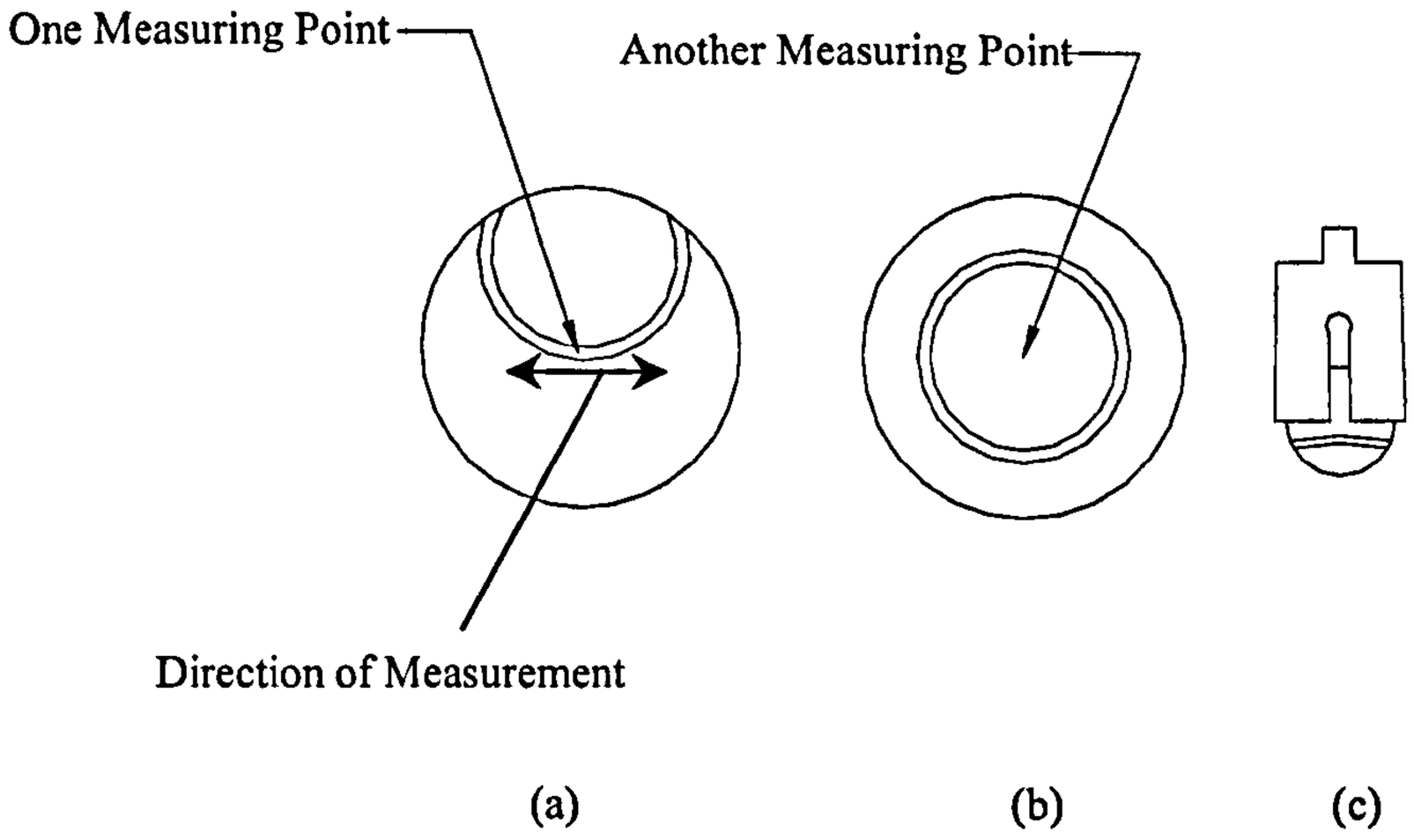

Fig 3-9 Residual stress measuring points

In order to investigate the residual stress field change during the RCF test, two points on each sample were measured: on the rolling track (Fig 3-9 (a)) and outside the rolling track at the centre of the rolling track circle (Fig 3-9 (b)). It was anticipated that this point at the centre of the rolling track circle (Fig 3-9 (b)) had endured least stress during the RCF test, because half of the ball surface was in the collet (Fig 3-9 (c)) during the RCF test and may have endured more stresses than this point.

The depth of the measurement was about 30 μm, and this was dependent on the X-ray source which penetrated the material. The area of the measurement was a circular area with a diameter of 1 mm which was determined by the diameter of the collimator. The direction of the measurement at the point on the rolling track was parallel to the rolling track (Fig 3-9 (a)). The direction of the measurement on the finished ball surface and on the point at the centre of the rolling track circle (Fig 3-9 (b)) is not relevant.

Each measurement took about 30 minutes. Appendix A3.9c shows the output of a typical measurement.

3.8 Contact Analysis

Contact stresses were calculated using classical Hertz elastic contact stress formulae. There are three different contact stress situations which will be described in the following three sections. The contact film thickness and lambda ratio were calculated according to classical Elastohydrodynamic Lubrication Theory.

3.8.1 Ball/Ball Contact Stress Analysis

Ball/ball contact resembles the situation in the 4-ball or 5-ball rolling test: one upper ceramic ball in contact with 3 or 4 lower steel balls. Detailed contact stress analysis in this situation is listed in Appendix 4, A4.1.

3.8.2 Ball/Flat Surface Contact Stress Analysis

Ball/flat surface contact is reproduced in the lapping test: ceramic balls being lapped in contact with the upper flat lapping plate (steel or cast iron). Detailed contact stress analysis in this situation is listed in Appendix 4, A4.2.

3.8.3 Ball/Conformed Curved Surface Contact Stress Analysis

Ball/conformed curved surface contact is presented in the lapping test, when the V-groove is worn and conformed to ceramic balls being lapped. Detailed contact stress analysis in this situation is listed in Appendix 4, A4.3.

3.8.4 Elastohydrodynamic Lubrication Regime Analysis

Rolling contact fatigue tests were conducted under lubricated conditions. It was envisaged that there would be a dynamic thin oil film separating the ball contact surfaces according to Elastohydrodynamic Lubrication Theory (Dowson and Higginson, 1966). The thickness of the film as well as a lambda ratio which predicts lubrication regime are very important in rolling contact failure analysis. The detailed Elastohydrodynamic lubrication regime analysis is listed in Appendix 5.

3.9 FEA Contact Modelling with Imposed Residual Stress

Finite Element Analysis was carried out using ANSYS software version 5.5.1 to model the two 12.7 mm diameter (0.5″) balls in contact (ceramic/steel and ceramic/ceramic) under different loading conditions. A model with imposed residual stresses (pre-stresses) on a ceramic ball was also built to predict the influences of residual stresses. An axisymmetric 2-D solid modelling technique was employed in all models to simplify the model building and calculation. The FEA modelling results are listed at Appendix 6.

PLANE 42 Element with an axisymmetric option was chosen as the basic element type to build up the models. Whilst in the contact area, two types of contact elements were used to take advantage of ANSYS new surface-surface contact algorithm. The upper ball (ceramic) edge was defined as CONTA171 Elements (contact object), and the lower ball (steel or ceramic) edge was defined as TARGE169 Elements (target object). The material properties used in these elements were as follows:

Steel		Ceramic (silicon nitride)	
Young's Modulus	207 GPa	Young's Modulus	315 GPa
Poisson's ratio	0.3	Poisson's ratio	0.27
Density	7,780 kg/m^3	Density	3,160 kg/m^3

Table 3-7 Material properties of steel and ceramic (silicon nitride) used in FEA Modelling

Meshes on the model were generated by the ANSYS Mesh Tool automatically. Appendix 6 A6.1 shows the overall mesh distribution. Meshes near the contact area were progressively refined three times, each time using a refinement factor of 2. Appendix 6 A6.2 and A6.3 show the detailed meshes within the contact region at different magnifications.

Appendix 6 A6.4~A6.6 illustrate the results of upper ceramic, lower steel contact under 400N load applied both to the topmost node of a ceramic ball and the

lowermost node of a steel ball along the axisymmetric axis (Y axis). Appendix 6 A6.4 is the stress contour of Y stress (along the axisymmetric axis). The maximum compressive stress was found to be 5.33GPa, compared with the result of 5.227 GPa calculated by the Hertz contact formula: only 2% difference. Appendix 6 A6.5 is the stress contour of X stress (perpendicular to the axisymmetric axis). The maximum tensile stress was found to be 0.617 GPa. Appendix 6 A6.6 is the stress contour of XY shear stress. The maximum shear stress was found to be 1.22 GPa.

Appendix 6 A6.7~A6.9 reveal the results of upper ceramic, lower steel contact under 400N load the same as Appendix 6 A6.4~A6.6, with the addition of imposed 200 MPa, –X direction residual stresses (pre-stresses) 30 μm from the surface in the contact region of ceramic ball. Appendix 6 A6.7 is the stress contour of Y stress (along the axisymmetric axis). The maximum compressive stress was found to be 5.603 GPa, compared with the result of 5.33 GPa without residual stress in Appendix 6 A6.4, the maximum compressive stress increased by 5.6%. Appendix 6 A6.8 is the stress contour of X stress (perpendicular to the axisymmetric axis). The maximum tensile stress was found to be 0.611 GPa, compared with the result of 0.617 GPa without residual stress in Appendix 6 A6.5. The maximum tensile stress decreased by 1%. Appendix 6 A6.9 is the stress contour of XY shear stress. The maximum shear stress was found to be 1.14 GPa, compared with the result of 1.22 GPa in Appendix 6 A6.6: a difference of 6.5%.

The conclusion from the results of FEA simulation is that the residual stresses within the ceramic ball subsurface 30μm from the surface in compression in the amplitude of 200 MPa will not greatly affect the contact stress field.

4.0 EXPERIMENTAL RESULTS & DISCUSSION, PART ONE: FINISHING PROCESS

This chapter presents the experimental results and discussion on the finishing process. The purpose of these experiments was to investigate the feasibility of accelerating the finishing process by using a novel eccentric lapping machine; to explore the material removal mechanism of the two-plate lapping method; and to study the influence of different lapping parameters on the surface quality of finished balls.

4.1 The Effects of Different Lapping Parameters on Material Removal Rate by Single Parameter Changing Method

This was the initial investigation on the influence of different finishing parameters. It served as a baseline with which to compare the later investigation using Taguchi Methods. The sample balls for this investigation were BBA and BBB procured direct from the manufacturers and described in Section 3.1.1. The lapping test procedure was described in Section 3.2.

4.1.1 Influence of Rotational Speed of Lower Lapping Plate

Fig 4-1 shows the effect of the rotational speed of the lower lapping plate on material removal rate (designated as average ball diameter reduction per hour and average ball weight lost per hour). The lapping fluid used was a mixture of 45 μm diamond paste and water based lubricant at a ratio 1g : 60 ml. The lapping load was 12.75 N/ball.

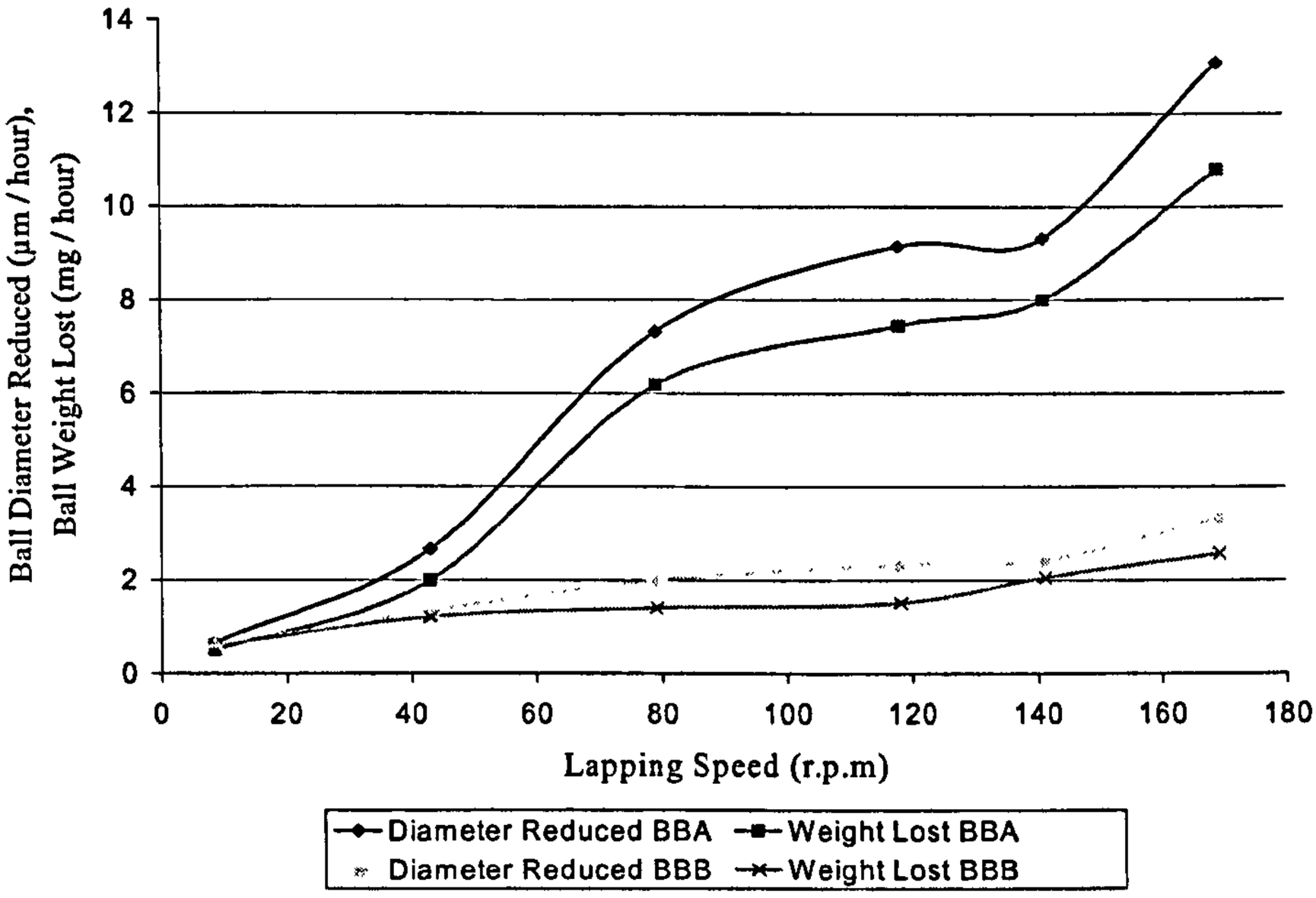

Fig 4-1 Material removal rate versus lapping speed

The material removal rate increased as the lapping speed increased. The increase was sharp (higher) from low speed to medium speed (8.5 rpm to79 rpm) and from medium speed to high speed (140 rpm~169 rpm). The increase was blunt (lower) within the medium speed range (from 79 rpm to 140 rpm). The interesting finding was that although the material removal rates for BBA and BBB were very different, they increased proportionately as the speed increased: BBA was 3~4 fold of BBB at all different lapping speeds except at very low speed. This illustrates that the material removal rate is strongly dependent on lapping speed. The hardness of BBA was higher than BBB, so the hardness dependent feature in a previous ceramic ball lapping investigation by Gardos and Hardisty (1993) does not correlate to this study.

4.1.2 Influence of the Diamond Particle Sizes

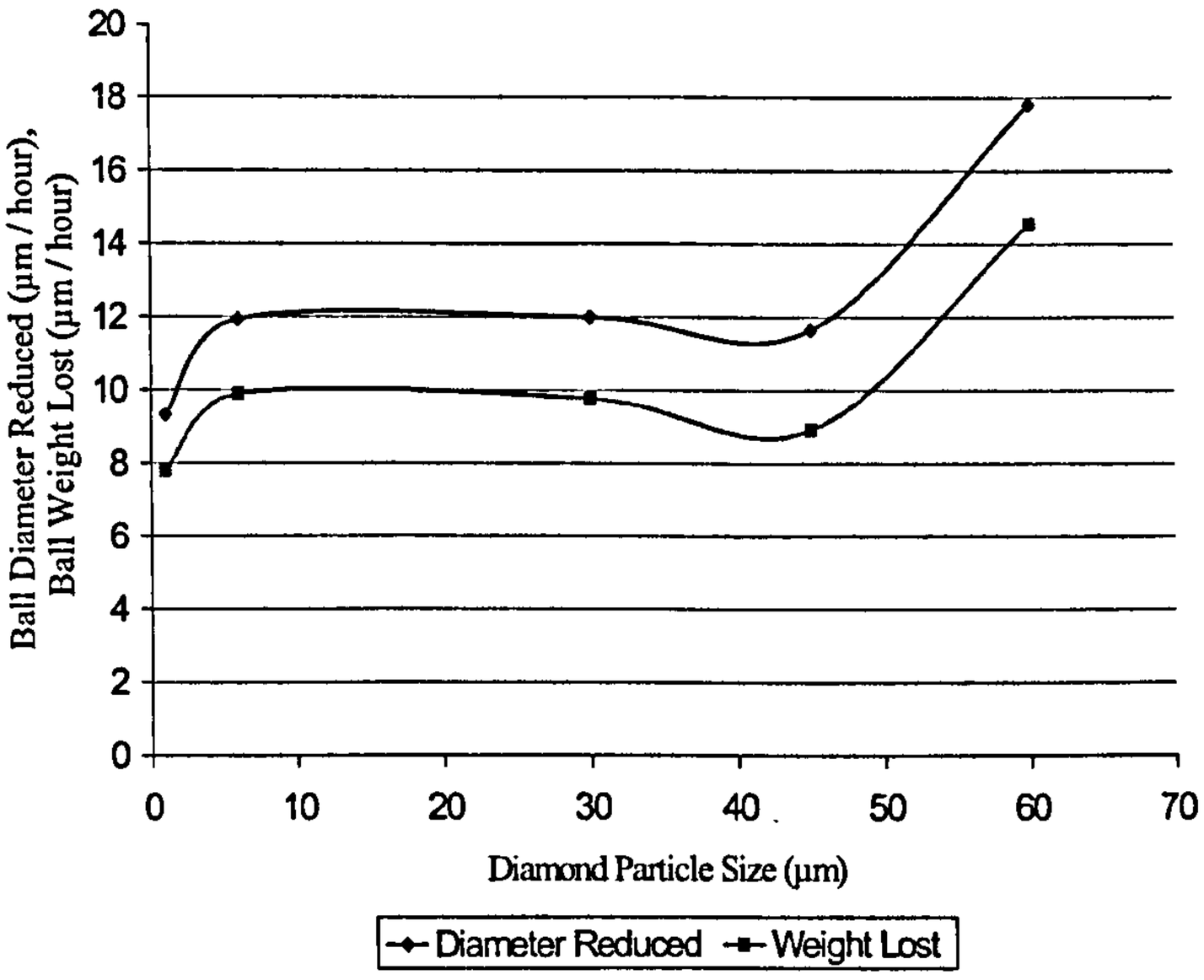

Fig 4-2 Material removal rate versus diamond particle size

Fig 4-2 shows material removal rates from experiments using diamond paste of varying particle sizes. When the diamond particle size was small (1µm), the material removal rate was low. With the diamond particle sizes between 6 µm to 45 µm, the material removal rate remained almost the same. When the diamond particle size was 60 µm, the material removal rate increased by 30%. This investigation was conducted on BBA, the lapping speed was 169 rpm and lapping load 12.75 N/ball.

4.1.3 Influences of Different Lapping Fluid and Mixture

During the finishing process of Si_3N_4, tribochemical reactions can play an important part. Water can accelerate the material removal rate on Si_3N_4. This has been reported by a number of researchers as reviewed in Section 1.2.3. The influences of different lapping fluids and mixtures were one of the major concerns in this research, and have been investigated both at the beginning and end of finishing tests.

4.1.3.1 The Results of Initial Investigation

Six types of lapping fluid and mixture were used to investigate their tribochemical reactions with silicon nitride. Table 4-1 is the summary of these fluid mixtures. The test was on BBB ball blanks, the lapping speed was 169 rpm and lapping load 12.75 N/ball. All the mixtures of 45 μm diamond paste and lubricant were at a ratio 1g : 60 ml. The experimental results are shown in Fig 4-3.

Type A	45 μm diamond paste, water based lubricant, distilled water
Type B	45 μm diamond paste, brake fluid
Type C	45 μm diamond suspension (water based)
Type D	45 μm diamond paste, oil based lubricant
Type E	45 μm diamond paste, water based lubricant
Type F	45 μm diamond paste, water based lubricant, 45 μm diamond suspension (water based)

Table 4-1 Different lapping fluids and mixtures used in initial investigation

The lowest material removal rate was found with type B fluid, a mixture of 45 μm diamond paste and brake fluid. Oil based lubricant (type D) was better than water based lubricant (type E). Adding distilled water to the mixture of water based lubricant and 45 μm diamond paste (type A) increased the material removal rate, but the consequence was severe surface pitting. The highest material removal rate was found with type F, a mixture of 45 μm diamond paste, water based lubricant, 45 μm water based diamond suspension. There was no surface pitting.

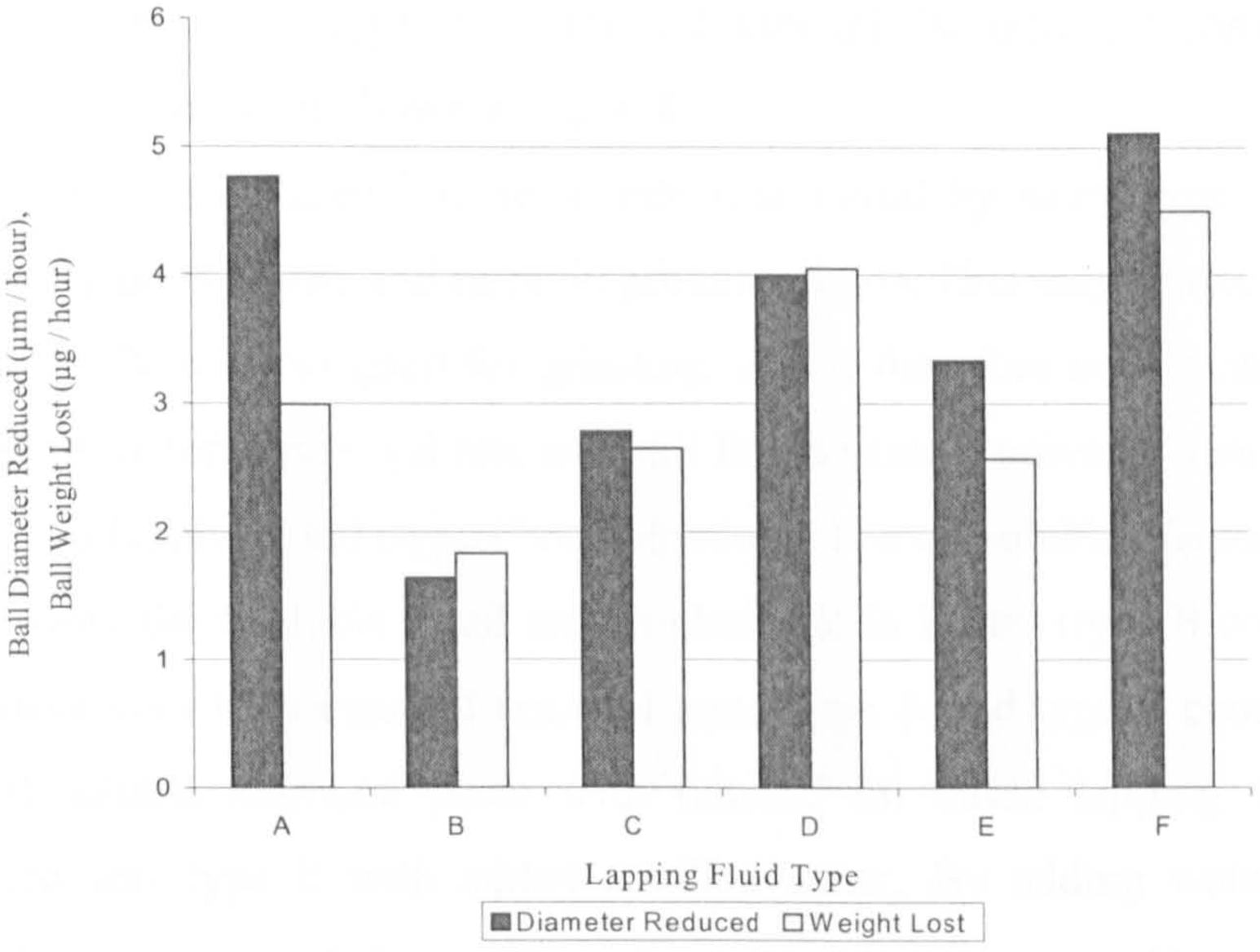

Fig 4-3 Initial investigation on material removal rate versus different lapping fluids and mixtures

4.1.3.2 The Results of Final Investigation

After the initial investigation, Taguchi Methods were used to optimise the lapping parameter and the lapping load was found to be most influential. The aggressive lapping test was then conducted, and a maximum material removal rate of 68 µm/hour on BBA was achieved. At this stage, a final investigation was conducted in order to explore the possibility of further increasing the material removal rate by using different lapping fluids and mixtures. All the other parameters were maintained as when the maximum material removal rate of 68 µm/hour was achieved, i.e. a lapping load of 42.87 N/ball, and a lapping speed of 169 rpm with a 45 µm diamond particle size and a paste concentration of 1g:30ml. When additional fluid was added to the basic lapping fluid, the additional fluid (distilled water or diamond suspension) was 50% of the total fluid volume.

Six different combinations of diamond paste and lapping fluid mixtures were used in the final investigation. Table 4-2 lists all the different combinations. The experimental results are shown in Fig 4-4.

The lowest material removal rate was found by using type D combination (universal diamond paste and ceramic grinding fluid). This may be due to the fact that this type of fluid is designed for grinding, and is therefore not suitable for lapping. The highest material removal rate was still found using a universal diamond paste and water based lapping fluid (type C combination). The oil soluble diamond paste with a low viscosity fluid soluble in oil and emulsifiable in water (type B combination) did not achieve very high material removal rate. Type A and type E combinations were both oil soluble diamond paste with mineral oil based lapping fluid, the only difference was type E with added distilled water. By adding water, the material removal rate increased from 50 μm/hour to 55 μm/hour. Although it has been reported that adding water can significantly increase the material removal rate, as reviewed in Section 1.2.3, in this study only a 10% increase was found. Type F was a combination of universal diamond paste and water based lapping fluid with added diamond suspension, under which the highest material removal rate was achieved during the initial investigation (also denoted as type F in Table 4-1 and Fig 4-3). But

Type	**Diamond Paste**	**Lubricating Fluid**	**Other Fluid**
A	Oil Soluble	Mineral Oil Based	—
B	Oil Soluble	Soluble in oil and emulsifiable in water, containing oil from natural products	—
C	Universal	Water based	—
D	Universal	Ceramic grinding fluid	—
E	Oil Soluble	Mineral Oil Based	Distilled water
F	Universal	Water based	Diamond suspension

Table 4-2 Different lapping fluids and mixtures used in final investigation

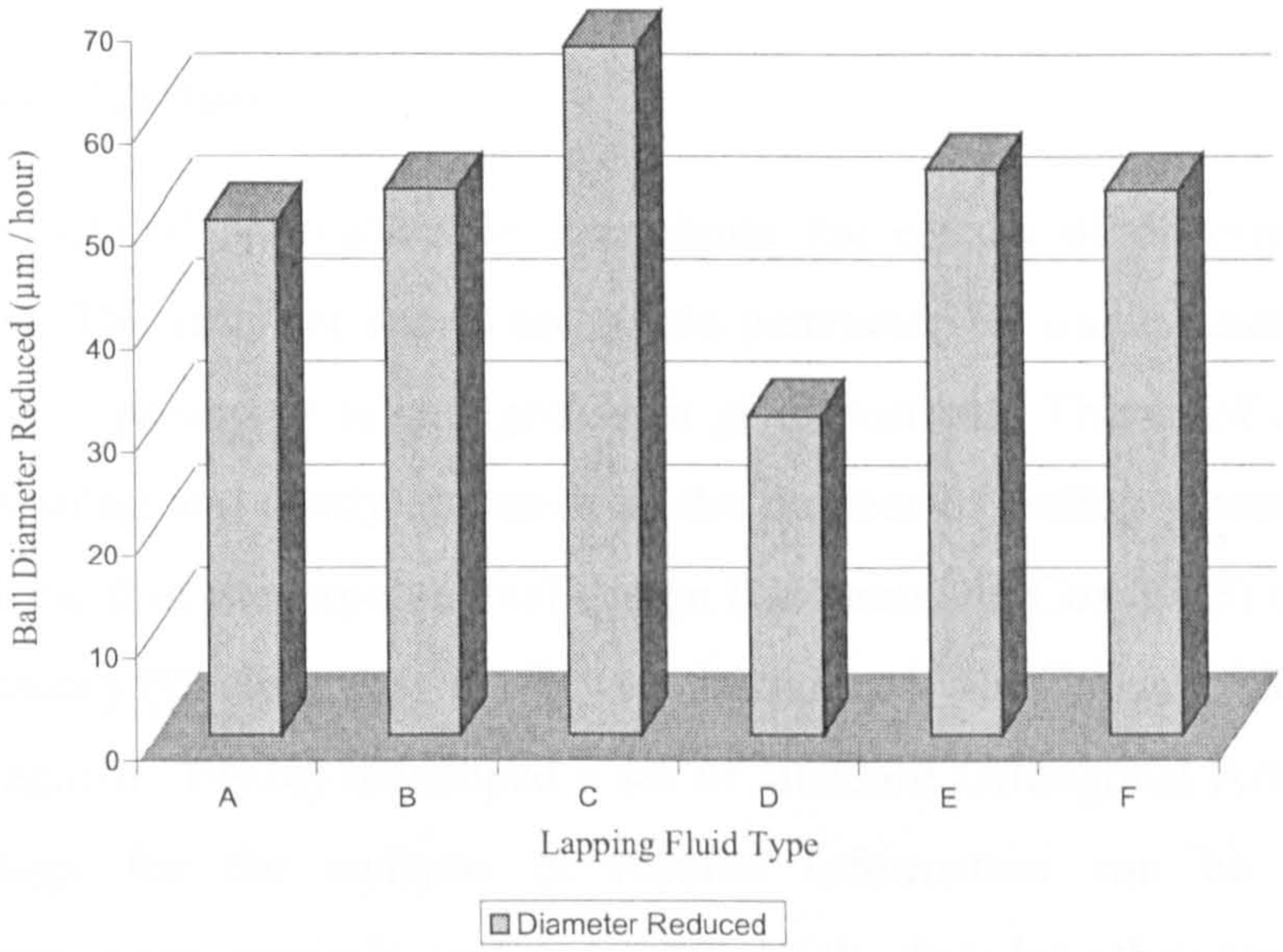

Fig 4-4 Final investigation on material removal rate versus different lapping fluids and mixtures

in the final investigation on type F combination, the material removal rate was only 53 µm/hour, which is 21 % lower than the highest material removal rate of 68 µm/hour.

If the results of the final investigation (Fig. 4-4) are compared with the results of the initial investigation (Fig. 4-3), it can be seen that the different lapping fluid mixtures have less effect on material removal rate under a higher lapping load (42.87 N/ball) apart from type D which is not suitable for lapping. This may suggest that under a higher lapping load, the predominant material removal mechanism is mechanical, although detailed discussion on the material removal mechanisms will follow in Section 4.6. Under a higher lapping load, water based lapping fluid assisted the mechanical removal process of material, thus the highest material removal rate was achieved. This assumption needs to be validated. The ball surfaces lapped by different lapping fluids were examined under a microscope, and no substantial surface damage or extraordinary features were found.

4.2 Application of Taguchi Methods to Optimise Lapping Parameters for Maximum Material Removal Rate

4.2.1 Introduction

There are several approaches to investigate the effects of different experimental parameters. The simplest one is the single-parameter by single-parameter approach, i.e., only one parameter is changed for a given test run. This is of course the most time-consuming and costly approach as the number of testing parameters increases. To overcome this, the experimental design (Cochran and Cox 1968) and dimensional analysis theory (Buckingham 1915) were introduced. The Taguchi Methods (Taguchi 1992a, Taguchi 1992b) developed a set of standard Orthogonal Arrays (OA) and a methodology for the analysis of results. Information can be extracted from experiments more precisely and more efficiently than by other approaches. Fewer tests are needed even when the number of parameters investigated is quite large.

Since Taguchi Methods have been proved successful in many manufacturing circumstances (Wu 1989) (Bendell 1989), they were chosen for this study. The purpose of this study is to investigate the effects of different lapping parameters systematically and ascertain the finishing rate potential.

The basic formulae and notations used in this study can be found in reference (Fowlkes and Creveling 1995)

4.2.2 Experimental Design

A standard Taguchi L9 (3^4) Orthogonal Array (OA) (Table 4-3) was chosen for this investigation as it can operate four parameters, each at three levels. This OA was chosen after preliminary work that identified four parameters as important lapping variables which affect the finishing rate : (A) lapping speed; (B) lapping load; (C) diamond particle size in paste; (D) paste concentration in lapping fluid. Sufficient details of the effect of different parameter values on experimental results can be obtained by choosing to investigate three levels for each parameter.

The criteria used for choosing the three-parameter levels are set to explore the maximum range of experimental variables. The range which has already been found to be of no interest was not included. It is also not necessary to have uniformly spaced

Run	A	B	C	D
1	1	1	1	1
2	1	2	2	2
3	1	3	3	3
4	2	1	2	3
5	2	2	3	1
6	2	3	1	2
7	3	1	3	2
8	3	2	1	3
9	3	3	2	1

Table 4-3 Standard L9 (3^4) Orthogonal Array used in Taguchi Methods

levels because of the counterbalancing property of the OA (Fowlkes and Creveling 1995). Previous lapping experiments, as described in Section 4.1, showed that when the lapping speed range was 8.5~80 rpm, the material removal rate was low, so for this investigation the speed level range was 120~270 rpm. Previous lapping experiments also showed that the material removal rate was fairly high when using 6 μm diamond particles; smaller than this greatly reduced the finishing rate, but the optimum material removal rate was achieved by using 60 μm diamond particles. So for this investigation, the three levels of diamond particle size parameter were chosen as 6 μm, 60 μm and 90 μm. The three levels for lapping load parameter and paste concentration parameter were also selected according to previous lapping experiences but extended to see their effects. The chosen parameters and their levels are shown in Table 4- 4.

The test run was designated by replacing the level number 1, 2, 3 of parameters A, B, C, D in L9 OA with the chosen parameter level values in Table 4-4. Each row of the array represents a test run parameter setting condition. Table 4-5 is the test run design.

Level	Parameters			
	A: Lapping Speed	B: Lapping Load	C: Particle Size	D: Paste Concentration
1	118.42 rpm	8.82N/ball (0.9kgf/ball)	6 μm	1g:30ml
2	168.75 rpm	13.034N/ball (1.33kgf/ball)	60 μm	1g:60ml
3	270 rpm	18.13N/ball (1.85kgf/ball)	90 μm	1g:120ml

Table 4-4 Chosen parameters and their levels for lapping test

Test No.	Parameters			
	A: Lapping Speed	B: Lapping Load	C: Particle Size	D: Paste Concentration
1	118.42 rpm	8.82N/ball (0.9kgf/ball)	6 μm	1g:30ml
2	118.42 rpm	13.034N/ball (1.33kgf/ball)	60 μm	1g:60ml
3	118.42 rpm	18.13N/ball (1.85kgf/ball)	90 μm	1g:120ml
4	168.75 rpm	8.82N/ball (0.9kgf/ball)	60 μm	1g:120ml
5	168.75 rpm	13.034N/ball (1.33kgf/ball)	90 μm	1g:30ml
6	168.75 rpm	18.13N/ball (1.85kgf/ball)	6 μm	1g:60ml
7	270 rpm	8.82N/ball (0.9kgf/ball)	90 μm	1g:60ml
8	270 rpm	13.034N/ball (1.33kgf/ball)	6 μm	1g:120ml
9	270 rpm	18.13N/ball (1.85kgf/ball)	60 μm	1g:30ml

Table 4-5 Lapping test run design

4.2.3 Data Evaluation and Analysis

4.2.3.1 Evaluation of Signal-to-Noise Ratio

Taguchi Methods use the S/N (signal-to-noise) ratio to analyse the test run results because the S/N ratio represents both the average (mean) and variation (scatter) of the

experimental results. The S/N ratio is also used in Analysis of Variance (ANONA). In this study the maximum material removal rate is the objective function, so that the larger-the-better S/N ratio was chosen..

$$S/N_{LTB} = -10\log[MSD] = -10\log\left[\frac{1}{n}\sum_{i=1}^{n}\left(\frac{1}{y_i^2}\right)\right] \tag{4-1}$$

Where S/N_{LTB} stands for larger-the-better Signal-to-Noise ratio, MSD is the mean square deviation around the target (infinity in this case), y_i is the individually measured response value (experiment result), n is the number of measurements taken in one test run.

Table 4-6 shows the results of each test run by the measurement of 15 balls being lapped (y_i), the average value of the batch, and the S/N_{LTB} value calculated from equation (4-1).

4.2.3.2 Level average response analysis

The level average response analysis is based on averaging the experiment results achieved at each level for each parameter. When performing level average response analysis for one level of one parameter, all the influences from different levels of other parameters will be counterbalanced because every other parameter will appear at a different level once. So the effect of one parameter at one level on the experiment results can be separated from other parameters. In this way, the effect of each level of every parameter can be viewed independently.

The level average response analysis is carried out by averaging the experimental results from three test runs corresponding to each level of each parameter, one by one, which is shown in Table 4-7 and plotted in Fig. 4-5. Table 4-8 and Fig. 4-6 give the results of level average response analysis by S/N ratio.

4.2.3.3 Analysis of Variance (ANOVA)

Analysis of variance is a computational technique to quantitatively estimate the relative contribution which each controlled parameter makes to the overall measured

Test No.	Measured material removal rate on each individual ball (μ/hour)															Average (μ/hour)	S/N_{LTB} (dB)	Weight 10^{-6}N/hour	Weight (mg/hour)	STDEVP
	1	2	3	4	5	6	7	8	9	10	11	12	13	14	15					
1	10	9.5	9.5	9	9	9	9	9	9	9	9	9	9	9	9	9.13	19.20	79.674	8.13	0.287
2	15	15	15	15	15	14.5	14.5	14	14	14	14	14	14	13.5	13.5	14.33	23.11	119.56	12.2	0.537
3	20	20	20	20	20	20	20	20	19.5	19.5	19.5	19.5	19	19	19	19.67	25.87	160.72	16.4	0.394
4	16	15	15	15	15	15	15	15	15	15	15	15	14.5	14	14	14.9	23.45	104.566	10.67	0.455
5	30	30	30	30	29	29	29	29	29	29	28	28	28	27	27	28.8	29.17	222.166	22.67	0.980
6	25	25	25	25	25	24	24	24	24	24	24	23	23	23	24	24.13	27.64	163.366	16.67	0.718
7	17	17	17.5	18	18	18	17	17	16	16	16	16	16	17	17	16.9	24.53	143.766	14.67	0.735
8	16.8	16.8	17.3	16.8	16.8	15.9	16.8	16.8	16.8	16.8	16.8	17.8	17.8	16.8	16.8	16.96	24.58	133.476	13.62	0.426
9	40	40	39	39	39	40	41	40.5	41	41	41	40	40	40	40	40.1	32.06	336.434	34.33	0.688

Table 4-6 Experimental results of each lapping test run

	Test Run No.	Average of each run (μ/hour)	Level Average Response (μ/hour)
Parameter A, Lapping Speed			
Level 1, 118.42 rpm	1	9.13	14.38
	2	14.33	
	3	19.67	
Level 2, 168.75 rpm	4	14.9	22.61
	5	28.8	
	6	24.13	
Level 3, 270 rpm	7	16.9	24.65
	8	16.96	
	9	40.1	
Parameter B, Lapping Load			
Level 1, 8.82N/ball (0.9kgf/ball)	1	9.13	13.64
	4	14.9	
	7	16.9	
Level 2, 13.034N/ball (1.33kgf/ball)	2	14.33	20.03
	5	28.8	
	8	16.96	
Level 3, 18.13N/ball (1.85kgf/ball)	3	19.67	27.97
	6	24.13	
	9	40.1	
Parameter C, Particle Size			
Level 1, 6 μ	1	9.13	16.74
	6	24.13	
	8	16.966	
Level 2, 60 μ	2	14.33	23.11
	4	14.9	
	9	40.1	
Level 3, 90 μ	3	19.67	21.79
	5	28.8	
	7	16.9	
Parameter D, Paste Concentration			
Level 1, 1g:30ml	1	9.13	26.01
	5	28.8	
	9	40.1	
Level 2, 1g:60ml	2	14.33	18.46
	6	24.13	
	7	16.9	
Level 3, 1g:120ml	3	19.67	17.18
	4	14.9	
	8	16.966	

Table 4-7 Level average response analysis for lapping test

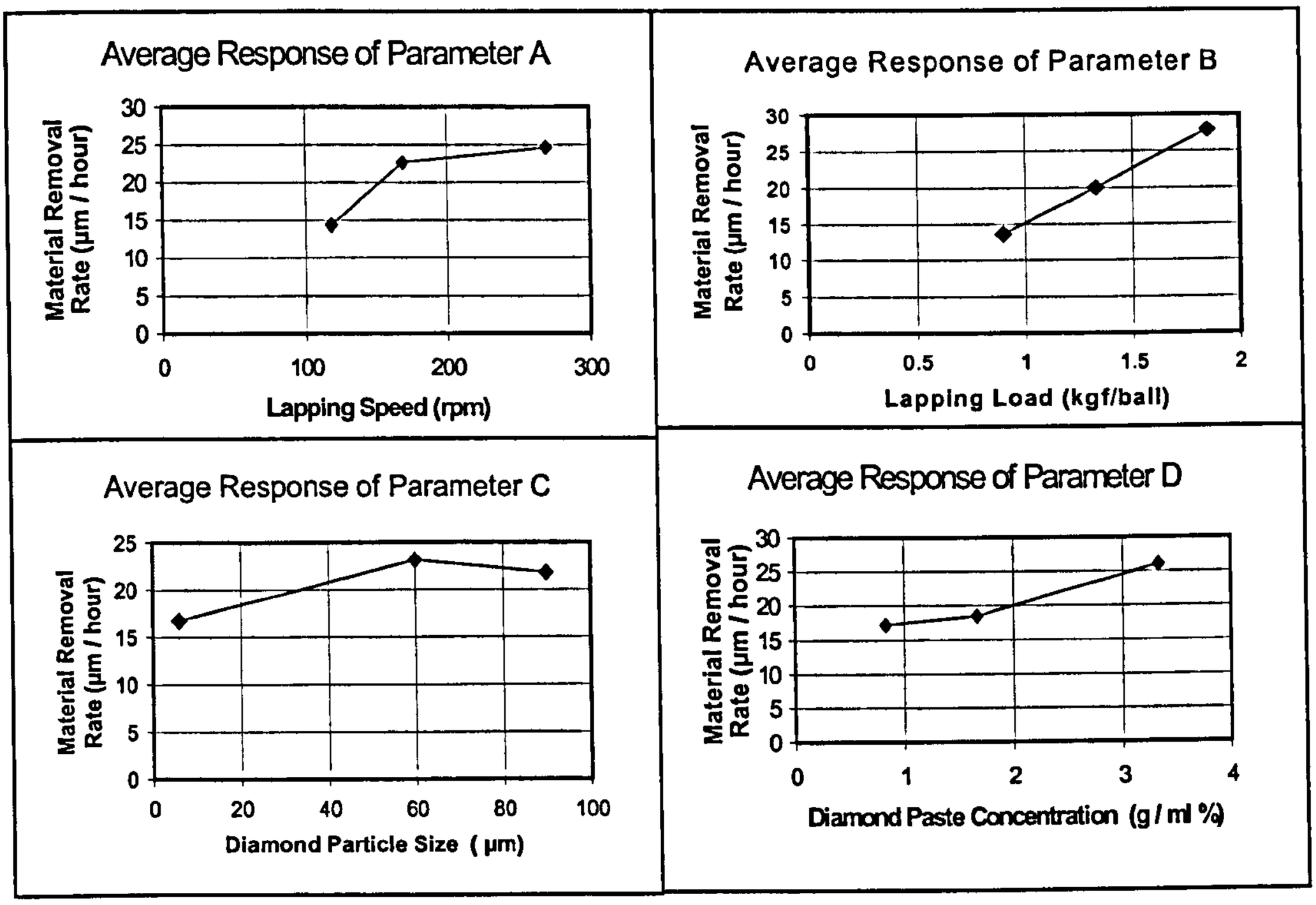

Fig. 4-5 Level average responses for parameters A, B, C, and D

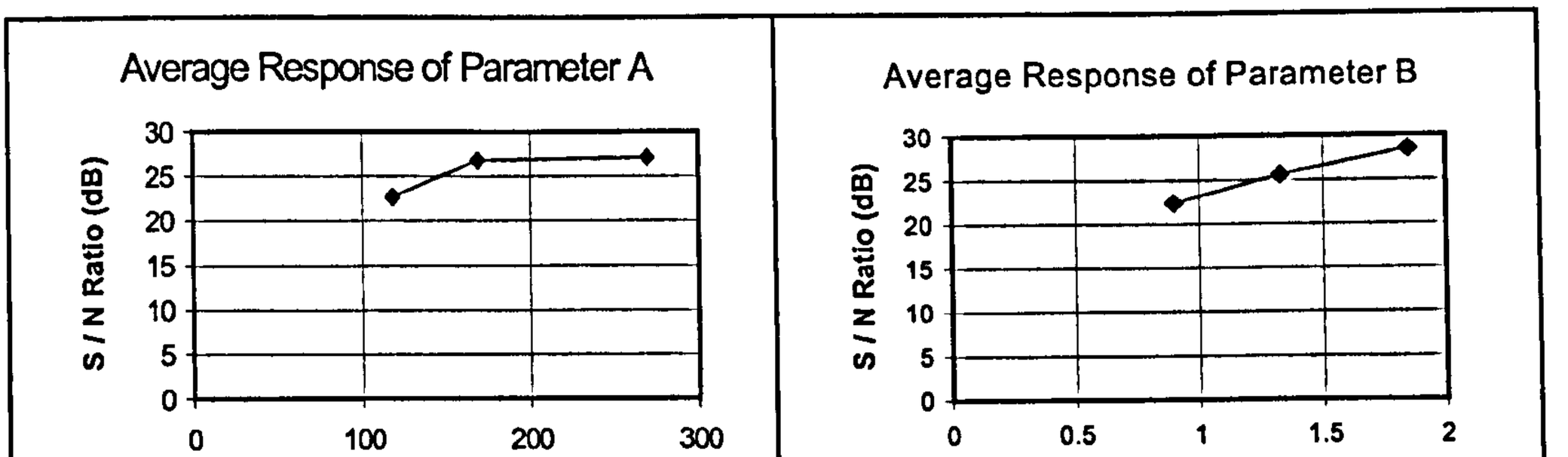

Fig. 4-6 Level average responses for parameters A, B, C, and D by S/N ratios

	Test Run No.	S/N_{LTB} of each run (dB)	Level Average S/N_{LTB} (dB)
Parameter A, Lapping Speed			
Level 1, 118.42 rpm	1	19.20	22.73
	2	23.11	
	3	25.87	
Level 2, 168.75 rpm	4	23.45	26.75
	5	29.17	
	6	27.64	
Level 3, 270 rpm	7	24.53	27.06
	8	24.58	
	9	32.06	
Parameter B, Lapping Load			
Level 1, 8.82N/ball (0.9kgf/ball)	1	19.20	22.40
	4	23.45	
	7	24.53	
Level 2, 13.034N/ball (1.33kgf/ball)	2	23.11	25.62
	5	29.17	
	8	24.58	
Level 3, 18.13N/ball (1.85kgf/ball)	3	25.87	28.52
	6	27.64	
	9	32.06	
Parameter C, Particle Size			
Level 1, 6 μ	1	19.20	23.81
	6	27.64	
	8	24.58	
Level 2, 60 μ	2	23.11	26.21
	4	23.45	
	9	32.06	
Level 3, 90 μ	3	25.87	26.52
	5	29.17	
	7	24.53	
Parameter D, Paste concentration			
Level 1, 1g:30ml	1	19.20	26.81
	5	29.17	
	9	32.06	
Level 2, 1g:60ml	2	23.11	25.09
	6	27.64	
	7	24.53	
Level 3, 1g:120ml	3	25.87	24.63
	4	23.45	
	8	24.58	

Table 4-8 Level average response analysis using S/N_{LTB} ratio

response and express this as a percentage. Thus information about how significant the effect of each controlled parameter is on the experimental results can be obtained. ANOVA uses S/N ratio responses to calculate results.

The overall mean from which all the variation (standard deviation) is calculated is given by

$$\overline{S/N} = \frac{1}{n}\sum_{i=1}^{n} S/N_i \tag{4-2}$$

In this study,

$$\overline{S/N}_{LTB} = \frac{1}{9}\sum_{i=1}^{9}(S/N_{LTB})_i = \frac{1}{9}(19.20 + 23.11 + 25.87 + 23.45 +$$

$$\ldots\ldots\ldots + 32.06) = 25.513$$

The grand total sum of squares GTSS is given by

$$GTSS = \sum_{i=1}^{n}(S/N_i)^2 \tag{4-3}$$

In this case,

$$GTSS = \sum_{i=1}^{9}(S/N_{LTB})_i^2 = (19.20)^2 + (23.11)^2 + (25.87)^2 +$$

$$\ldots\ldots\ldots + (32.06)^2 = 5970.844$$

The GTSS can be decomposed into two parts, the sum of the squares due to the overall mean and the sum of the squares due to variation around the overall mean:

$$GTSS = SS_{mean} + SS_{variation} \tag{4-4}$$

1. The sum of the squares due to the overall mean:

$$SS_{mean} = n \times (\overline{S/N})^2 \tag{4-5}$$

Where n is the number of total test runs.

In this case,

$$SS_{mean} = 9 \times (\overline{S/N}_{LTB})^2 = 9 \times (25.513)^2 = 5858.245$$

2. The sum of the squares due to variation around the overall mean:

$$SS_{variation} = \frac{1}{n}\sum_{i=1}^{n}(S/N_i - \overline{S/N})^2 \qquad (4\text{-}6)$$

In this study,

$$SS_{variation} = \frac{1}{9}\sum_{i=1}^{9}((S/N_{LTB})_i - \overline{S/N}_{LTB})^2 = (19.20 - 25.513)^2 +$$

$$(23.11 - 25.513)^2 + \ldots\ldots\ldots + (32.06 - 25.513)^2 = 112.6$$

The $SS_{variation}$ can be further decomposed into the sums of the squares of the variation induced by individual parameter effects around the overall mean. From Section 4.2.3.2, it is known that when doing level average response analysis for one level of one parameter, all the influences from different levels of other parameters will be counterbalanced. So, the level average S/N minus overall mean S/N is the variation caused by that parameter at that level.

For parameter A, the sum of the squares due to variation around the overall mean is

$$SS_A = n_{A1} \times (\overline{S/N}_{A1} - \overline{S/N})^2 + n_{A2} \times (\overline{S/N}_{A2} - \overline{S/N})^2 + n_{A3} \times (\overline{S/N}_{A3} - \overline{S/N})^2 \qquad (4\text{-}7)$$

Where n_{Ai} is number of tests conducted at level i of parameter A

Where $\overline{S/N}_{Ai}$ is the level average S/N of parameter A at level i

In this case,

$$SS_A = 3 \times (22.73 - 25.513)^2 + 3 \times (26.75 - 25.513)^2 +$$

$$3 \times (27.06 - 25.513)^2 = 35.095(\text{dB})^2$$

Similarly,

$$SS_B = 56.379\ (\text{dB})^2$$

$$SS_C = 13.237\ (\text{dB})^2$$

$$SS_D = 7.895\ (\text{dB})^2$$

The percentage contribution of each parameter is found:

$$\text{Percentage contribution of Parameter j} = (SS_{\text{parameter j}} / SS_{\text{variation}}) \quad (4\text{-}8)$$

In this study (j=A, B, C, D),

Parameter A, Lapping Speed: $(35.095/112.6) \times 100 = 31.17\%$

Parameter B, Lapping Load: $(56.379/112.6) \times 100 = 50.07\%$

Parameter C, Particle Size: $(13.237/112.6) \times 100 = 11.76\%$

Parameter D, Paste Concentration: $(7.895/112.6) \times 100 = 7.01\%$

The percentage contributions for parameters A, B, C, and D are shown in Fig. 4-7.

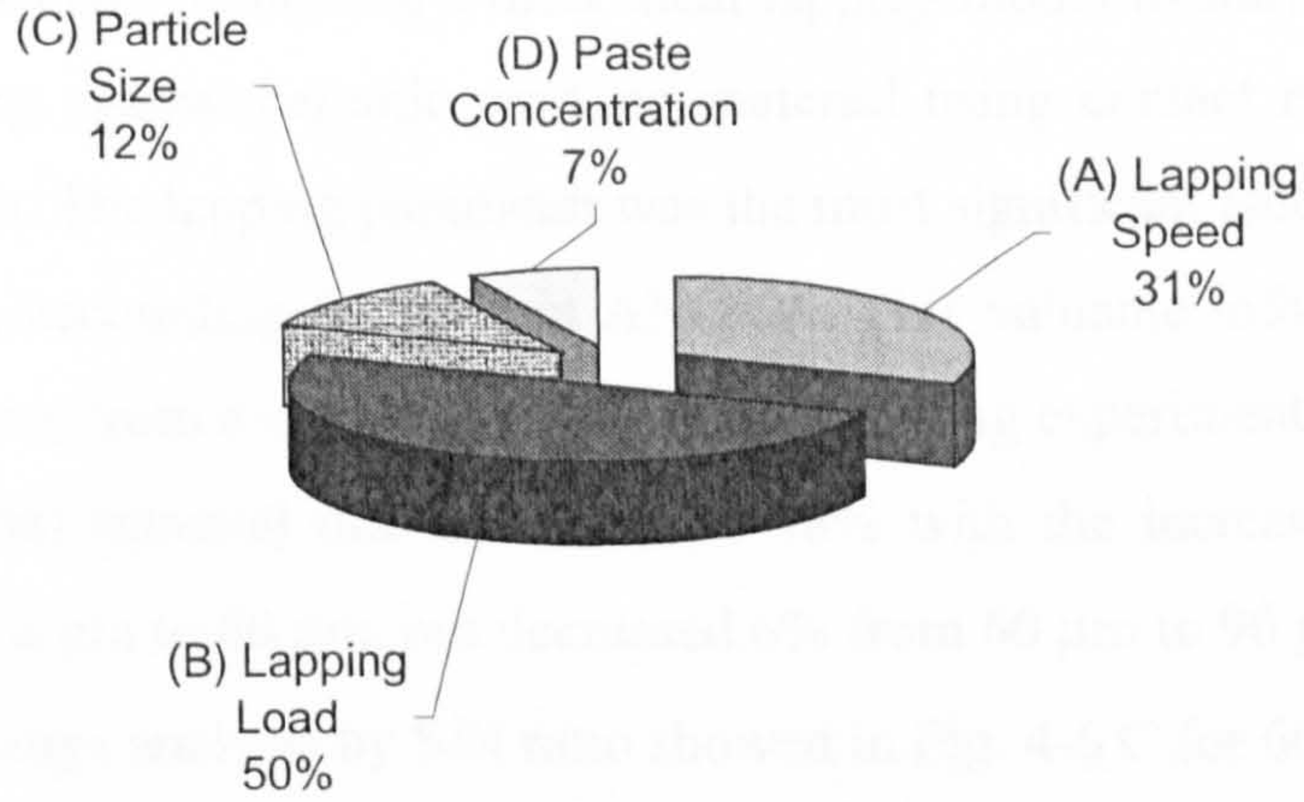

Fig. 4-7 Percentage contributions for parameters A, B, C, and D by ANOVA

4.2.4 Results and Discussion

Table 4-6 shows the experimental results for the lapping programme. The influences of individual lapping parameters on the material removal rate can be clearly seen in Fig.4-5. Generally, the material removal rate increased as the lapping speed, lapping load and paste concentration increased. For the lapping speed parameter, the material

removal rate increased sharply as the speed increased from 118.42 rpm to 168.75 rpm, an increase of 57%. From 168.75 rpm to 270 rpm, although the speed increase was 60%, the material removal rate increased only 9%. This is consistent with a previous single parameter experiment, see Section 4.1.1. It seems that there is a threshold for the lapping speed, below which the material removal rate is very low. The speed below this threshold is suitable for polishing (second step of finishing). The abrasive wear process above this speed threshold is predominantly by micro-crack. This view is supported by the microscope and SEM observations on previous lapping samples by the author. This kind of micro-crack will increase as the lapping speed increases, but to a certain amount the increase will slow down.

Surprisingly, the material removal rate increased almost linearly with the increase of lapping load at a slope of 15μm × lapping load (kgf/ball). This was also the case in the level average analysis by S/N ratio, see Fig. 4-6 B. This information is extremely useful when establishing a theoretical lapping model to show the diamond particles ploughing against ceramic working material using contact mechanics and fracture mechanics. The lapping parameter was the most significant factor influencing the finishing rate, accounting for 50% in ANOVA. This valuable information could not have been drawn from a simple one-parameter changing experiment.

The material removal rate increased by 38% with the increase of diamond particle size from 6 μm to 60 μm, but decreased 6% from 60 μm to 90 μm. The result from the level average analysis by S/N ratio showed in Fig. 4-6 C for 60 μm to 90 μm was almost the same. To verify this, two more test runs were conducted with diamond particle sizes 60 μm and 90 μm respectively, all other three parameters were set at the highest level (load 18.13N/ball (1.85kgf/ball), speed 270 rpm, paste concentration 1g:30ml). The results were consistent, for 60 μm diamond particles, the material removal rate was around 40 μm/hour, for 90 μm diamond particles, around 36 μm/hour. So for diamond particle size parameter, 60 μm is considered as optimum. This is also because the two highest standard deviation values (STDEVP) were found in test run No. 5 (0.980) and test run No. 7 (0.735) which are associated with 90 μm diamond particles. This implies that too large diamond particles will cause ball diameter scatter, especially under medium and higher load.

For parameter D, diamond paste concentration, the material removal rate increased as the paste concentration increased. The increase was higher from 1.67 g/ml % to 3.33 g/ml % than from 0.83 g/ml % to 1.67 g/ml % as shown in Fig. 4-5 D. The level average analysis by S/N ratio shown in Fig. 4-6 D is the same.

The level average response analysis by S/N ratio is shown in Table 4-8 and Fig. 4-6. Although the physical meaning of S/N ratio (dB) is not as straightforward as simple level average response analysis by values (μm/hour), it is more objective towards the target because the S/N ratio reflects both the average (mean) and the scatter (variance). The line trends in Fig. 4-6 A, B, D are the same as in Fig 4-5 A, B, D, this gives confidence in the conclusions drawn from the experiment. The line trend in Fig. 4-6 C is a little different from Fig 4-5 C which was confirmed by further investigation, as discussed previously.

From the level average response analysis, the optimum lapping parameter combination was found to be lapping speed 270 rpm, lapping load 18.13 N/ball (1.85kgf/ball), diamond particle size 60 μm and paste concentrations 1g:30ml (or 3.33 g/ml %). This was verified by a further lapping test run arranged immediately afterwards. The material removal rate achieved of 40 μm/hour was much higher than by conventional concentric lapping, where the material removal rate is usually only a few μm/hour. This indicates that this novel eccentric lapping is very promising.

The analysis of variance (ANOVA) shows that within the experimental level ranges, the most significant lapping parameter was lapping load, which accounted for 50% of the total, followed by lapping speed (31%). Particle size and the paste concentration parameters only accounted for 12% and 7% respectively. It should be noted that this percentage contribution of each lapping parameter to the material removal rate is only valid within the experimental parameter setting level ranges, that is, lapping speed from 118.42 rpm to 270 rpm, lapping load from 8.82 N/ball (0.9 kgf/ball) to 18.13 N/ball (1.85 kgf/ball), particle size from 6 μm to 90 μm and paste concentration from 1g:30 ml to 1g:120 ml. An earlier single parameter changing experiment concerning the lapping speed ranging from 8.5 rpm to 168.75 rpm showed the material removal rate was low at speeds below 80 rpm. If the lower level of lapping speed chosen in the L9 OA in this study were low, the percentage

contribution of lapping speed would be much higher.

The overall results from the application of the Taguchi Methods experimental design and data analysis are satisfactory. Only nine test runs were conducted and much precise information on the parameters affecting the finishing rate was obtained at the experimental levels. This gives a clear overall picture on the influence of each of the four important parameters on this novel eccentric lapping of advanced ceramic balls.

4.2.5 Conclusion from the Application of Taguchi Methods

(1) Increasing the lapping load, lapping speed and paste concentration parameters causes a corresponding increase in material removal rate. The increase in the material removal rate is most significant as the lapping speed parameter increases from 118.42 rpm to 168.75 rpm. The increase in the material removal rate is almost linear (proportional) with the increase of lapping load throughout the parameter range. The increase in the material removal rate is higher when paste concentration parameter changes from 1.67 g/ml % to 3.33 g/ml %.

(2) The optimum lapping parameter combination within the experimental level ranges is found to be high speed, high load, 60 μm diamond particles and high paste concentration.

(3) The material removal rate achieved of 40 μm/hour is much higher than by conventional concentric lapping. This indicates that this novel eccentric lapping is very promising.

(4) Within the experimental level ranges, the most significant influencing parameter is lapping load, which accounts for 50% of the total effect, followed by lapping speed (31%). Particle size and the paste concentration parameters only account for 12% and 7% respectively.

4.3 The Effects of Aggressive Lapping on Ball Surface Integrity

Section 4.2 described the Taguchi Methods used to optimise four lapping parameters—lapping load, lapping speed, diamond particle size and paste concentration. The analysis of variance (ANOVA) showed that the most significant lapping parameter was lapping load, which accounted for 50% of the total. During that study, the lapping loads were varied from 8.82 N/ball to 18.13 N/ball, which is representative of loads on balls in conventional lapping. Within that load range material removal rate increased almost linearly with load. What is not yet known are the limits for ball loads and speeds under conditions of aggressive lapping and what are the side effects of high loads and speeds on ball surface and sub-surface integrity. Since the finished balls are subjected to high contact stresses in bearing applications, any surface or sub-surface damage will be detrimental. This Section will describe the experimental study in the first step aiming to resolve these uncertainties. The second step: rolling contact fatigue tests on balls finished at high loads will be described in Section 5.4.

4.3.1 Test Programme

The test programme consisted of two series of lapping tests (high load and high speed) and post-test ball surface inspection. In the high load tests, BBA were used and 8 tests were carried out with nominal lapping loads of 18.13 N/ball, 21.76N/ball, 25.19 N/ball, 30.97 N/ball, 42.87N/ball, 58.8 N/ball, 77.91 N/ball, and 106.63 N/ball. All the other lapping parameters were maintained equally — speed 169 rpm, diamond particle size 45 μm and diamond paste concentration 1g:30ml. The second series of tests (high speed test) was on BBB, and covered two speeds — 270 rpm and 500 rpm — using a lapping load of 18.13 N/ball, diamond particle size 15 μm and diamond paste concentration 1g:30ml. The test procedure for the two series followed Section 3.2.

In order to further reveal possible sub-surface damage of the balls under high lapping load, some of the balls lapped at 106.63 N/ball and 42.87 N/ball were

polished using a ¼ μm diamond paste and lubricating fluid under a light load and low speed to remove a 5 μm layer from the top surface, equivalent to a ball diameter reduction of 10 μm.

After each test, half of the batch of balls (7 or 8 balls) was processed directly in fluorescent dye penetrant. Because some small cracks or other defects can become filled by lapping fluid and debris particles which hinders penetration by the fluorescent chemical, the other half of the balls in each test batch were treated in a furnace to 500 °C for one hour then cooled in air in order to 'burn out' residues in any small surface defects. Ball surfaces were inspected using optical microscopy at different magnifications under white light and ultra-violet (UV) light.

4.3.2 The Effects of Load and Speed on Material Removal Rate

The material removal rate, as defined by the decrease in diameter per hour, at first increased as the lapping load reached the maximum of 68μm/hour at a load of 42.87 N/ball. At higher loads, the material removal rate decreased to 55 μm/hour at a load of 58.8 N/ball, 25 μm/hour at 77.91 N/ball and 20 μm/hour at 106.63 N/ball. At the two highest loads (i.e., 77.91 N/ball and 106.63 N//ball), the lapped ball roundness error appeared much bigger, typically 3~4 μm, some individual balls even recorded 6 μm, in sharp contrast to the balls lapped at a load of 58.8 N/ball or less which showed a typical roundness error of only 1~2 μm. It was assumed that at these extreme high load conditions, the balls being lapped were not rolling freely, so the material removal rate decreased and the ball roundness error increased. This needed to be validated both theoretically and experimentally. The material removal rates at lapping speeds 270 rpm and 500 rpm were 10 μm/hour and 11 μm/hour respectively.

4.3.3 The Effects of High Lapping Load on Ball Surface and Sub-Surface Damage

The surface and sub-surface damage effects on balls lapped at the highest load of 106.63 N/ball were clearly revealed after polishing, Fig 4-8 shows typical examples of surface damage. Fig 4-8 (a) and (b) are the same surface spall under white light

and UV light respectively. The dimensions of this spall are approximately 170μm×100μm with the maximum depth about 35 μm. The white fluorescent regions shown in Fig 4-8 (b) indicate sub-surface lateral cracks adjacent to the spall. Fig 4-8 (c) and (d) show typical surface damage under white light and UV light. Again, there is evidence of sub-surface cracking. These types of damage could be due to the macro-fracture caused by the excessive lapping load. A point or 'star' type feature is shown in Fig 4-8 (e) and (f). This type of defect is considered to be due to a point overload caused by the over-rolling of a large unbroken diamond particle. Radial cracks are formed similar to those that occur during hardness testing with a diamond indenter. Further lapping removes the dent but the cracks and sub-surface damage are revealed with UV light. No significant surface or sub-surface damage was found on balls lapped at loads 42.87 N/ball or less. Fig 4-9 (a) and (b) show the typical surface appearance of balls lapped at 42.87 N/ball load under white light and UV light.

4.3.4 The Effects of High Lapping Speed on Ball Surface and Sub-Surface Damage

Ball surface damage after lapping at a speed of 500 rpm was characterised by spalls of varying sizes. The largest spall observed which was 143μm×214μm in extent is shown in Fig. 4-10 (a). A typical small spall is shown in Fig 4-10 (b); this was only 28μm×21μm. The large spalls may be caused by ball collisions, while the small spalls are thought to be due to the incursion of diamond particles. No significant ball surface damage was found on balls lapped at the lower speed of 270rpm, except C-cracks which will be discussed in the following section.

4.3.5 C-Cracks and Lapping Speed

C-cracks are part-circular Hertzian cracks that can be present on silicon nitride balls with diameters of 10 mm and above. Large C-cracks are typically formed by balls impacting during improper handling, while smaller C-cracks are thought to be the result of collisions between balls during the lapping processes. Small C-cracks are

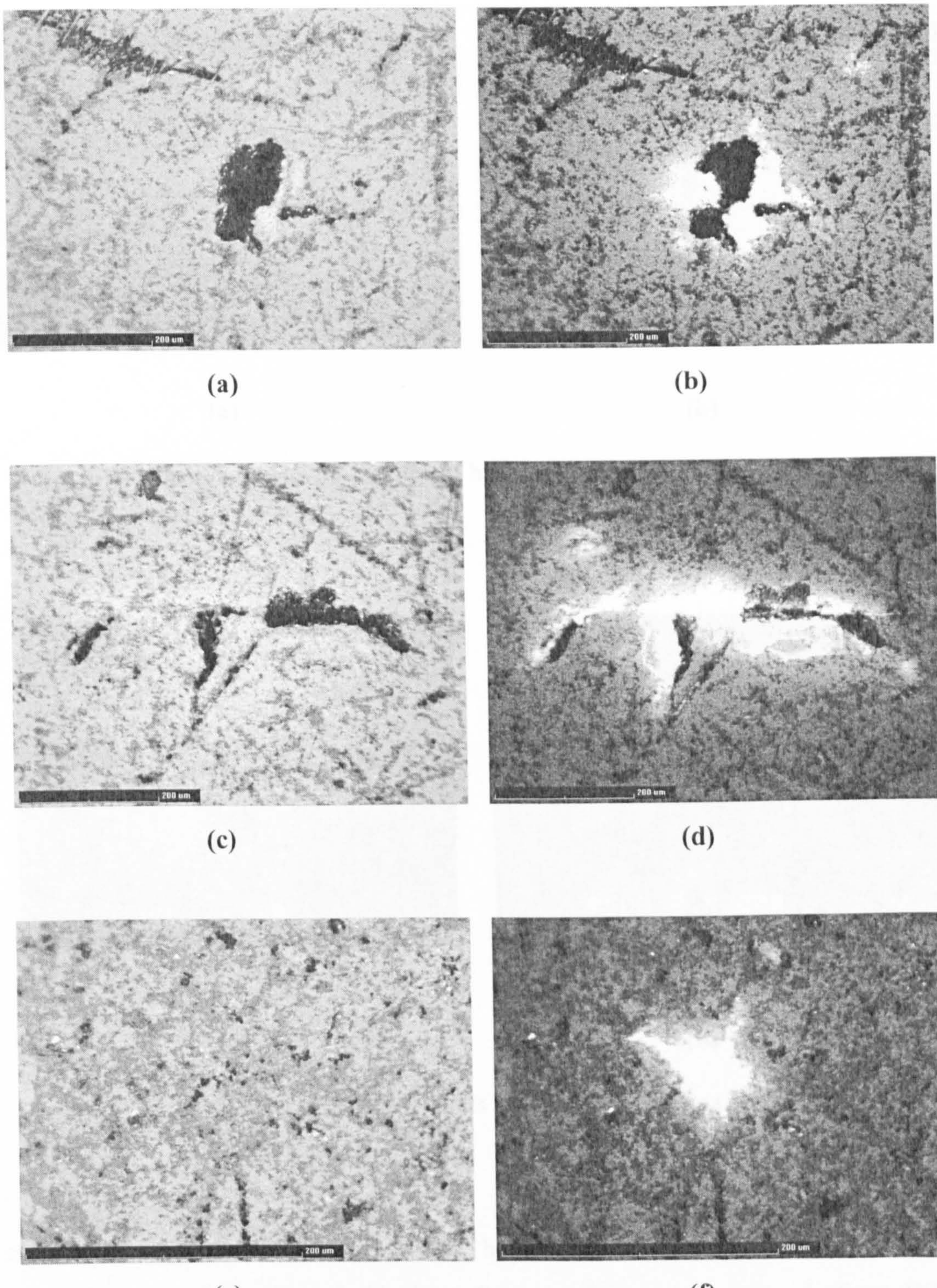

Fig 4-8 Typical surface and sub-surface damage on balls lapped under a load of 106.63 N/ball

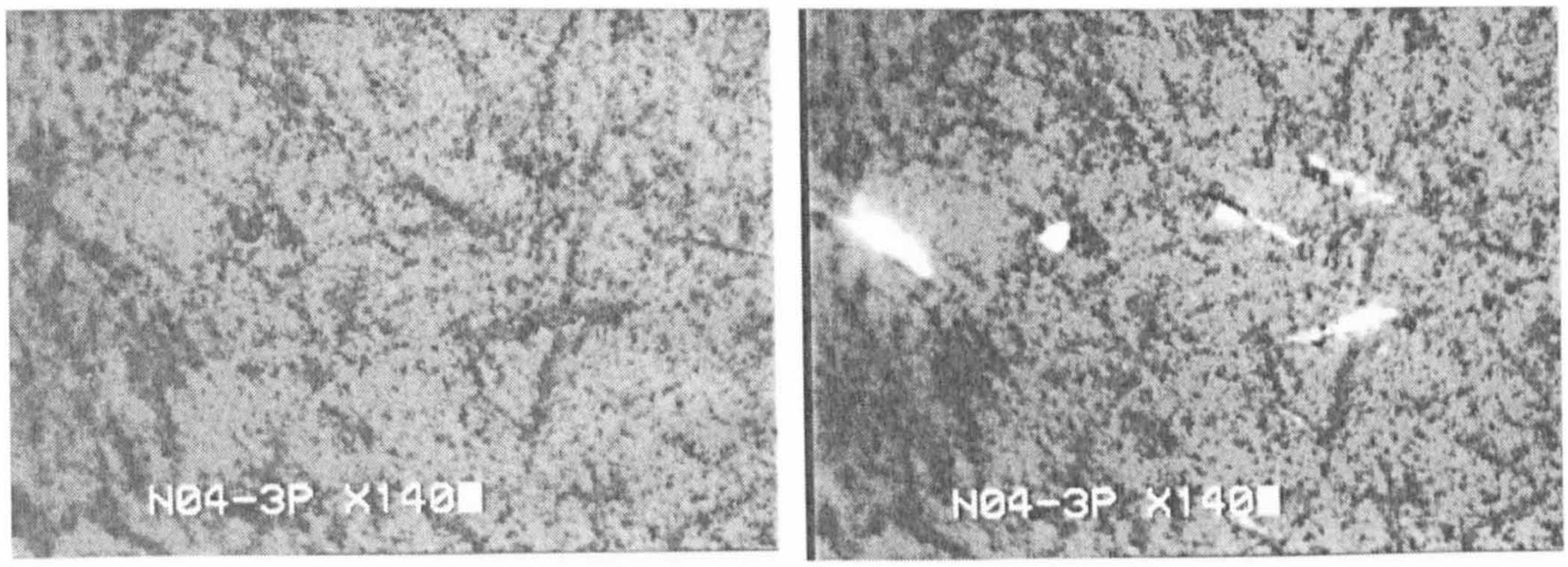

(a) (b)

Fig 4-9 Typical surface appearance of balls lapped under a load of 42.87 N/ball

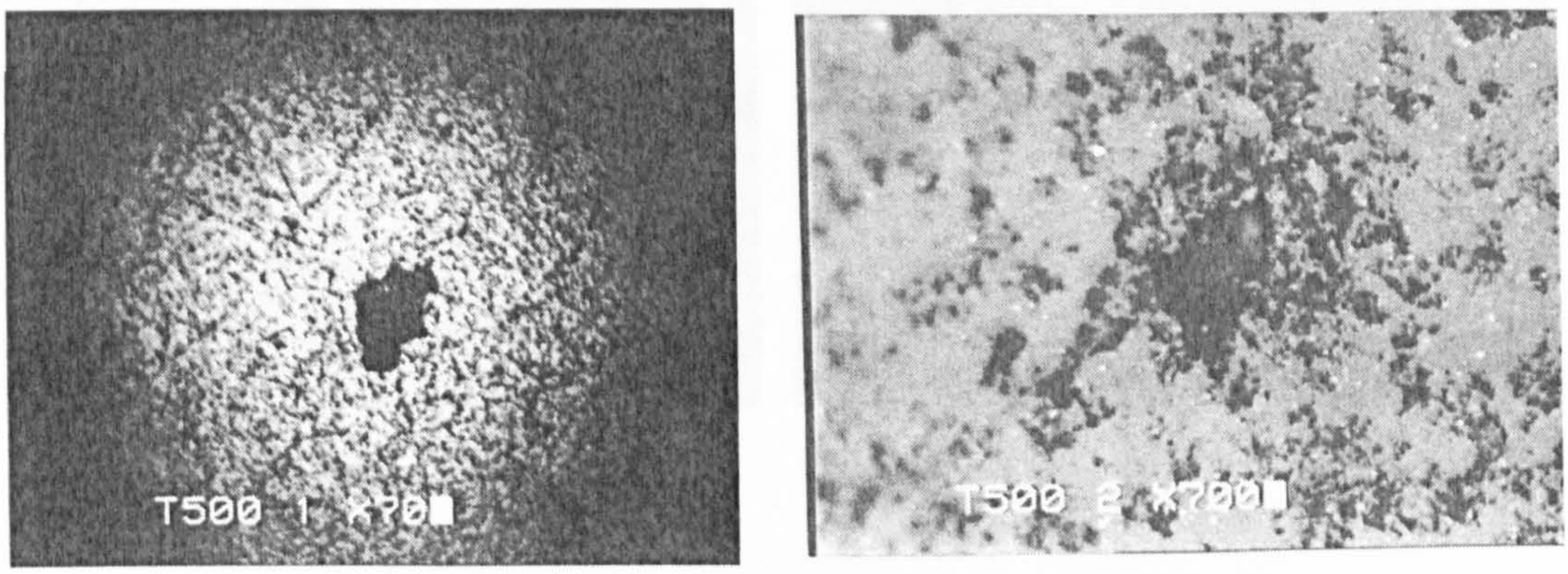

(a) (b)

Fig 4-10 Large and small spalls on balls lapped at a speed of 500 rpm

more easily observed if the balls are heat-treated before fluorescent penetrant inspection. Fig. 4-11 (a) and (b) show C-cracks found on balls made from BBB lapped at a speed of 270 rpm with a load of 18.13 N/ball. The radii of these C-cracks were between 0.4~0.425 mm. Fig 4-11 (c) and (d) show C-cracks on balls made from BBA, lapped at a lower speed of 169 rpm but also at a load of 18.13 N/ball. These

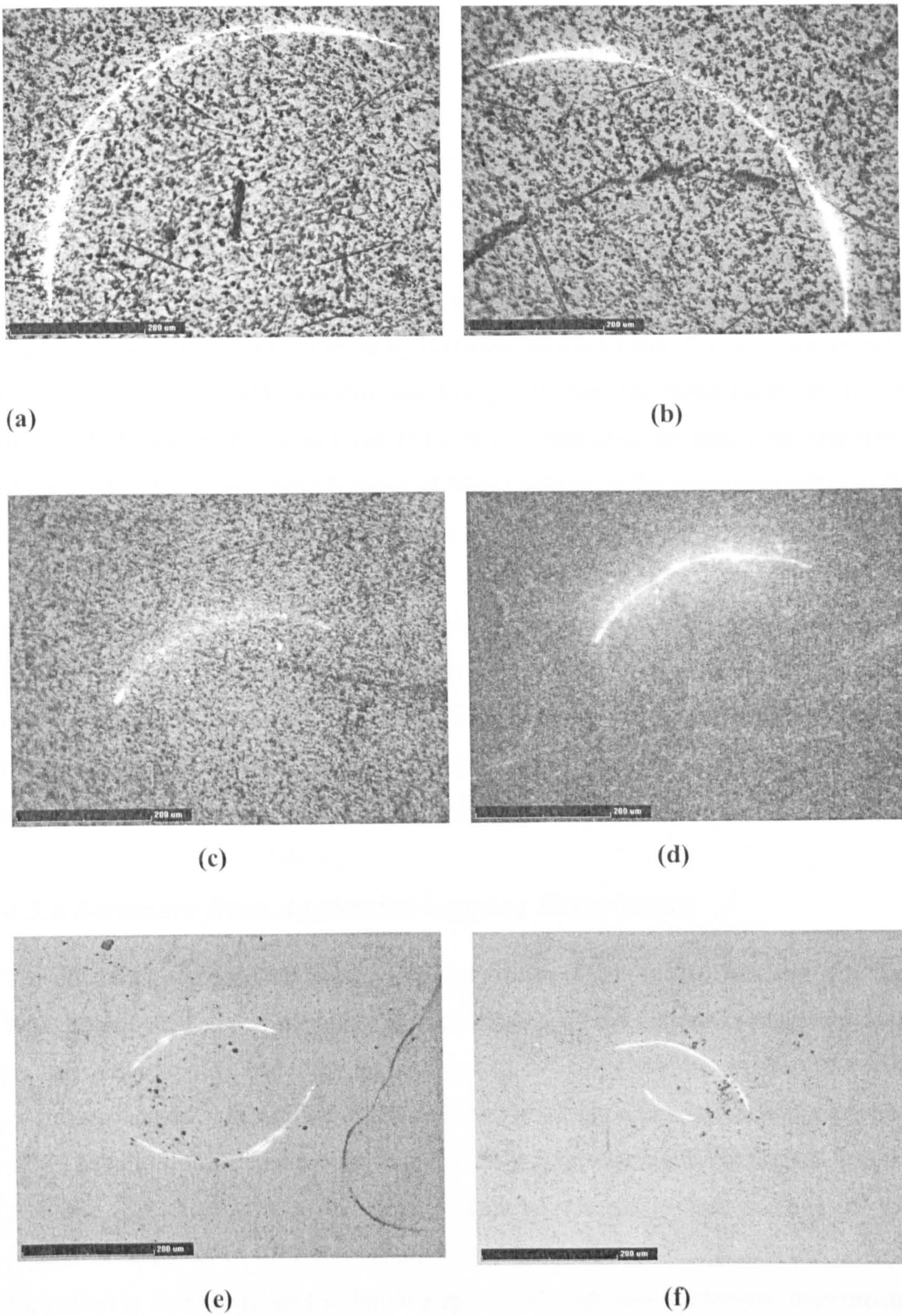

Fig 4-11 Typical C-cracks found on balls lapped at different speeds

smaller C-cracks had radii of 0.25 to 0.275 mm. Fig 4-11 (e) and (f) show C-cracks present on balls supplied in the finished state by the manufacturer of BBB. These C-cracks were of a smaller radius (0.15 to 0.175 mm). However no C-cracks were observed on balls lapped at the highest speed of 500 rpm. Also, no C-cracks were found on different batches of BBA and BBB balls lapped at speeds of 169~270 rpm then polished at speeds of 60~94 rpm. One possibility is that the C-crack formation is closely related to the final lapping (polishing) speed: within a certain speed range, C-cracks are most likely to be formed by collision between balls. C-cracks are unlikely to be formed above and below this speed range. Within this speed range, the higher the speed, the larger the C-crack radius formed. In this case, the final polishing speed of the grade 5 balls from manufacturer of BBB could be in the range equivalent to the lapping speeds of 94 rpm to 169 rpm on the eccentric lapping machine. This also suggests that if the tangential speed of the rotating lapping plate at the contact points with the balls is from 0.4 m/s to 0.7 m/s, then there is a possibility of C-cracks being generated during lapping. The ball motion in an eccentric lapping machine is much more complicated than in a conventional concentric lapping machine, since there are ball accelerations and decelerations, changes in ball spin angle and skidding. More experimental studies and theoretical analysis are needed.

4.3.6 Summary from Aggressive Lapping Experiments

The effects of aggressive lapping on HIPed silicon nitride ball surface integrity have been investigated experimentally. Surface spalls and sub-surface cracks were found on balls after lapping under the highest load of 106.63 N/ball. No substantial surface or sub-surface damage was observed on balls lapped under a nominal lapping load of 42.87 N/ball. Surface spalls were found on balls after lapping at the highest speed of 500 rpm, but there was no evidence of lapping-induced surface damage on balls lapped at a speed of 270 rpm apart from the C-cracks. It appears that C-crack formation is directly related to lapping speed although more extensive experimental study and theoretical analysis are needed.

4.4 Factors Influencing the Final Surface Quality at Polishing Stage

The second step in the finishing process is polishing, in which the ball surface roughness, roundness, dimensional and geometric accuracy are achieved. The polishing tests were also conducted on this eccentric lapping machine using a pair of steel plates (EN1A) with 8 mm eccentricity. The difference between lapping and polishing, as defined by Marinescu et al (2000), is that the abrasive particle size for lapping is normally 1~30 μm, while for polishing, the abrasive particle size is < 1 μm; The size of the chips (stock removal) for lapping is in the range of 10^{-3}~10^{-7} m, while for polishing, in the range of 10^{-7}~10^{-9} m. A damaged layer and micro-cracks were very often induced by lapping but not by polishing. The applied load and speed for polishing were both normally lower than for lapping.

4.4.1 The Effects of Polishing Load, Speed and Diamond Particle Size on Surface Roughness R_a assessed by Taguchi Methods

A standard two-level, three-parameter L4 orthogonal array was chosen for this study, as shown in Table 4-9. The three parameters to be investigated and the two level values were listed in Table 4-10.

Run	A	B	C
1	1	1	1
2	1	2	2
3	2	1	2
4	2	2	1

Table 4-9 Standard L4 Orthogonal Array used in Taguchi Methods

The balls polished were BBA as procured from the manufacturer described in Section 3.1. With an initial surface roughness value R_a 0.202 μm, the polishing test set a low R_a value as a target. The polishing test procedure was described in Section 3.3. Each polishing test lasted 24 hours. Table 4-11 shows the test results of each test run measured from 10 samples.

Level	Parameters		
	A: Polishing Speed	B: Polishing Load	C: Particle Size
1	20.83 rpm	4.58 N/ball (0.47 kgf/ball)	0.25 μm
2	93.75 rpm	8.82 N/ball (0.9 kgf/ball)	1 μm

Table 4-10 Chosen parameters and their levels for polishing test

Test Run	Measured R_a values from 10 samples										AVG R_a
1	0.0481	0.0569	0.0349	0.0506	0.047	0.053	0.0514	0.0458	0.05	0.0469	0.04846
2	0.0322	0.0298	0.0347	0.0283	0.0326	0.0337	0.0252	0.0247	0.0321	0.0263	0.02996
3	0.0379	0.0437	0.0422	0.0444	0.0428	0.0437	0.0375	0.0429	0.0472	0.0414	0.04237
4	0.0304	0.0316	0.0318	0.0318	0.0267	0.024	0.0344	0.0295	0.0317	0.03	0.03019

Table 4-11 Polishing test results.

Parameter	Level	Level Average Response of R_a Value (μm)
A. Polishing Speed	Level 1, 20.83 rpm	0.0392
	Level 2, 93.75 rpm	0.0363
B. Polishing Load	Level 1, 4.58 N/ball	0.0454
	Level 2, 8.82 N/ball	0.0301
C. Diamond Particle Size	Level 1, 0.25 μm	0.0393
	Level 2, 1 μm	0.0362

Table 4-12 Level average response analysis for polishing test

The level average response analysis, with principles as described in Section 4.2.3, was used to assess the effects of each polishing parameter. Table 4-12 shows the results of level average response analysis. The polishing speed of 93.75 rpm gave better results than at 20.83 rpm, but the difference was very small: only 8%. This indicates that the surface roughness R_a value will not be improved by lowering the

polishing speed. A change of polishing speed within this range has less effect. Much better surface roughness R_a value was achieved by a polishing load at 8.82 N/ball than at 4.58 N/ball: the R_a value decreased by 34%. This also implies that the polishing load has significant influence on the R_a value. The difference between using 0.25 μm and 1 μm diamond particle sizes was also very small: 8%, although the 1 μm diamond particle size proved slightly better. This means 1 μm diamond particle size is suitable in the initial polishing stage for quickly reducing the R_a value. But in the final polishing stage, 0.25 μm diamond particle size was found to be better.

4.4.2 Other Influencing Factors

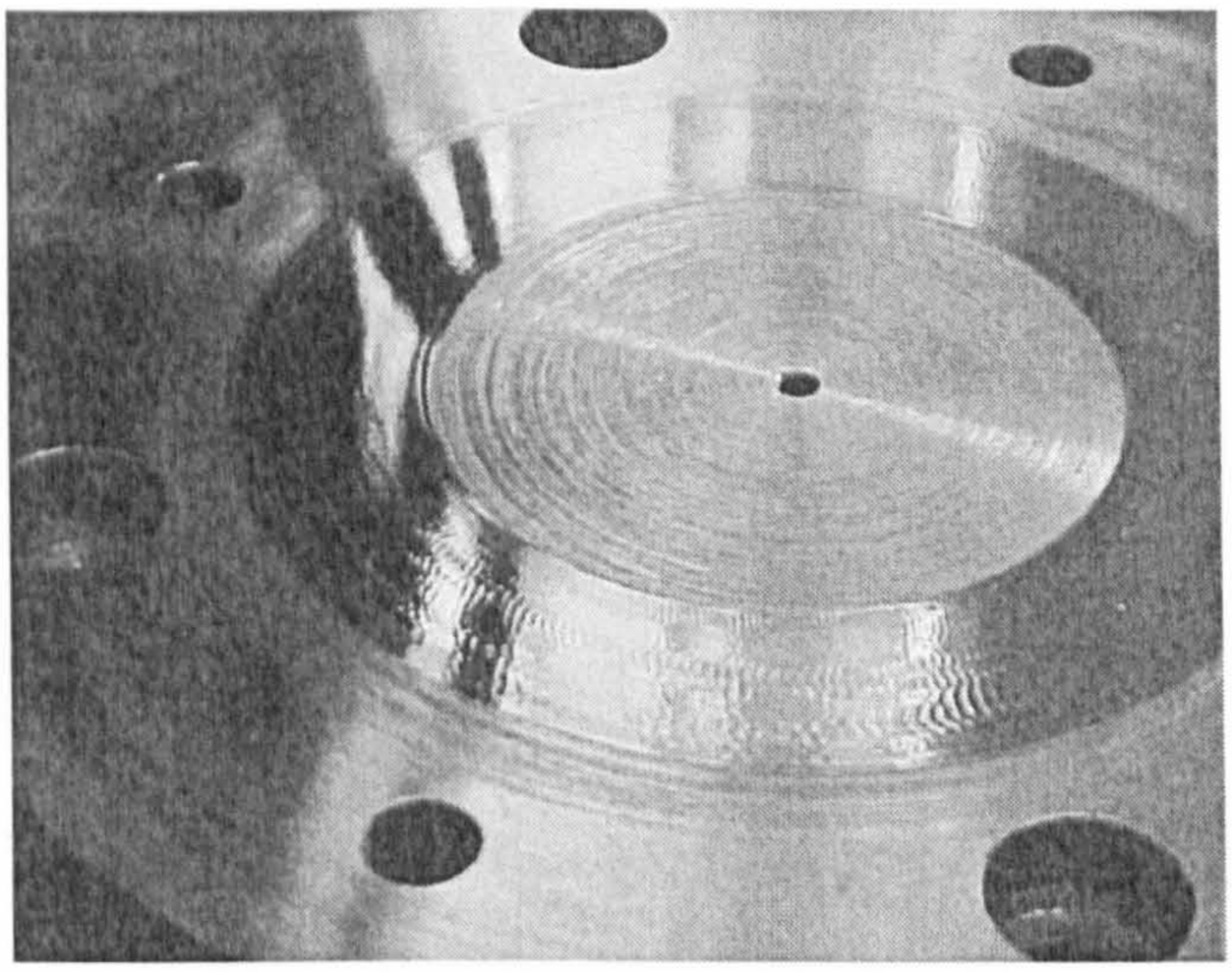

Fig. 4-12 Condition of upper plate lapping area

The other most influential factor in the polishing stage is the condition of the top plate. The best polishing results were achieved when the upper plate lapping area was shiny, a mirror-like surface was generated due to the self-polishing effect. In an attempt to explore the self-polishing effect of the top plate, a rough turned upper plate was used for polishing under a 14.7 N/ball polishing load. Fig. 4-12 shows a waviness in the appearance of the upper plate lapping area. This waviness may be due to the initial lapping surface having been too rough (see centre of the plate), or to the polishing load having been too high. Under these conditions, the comparative surface

roughness value of the polished ball was seen to be high under the microscope. This implies that the initial surface quality of the upper plate should be reasonably high.

The deep mark left on the ball surface by diamond particle ploughing during a previous lapping process (Fig. 4-13) could be difficult to remove during the polishing process, when stock removal is very small. This suggests that in order to obtain better surface quality, the diamond particle size should be reduced gradually, to avoid leaving any deep marks on the surface.

Other factors which could influence the polishing quality are the condition of the V-groove in the lower plate and contamination of the polishing fluid by large diamond particles previously left in the pipeline, etc..

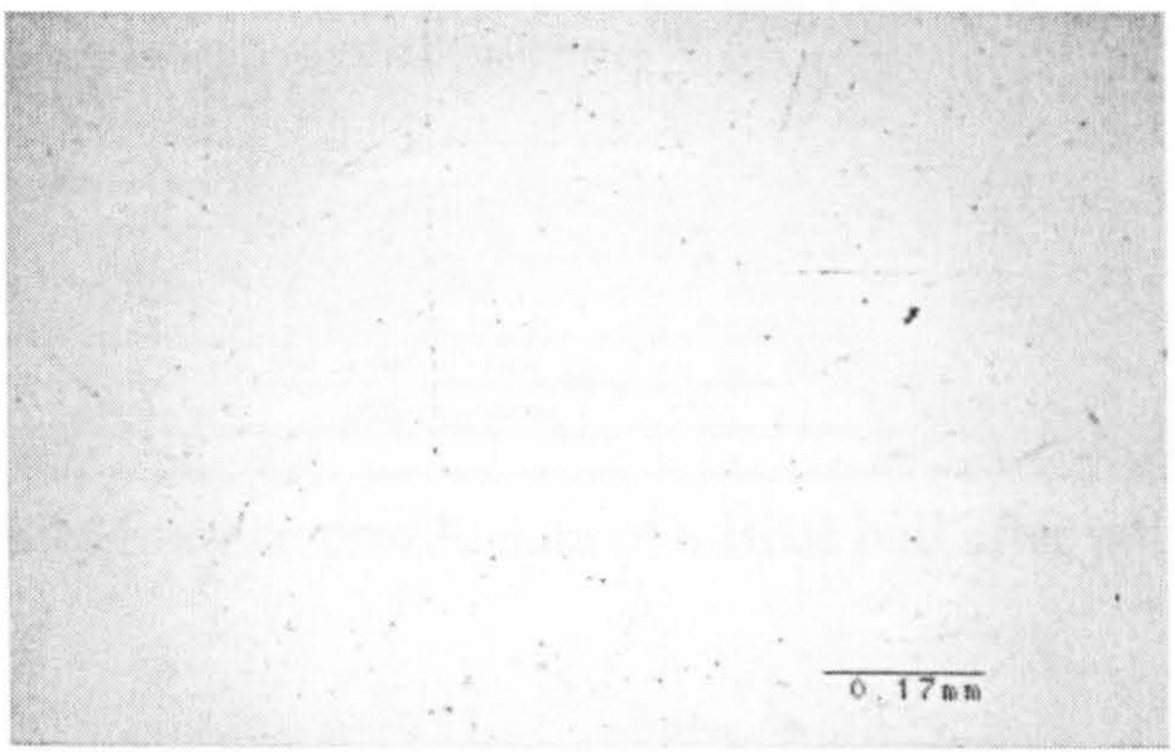

Fig. 4-13 Mark on the ball surface left from previous lapping process

4.4.3 Polishing Results

The best polishing results so far achieved for the polished BBB balls are a surface roughness value R_a of 0.003 μm which is above the grade 3 specification for precision bearing balls, a ball roundness of 0.08~0.09 μm which is above the grade 5 and close to the grade 3 specification for precision bearing balls. Fig. 4-14 shows the surface profile data of a BBB ball after polishing. This was analysed using a Zygo New View three-dimensional imaging surface structure analyser. Fig. 4-15 shows the roundness profile of a BBB ball after polishing using a Taylor-Hobson Talyrond 73 roundness profiler.

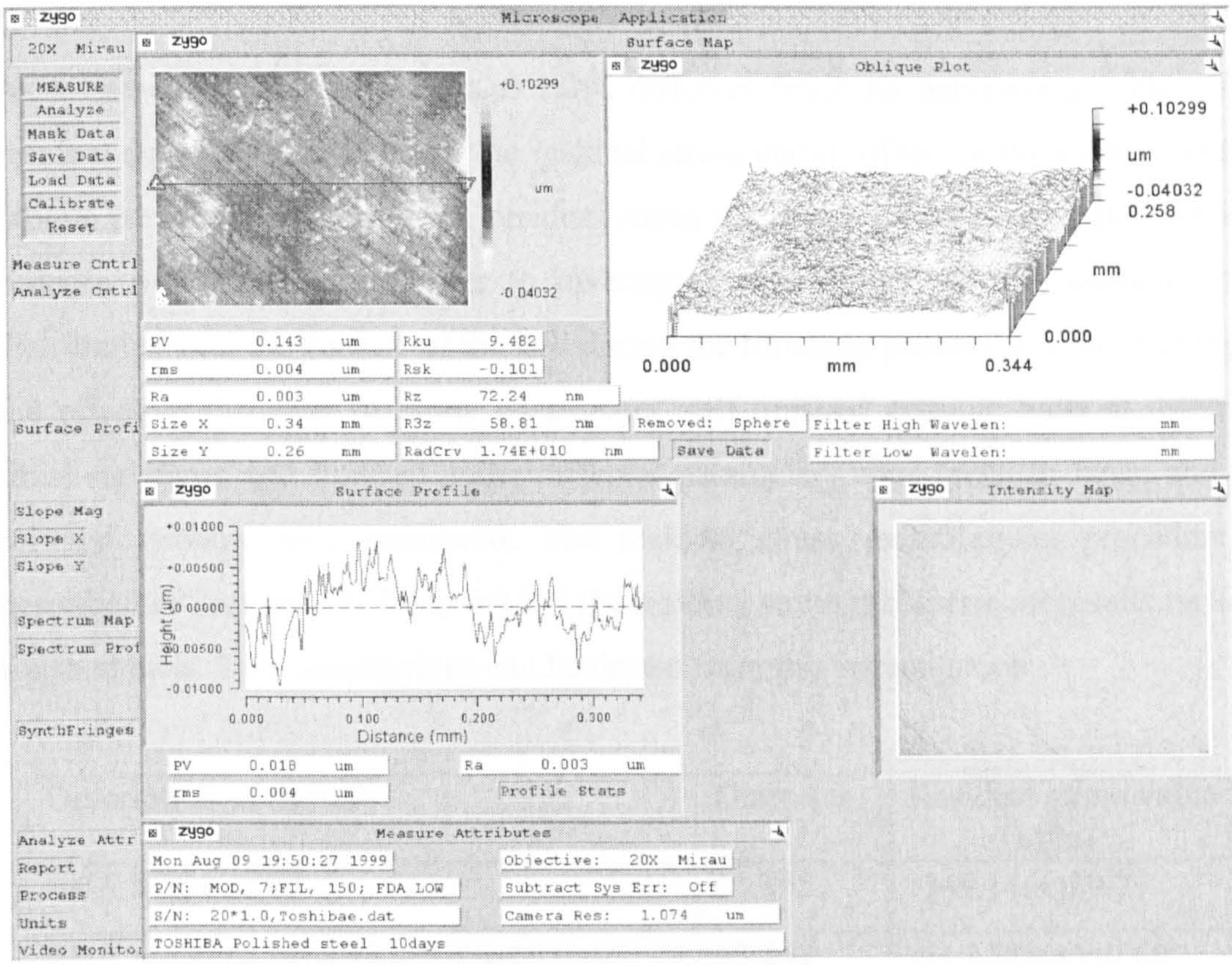

Fig. 4-14 Surface profile data of a BBB ball after polishing

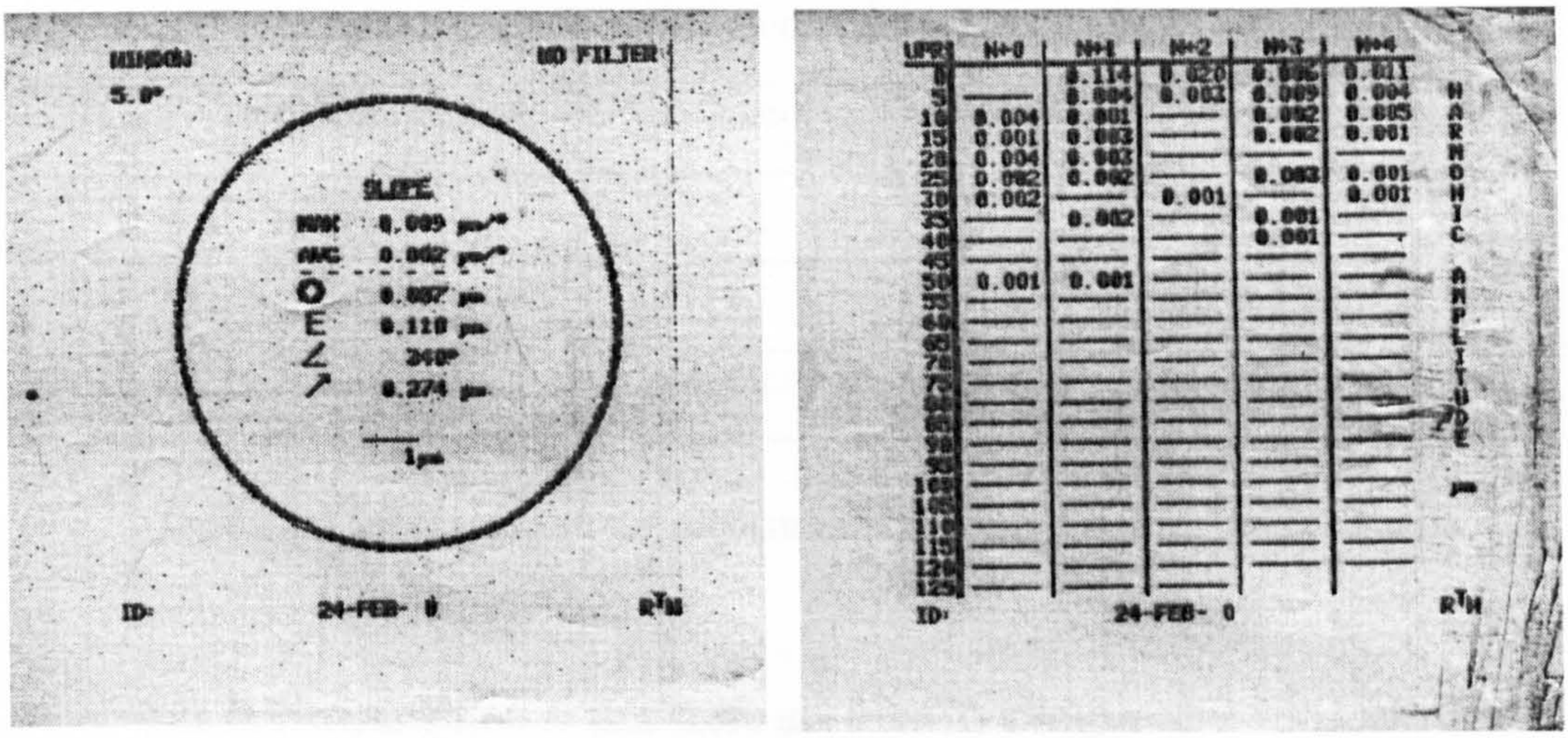

Fig. 4-15 Roundness profile of a BBB ball after polishing

4.5 Finishing Process Induced Residual Stresses

As reviewed in Sections 1.2.3 and 1.2.4, different finishing parameters could affect residual stress distribution, and the residual stress could influence the rolling contact fatigue performance. Therefore, residual stress induced by the finishing process is a concern of this study. In order to investigate any changes in the residual stress distribution near the surface of the ball during the finishing process, and to investigate the effect of different finishing parameters, self-finished ceramic balls at different finishing stages and finished under different parameters were taken to Japan and the residual stresses were measured. The residual stress measurement procedure is described in Section 3.7. Table 4-13 is the residual stress measurement results on self-finished balls. Two assumptions can be drawn from this investigation.

Description of the ball	Diameter	Residual stress value (MPa)
BBA as procured	13.255	-149.11(±)29.29
BBA polished from as procured	13.252	-117.721(±)40.69
BBA 106.63 N/ball lapped, then polished	12.698	-142.341(±)38.91
BBA 42.87 N/ball lapped, then polished	12.698	-92.1(±)50.71
BBA 30.97 N/ball lapped, then polished	12.704	-78.321(±)36.20
BBA 12.75 N/ball lapped, then polished	12.703	-11.954(±)34.21
BBB as procured	13.5	-803.699(±)58.28
BBB 18.13 N/ball lapped	13.4	-237.667(±)47.32
BBB 12.75 N/ball lapped, then polished	13.051	-41.357(±)37.10

Table 4-13 Residual stress measurement results on self-finished balls

The first assumption is that there are initially compressive residual stresses on the ball blank surfaces due to previous HIP processes. This compressive residual stress layer takes about 0.3 mm of the radius measurement on a ball with a final diameter of 12.7 mm (ball blank diameter was 13.25~13.5). Very high compressive

value is evident at the ball blank surface. This gradually reduces towards the core of the ball. This residual stress layer will be partly or entirely removed during the finishing process.

This assumption is supported by the very high compressive value (-803.7 MPa) measured on the BBB blank with a diameter of 13.50 mm. After lapping to a diameter of 13.40 mm the compressive value had reduced to –237.7 MPa and finally after lapping and polishing to a diameter of 13.05 mm, the compressive value dropped to –41.4 MPa.

For BBA blanks, the measured compressive residual stress values were –149.1 MPa before polishing and –117.7 MPa after polishing. The measured compressive residual stress values for the BBA blanks were not very high. There are two possible reasons for this. One possibility is that the previous manufacturing process for BBA was directly HIPed which introduced less compressive residual stress than the Sinter + HIPed process employed for BBB. Another possibility is that after the directly HIPed process, the BBA were roughly ground before being supplied as ball blanks. The most compressive residual layer would then have been removed during this rough grinding process.

It seems that this compressive residual stress is concentrated near the surface layer of the ball blank. This is supported both from the measurement results of the BBB ball, –41.36MPa at a diameter of 13.051 and from the measurement results of the BBA ball, –11.95MPa at a diameter of 12.703. They were both lapped at a load of 12.75 N/ball, removed a layer of 0.45~0.55 mm in diameter, assuming the residual stress change induced under this light lapping load can be ignored. A previous investigation by Stolarski and Tobe (1977) on 6.5 mm nominal diameter balls also reported that the residual compressive stress decreases as the amount of material removed grows.

The second assumption is that the higher lapping load will generate higher compressive residual stresses on the balls. The residual stresses were measured on BBA lapped under different loads to nearly the final diameter of 12.7 mm. In order to eliminate the influences of surface profile and damage from the measured values of residual stresses, balls lapped under different loads were polished at 8.82 N/ball for

24 hours. The results showed that there was almost a linear increase of the compressive residual stress as the lapping load increased. Under a lapping load of 12.75 N/ball, the residual stress was –11.95 Mpa, and at the highest lapping load of 106.63 N/ball, the residual stress was –142.34 MPa. The residual stress change from the lowest lapping load to the highest lapping load was only about –130 MPa.

It was shown in Section 4.3 that under the highest lapping load of 106.63 N/ball, severe surface and subsurface damage occurred, although the lapping rate was not high. The recommended lapping load is 42.87 N/ball or less. Under these circumstances, the residual stresses induced by the lapping process will be within –100 MPa. This will have little influence on the contact stress field distribution as shown by a FEA modelling in Appendix 6.

4.6 Exploration of the Material Removal Mechanisms

As illustrated in Fig. 1-6, it is only through material removal mechanisms that the nature of the relationship between finishing parameters and surface quality can be revealed. Although detailed theoretical studies on the material removal mechanisms were not possible within the scope of this PhD study, effort has been made to understand the material removal mechanisms experimentally by optical microscope and SEM observations.

The material removal mechanisms during the lapping process of ceramic balls are very complicated. Lapping can be considered as a three-body wear, with abrasive particles acting like indenters sliding and rolling between the lapping plate and the workpiece. The lapping fluid serves as lubricant and may also have tribochemical reactions with the workpiece. During lapping, as the stock is being removed from the workpiece, the abrasive particles will be worn and broken down to a smaller size, and the lapping plates will also be worn. These worn debris will be constantly added to the lapping fluid thus changing the viscosity of the fluid. Abrasive particles can be embedded in the lapping plate and it then will also act like a grinding wheel. In the lapping process of ceramic balls, the balls are rolling and spinning in between the two

lapping plates. Diamond particles will be brought into contact between balls and plates, and some of these will be left after this contact. This unique ball-lapping kinematics makes theoretical analysis more difficult than the lapping on a flat surface.

As shown by the experimental results described in Section 4.1.3 and the microscopy and SEM observations on the ball surfaces the predominant material removal mechanism during the lapping of ceramic balls was still mechanical. The indentation model on brittle materials developed by Lawn and Wilshaw (1975), can be used to assist the explanation of the material removal process. In that model six stages were identified: plastic deformation below the indenter, median vent formation during loading, growth of the median vent into a median crack, closing of the median crack on unloading, lateral cracks appearing under the plastic zone, large lateral cracks leading to chipping.

Fig. 4-16 show the microscopy and SEM observations on the surfaces of BBA and BBB lapped under normal conditions, i. e., lapping load 18.13 N/ball, lapping speed 169 rpm and diamond particle size 45 μm. In order to make a comparison between the two kinds of ball blanks, all the observations on the BBA are in the left column of Fig 4-16, and all the observations on the BBB are in the right column. Fig 4-16 (a) and (b) are microscopy observations at a magnification of 70×, and Fig 4-16 (c) and (d) are microscopy observations at a magnification of 700×. These are the typical microscopy appearances for BBA and BBB lapped without substantial surface damage throughout the finishing tests.

Fig 4-16 (b) shows scratch marks on the BBB surface, which suggest abrasive wear by diamond particles. On the BBA surface in Fig 4-16 (a), scratch marks are not obvious. Instead, it features many small, dense and evenly distributed dark areas. Fig 16 (c) shows these small, dense and evenly distributed dark areas under microscopy at high magnification. The dark and bright areas are of approximately equal distribution. In contrast, in Fig 4-16 (d), which is a BBB surface under microscopy at the same magnification, the bright area dominates and the dark area is concentrated not uniform. One possible reason for this difference is that although BBA and BBB are both made from brittle materials (HIPed Si_3N_4), the material property for BBB is less brittle than that for BBA. The measured surface hardness for a BBB is 1532 (HV10),

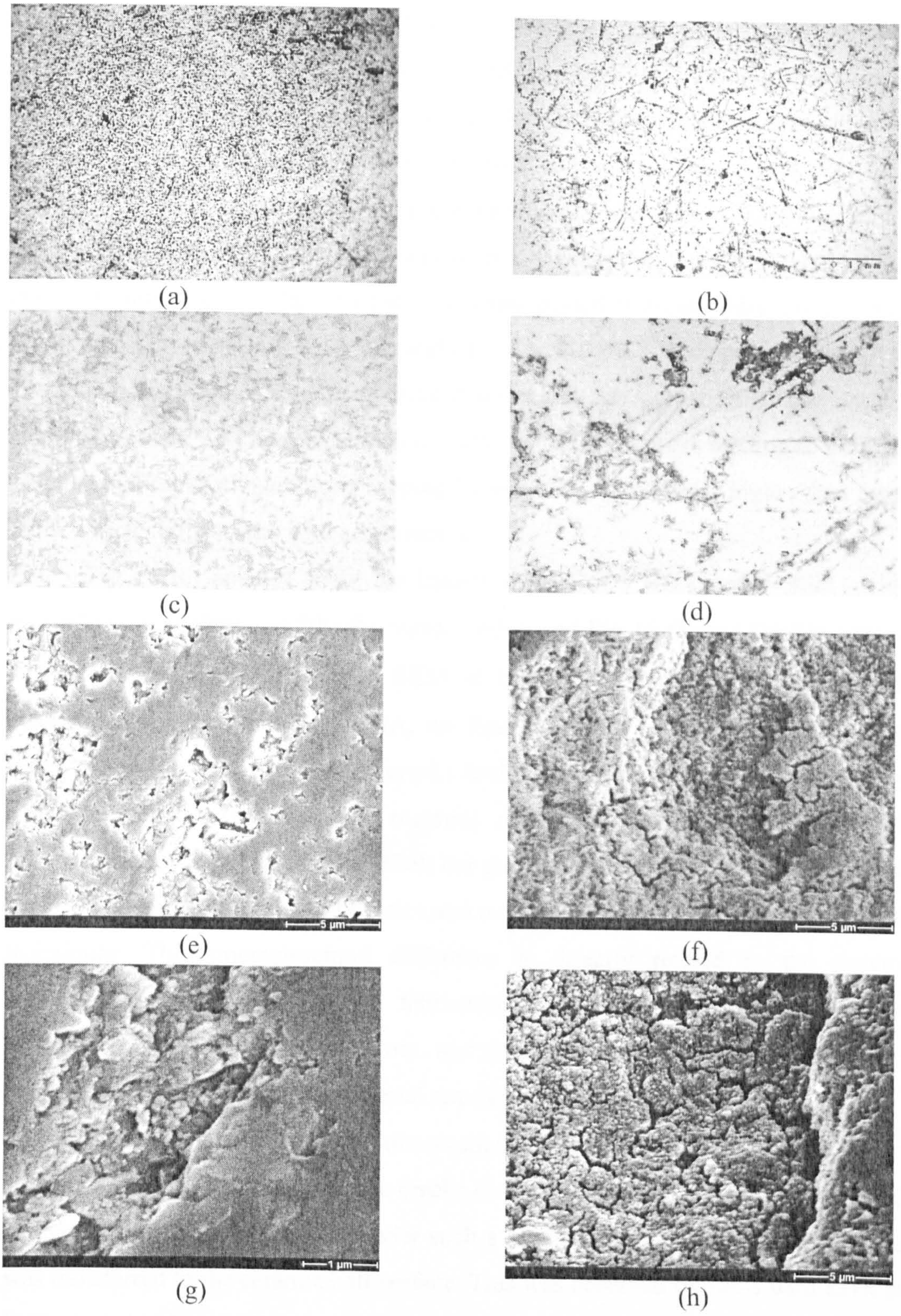

Fig. 4-16 Microscopy and SEM observation on lapped surfaces, (a), (c), (e), (g) from BBA; (b), (d), (f), (h) from BBB

lower than BBA which is 1682 (HV10). The fracture toughness for BBB is 6.6 MPa $m^{1/2}$, while for BBA it is 5.3 MPa $m^{1/2}$ (Cundill 1997). Using the indentation model developed by Lawn and Wilshaw to explain the material removal process, there will be a wider plastic deformation zone for the BBB in the first stage, and in later stages there will be fewer median and lateral cracks which would lead to chipping due to it being less hard and tougher. The wider plastic deformation zone generated by each diamond particle during lapping leads to wider smoother areas which are the wider bright areas shown in Fig 4-16 (b) and (d). For the BBA, because it is harder and less tough, there will be smaller plastic deformation zones in the first stage, and in later stages there will be more median cracks and lateral cracks leading to chipping. The material removal rate during lapping for the BBA is 3~4 times higher than for the BBB, which confirms the above assumption.

Fig 16 (e) and (g) show the lapped surface of a BBA under SEM at high magnification (5000× and 20000× respectively), and Fig 16 (f) and (h) illustrate the lapped surface of a BBB under SEM at a magnification of 5000×. The SEM observation suggests that for a BBA, the final material removal (stage six in Lawn and Wilshaw's model: large lateral cracks leading to chipping) features grain pull-out, and for BBB, it features bulk material removal by micro-cracks. The SEM observation also suggests that for BBB, the grain size is more uniform and finer than for BBA, although the actual grain size and morphology need to be proved by etching techniques. This microstructural difference is directly related to the previous manufacturing processes, i.e. the fabrication of powder and fibre, blending of additives, densification processes, etc. and could have some effect on the material properties thus influencing the material removal process during lapping.

Fig. 4-17 shows the SEM observation on high load (106.63 N/ball) lapped surfaces of a BBB ball. The surface cracks can be seen in Fig. 4-17 (a). Fig.4-17 (b) shows the detail inside a crack. Under such a high load, steel from the lapping plate was transferred to the ceramic ball surface. This was observed by SEM with EDX and is illustrated in Fig. 4-18.

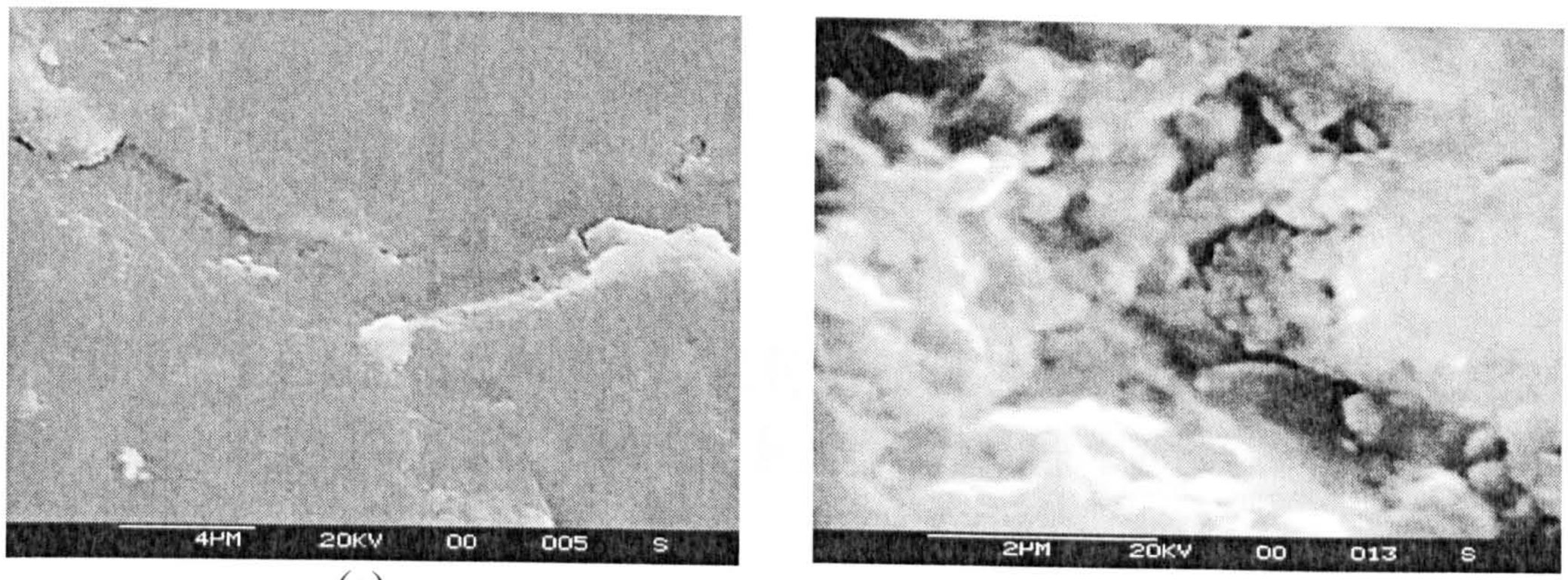

(a) (b)

Fig. 4-17 SEM observation on high load lapped surfaces

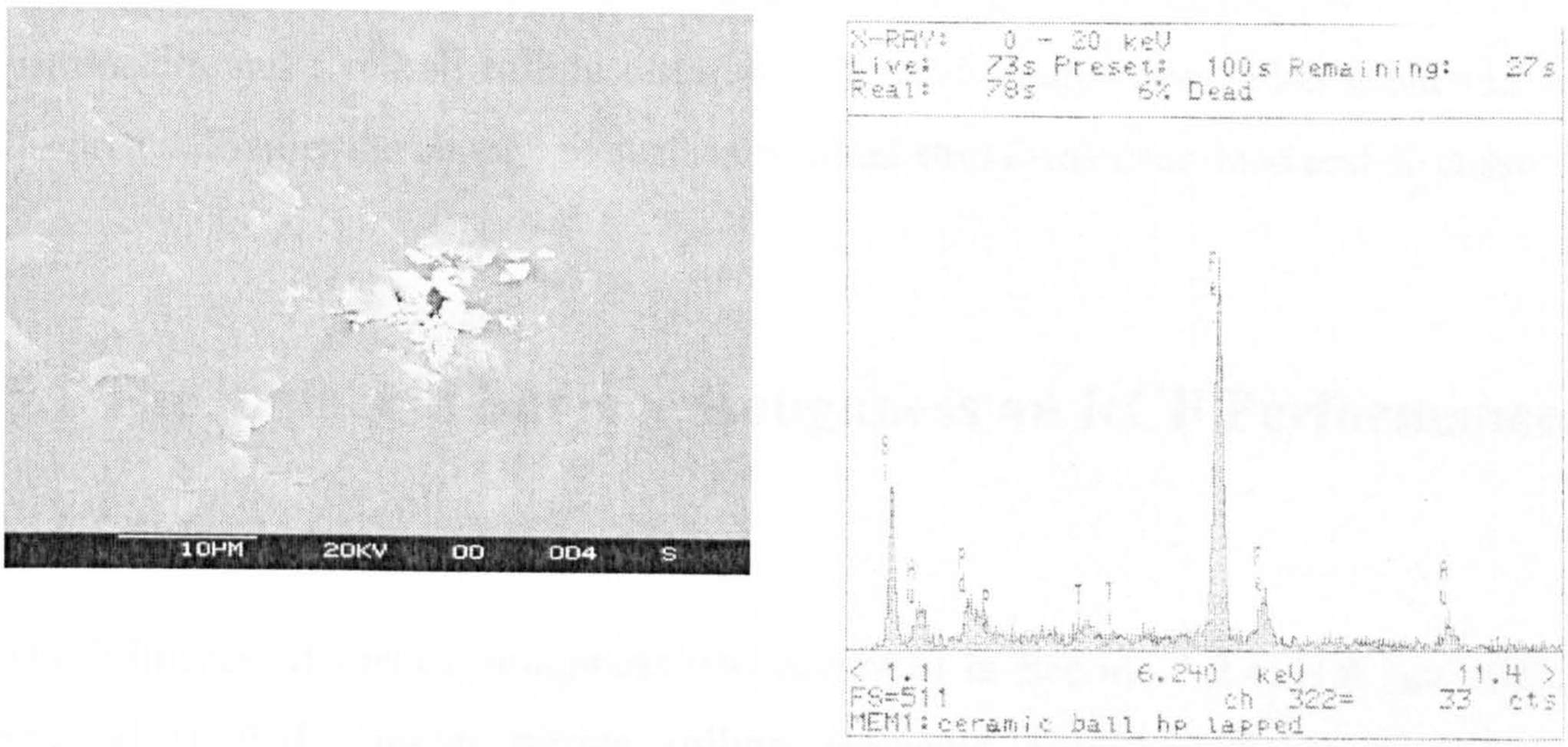

(a) (b)

Fig. 4-18 SEM with EDX observation on steel transferred to ceramic ball surface

5.0 EXPERIMENTAL RESULTS & DISCUSSION, PART TWO: FATIGUE TEST

This chapter presents the experimental results and discussion on rolling contact fatigue tests. The effects of surface roughness, surface heterogeneous porosity and surface defects, such as star defects, grinding defects and C-crack defects, on RCF life and failure modes were assessed and discussed. The influences of finishing parameters and five-ball rolling tests on RCF performance were also evaluated and discussed. Finally the change of surface residual stress was examined and discussed.

5.1 The impact of Surface Roughness on RCF Performance

5.1.1 Introduction

The influence of surface roughness was reviewed in Section 1.2.4. Hot isostatically pressed (HIPed) silicon nitride rolling elements give significant performance advantages in hybrid bearings and all-ceramic bearings. The only restriction hindering widespread application is the high manufacturing cost of these rolling elements. Because these rolling elements are subjected to high cyclic contact stresses, currently they are finished to the best possible surface roughness value to reduce the risk of rolling contact fatigue failure according to experience with steel rolling elements. The material properties of ceramics are very different from steel, especially following the technological advances of powder manufacture and material densification. This philosophy of obtaining the best possible surface roughness may lead to over-engineering of ceramic rolling elements. The surface roughness

parameters, which are considered to be the most influential in rolling contact fatigue, are therefore of interest and concern to both industry and academia.

In this study, the test samples were four kinds of HIPed silicon nitride balls with diameters of 12.7 mm (½"), commercially finished to grade 5, from different manufacturers, designated as A, B, C and D, and two different kinds of HIPed silicon nitride ball blanks lapped and polished to 12.7 mm by the author using an eccentric lapping machine, designated as E, F and G. The same ball blank material was used for balls F and G; F being rough lapped only and G lapped and then polished. E represents balls lapped from another ball blank material. Detailed descriptions of the seven-ball samples and surface examination before testing were given in Section 3.1.2 (See Table 3-2 and Fig. 3-2, Fig. 3-3). The different surface roughness R_a values are well reflected by the microscopy images (Fig. 3-3), with higher R_a values corresponding to more dark areas in the pictures in the sequence of E, F, B, G, A, C, D. The microscopy images of samples A, C and D are similar, with D the brightest. However, the 3D surface analysis reveals that although its R_a and R_q (rms) values are the lowest in all of the samples, it has a positive skewness value R_{sk} of 2.64 and a very high kurtosis value R_{ku} of 47.8 which means that the surface of D is "spiky". In contrast, both A and C have a negative skewness value R_{sk}, which implies that the bulk material is above the mean line (the surface has more valleys than peaks). Many scratches left by the previous lapping process can be observed on the surface of sample G and these scratches are also revealed by 3D topography profiles and a negative skewness value R_{sk} of –0.868 (Fig. 3-2G). Whether these parameters would affect the rolling contact fatigue life is therefore of interest. Samples A, B, C and D were also measured by a Talysurf 2D surface profiler, for each kind of sample with three measurements on three balls. The statistical analysis values for different roughness parameters (R_a, R_q, R_z, etc.) are very close to the values measured by the 3D surface structure analyser.

The test machine was described in Section 3.4.1, and the experimental procedure in Section 3.4.2. The measured geometric and physical properties of steel testing balls are listed in Table 3-5. In this study, the Plint machine load was 1.96 kN

and shaft speed 10,000 rpm. The contact stress cycles of upper silicon nitride balls exceeded 135 million by changing the lower steel balls.

5.1.2 Experimental Results Analysis

A summary of the rolling contact fatigue test records is given in Table 5-1 (the decimal of hours were converted from minutes and seconds recorded in the computer files). The calculated Hertz contact stresses are shown in Table 5-2. The calculated minimum film thickness and lambda ratio is shown in Table 5-3. In all of the tests, no typical fatigue spall of comparable dimensions to the rolling track was found on any of the silicon nitride balls. Fig. 5-1 and Fig. 5-2 show the microscopy observations and the interference profilometry images respectively, of the rolling tracks of samples A to G after testing.

An analytical balance was used to measure the mass of the sample balls before and after RCF testing. The mass loss of each of the sample balls after testing was in the range of 0.1 mg ~ 1mg. If this is converted to volume loss, it will be in the range of 0.3 ~ 3×10^{-10} m^3. Although the readability of this balance is 0.1/0.01mg, the repeatability of the measurement result is within a few tenths of 1 mg. In addition, oil residues can be deposited on to the rolling track which can influence the accuracy of mass loss. So, in this study the mass loss or volume loss was not used to quantify the rolling contact performance of the sample balls. Instead, changes to the surface topography on the rolling track was the major factor used in this study.

5.1.2.1 Surface Examination Analysis for Each Sample

Sample A is a commercially finished ball with an R_a value 0.005 μm and a negative skewness value –1.38. After 134.35 hours RCF test (181 million stress cycles), no difference can be observed on the rolling track under optical microscope (Fig. 5-1 A) except for the oil stain deposited on the outer edge of the rolling track which could not be removed by ultrasonic cleaning. Fig. 5-3 shows the oil stain on the outer edge of the rolling track under higher magnification. Fig. 5-4 is the analysis of the rolling

Sample	Total RCF test duration (hours)	Total contact stress cycles (million)	Lower balls changed after (hours)	Final temperature (°C)	Test termination and observations
A	134.35	181.3725	17.083, 49.867, 67.4	63.8	Oil residues on upper ball
B	100.72	135.972	39.68, 10.2, 50.84	62.2	One lower ball small spall, small amount of dark debris in oil
C	110.48	149.148	8.07, 102.41	65.6	Oil residues on upper ball
D	131.85	177.9975	22.57, 8.91, 100.37	64.2	Oil residues on upper ball, Some rust-like debris in the oil at the bottom of the retainer cup
E	146.19	197.3565	43.48, 1.74, 100.97	59	Terminated (without incident)
F	136.37	184.1	22.6, 67.02, 46.75	61.3	Terminated (without incident)
G	137.82	186.057	25.77, 62.37, 49.68	60.1	Terminated (without incident) small amount of dark debris in oil

Table 5-1 Rolling contact fatigue test records for samples A~G

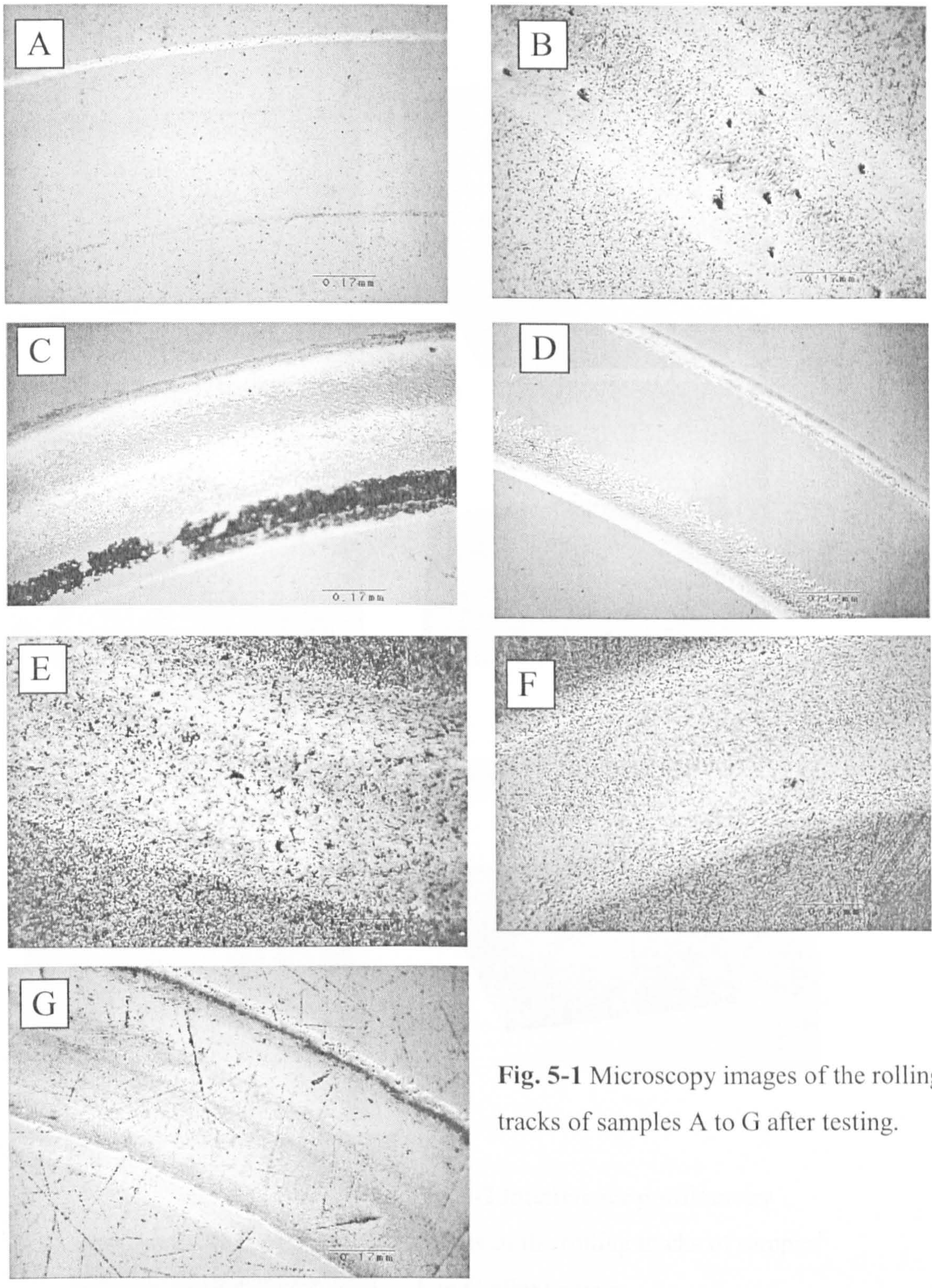

Fig. 5-1 Microscopy images of the rolling tracks of samples A to G after testing.

track by the 3D surface analyser. From the oblique plot of Fig. 5-4, slight wear on the rolling track can be seen. This wear on the rolling rack is not evenly distributed,

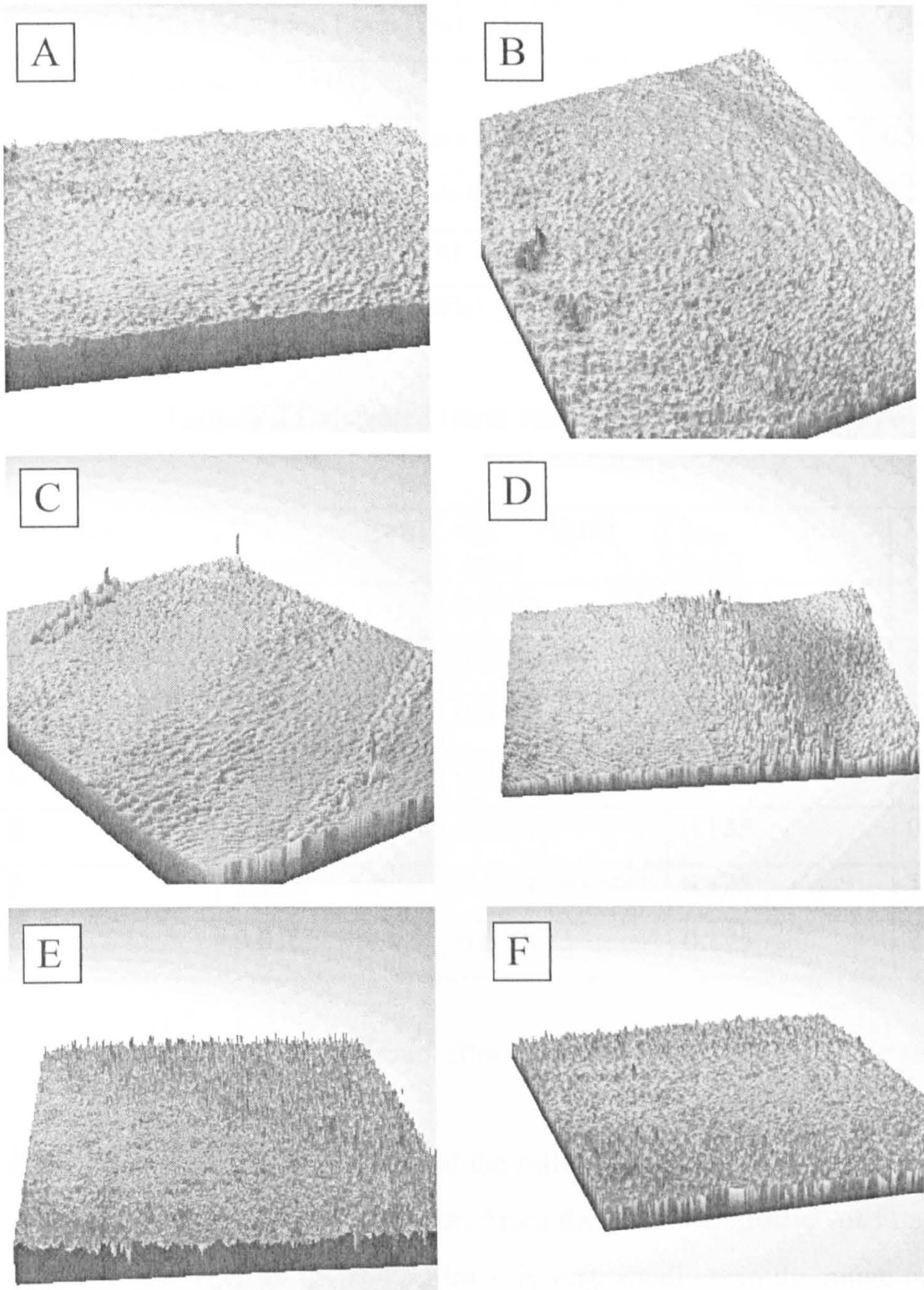

Fig. 5-2 Interference profilometry images of the rolling tracks of samples A to G after testing.

Plint Machine Load (kN)	1.96
Contact Load (N)	800
Max. Compressive Stress (GPa)	6.58
Radius of Contact Circle (mm)	0.24
Max. Shear Stress (GPa)	2.04
Max. Tensile Stress (GPa)	1.01

Table 5-2 Calculated Hertz contact stresses for samples A~G

Samples	R_{q1} (μm) ceramic	R_{q2} (μm) steel	h_{min} (μm)	λ
A	0.007	0.0376	0.125	3.26
B	0.021	0.0376	0.125	2.89
C	0.004	0.0376	0.125	3.29
D	0.003	0.0376	0.125	3.30
E	0.132	0.0376	0.125	0.91
F	0.118	0.0376	0.125	1.00
G	0.010	0.0376	0.125	3.20

Table 5-3 Calculated minimum film thickness and lambda ratio for samples A~G

featuring less wear in the middle of the rolling track. This is a common characteristic, and will be discussed in detail later. From the "Surface Profile" of Fig. 5-4, it can be seen that the wear on the rolling track is very small — in the range of 0.05~0.1μm; the height of the oil stain is in the region of 0.15μm. The values of surface roughness parameters are increased nearly 10 times compared to the values in Fig. 3-2A before testing, with R_a increased from 0.005μm to 0.067μm, R_q (rms) from 0.007 to 0.090 and R_z from 108.35nm to 799.76nm. Although the roughness values in Fig. 5-4 are the average values from the measured area which includes the oil stain at the edge of the rolling track and some areas outside the rolling track, most of the measured area is the rolling track. In addition, the roughness parameter R_a is an arithmetic average

so that occasional higher values, such as those caused by oil deposits, will have less effect than the vast majority of values inside the rolling track. These results reflect the tendency of the surface in the rolling track to become rougher due to wear. The skewness value changed from –1.38 before the RCF test to –0.465, which means the bulk material is still above the mean line but there may be more peaks than before. The surface topographic change and wear on the rolling track cannot be observed in the interference profilometry image in Fig. 5-2 A; only the oil stain on the outer edge of the track can be seen.

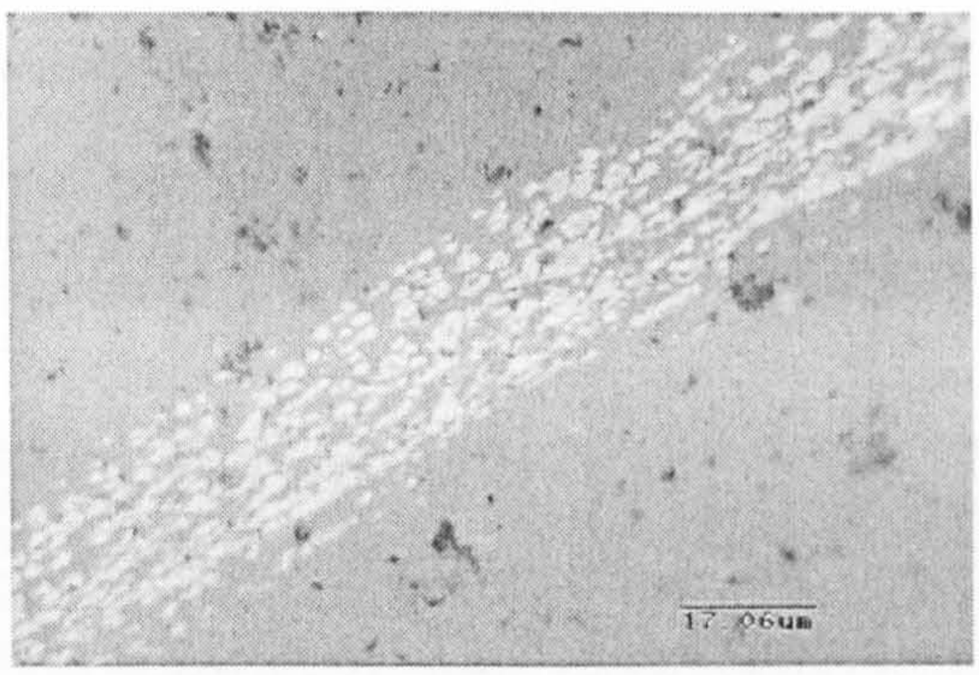

Fig. 5-3 Outer edge of the rolling track of sample A

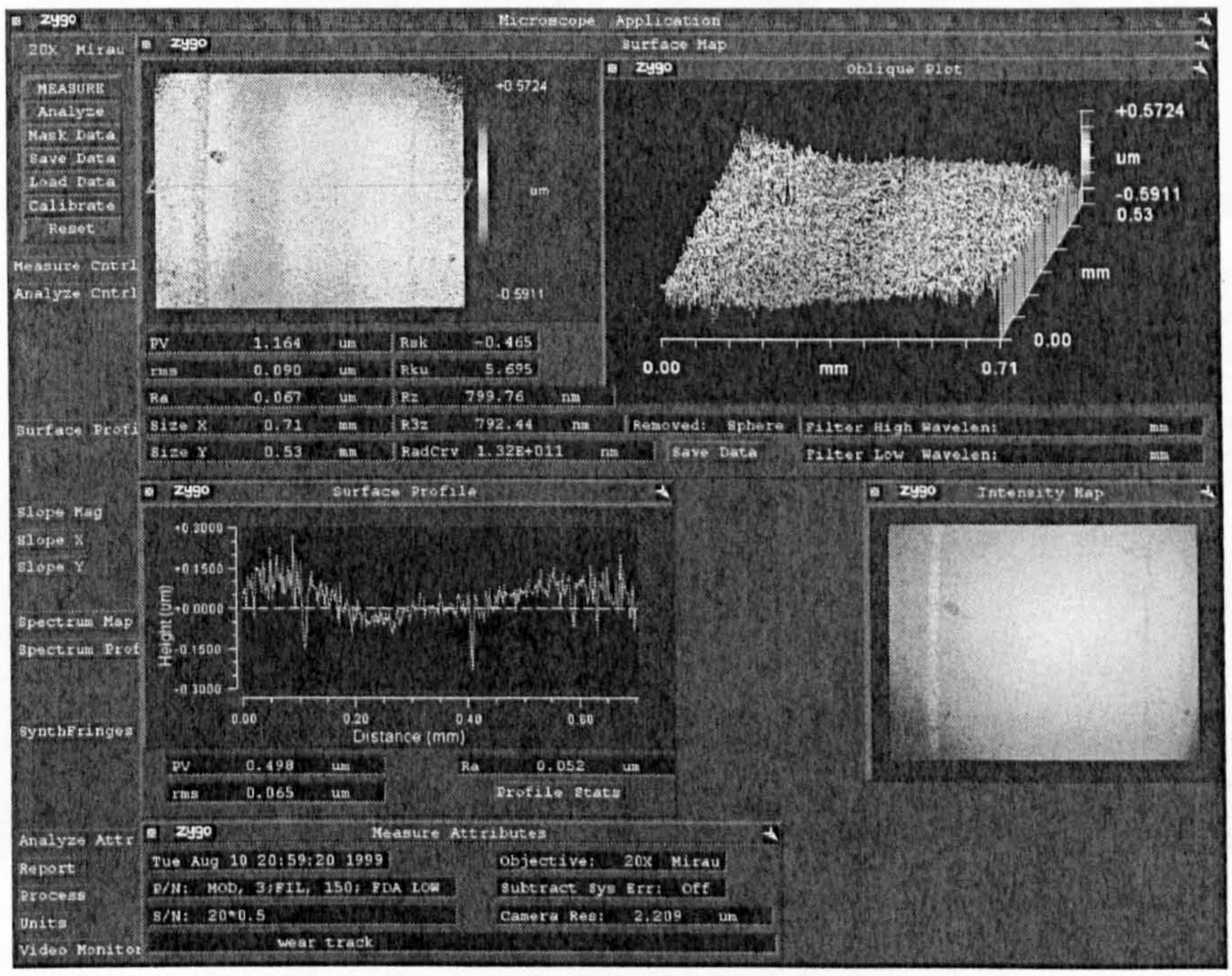

Fig. 5-4 Rolling wear track of sample A observed by 3D surface analysis

Sample B is also a commercially finished ball but with an R_a value of 0.016 μm and a small positive skewness value of 0.077 before testing. After 100.72 hours RCF test (135 million stress cycles), optical microscopy observation (Fig. 5-1 B), revealed that surface pitting had appeared on the rolling track and the sides of the rolling track had become smoother. To verify this, a Scanning Electron Microscopy investigation was carried out. Fig. 5-5 shows the SEM micrographs of sample B, (a) and (b) outside the rolling track, (c) and (d) inside the rolling track. The SEM investigation leads to an assumption that during the rolling contact test, the vast majority of the small and shallow pits disappeared due to the "running in" wear process and the surface became smoother. However, some of the larger and deeper pits developed into surface pitting due to microcracking. To further confirm the smoothing of the rolling track, an area at one edge of the rolling track without surface

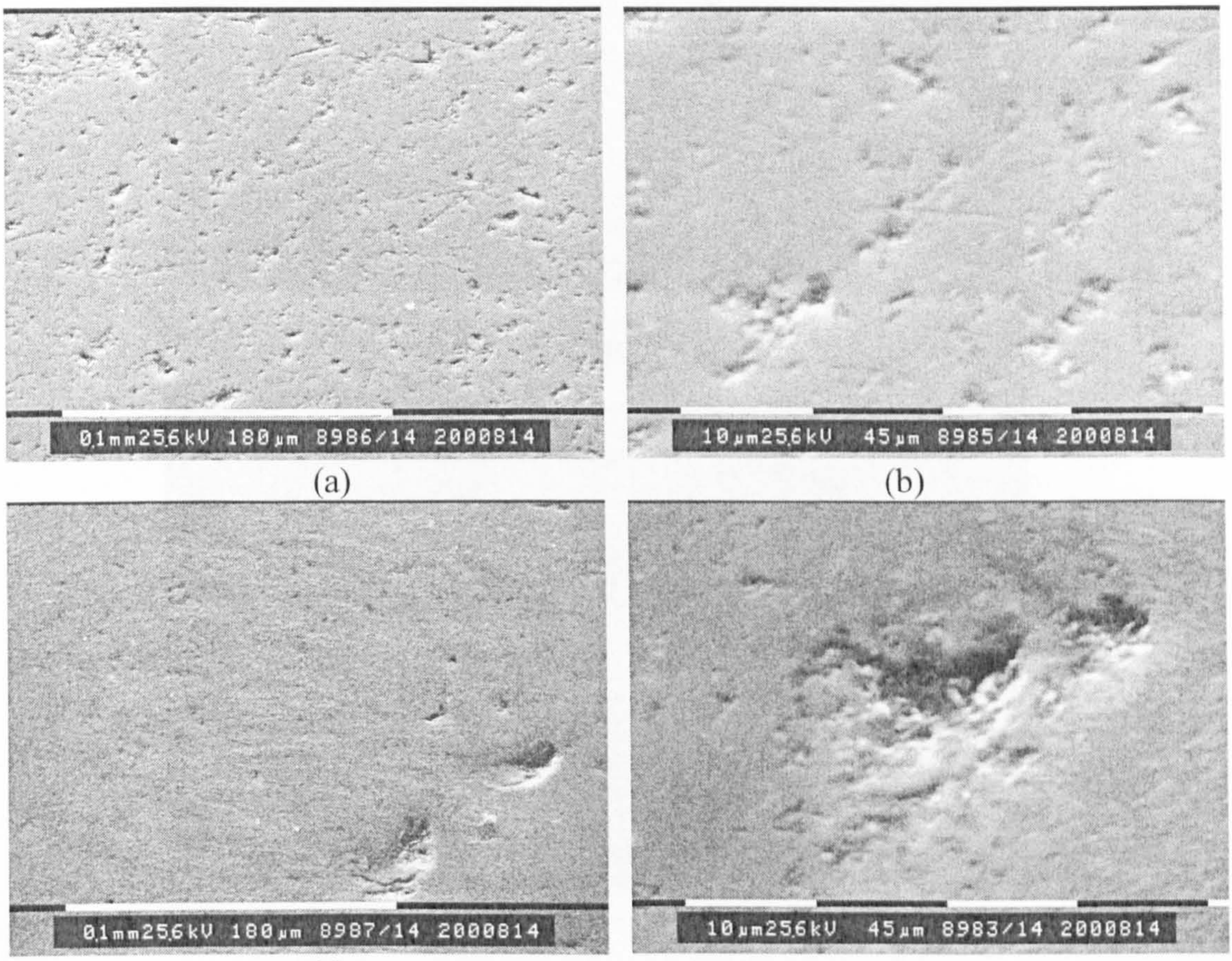

Fig. 5-5 SEM micrographs of sample B,
(a) and (b) outside the rolling track, (c) and (d) inside the rolling track.

pitting was examined using an atomic force microscope. The result of the AFM examination (Fig. 5-6) did show a decrease of the roughness parameter values. Compared with Fig. 3-2 B, PV (roughness peak to valley) had decreased from 0.529μm to 0.248μm, R_q from 0.021μm to 0.018μm, R_a from 0.016 to 0.014 μm and R_z from 403nm to 248 nm. The interference profilometry images in Fig. 5-2 B shows two surface pits near the middle of the rolling track.

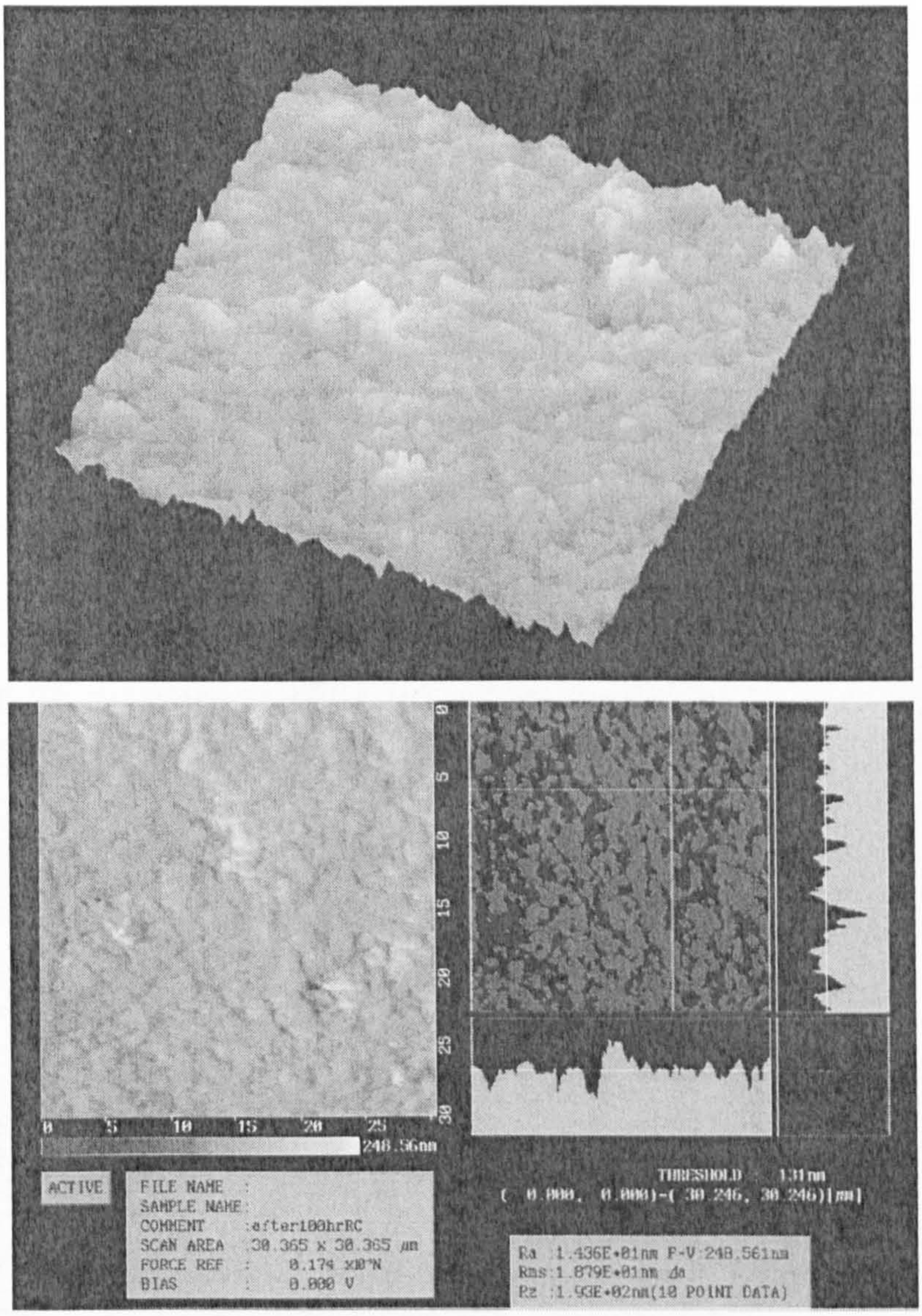

Fig. 5-6 AFM image of the rolling track of sample B after testing.

Sample C is a commercially finished ball with an R_a value of 0.003 μm and a negative skewness value of –0.597 before the RCF test. After 110.48 hours RCF test (149 million stress cycles), the surface of the rolling track became rougher under optical microscope observation (Fig. 5-1C). Fig. 5-7 shows the rolling track of sample C examined by the 3D surface analyser. Compared with the 3D roughness parameters measured before the test in Fig. 3-2 C, the values of PV, R_q, R_a and R_z have increased 30 times. Taking the factors influencing the 3D measurement result into account as described with sample A, the surface of the rolling track definitely became rougher. The amount of wear and the height of the oil deposits are similar to sample A. The oil stains at the two edges of the rolling track shown in the "Oblique Plot" of Fig. 5-7 are similar to those as observed in the interference profilometry image in Fig. 5-2 C.

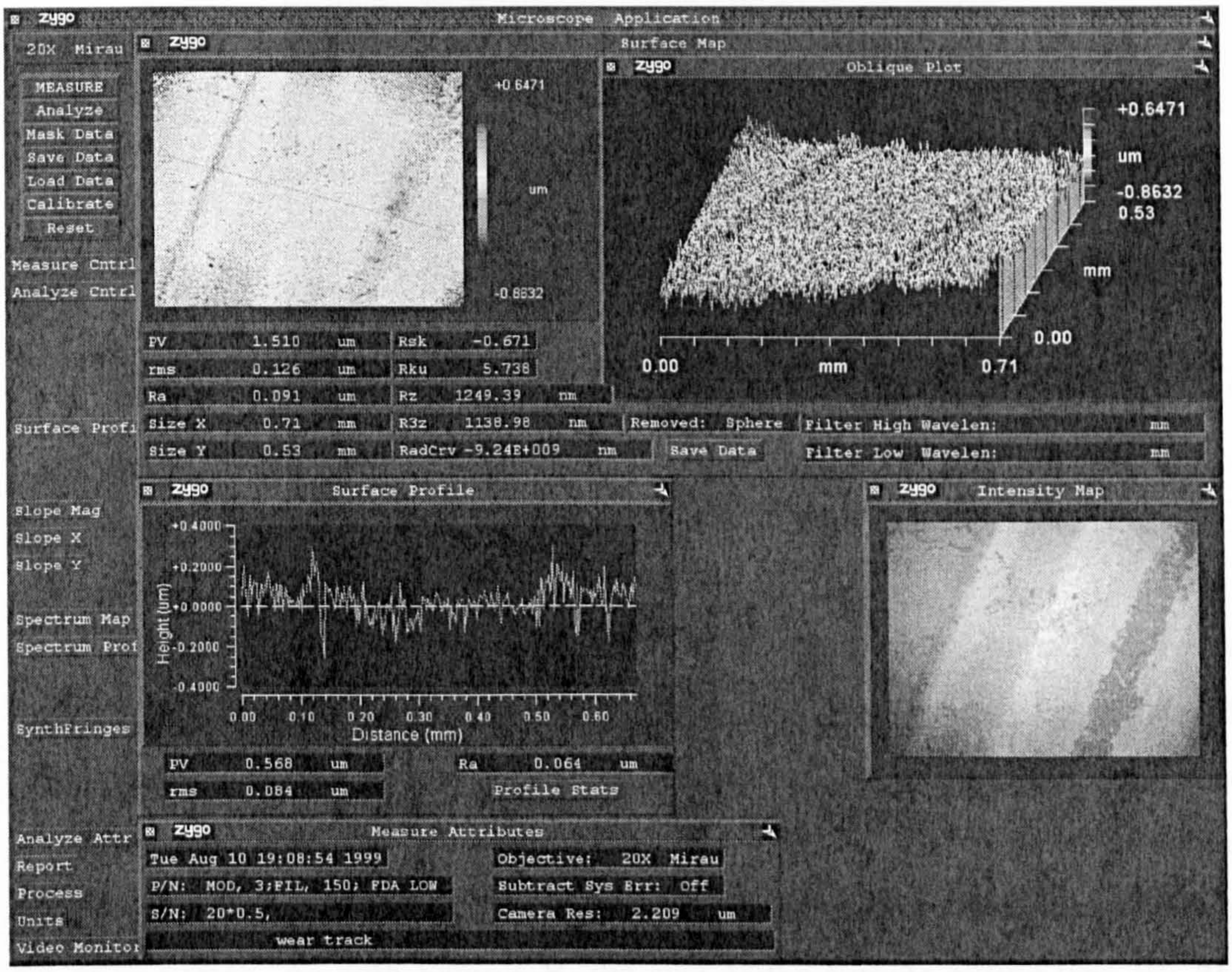

Fig. 5-7 Rolling track of sample C observed by 3D surface analysis

Sample D is a commercially finished ball with an R_a value of 0.002μm and an R_q value of 0.003μm, the lowest values of the 7 samples, but PV and R_z values are higher than those of Sample C. Sample D had a high positive skewness value R_{sk} of 2.64 and a very high kurtosis value R_{ku} of 47.8 before the RCF test. After 131.85 hours (177 million stress cycles), no difference on the rolling track except for oil stains at the track edges could be observed under optical microscopy (Fig. 5-1 D). The high skewness and kurtosis values did not make any difference. The interference profilometry image in Fig. 5-2 D shows the oil stain at the outer edge of the track. Small and shallow pitting around 2μm in size was observed with the SEM. Fig. 5-8 shows the SEM micrograph of small pits on the rolling track of sample D.

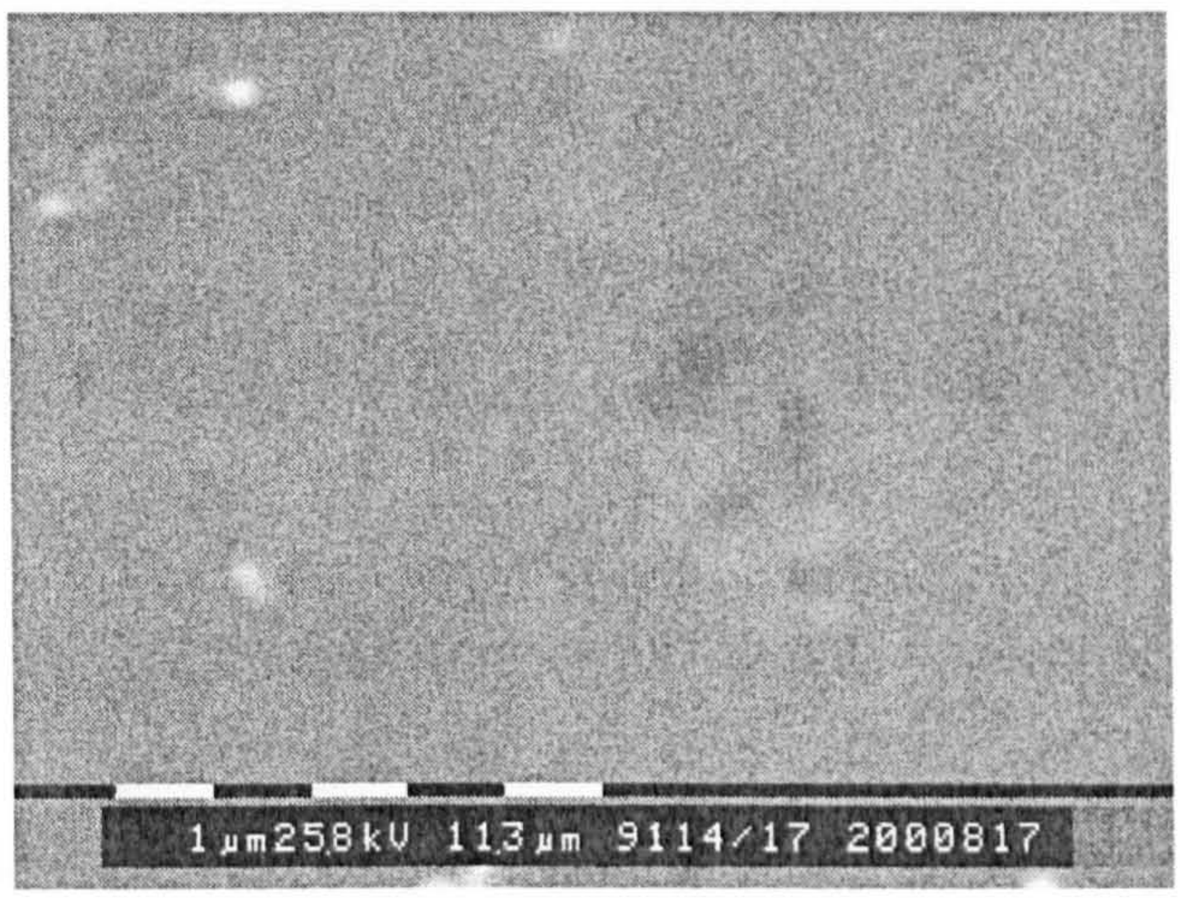

Fig. 5-8 Small pitting on the rolling track of sample D.

Sample E is a ball with an R_a value of 0.094μm, rough lapped by the author from BBB. After 146.19 hours RCF test (197 million stress cycles), the surface of the rolling track had the same features as Sample B; the rolling track had become smoother and there was some surface pitting (Fig. 5-1 E). SEM micrographs of sample E are shown in Fig. 5-9, (a) and (b) outside the rolling track, (c) and (d) inside the rolling track. As with Sample B, the size of the surface pitting was 10~20 μm. The interference profilometry image shows the smoother nature of the rolling track (Fig. 5-2 E).

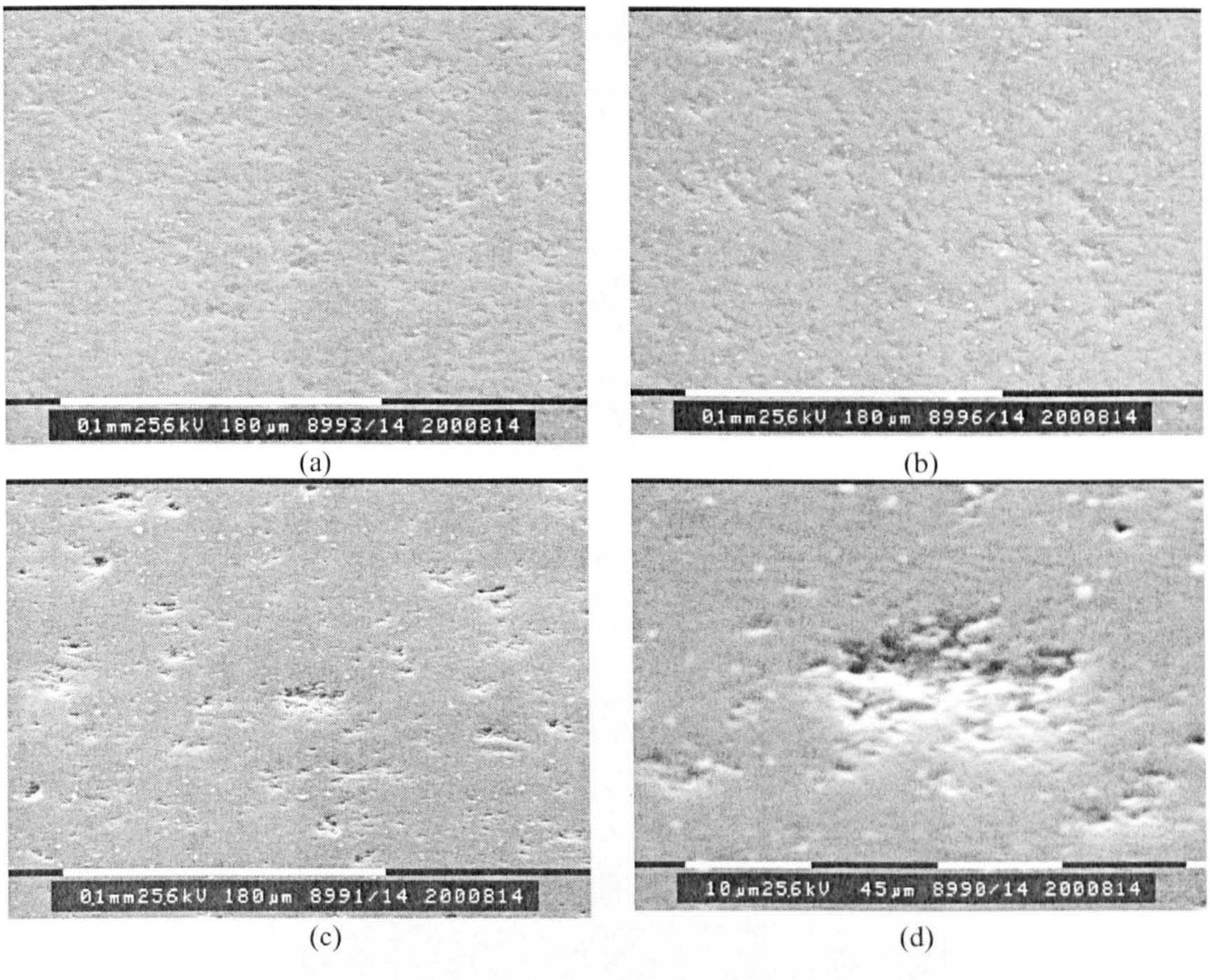

Fig. 5-9 SEM micrographs of sample E,
(a) and (b) outside the rolling track, (c) and (d) inside the rolling track.

Sample F is a ball rough-lapped from BBA by the author, with an R_a value of 0.080μm. After running for 136.37 hours (184 million stress cycles), the surface of the rolling track appeared smoother under optical microscopy (Fig. 5-1 F) and interference profilometry (Fig. 5-2 F) examination. Occasional surface pitting was found on the rolling track (Fig. 5-1 F). The characteristic of this sample was many small arc cracks parallel to the rolling direction at the two edges of the rolling track as illustrated Fig. 5-10.

Sample G is a ball firstly lapped then polished from BBA by the author to an R_a value of 0.008μm. It featured surface scratches left over from the rough-lapping process which formed some large valleys on the surface (Fig. 3-2G). After 137.82 hours RCF test (186 million stress cycles), some scratches had become larger, but did not lead to surface failure (Fig. 5-11). Some small arc cracks parallel to the rolling

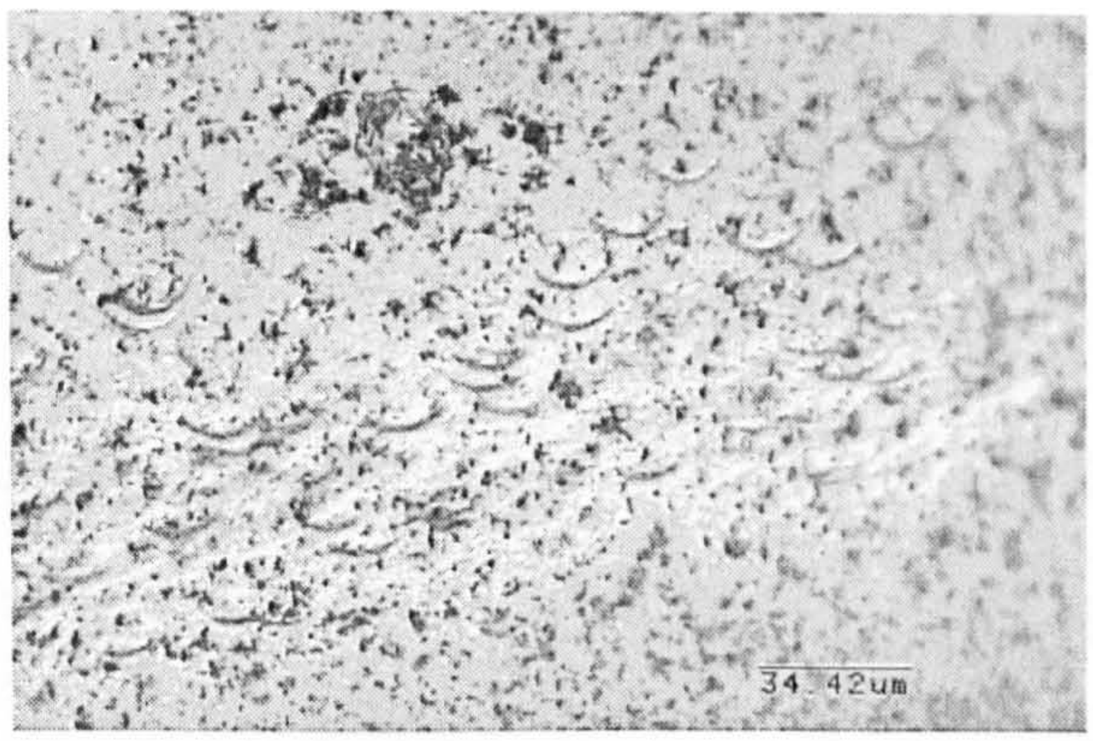

Fig. 5-10 Small arc cracks at the edge of the rolling track, and surface pitting of sample F

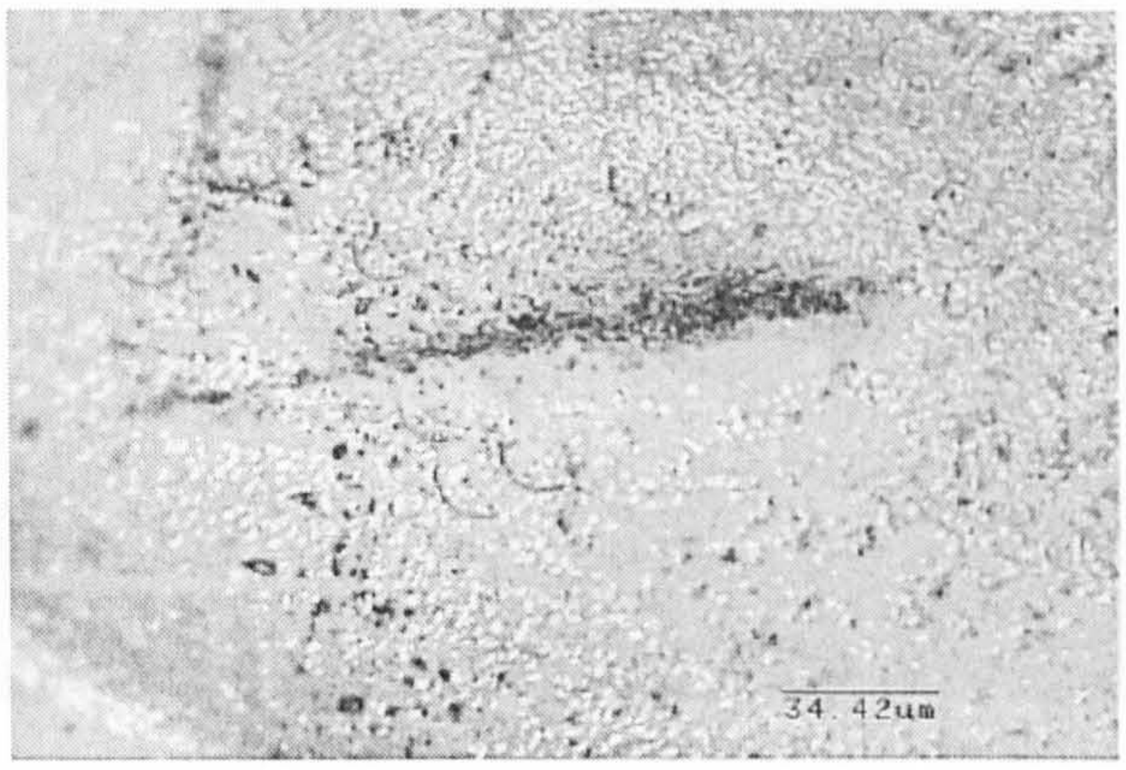

Fig. 5-11 Further developed scratch and small arc cracks on the rolling track of sample G

direction can also be seen (Fig. 5-11). These small arc cracks were common features for samples G and F and will be discussed later. The extraordinary feature of this sample is a continuous groove formed on the outer edge of the rolling track. This can be clearly seen on the interference profilometry image (Fig. 5-2 G) and on the AFM image (Fig.5-12). The depth of this groove is about 1~1.5μm from the section view of the AFM image (lower right in Fig. 5-12). The cause of this groove is unclear, it may be related to the Hertzian maximum tensile stress which is near to the edge of the contact zone.

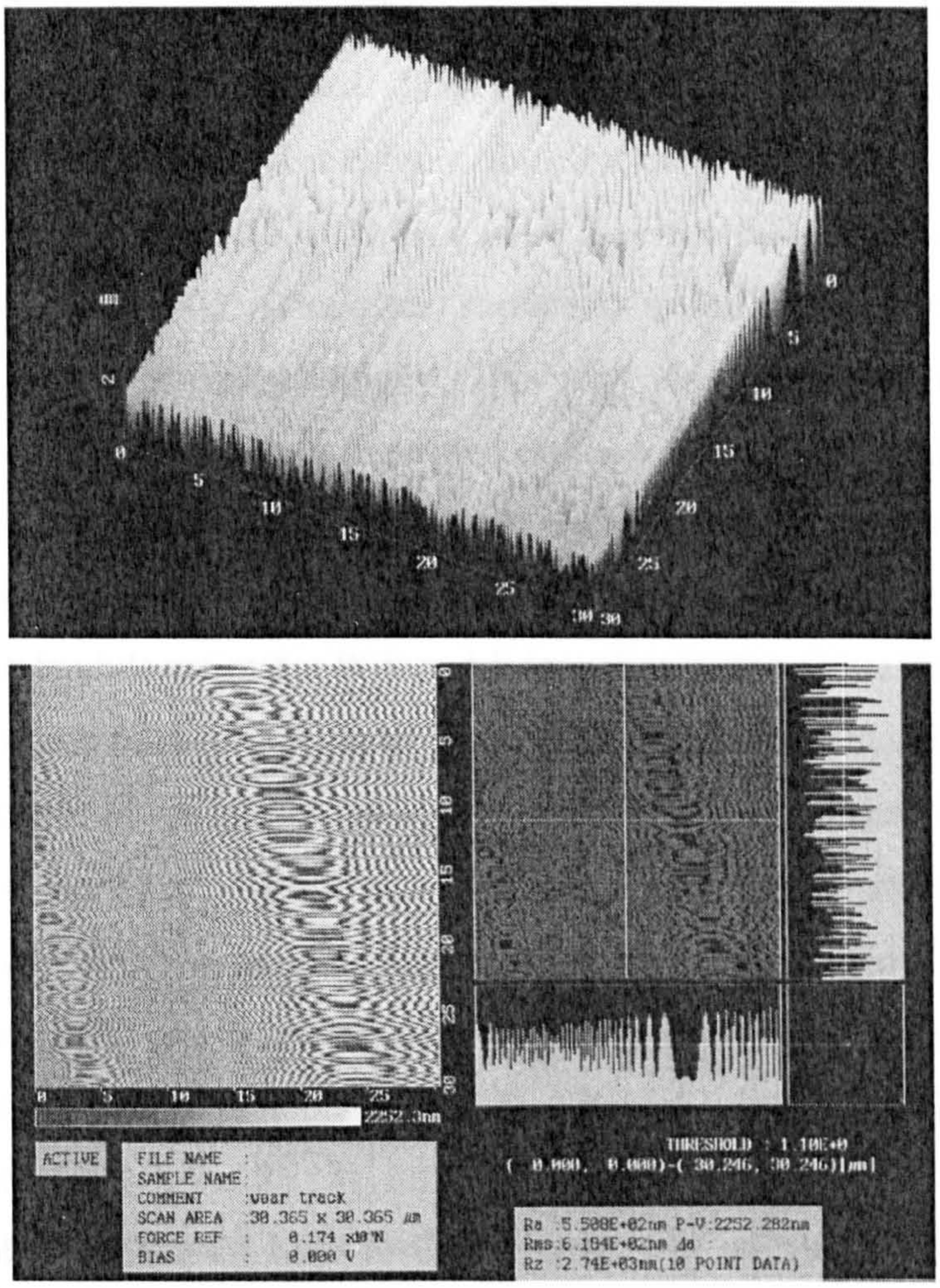

Fig. 5-12 AFM image of sample G after running for 146 hours.

5.1.2.2 Discussions on Common Characteristics

There are some common characteristics in the tests. In all of the three rougher surfaces — samples B, E and F with roughness values R_a ranging from 0.016 to 0.094, surface pitting occurred, the size of a typical pit being 10~20μm. Also, there was a tendency for those surfaces to become smoother due to "running in" polishing wear. In all of the four smoother surfaces — samples A, C, D, and G with roughness values R_a from 0.002~0.008, there was a tendency for the surfaces to become rougher during the RCF tests, with oil residues deposited on the edges of the rolling tracks.

Film thicknesses between the contact surfaces and the lubrication regime were calculated using the classical Elastohydrodynamic (EHD) equations and are listed in Table 5-3. Calculated minimum film thickness is 0.12μm, and the lambda ratios for A, C, D, G are 3.26, 3.29, 3.3 and 3.2 respectively. This means that with samples A, C, D and G, (smoother surfaces), a full fluid film separated the ceramic/steel contact surfaces initially. This may also be related to the common characteristics of the oil residues deposited on the edges of rolling tracks and lesser surface pitting. As the rolling contact process continued, the ceramic/steel contact surfaces became rougher as a result of rolling wear and the lambda ratios probably decreased. The lambda ratios for B, E and F (rougher surfaces) are 2.89, 0.91 and 1.0 respectively, and this may be related the common characteristics of larger surface pitting. For sample B, the lubrication regime will be partial or mixed EHD throughout testing based on an R_q of 0.019μm (Fig 5-6) on the rolling track after testing giving a lambda ratio of 2.96. For samples E and F, the lubrication regime will initially be between mixed EHD and boundary lubrication. As a result of "polishing wear" the ceramic surfaces become smoother and the lubrication regime will be within the mixed EHD region.

The phenomenon of wear or contact marks at the two edges of the rolling track being different from the middle of the rolling track, which can be seen in Figs. 5-1B, 5-1C, 5-1E and 5-1F, could be related to the distribution of Hertz contact shear stress. It is well known that the contact XY shear stresses are concentrated at the two sides of the contact zone although the maximum shear stresses are located a few tens of μm beneath the surface (see the FEA modelling in Appendix 6, A6.6). It was believed that shear loading encourages plastic deformation and this mode of deformation is prompted by the presence of normal compressive stresses during wear [1].

It seems that R_a or R_q (rms) are still the most important roughness parameters. The R_a and R_q values for samples A, C and D are of the same order and after testing the appearances of the rolling tracks are similar. Although sample D initially had a high positive skewness value R_{sk} of 2.64 and a very high kurtosis value R_{ku} of 47.8, this did not make any difference to the rolling track. The surface of sample G initially

contained many large valleys left by the previous rough lapping process (Fig. 3-2G). Only occasional valleys were developed further. In this case most of the valleys produced by the previous lapping process were bigger and deeper than would normally be found elsewhere, and did not tend to develop further or fail during the RCF test. This implies that some deeper lapping marks on the surface can be further developed during RCF, but in general the shape of the valley does not have a significant effect on RCF life. Therefore, the wear model based on surface valleys established by Westkaemper (Westkaemper and Hoffmeister 1996, Westkaemper and Hoffmeister 1997) could not be proved by this study.

Small arc cracks were found on samples F and G. The shape and the orientation of these cracks along the rolling track were the same for both samples. As samples G and F were from the same batch of ball blanks and had both been rough lapped using the eccentric lapping method, it is possible that the arc cracks were small Hertzian cracks formed by asperity contacts. These asperities may be formed during the rough lapping process. Further polishing removed some of these asperities, although some remained with their peaks removed. There are many asperities lying within the contact zone, true contact only thus occurring at the tips of these asperities, which are compressed as elastic solids under normal contact conditions and their deformations are explored by the classic Hertz theory (Stolarski 1989). It may also be related to the material properties. On the "rougher" surface (sample F), more small arc cracks were found on the edges of the rolling track. On the "smoother" surface (sample G), a groove was observed on the outer edge of the rolling track. Whether this groove resulted from the further development of the small arc cracks at the edge of the rolling track is not clear. If it did, then a "rougher" surface has some advantages over a "smoother" surface. Further studies are needed on this issue.

5.1.3 Summary of Experimental Results

Seven HIPed silicon nitride ball samples with different surface roughness values were tested in rolling contact against steel balls under lubricated conditions at a maximum compressive stress of 6.58GPa and at a speed of 10,000 rpm for 135~200 million stress cycles. No typical fatigue spalls occurred on any of the silicon nitride samples

and the wear was also very slight: in the range of $0.3\sim3\times10^{-10}$ m^3. Based on the test results, the following conclusions were made:

(1) For HIPed silicon nitride balls with a rough surface (0.016 to 0.094 μm R_a) it is more likely that the surface will become smoother due to polishing wear. Surface pits in the sizes of 10~20 μm may occur.

(2) For HIPed silicon nitride balls with a smooth or highly polished surface (0.002 to 0.008 μm R_a) it is more likely that the surface will become rougher and for oil residues to be deposited at the edges of the rolling track. Slight, shallow surface pitting about 2 μm in extent may also occur.

(3) Scratch marks left on HIPed silicon nitride ball surfaces by previous lapping processes can be further extended during RCF testing, although no failure from these was observed.

(4) It appears that R_a and R_q remain the most important surface parameters in relation to RCF life. The effects of other surface roughness parameters such as the shape of the valley, R_{sk} and R_{ku} were not obvious in this study.

5.2 The Influence of Heterogeneous Porosity on RCF Failure Modes

5.2.1. Introduction

In this study, lubricated rolling contact 4-ball tests were performed on 12.7mm diameter HIPed silicon nitride ball samples which contained localised heterogeneous porosity defects at and near the ball surface as procured from a manufacturer. The porosity and wear performance of silicon nitride was investigated in the early 1970s (Burke et al 1974, 1978). Since then the manufacturing technology of silicon nitride has advanced, both in material composition and processes. At present, there are two approaches to increase the density and reduce the porosity. One is a compositional approach, which involves additive selection, impurity effects and phase equilibrium studies. The other is a micro-structural approach, which relies on the characteristics of the initial material and optimum selection of process parameters (Gazza et al 1979).

Porosity of silicon nitride can be largely eliminated through the above mentioned two approaches. Presently, hot isostatic pressed silicon nitride is widely used in advanced heat engines, bearings, metal processing, etc. The hot isostatically pressing produces a high-density grade silicon nitride that can endure high contact pressure for rolling bearing application. Although HIPed silicon nitride commonly approaches a theoretical full density, there is usually some residual, often heterogeneous, porosity e.g., 0.01% to a few tenths of one percent (Rice 1998). This kind of heterogeneous porosity within the product occurs often in or near the surface region. This defect is difficult to detect during high volume production; hence study on its influence on rolling contact performance is needed.

Before testing, the specimen ball surfaces were examined by microscope under white and ultra-violet light using a dye penetration technique. Micro-hardness at different areas of the specimen ball surfaces were measured and compared with other steel and ceramic balls (Fig.5-13). Specimen ball subsurface investigations were conducted after sectioning and polishing. Scanning Electron Microscopy (SEM) was employed to observe the microstructure of the localised heterogeneous porosity, normal area, and the interface region. Accelerated rolling contact fatigue tests were performed using a rotary tribometer at different loads and lubricants. Contact stresses and minimum film thickness values during test were calculated (Table 5-4). The ball surfaces were examined under a light microscope after the rolling experiments using a dye penetration technique and by a Talysurf series surface profiler to measure wear scar areas. The wear scar areas were also observed by SEM.

The test machine was described in Section 3.4.1. All of the present tests were conducted at a shaft speed of 5000 rev/min. The experimental procedures refer to Section 3.4.2 Rolling Contact 4-Ball Test and Section 3.4.4 Positioning the Defect Area on the Rolling Track. This study is concerned with the effect of the lubricant and lubrication regime on the rolling contact fatigue performance of these silicon nitride balls. Two different lubricants were chosen, one low viscosity lubricant (LV, synthetic oil), the other high viscosity lubricant (HV, a mineral oil). The film thickness between the contact surfaces and the lubrication regime are calculated using the classical Elastohydrodynamic (EHD) equation as described in Appendix 5. The

contact stresses at the upper-ball/lower-ball interface are calculated using Hertz theory as described in Appendix 4. Table 5-4 summarises the calculated lubrication and contact stresses conditions of each test.

Test	Contact load (N)	Min. Film Thickness (m)	Lambda Ratio	Maximum Compressive Stress (GPa)	Radius of Contact Circle (μm)	Max. Shear Stress (GPa)	Max. Tensile Stress (GPa)	Depth of Max. Shear Stress (μm)
A1	480	7.08E-08	2.36	5.55	203	1.72	0.85	97.6
A2	320	7.29E-08	2.43	4.85	178	1.50	0.74	85.2
A3	160	7.67E-08	2.56	3.85	141	1.19	0.59	67.7
B1	480	8.96E-08	2.99	5.55	203	1.72	0.85	97.6
B2	320	9.23E-08	3.08	4.85	178	1.50	0.74	85.2
B3	160	9.71E-08	3.24	3.85	141	1.19	0.59	67.7

Table 5-4 Calculated lubrication and contact stress conditions

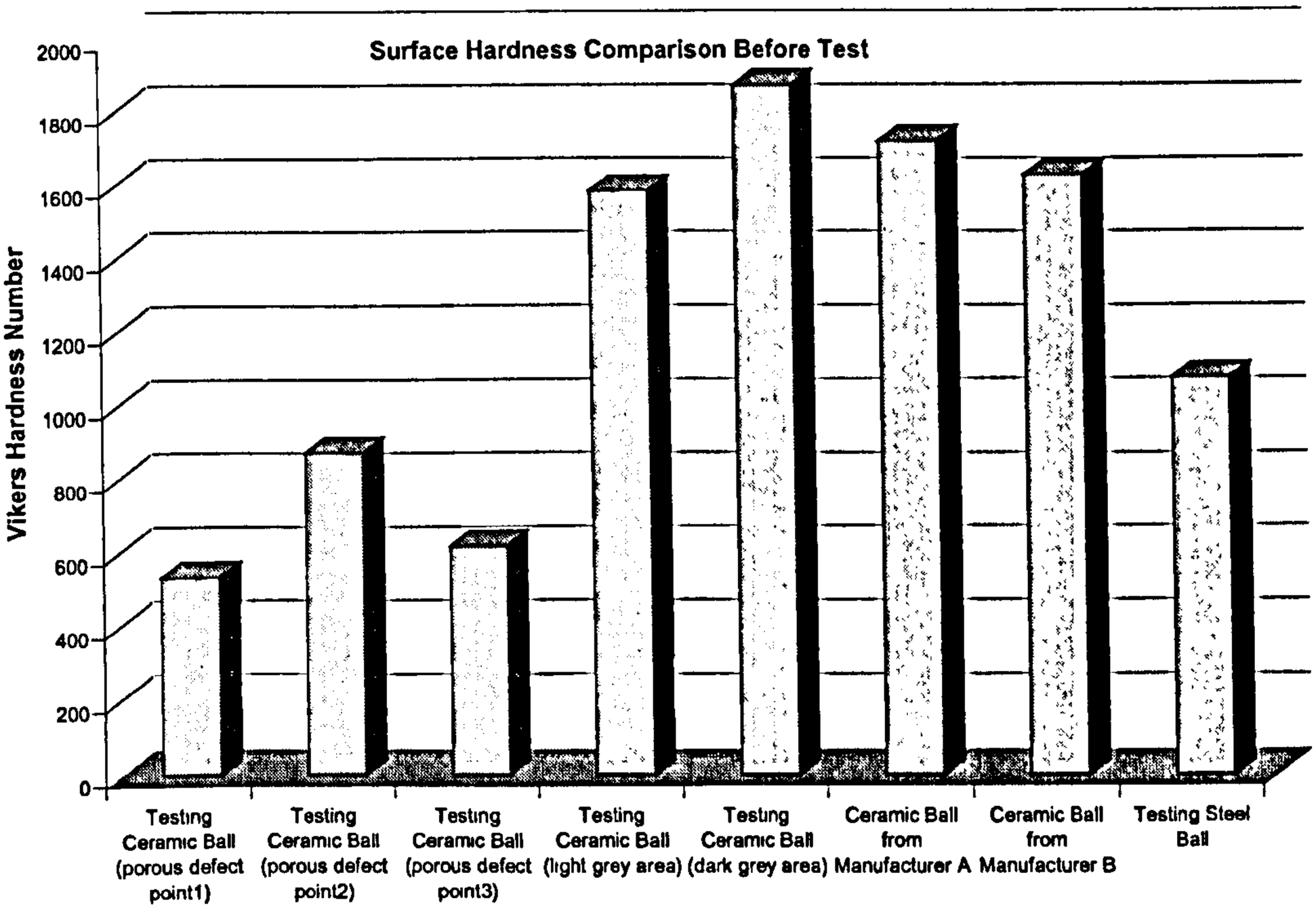

Fig. 5-13 Surface Hardness Comparison before Test

The purpose of this study was to investigate to what extent these localised heterogeneous porosity defects affect the wear and fatigue performance of silicon nitride, and to examine the effect of different lubricants and lubrication conditions on the heterogeneous, porous microstructure of silicon nitride under lubricated rolling contact.

5.2.2 Pre-test Examination

Each testing specimen was a finished 12.7 mm diameter HIPed silicon nitride ball, which contained localised heterogeneous porosity defects. The localised heterogeneous porosity defect is difficult to detect during high volume inspection, but it is possible to detect after dye-penetration using a microscope and ultra-violet light source. Fig 5-14 is an overview of a typical specimen ball (B2). The diameter of the localised heterogeneous porosity defect was 6 mm; the surface area approximately 30 mm^2 which accounted for 6% of the total ball surface. The rolling contact path during the test was through both this area and the normal area.

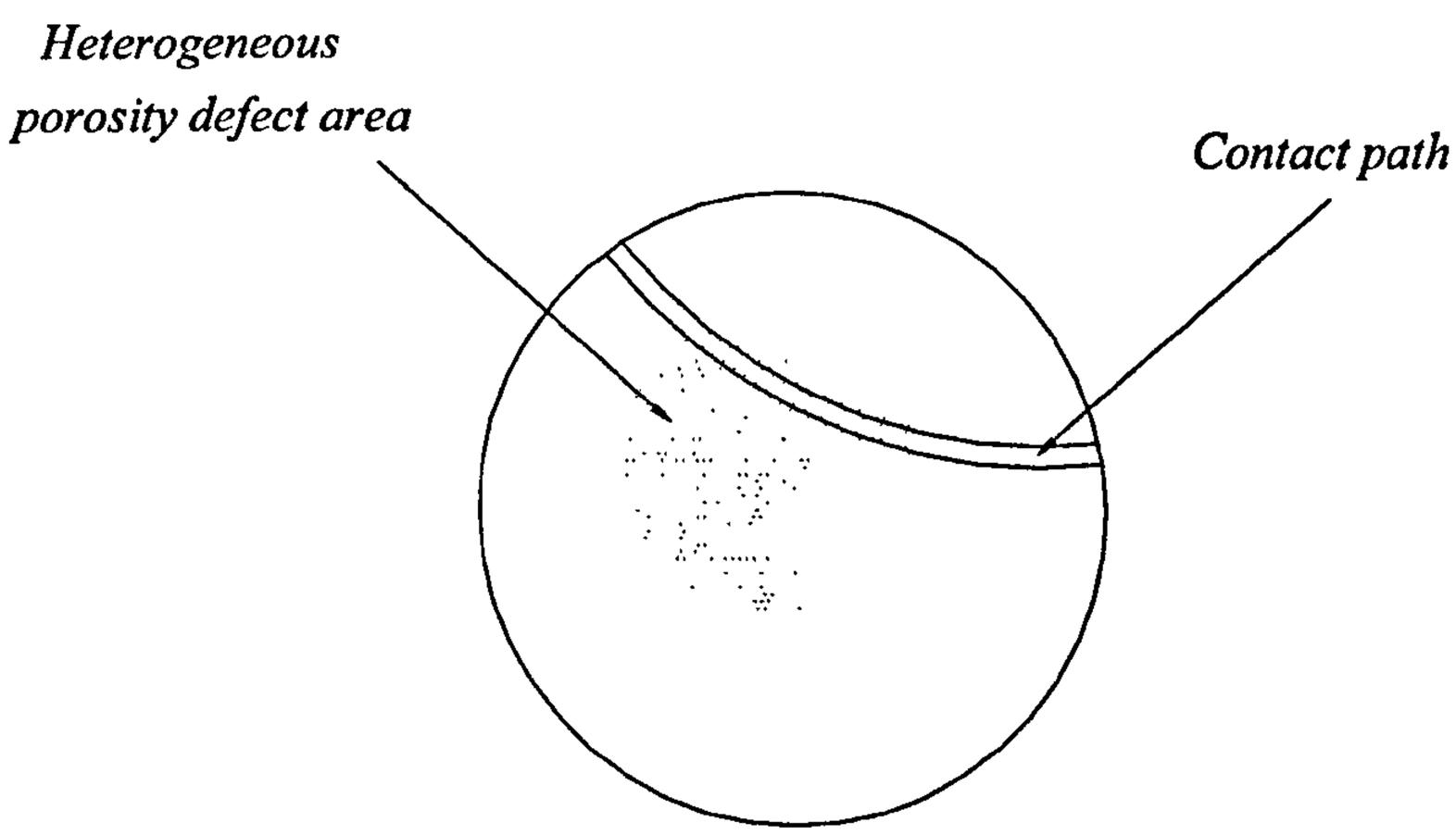

Fig 5-14 Overview of a specimen ball

Fig 5-15 illustrates the features of heterogeneous porosity within a typical silicon nitride ball. Fig 5-15(a) shows the overview of the section; the lower left area of the section is the localised heterogeneous porosity defect area. The diameter of the

defect was 8.4 mm, the surface area approximately 63.5 mm^2 which accounted for 12.5% of the ball surface. The volume of the defect was approximately 46.8 mm^3, which accounted for 4% of the total ball volume (Fig 5-15 b). Fig 5-15 (c) and (d) show the interface region between the localised heterogeneous porosity defect area (lower left) and normal area (upper right), which are in sharp contrast to each other.

Fig 5-16 illustrates the SEM comparison of the microstructures within localised heterogeneous porosity defect and normal areas at different magnifications. There was also some porosity in the normal area. Fig 5-16 (a) and (d) are at the magnification of 160×. These two sections were compared with ISO 4505-1978(E)

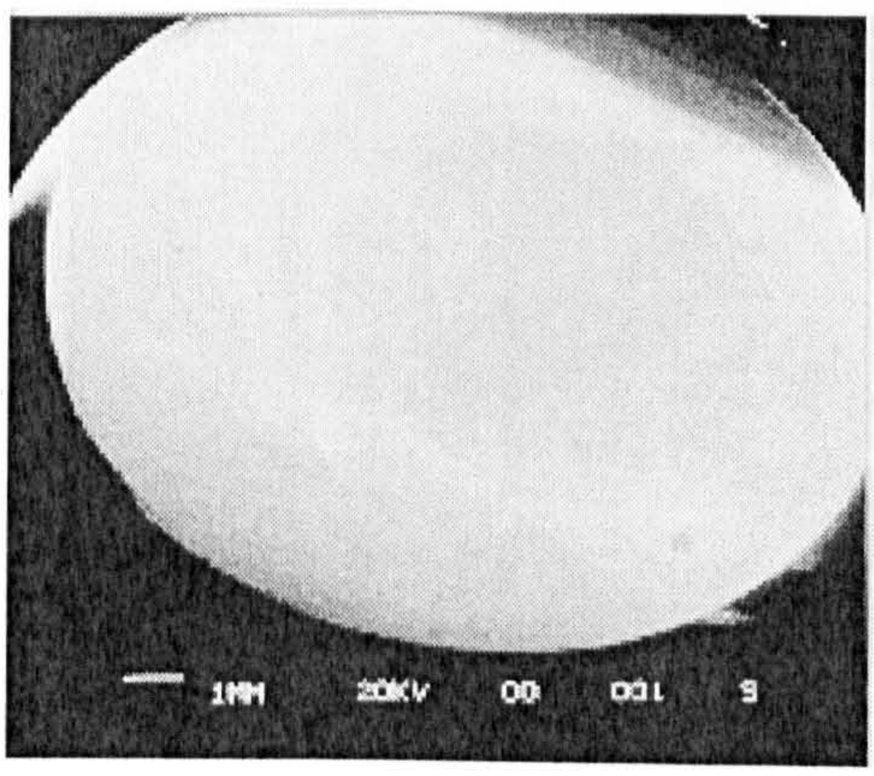

(a) Overview of section

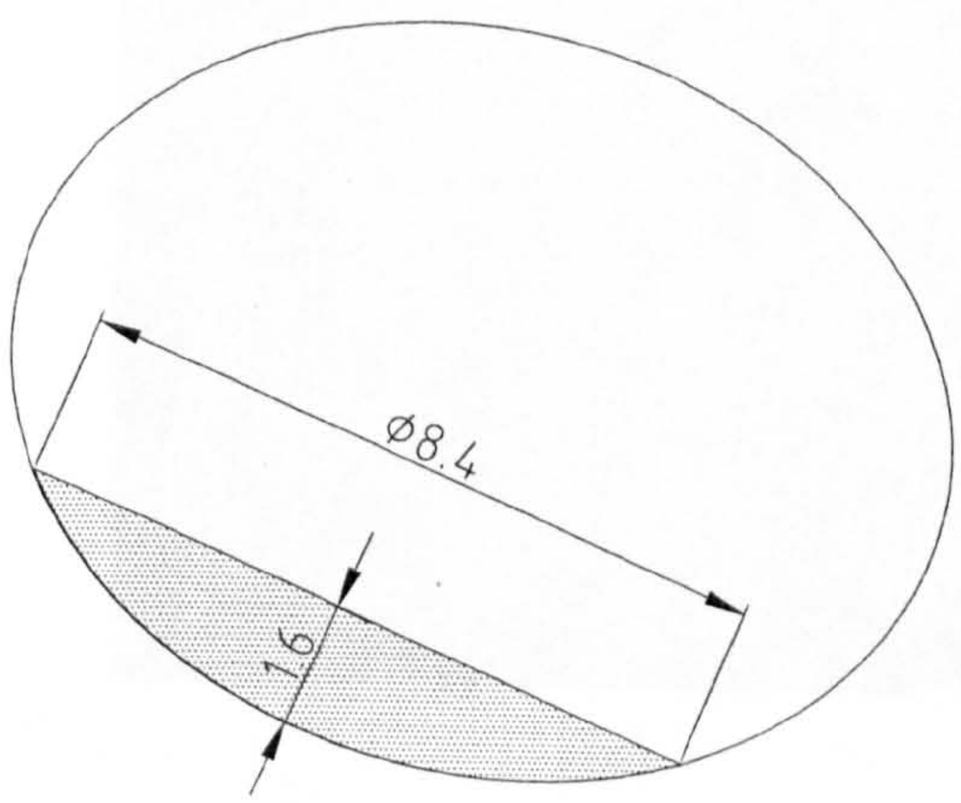

(b) Dimension of localised heterogeneous porosity defect (in mm)

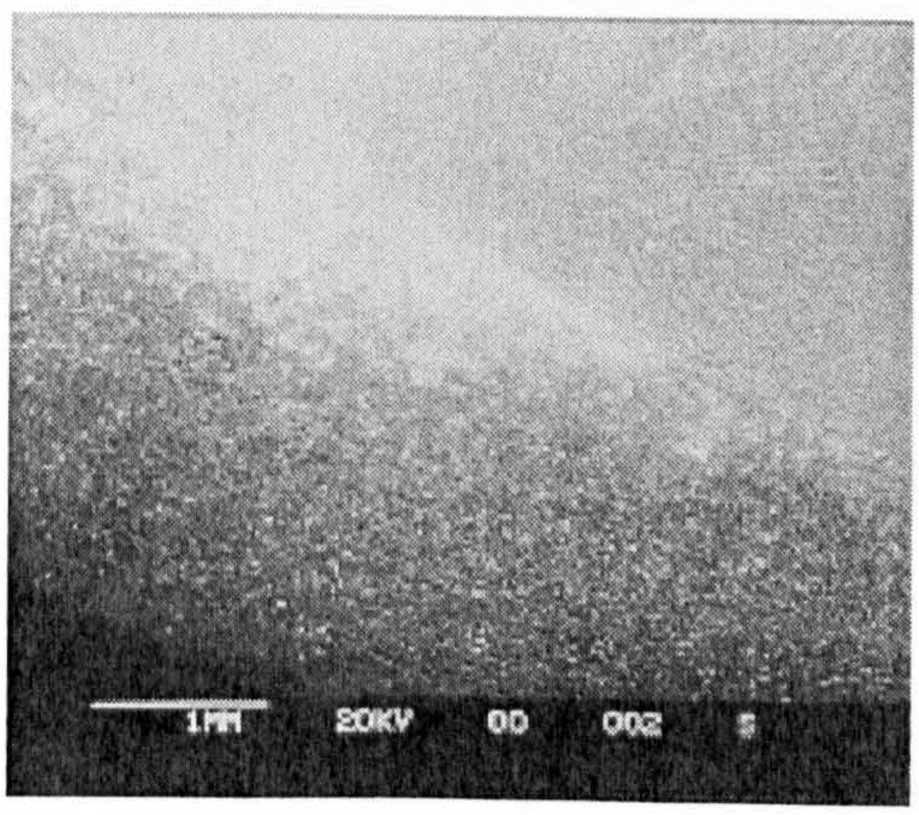

(c) Localised heterogeneous porosity defect interface

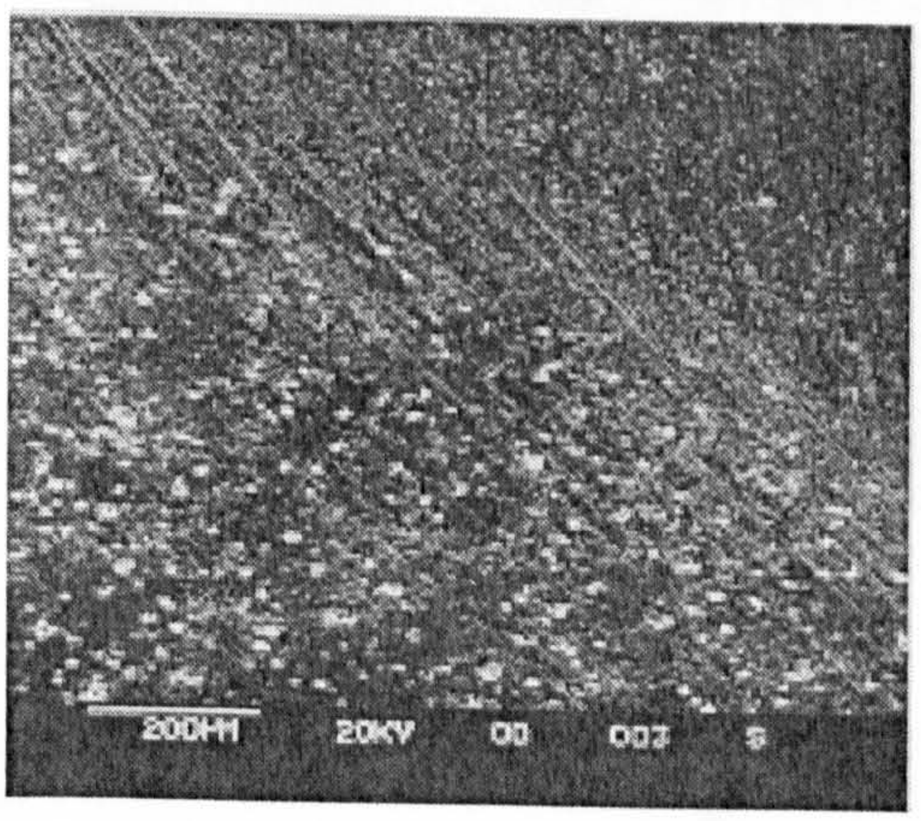

(d) Detail of interface region

Fig 5-15 Section through a silicon nitride ball (B series)

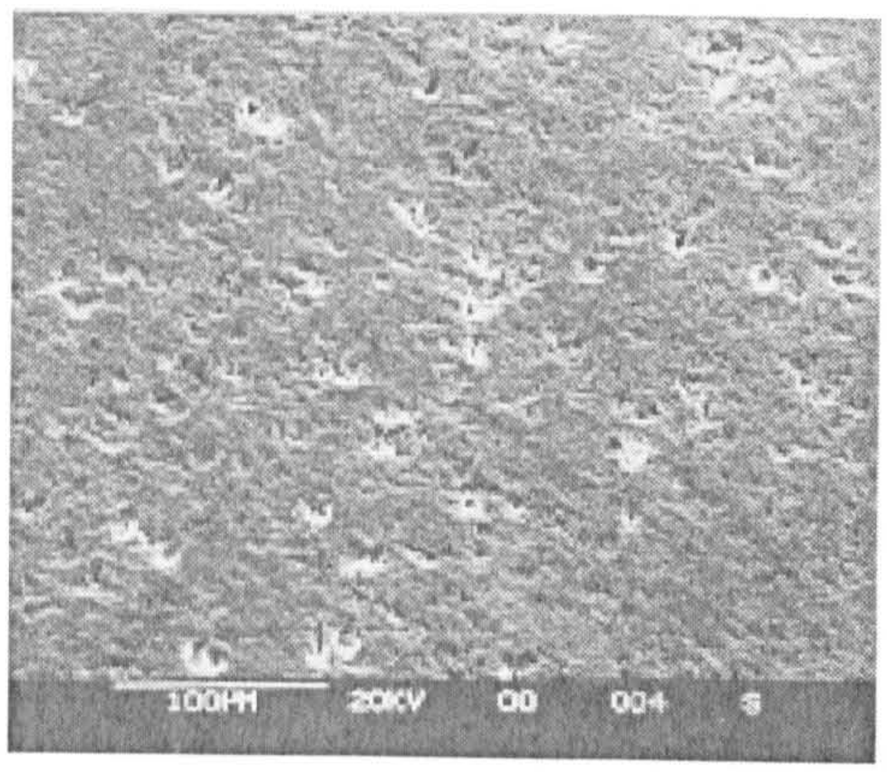

(a)

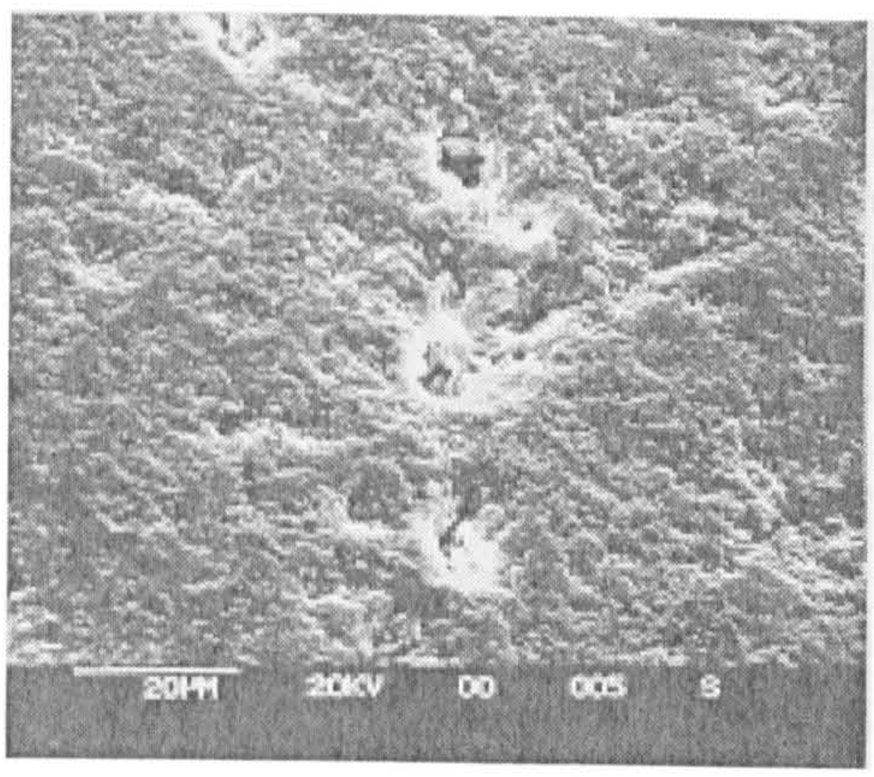

(b)

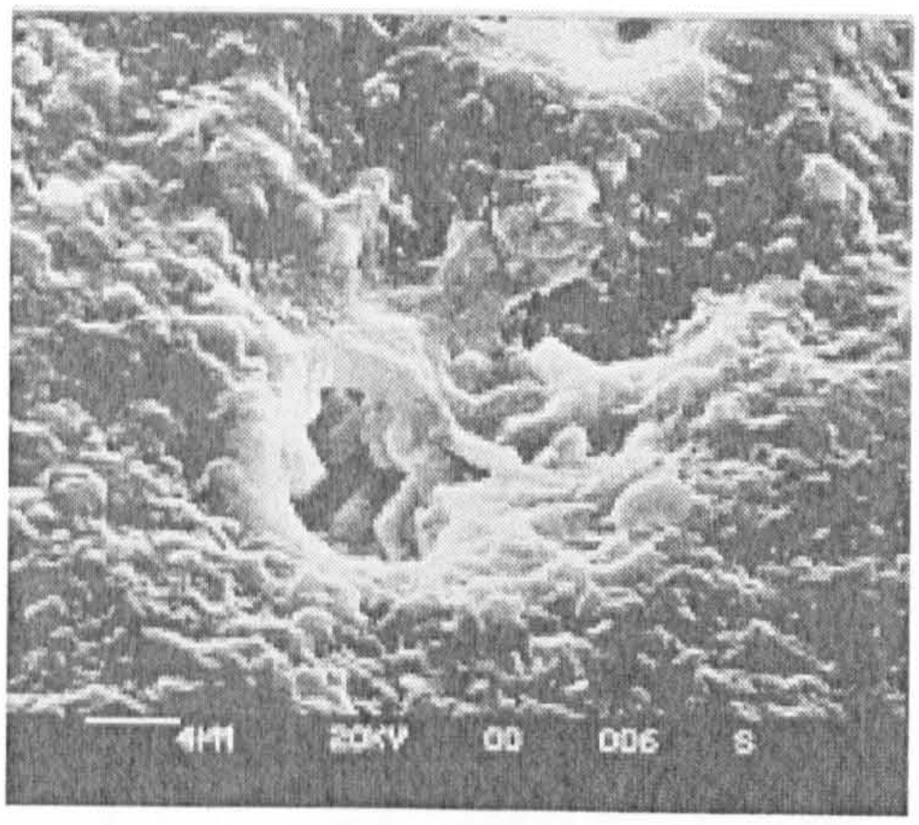

(c)

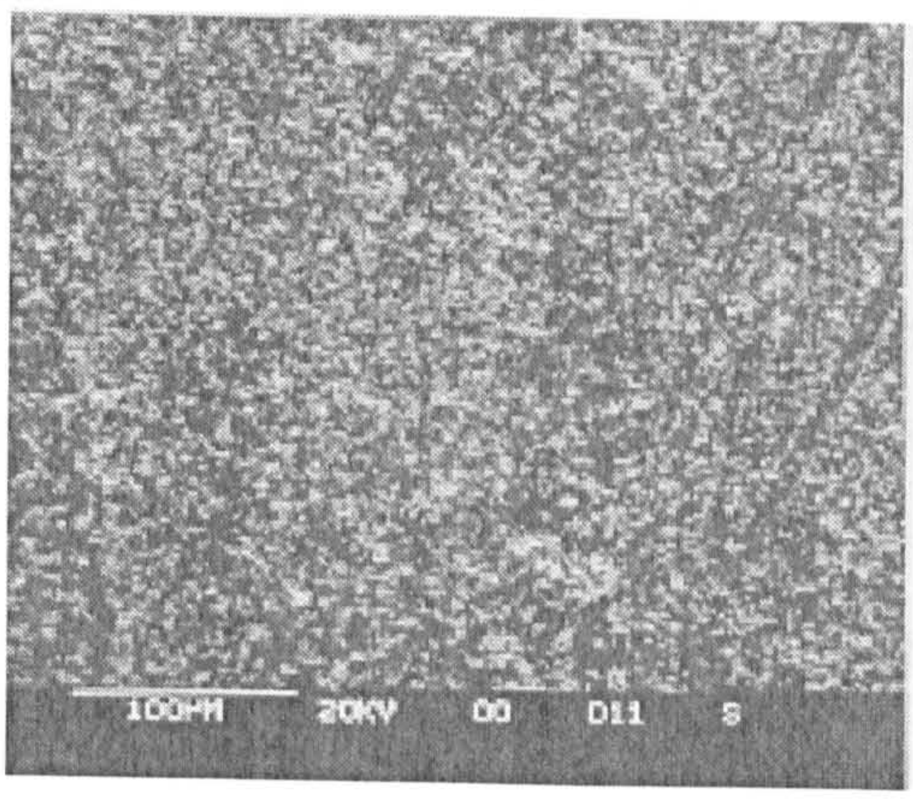

(d)

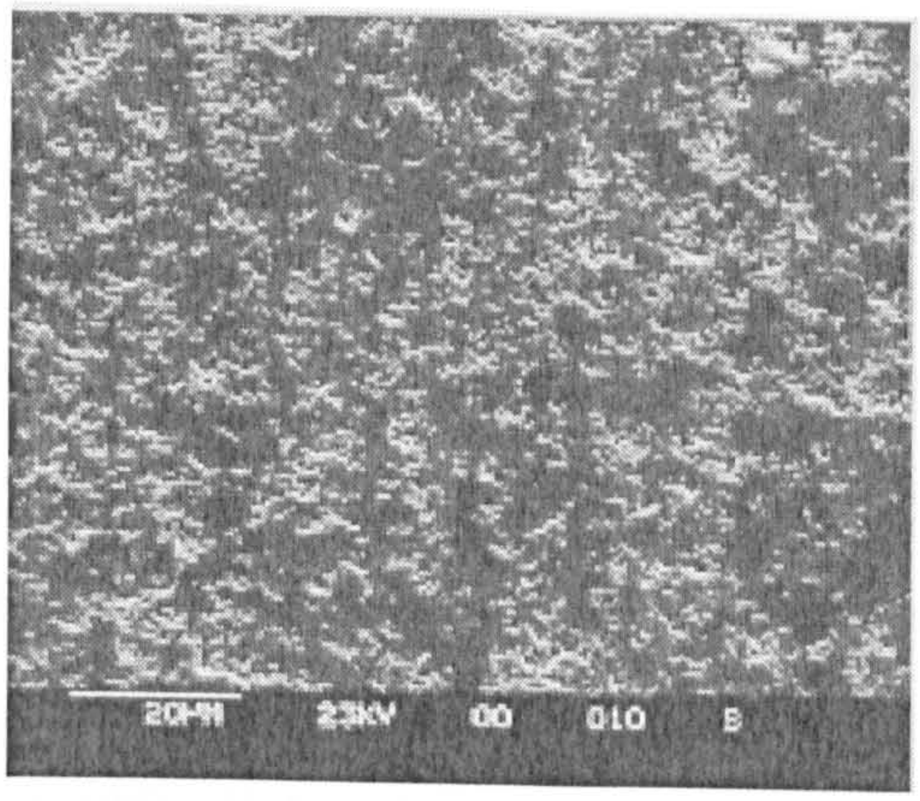

(e)

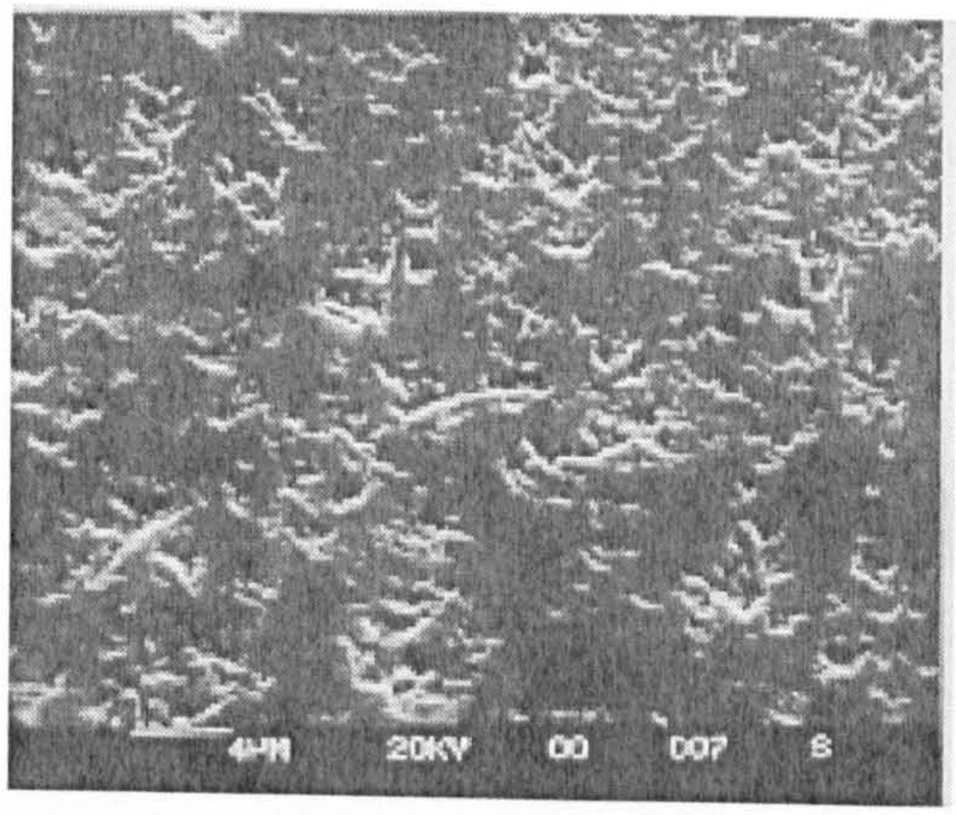

(f)

Fig 5-16 Comparison of section (a), (b) and (c) localised heterogeneous porosity defect area; (d), (e) and (f) normal area

Hardmetals—Metallographic Determination of Porosity and Uncombined Carbon (ISO 4505,1978). Fig 5-16 (a) is close to B08, type B apparent porosity at 100× magnification, with 4000 pores/ cm^2 and 0.6% porosity by volume. Fig 5-16 (d) is close to A08 at 100× and 200× magnification and 0.6% porosity by volume. The only difference between the localised heterogeneous porosity defect area and the normal area is the shape and size of the pores. In ISO 4505-1978(E), the pore size is defined as the maximum dimension of the pore in the section. The A series (including A08) was used to assess pores with sizes up to 10 μm, whilst the B series (including B08) was used to assess pores with sizes ranging from 10 μm to 25 μm. In order to distinguish the shape of a pore, a new parameter to describe the pore: the diameter of the pore was proposed by the author. The minimum dimension of a pore in all directions is defined as the diameter of the pore, which is different from the pore size. In the localised heterogeneous porosity defect area, the diameters of pores were found to be mainly between 4 and 20 μm. In the normal area, the diameters of pores are usually less than 2 μm. To characterise surface porosity defects, a dye-penetration method and microscope with ultra-violet light source was utilised to enhance the detection of surface porosity. Fig 5-17(a) shows a white-light microscopic image of a silicon nitride ball surface; the localised heterogeneous porosity defect area can be seen on the left. Fig 5-17(b) shows the same area under ultra-violet light, after dye-penetration treatment.

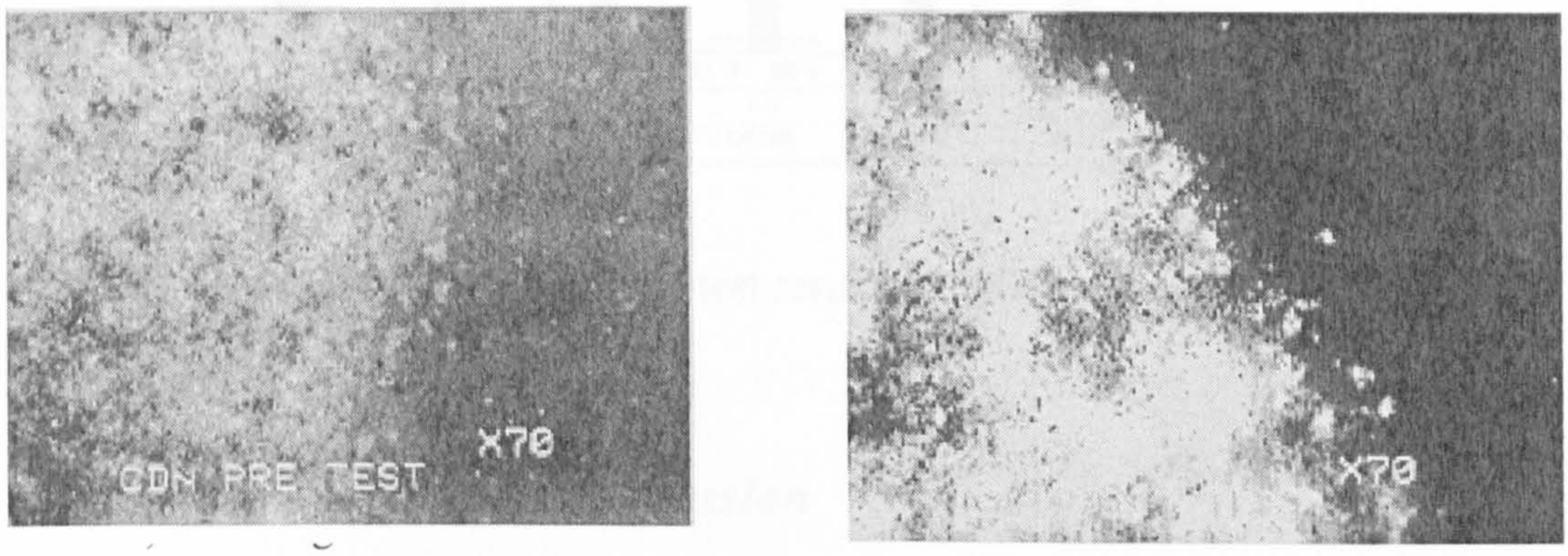

Fig 5-17 Pre-test ball surface ('B' series)

Surface hardness of the different areas on the specimens (defect area and normal area) was measured, and compared with other steel and ceramic ball surfaces. In this study Vickers hardness was measured using a load of 0.5kgf (4.903 N). Results show that the hardness in the localised heterogeneous porosity defect areas was fairly low. Fig. 5-13 shows a comparison between the hardness of the localised heterogeneous porosity defect area and the normal area of the specimen balls, as well as other brands of ceramic and steel balls. Measurements were taken at three points on the localised heterogeneous porosity defect area. The hardness at these points was even lower than steel balls, ranging from one third to one half of the hardness value of the normal area.

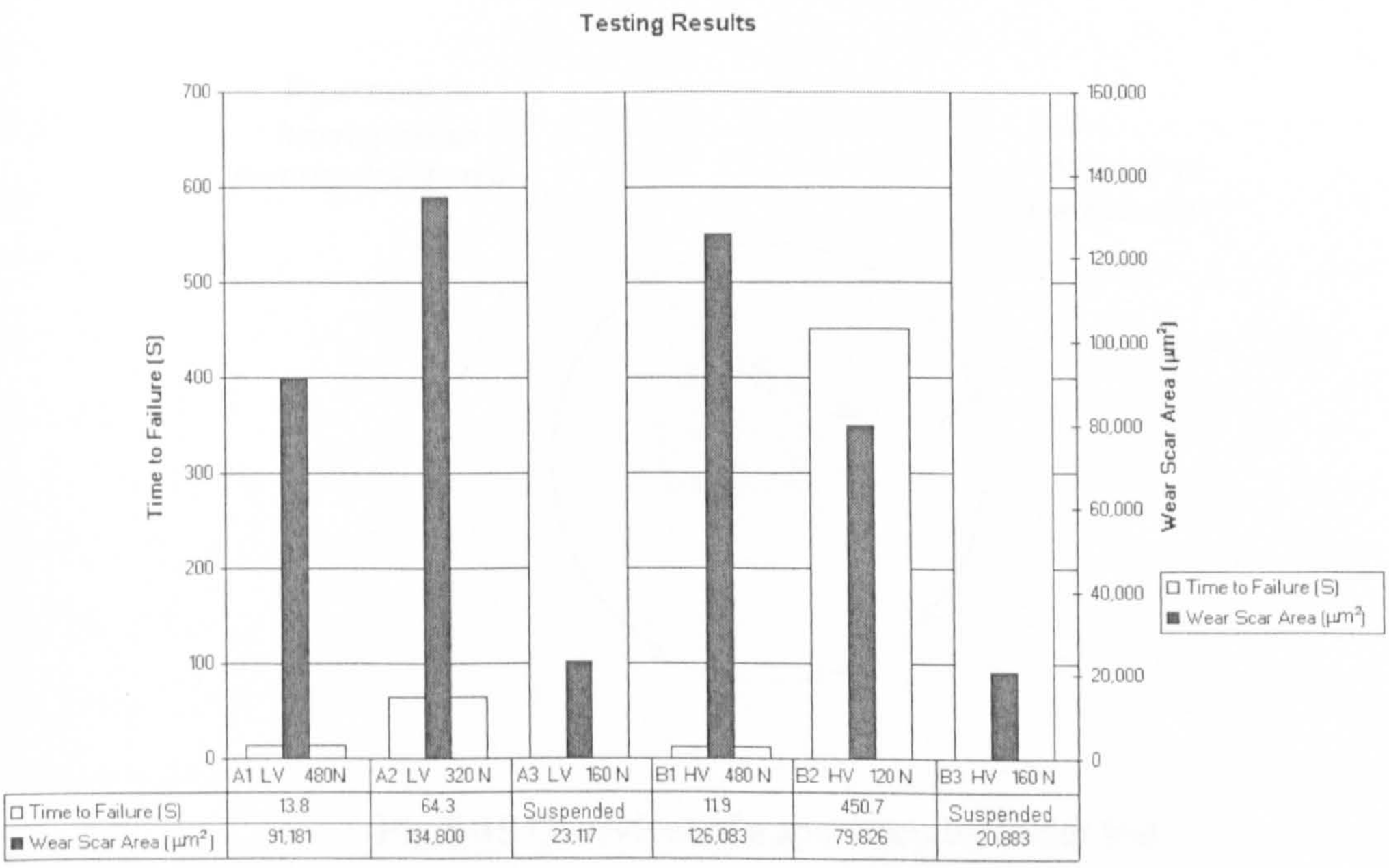

Fig 5-18 Summary of test results at 5000 rev/min

5.2.3 Post-test Analysis and Discussion

Two test series were performed, using a low viscosity lubricant (LV, synthetic oil) and a high viscosity lubricant (HV, mineral oil), under three different contact loads

(160 N, 320 N, 480N) at a constant speed 5000 rev/min. After each test, the ball surfaces were examined using a Talysurf series surface profiler and the wear scar areas calculated using a graphical integration method. Fig 5-18 summarises the test results in graphical form.

The calculated minimum film thickness and lambda ratio for the upper-ball/lower-ball contacting surfaces were summarised in Table 5-4. The most important finding from these calculations was that the lambda ratios under different load for the LV lubricant were between 2.56 to 2.36. This means that a "mixed" EHD lubrication regime exists during testing at these conditions and hence some asperity contact will take place. In the case of the HV lubricant ratios under different loads, lambda values of from 3.24 to 2.99 were calculated. Hence, in theory, full film separation exists and almost no asperity contact is envisaged.

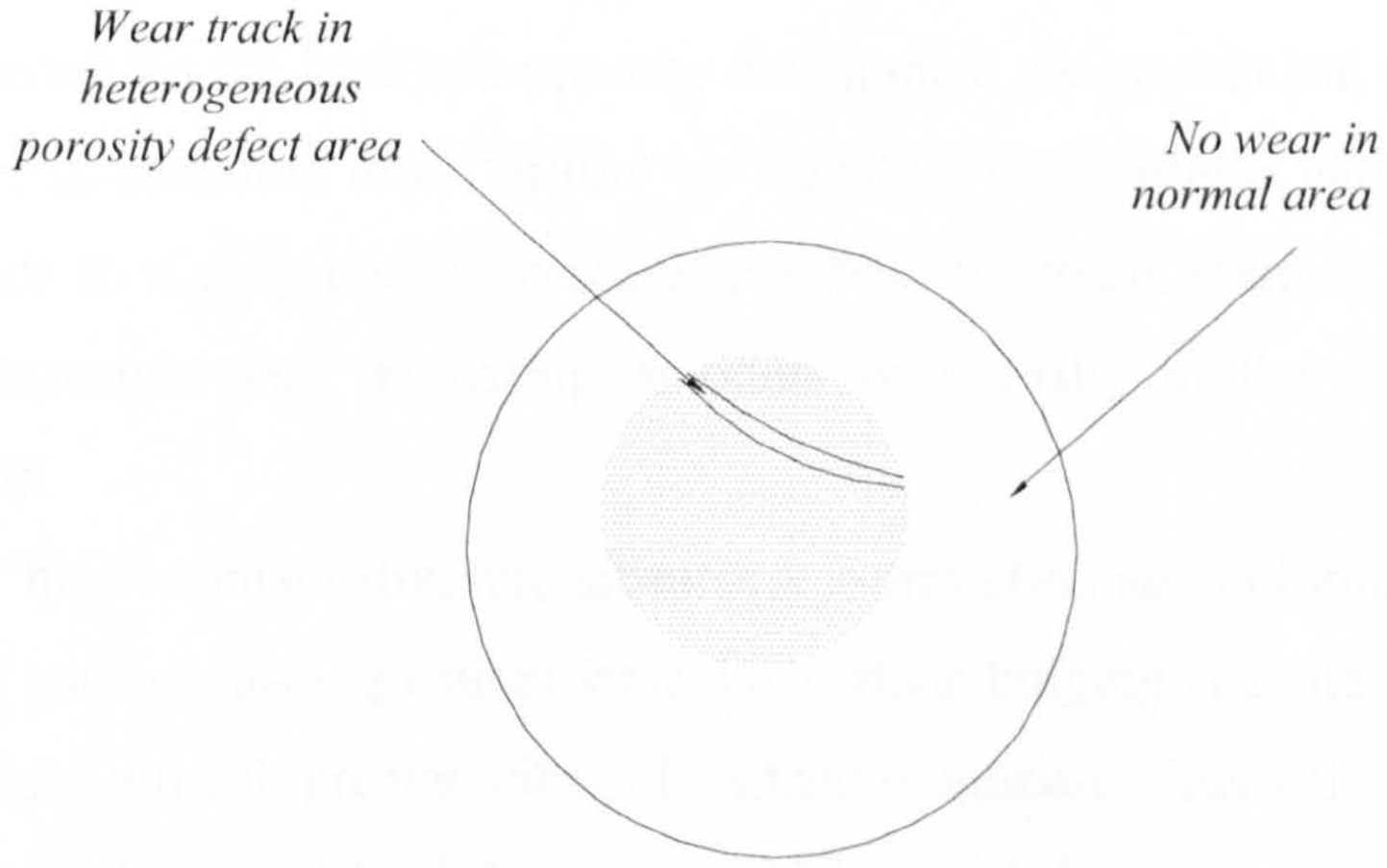

Fig 5-19 Overview of a specimen ball after test

All wear scars occurred on the localised heterogeneous porosity area and little or no wear was found on the normal area, regardless of different contact stresses and different lubricants (Fig 5-19). Because there is some porosity within the normal area (described in Section 5.2.2), it follows that there is a critical pore diameter above which severe wear will occur. In the case of this HIPed silicon nitride under rolling contact, the critical pore diameter is approximately 4 μm. There is an allowable upper

size limit for residual pores under which the wear and fatigue performance is not much affected under lubricated rolling contact. This allowable pore diameter is 2 μm. This is in conformation with a previous disk-on-rod rolling contact study which showed that HIPed silicon nitride rod containing micro-porosity performed much better than bearing steel rod (Hadfield and Stolarski 1995b).

The contact stresses are the dominant factors in rolling contact wear in the localised heterogeneous porosity defect area. For both test series 'A' and 'B', when contact stresses were "low" i.e. maximum compressive stress 3.85GPa and maximum shear stress 1.19GPa, the tests were suspended after the test run reached the pre-set number of revolutions. The wear scar areas were small (23,117μm^2 and 20,883μm^2 respectively). When contact stresses were "high" i.e. maximum compressive stress 5.55GPa and maximum shear stress 1.72GPa, the test times were 13.8 s and 11.9 s. The wear scar areas were then larger (91,182μm^2 and 126,083μm^2 respectively). This is because within the localised porosity defect area, the mechanical properties of the material are in transition from "brittle" to "ductile". The hardness variation (Fig 5-13) corresponds to a progressive decrease in elastic modulus, thermal conductivity and flexural strength with increasing amounts of porosity in the microstructure (Divakar 1994).

With "high" contact stresses, subsurface compaction and deformation occurs. Cyclic rolling contact loading causes irregular surface bulging (Latella 1997) which will then produce a much greater value of surface roughness. This will in turn affect the lambda ratio: the actual lambda ratio would be much less than calculated due to asperity contact. At these asperity contact regions, pores cause high stress concentration and microcracking will occur along pore grain boundaries (He et al 1997). Under LV lubrication, hydrostatic cracking also play an important part, the fatigue crack growth is accelerated by hydraulic pressure of the lubricant (Murakami et al 1985). The rolling wear mechanism is illustrated in Fig. 5-20 which shows the formation and removal process of material debris in the pore. Further debris can be seen forming in the upper right corner of the same pore. Under heavy cyclic loading, this subsurface compaction and deformation, surface bulging, microcracking and material removal process will repeat. Fig 5-21 is the overview of the wear track in the

porous area of test 'B1' ball, some material debris within pores is observed.

Fig 5-20 SEM of a pore with debris on wear track from Test 'B1'

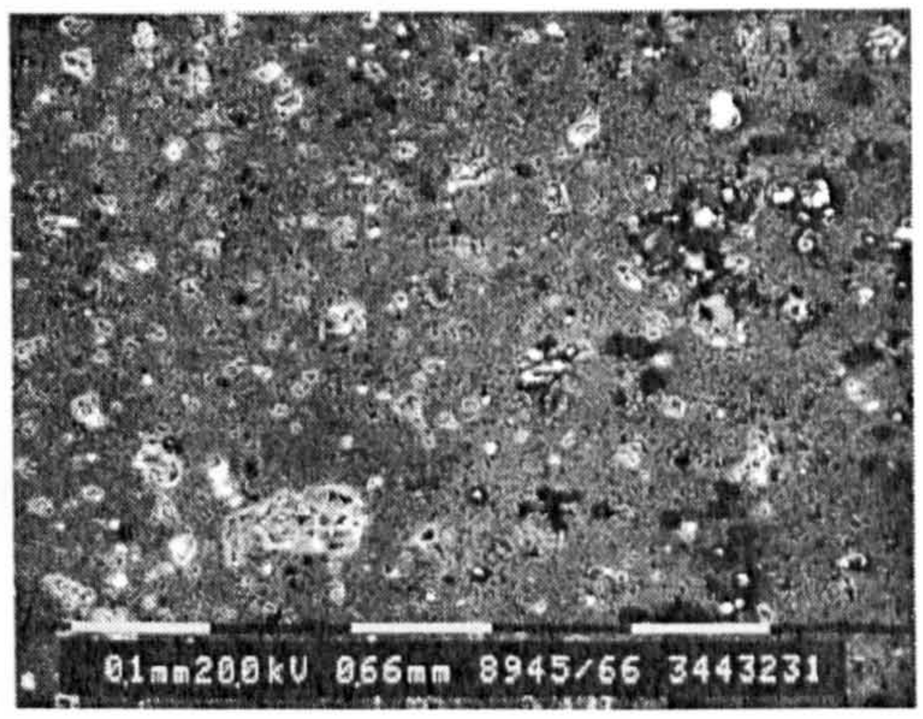

Fig 5-21 SEM of wear track from Test 'B1'

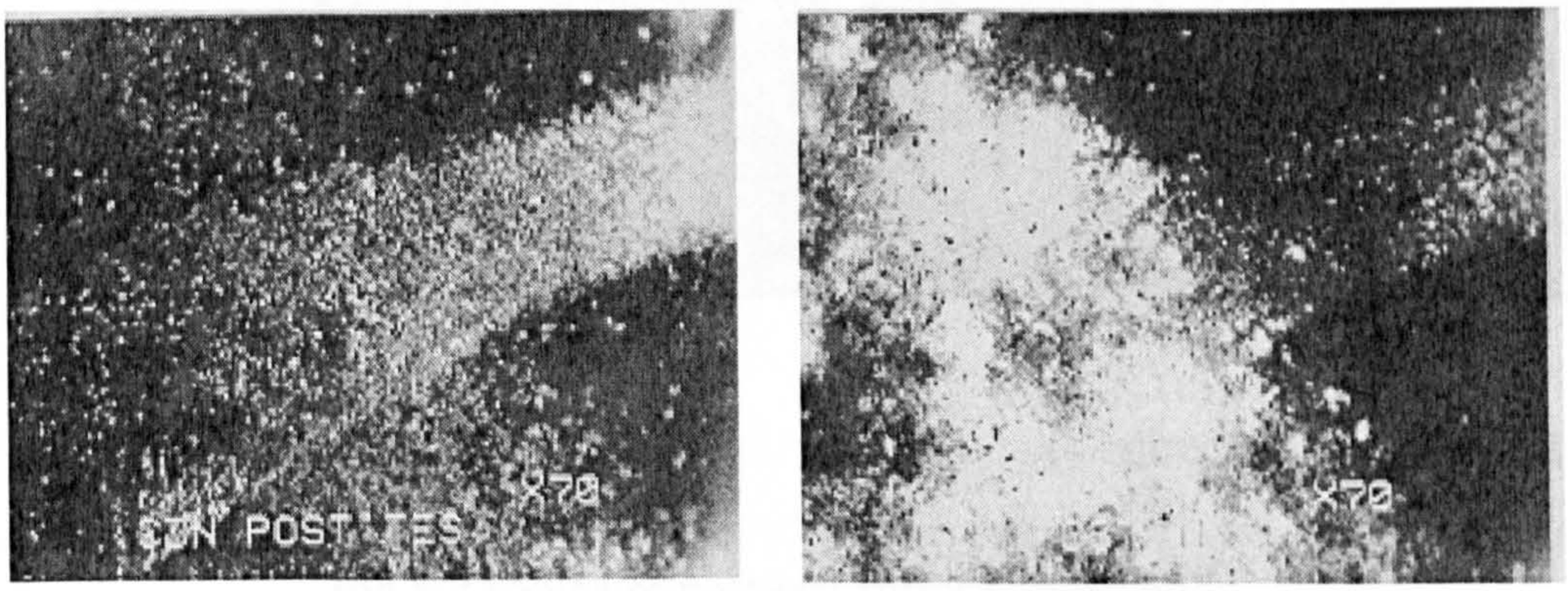

a) white light

b) untra - violet light

Fig 5-22 Post-test ball surface ('B' series)

Fig 5-22 shows light microscopic images of a silicon nitride ball surface after test, (a) under white-light and (b) the same area under ultra-violet light, after dye-penetration treatment. This post-test illustration can be compared to Fig 5-16 which is the same area before the test. The wear track is wider in the localised

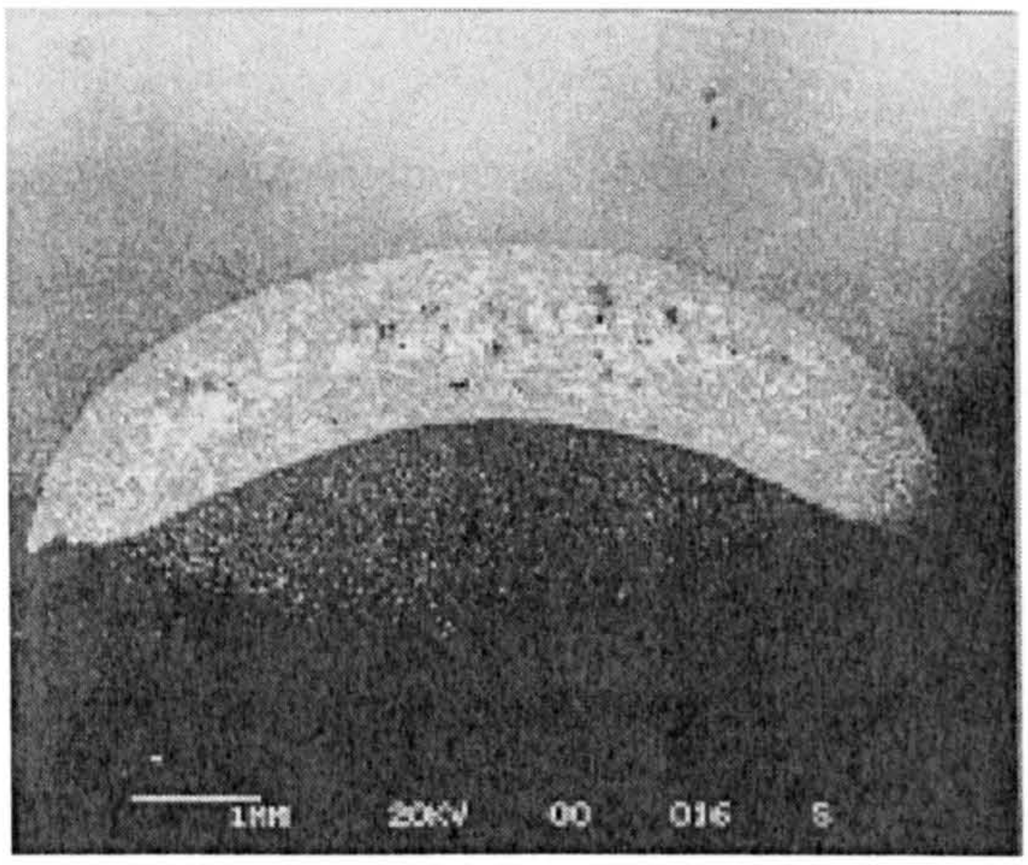

(a) Overview of localised porous area (← direction of rolling test)

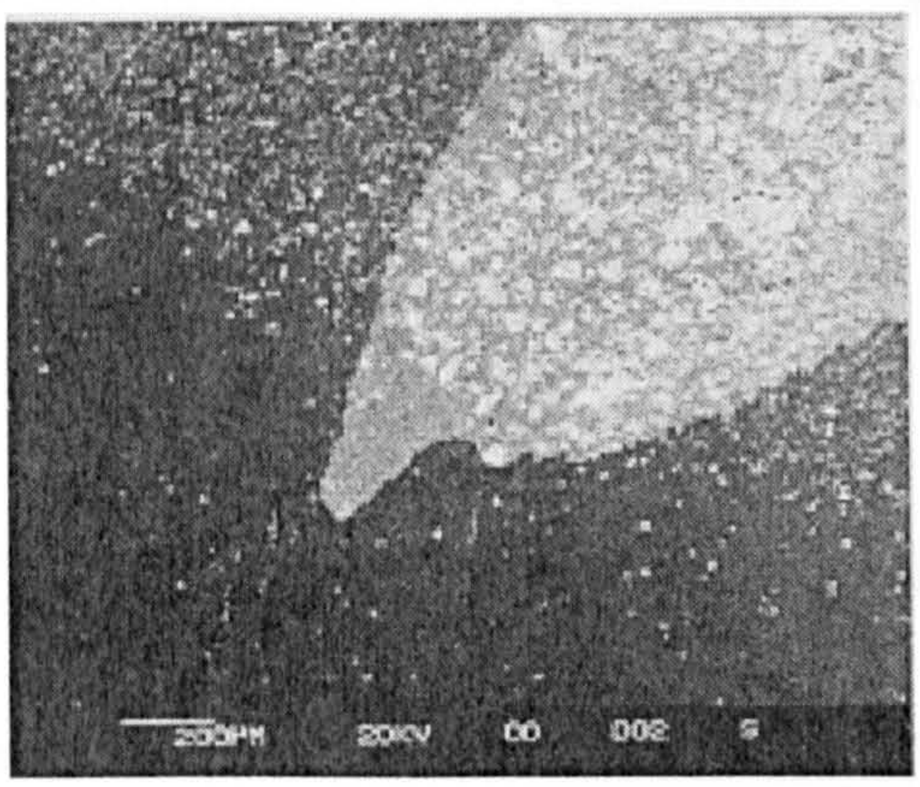

(b) left edge
(← direction of rolling test)

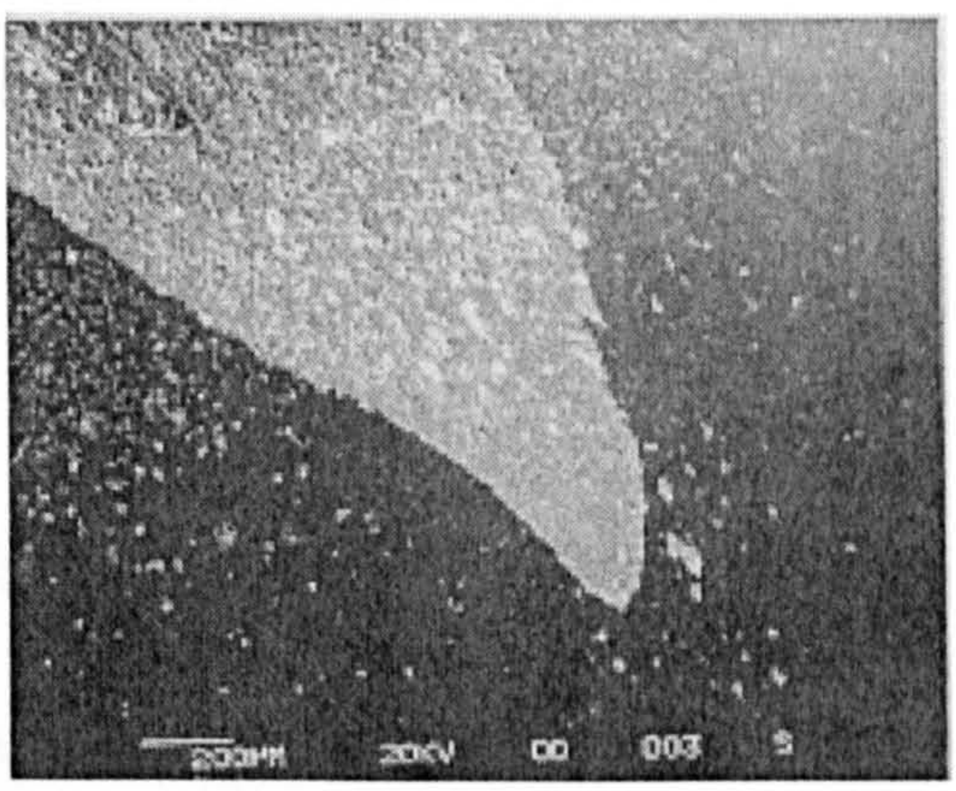

(c) right edge
(← direction of rolling test)

Fig 5-23 SEM of post-test surface observation

heterogeneous porosity defect area and the irregular emission of light illustrates the variation of the localised porosity. Fig 5-23 shows a typical wear scar (from Test A2), which has occurred in the localised heterogeneous porosity defect area. No wear scar is observed in the normal area. Fig. 5-23(b) and (c) shows the wear scar shrink edge. There is no evidence of delamination type fatigue failure, i.e., no cliff edges or fatigue failure dependency on rolling direction as found in previous studies (Hadfield and Stolarski 1993d).

5.2.4 Summary

The dye-penetration method and light microscopy with an ultra-violet light source can enhance the detection of surface and subsurface localised heterogeneous porosity defects within HIPed silicon nitride. A new parameter to describe the pore: the diameter of the pore was proposed by the author, which is the minimum dimension of a pore in all directions. The critical diameter of the pore is 4 μm above which severe wear will occur in lubricated rolling contact. The allowable diameter of the pore is 2 μm under which it does not affect the wear and fatigue performance. HIPed silicon nitride with localised heterogeneous porosity defects is extremely susceptible to the rolling contact stress level. In high stress applications, localised heterogeneous porosity defects must be fully eliminated. High viscosity lubricant is preferable to low viscosity lubricant for silicon nitride with localised heterogeneous porosity defects.

5.3 The Influence of Surface Defects on RCF Failure Modes

Surface defects on HIPed Si_3N_4 rolling elements can be introduced at any stage of manufacturing or handling. These surface defects could be fatal since the surface is subjected to very high stress levels in the rolling bearings. The influences of three common kinds of surface defects: star defects, grinding defects and C-crack defects, on the RCF failure modes were investigated. The surface defects tested were found on commercially finished balls and self-finished balls, which were naturally generated not artificially induced.

All of these tests were conducted under the typical 4-ball rolling test condition employed throughout this thesis (Plint Machine load 1.96 kN, max. compressive stress 6.58 GPa, 10,000 rpm, fully lubricated with Talpa 20, etc.) as described in Section 3.4.1 and Section 3.4.2. The surface defect area in each test was positioned on the rolling track according to Section 3.4.4.

5.3.1 The Influence of Star Defects

Star defect (point defect) is a group of radial cracks initiated from one point, and is best revealed under dye-penetrant and UV light microscopy inspection. Fig. 5-24 (a) shows a star defect like a five-pointed star, with five crack lines initiated from one point. Fig. 5-24 (b) illustrates actually two star defects adjacent to each other, which are three crack lines initiated from one point (upper) and two crack lines initiated from another point (lower). The lengths of these cracks under UV light illumination in Fig. 5-24 (a) and (b) are around 30 μm. The star defect is considered to be due to a point overload caused by the over-rolling of a large unbroken diamond particle. Radial cracks are formed similar to those that occur during hardness testing with a diamond indenter. Further lapping removes the dent but the cracks and sub-surface damage are revealed with dye penetrant and UV light.

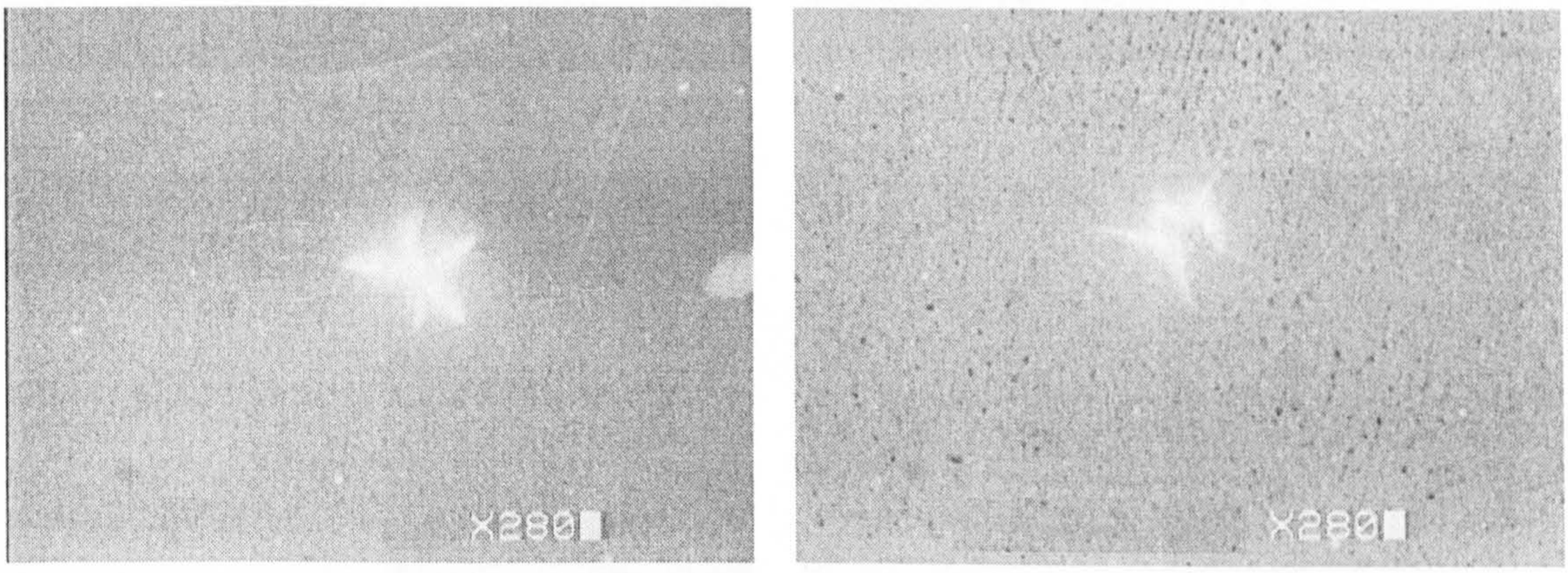

(a) (b)

Fig. 5-24 Star defects after dye penetrant under UV light microscopy inspection

Two D1 balls (No. 3 and No. 11) with star defects were tested to assess the influence of this kind of surface defect. Fig. 5-25 (a) and (b) show No. 3 and No. 11 star defects respectively after dye penetrant under UV light microscopy inspection. The measurement for two opposite crack lines, in No. 3 (Fig. 5-25 (a)) from left to right is 90 μm and from top to bottom is 80 μm, and in No. 11 (Fig. 5-25 (b)) from left to right is 95 μm and from upper left to lower right is 110 μm. Fig. 5-25 (c) and (d) show the comparison of white light (on the left) and UV light (on the right)

observations of No. 3 (Fig. 5-25 (c)) and No. 11 (Fig. 5-25 (d)) star defects after they were positioned on the rolling track just before the RCF tests. Under white light observation, No. 3 was seen that some material had already peeled away from the surface on the left side and on the right side near the centre of the star defect. The trend for the crack lines from top left to lower right can also be seen. For No. 11 star defect observed under normal white light, any trend for crack lines is hard to find.

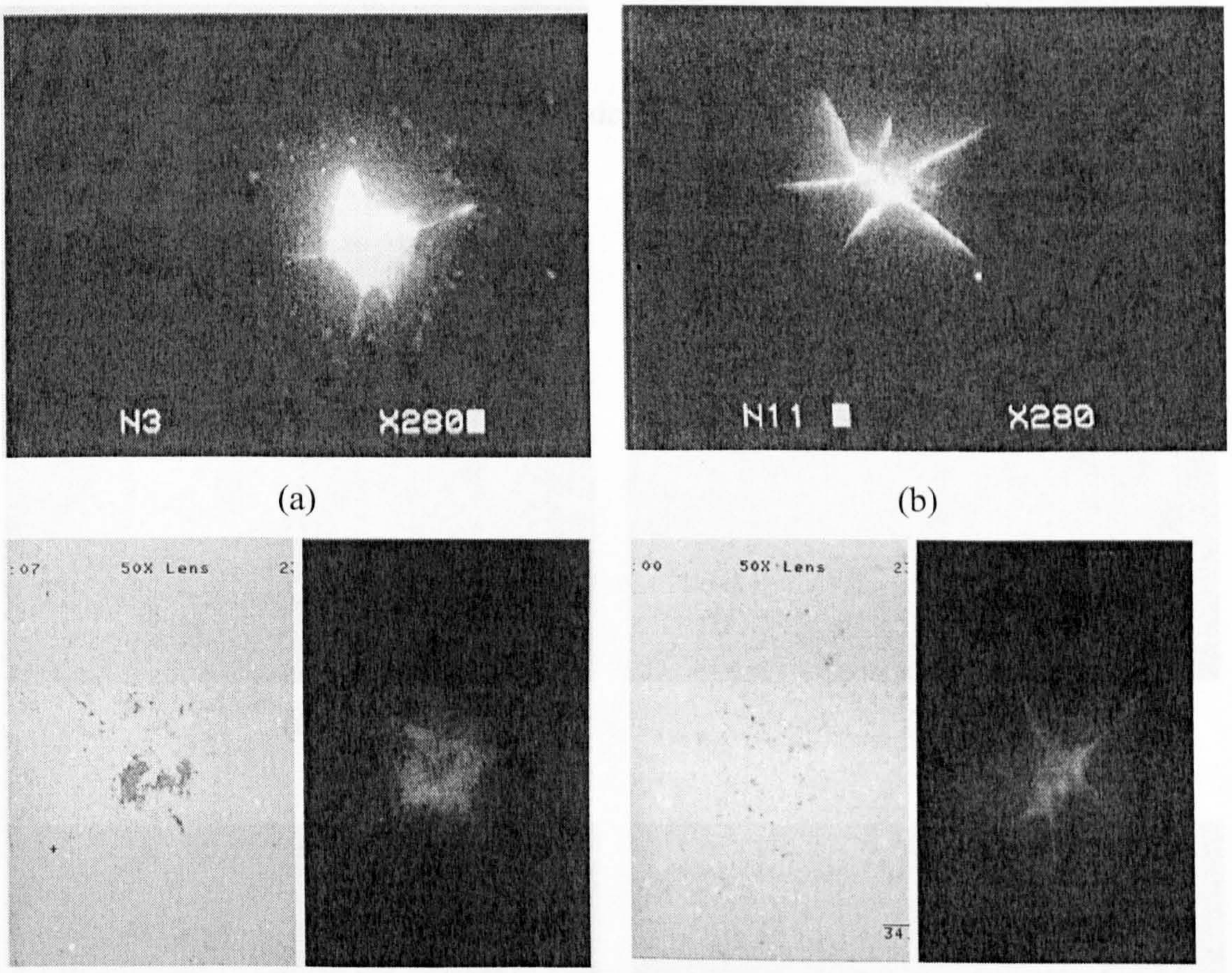

(a) (b) (c) (d)

Fig. 5-25 No. 3 (a, c) and No. 11 (b, d) star defects before RCF tests

The star defect No. 3 failed after 1 hour and 32 minutes RCF test (2.07 million stress cycles). Fig. 5-26 shows No. 3 star defect after RCF test, with Fig. 5-26 (a) under white light and Fig. 5-26 (b) under UV light. The failure is a shallow pitting around the centre of the star defect. Compared with Fig. 5-25 (c), the material peeling

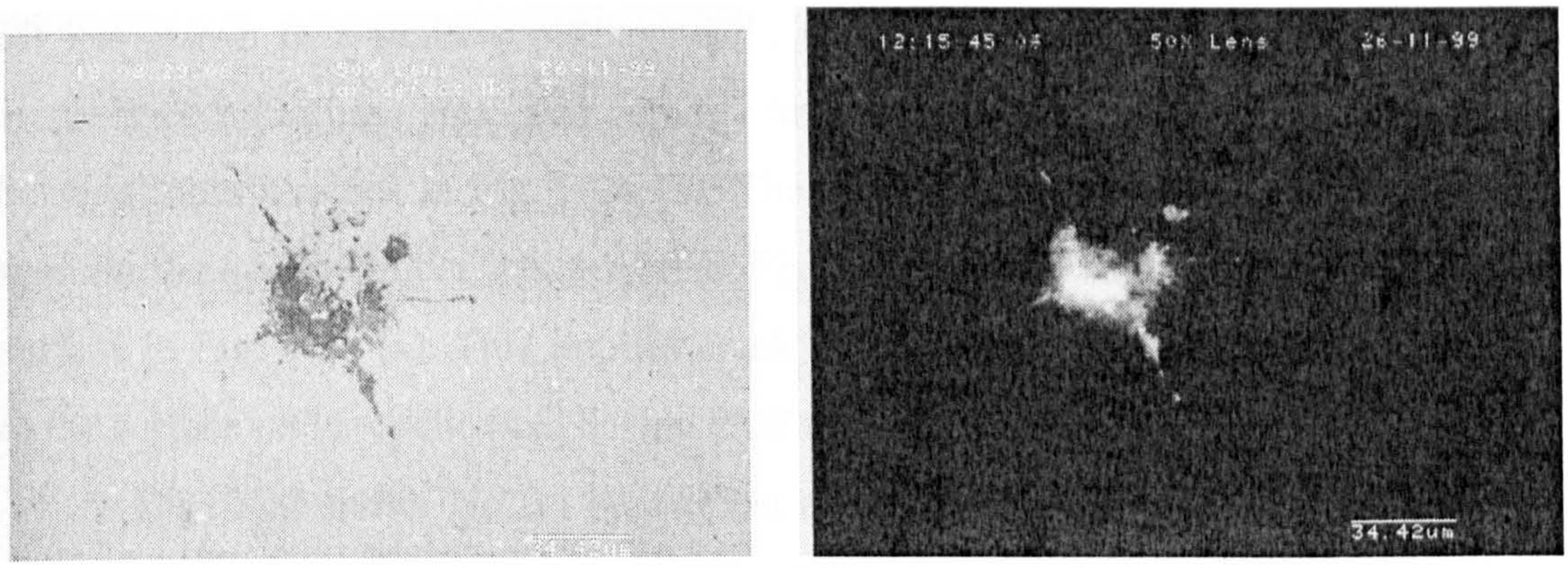

(a) (b)

Fig. 5-26 No. 3 star defects after RCF tests

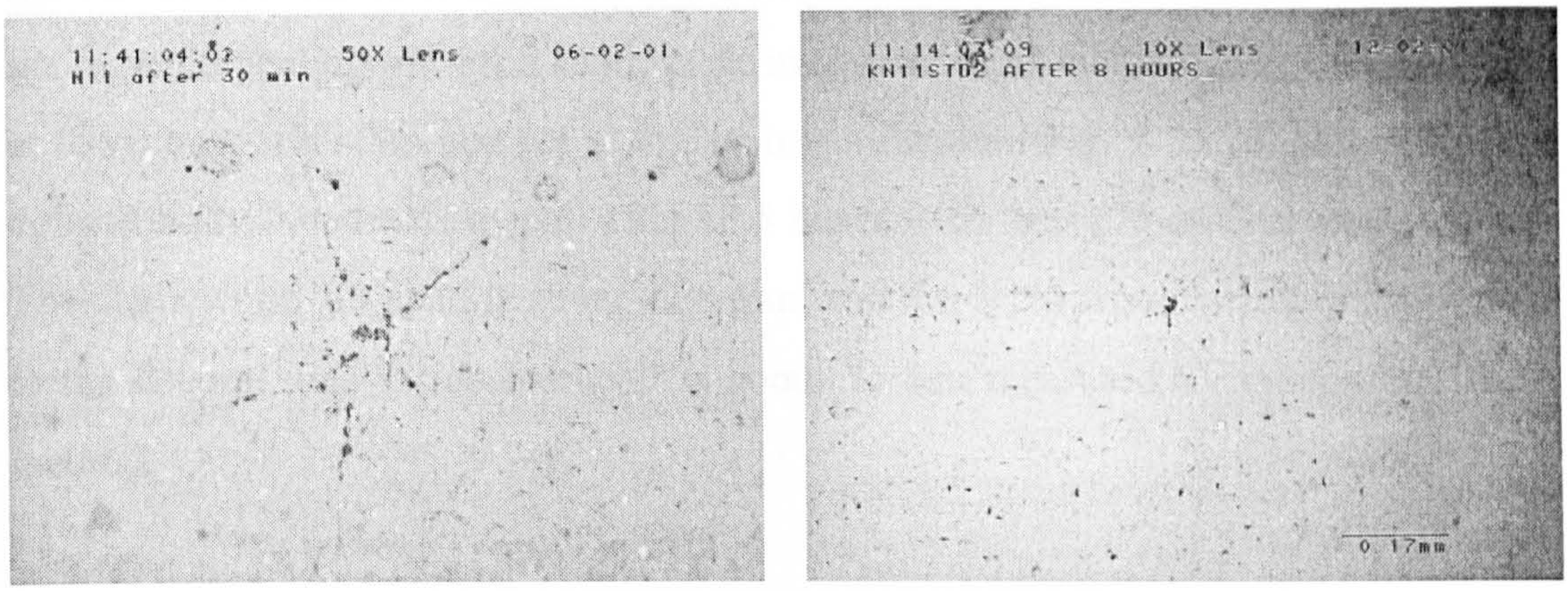

(a) (b)

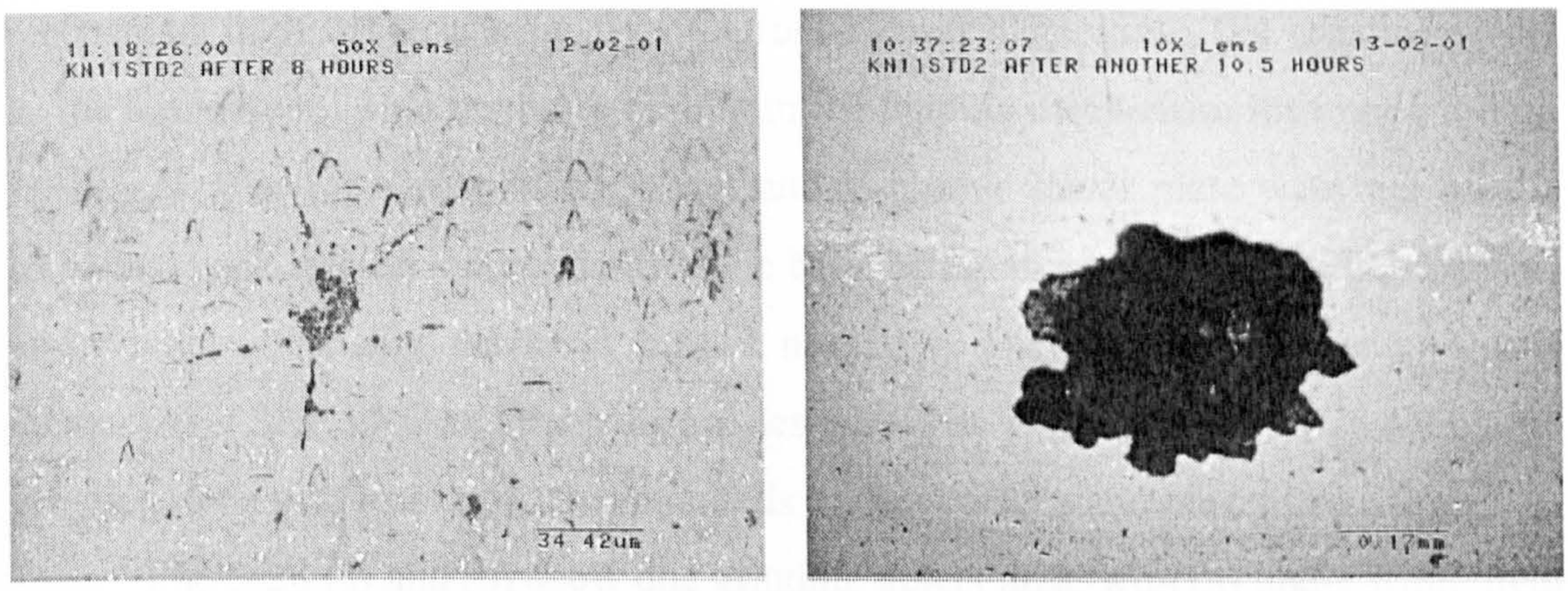

(c) (d)

Fig. 5-27 No. 11 star defects after RCF tests

off has grown to a shallow pitting nearly three-quarters of a full circle within the crack lines initiating area, and crack lines from top left to lower right have become more obvious in Fig. 5-26 (a). The crack lines from left to right can not be seen on the surface under white light in Fig 5-25 (c), but they have appeared on the surface in Fig. 5-26 (a). This implies crack propagation from underneath the surface to the surface under cyclic load during RCF testing.

Fig. 5-27 shows No. 11 star defect area during and after RCF test. Fig. 5-27 (a) reveals after 30 mins RCF test (0.675 million stress cycles), some material already starting to peel off along the star defect crack lines and the crack lines becoming more obvious, compared with Fig 5-25 (d). Fig. 5-27 (b) and (c) illustrate the appearance of the star defect area after 8 hours RCF test (10.8 million stress cycles), showing that the material peeling off left a shallow pit in the centre of the star defect area with (b) at lower magnification and (c) at higher magnification. Fig. 5-27 (d) shows the star defect finally failed with a spall after 18.5 hours RCF tests (25 million stress cycles). The diameter of this spall is about 0.28 mm, and the depth from the edges of the spall to the deepest area inside the spall is about 75 μm measured by microscopy focus method.

5.3.2 The Influence of Grinding Defects

The grinding defect is a crack caused by aggressive grinding processes. The grinding mechanism in this case is basically a V-groove lower plate with a flat grinding wheel as the top plate to grind the balls, similar to the lapping mechanism illustrated in Fig. 1-3 upper. The top flat grinding wheel and V-groove lower plate were not on the same axis, and rotated independently. The balls being ground are from BBB material and do not show any cracks if lapped normally. The grinding of the balls was conducted at SKF ERC and the balls are designated as TEO balls. Fig. 5-28 shows the grinding defects. Some balls have hundreds of these cracks and others just a few.

Fig. 5-28 (a) and (b) show one grinding defect area, with (a) under white light and (b) under UV light. The horizontal crack line which can be seen on the surface in (a) under white light is about 600 μm in length, while the vertical crack line which

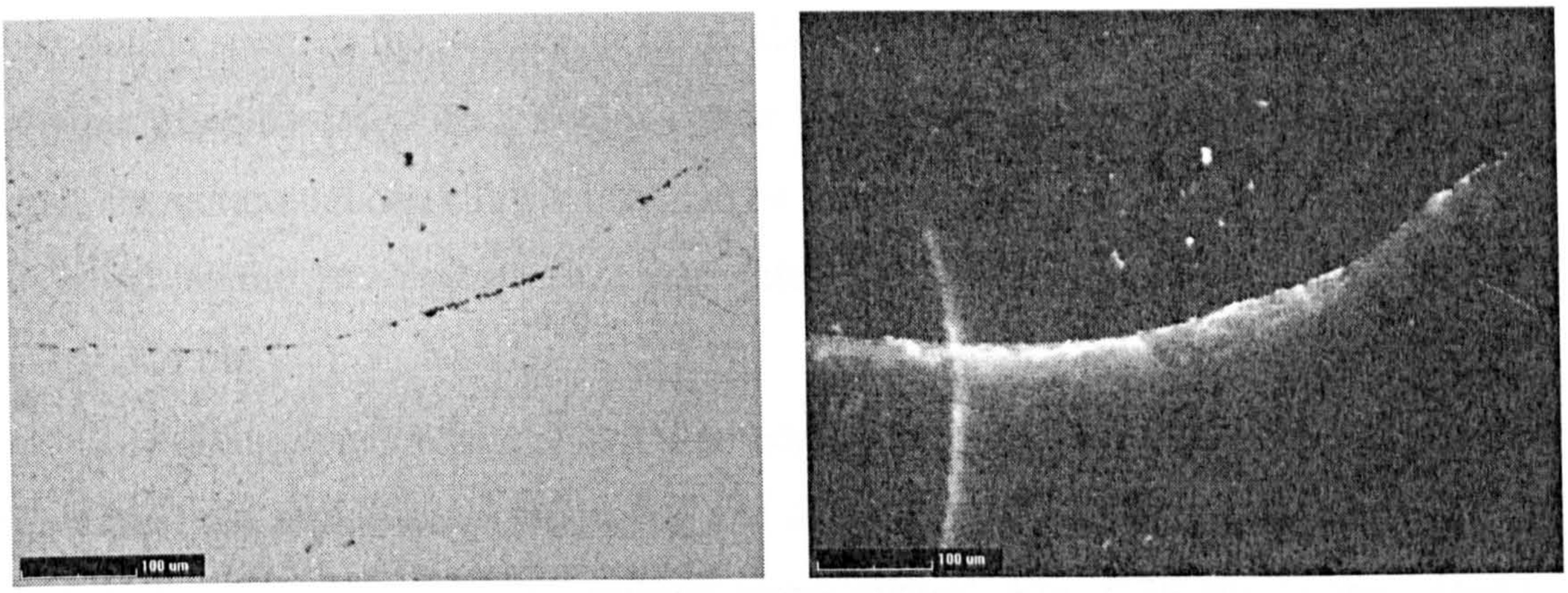

(a) (b)

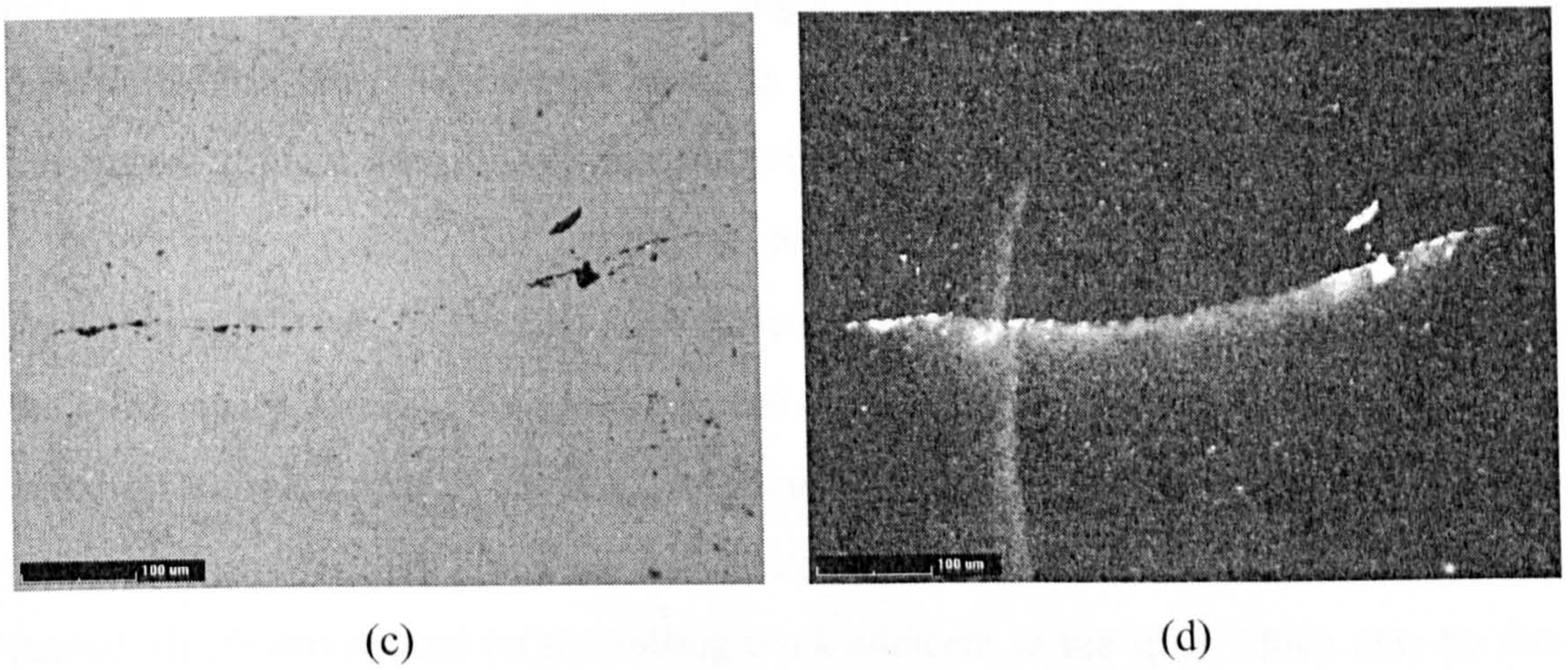

(c) (d)

Fig. 5-28 Grinding defects

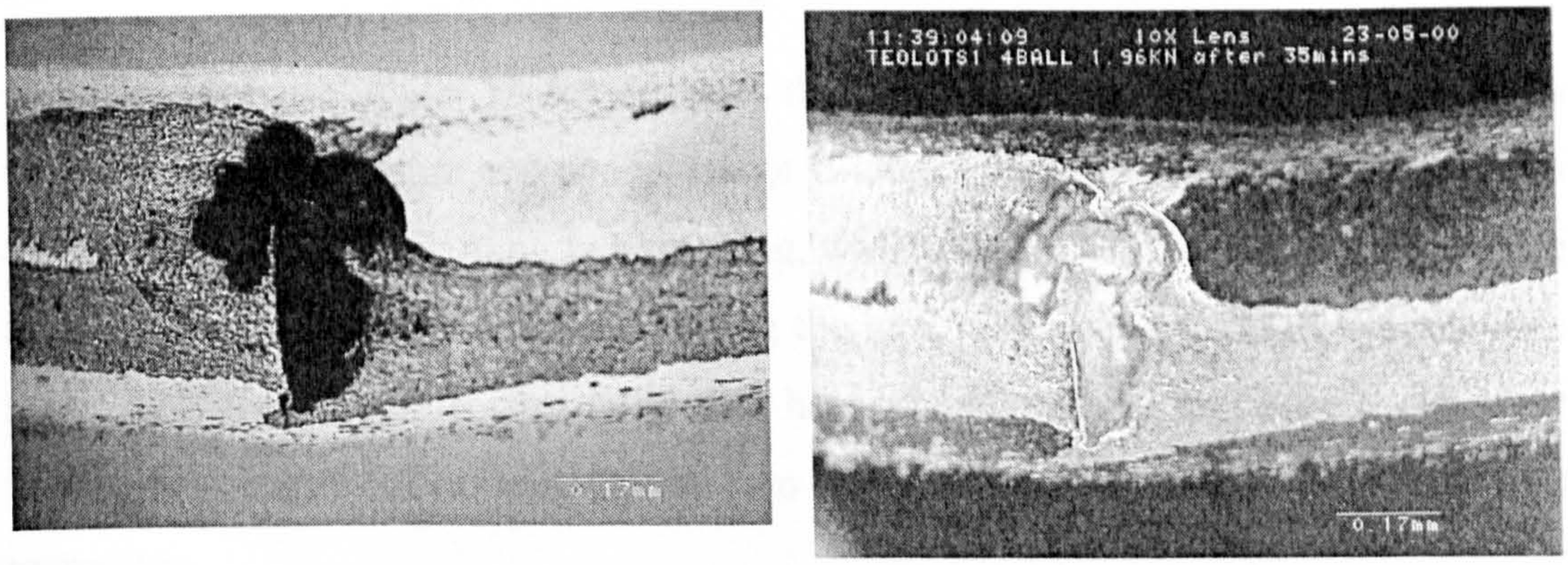

(a) (b)

Fig. 5-29 Grinding defect after RCF tests

can not be seen on the surface in (a) is about 250 μm. Fig. 5-28 (c) and (d) show another grinding defect area, with (c) under white light and (d) under UV light. In this case, the horizontal crack line which can be seen on the surface in (c) is about 500 μm in length, while the vertical crack line which can not be seen on the surface in (c) is about 300 μm.

Rolling contact fatigue test was conducted on a ball with a grinding defect. This ball was provided by SKF ERC and designated as "TEO". The grinding defect failed after 35 minutes (0.788 million stress cycles). Fig. 5-29 shows this grinding defect after RCF tests, (a) under white light bright-field and (b) under white light dark-field. The failure was a spall along an almost straight vertical line. It is assumed this almost straight vertical line was the original grinding crack line. As it was deep, it failed very quickly. The dimension for this spall is, vertically 470 μm and horizontally 340 μm. The depth from the edges of the spall to the deepest area inside the spall, which is offset along the vertical crack line near the centre of the spall, is about 80 μm measured by microscopy focus method. The shape of this spall is very different from other fatigue spalls which are normally circular in shape. Material had peeled off (delamination) on the rolling track adjacent to the spall which may be due to the abrasive wear of the material broken off from the spall.

5.3.3 The Influence of C-Crack Defects

C-cracks are part circular Hertzian cracks that can be present on silicon nitride balls with diameters of 10 mm and above. Large C-cracks are typically formed by impacts between balls caused by improper handling, while smaller C-cracks are thought to be a result of collisions between balls during the lapping processes. Small C-cracks are more easily observed if the balls are heat-treated before fluorescent penetrant inspection. Fig. 5-30 (a) and (b) are two cases of multi-C-cracks under UV light inspection.

An extensive study on the rolling contact fatigue performance of the C-cracks found on commercially finished HIPed silicon nitride balls was carried out by Wang and Hadfield (2000a, 2000b). The influences of the location and the orientation of the

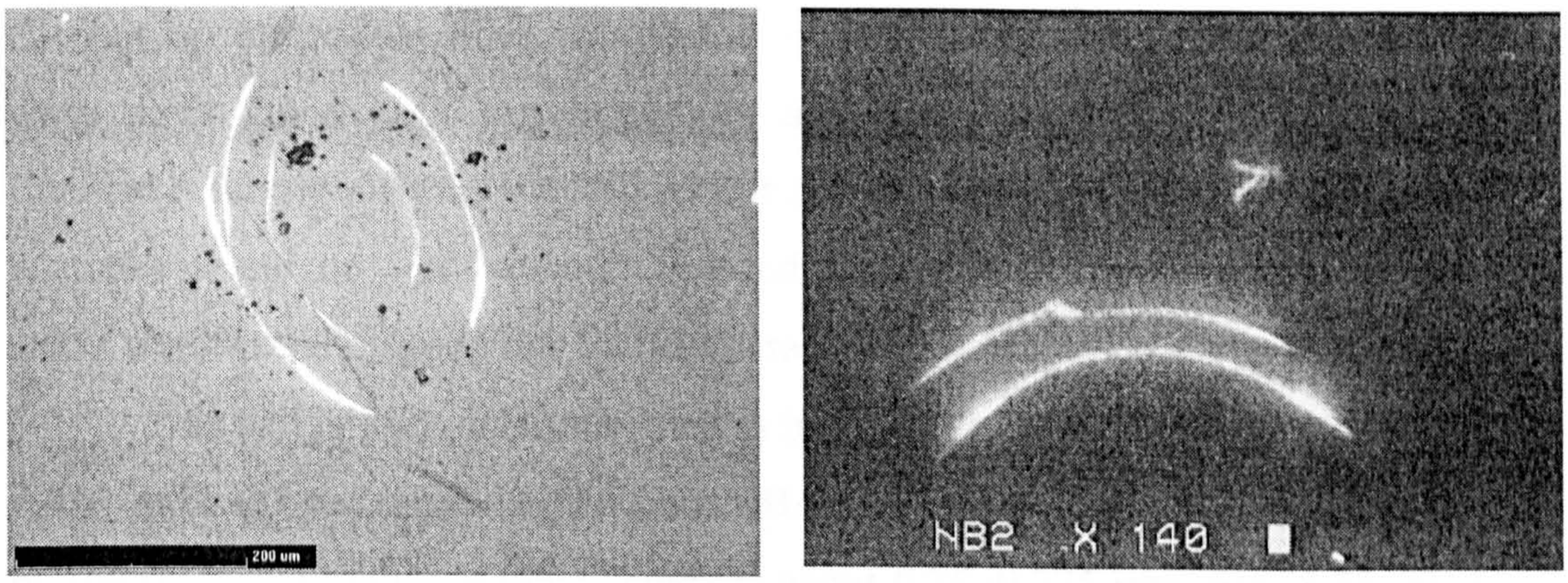

(a) (b)

Fig. 5-30 Multi-C-cracks under UV light inspection

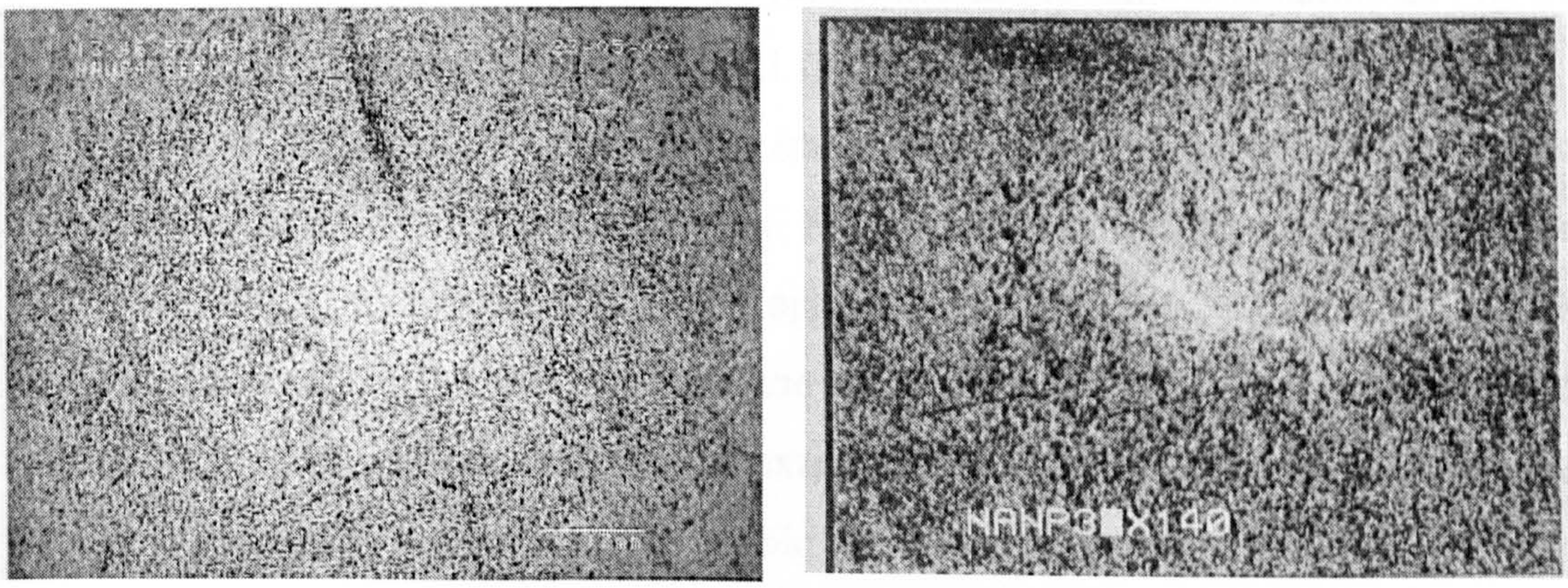

(a) (b)

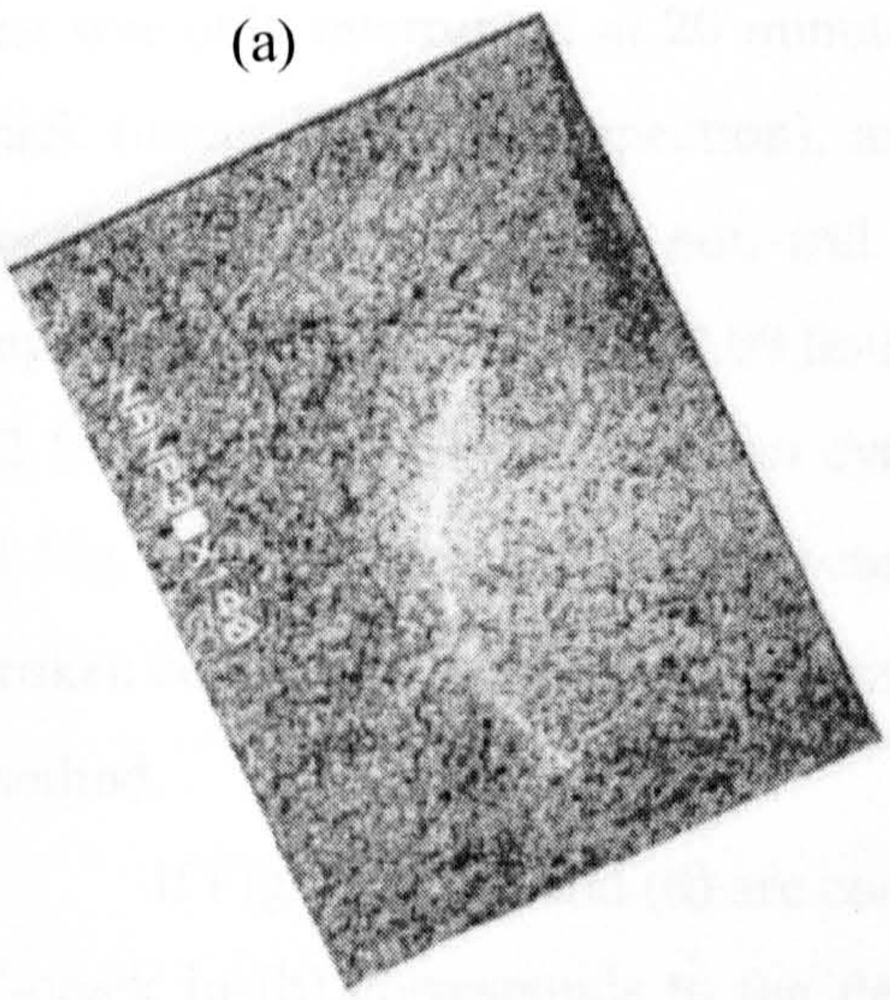

(c) rolling direction →

Fig. 5-31 A rough-lapped ball with a C-crack on it before RCF tests

C-crack on the rolling track at different contact loads under lubricated conditions were investigated both experimentally and theoretically by BEASY Boundary Element Analysis software modelling. It is not necessary to repeat the RCF test on the C-cracks found on commercially finished HIPed silicon nitride balls. So, in this study, a self-rough lapped ball with a C-crack on it was chosen to run RCF test.

This ball is from the same batch as in Fig 4-11 (c) and (d) described in Section 4.3.5, and has been rough-lapped from BBA at a load of 18.13 N/ball and at a speed of 169 rpm. The radius of this C-crack is about 0.25~0.275 mm. Fig. 5-31 (a) shows the surface of this C-crack under white light inspection after it was positioned on the rolling track just before the RCF test, the C-crack is in the subsurface (underneath the surface), which can not be seen. Fig. 5-31 (b) and (c) show the same surface area under UV light inspection, with Fig. 5-31 (c) rotated to the same orientation as Fig. 5-31 (a) (the horizontal direction of Fig. 5-31 (a) is the rolling direction).

Fig. 5-32 (a) shows the rolling track after 20 minutes RCF test. At this moment the C-crack still can not be seen. Fig 5-32 (b) shows the rolling track after 17.09 hours RCF test. The C-crack has appeared on the surface. This may be due to the propagation of the C-crack from the subsurface to the surface, or due to the rolling wear of the surface, or both. The exact time when the C-crack appeared on the surface is unknown, since it is not desirable to constantly interrupt the RCF test. The test was only interrupted at 20 minutes to make sure the C-crack was on the rolling track (under UV light inspection), and at 17.09 hours to check if the C-crack had appeared on the surface or not, and to change the lower balls and lubricant oil. It happened some time before 17.09 hours. After another 5.09 hours (total RCF test time 22.18 hours, 29.943 million stress cycles), the C-crack failed with a big spall, shown in Fig. 5-32 (c) and (d). The diameter of this spall was about 600 μm including the broken edges, and the depth of the spall about 100 μm measured by microscopy focus method.

If Figs 5-32 (b) and (d) are compared which are in the same magnification, the C-crack in (b) corresponds to the deepest spall area in (d). The C-crack may have originally been so deep or propagated to such a depth before it finally failed. At the edges of the spall, some material had broken off. This may be due to the fact that the

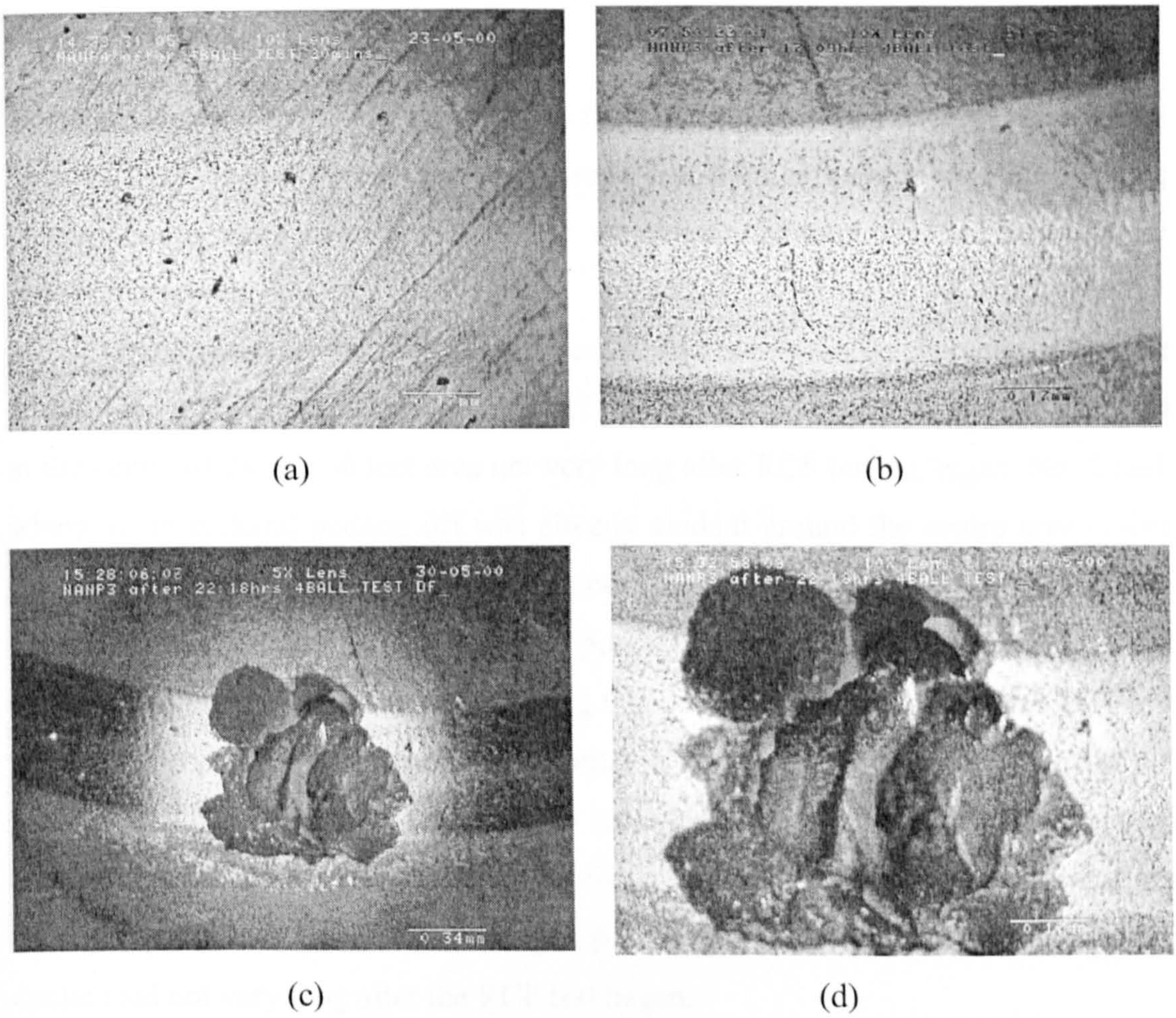

(a) (b)

(c) (d)

Fig. 5-32 A rough lapped ball with a C-crack on it after RCF test

machine was still running after the material peeled off from the C-crack spall, because it is not possible to stop the machine immediately. This peeled off material may also have played a part in breaking the material at the edges of the spall.

A ball from the same batch without a C-crack defect was tested in Section 5.1 as sample F to assess the influence of surface roughness. No failure was found except occasional pitting on the rolling track after running 136.37 hours RCF test (Fig. 5-1 F in Section 5.1). Compared with sample F in Section 5.1 the C-crack on a rough surface is detrimental. The surface pitting also occurred on the rolling track, on the right side and left side of the spall on Fig. 5-32 (c). This confirms the results of sample F in Section 5.1, which means the surface pitting is more likely to occur on a rough surface.

5.3.4 Discussion

Three kinds of surface crack type defects (star defects, grinding defects and C-crack defects) were positioned on the rolling track and their influences on RCF life and failure modes were investigated. There are some common characteristics worth further discussion.

Two balls with star defects were tested, and two common characteristics were found. One is that the material peeling off (delamination or surface pitting) occurred at the centre of the star defect area not very long after RCF testing began. No. 3 ball, where some material peeling off was already evident around the centre area before the RCF test, was observed after 1hour and 32 minutes of testing. No. 11 ball was observed after 8 hours of testing. The peeling off must have happened after 30 minutes and before 8 hours because during this period no interruption of the RCF test and no observations were made. This common characteristic may be related to the formation of the star defect (referring to section 5.3.1). A large unbroken diamond particle acted like a hardness indenter, leaving a plastic deformation zone at the centre of a group of crack lines. This damaged plastic deformation zone peeled off under cyclic load not very long after the RCF test began.

Another common characteristic from the two star defects tested is that the growth of the crack lines from underneath the surface to the surface is quick under cyclic load. For No. 3 ball, this was observed after 1 hour and 32 minutes RCF testing by the crack lines from upper right to lower left becoming more obvious and the crack lines from left to right appearing on the surface (compare Fig 5-25 (c) with 5-26 (a)). For No. 11 ball, this was observed after 30 minutes RCF testing by the crack lines which had not been visible appearing on the surface (compare Fig 5-25 (d) with 5-27 (a)). The growth of a C-crack from underneath a rough surface to the surface took more than 20 minutes and less than 17.09 hours. These facts suggest an assumption, that these surface crack type defects, if the crack is underneath the surface, are not far from the surface. The time taken for the crack underneath the surface to grow to the surface under cyclic load is dependent on how far the initial crack is from the surface. The closer it is to the surface, the shorter time it takes. To quantify this assumption, however, more balls with surface crack type defects need to

be sectioned and more RCF tests frequently interrupted to find out the exact time for the growth of the crack from underneath the surface to the surface.

The second assumption, based on the failure time and the depth of the spall of the three failed balls, is that the failure time may be related to the depth of the initial crack. If the depth of the initial crack is nearly or in excess of 100 μm, it will fail very quickly under RCF test like the grinding defect tested. If the depth of the initial crack is not as deep as 100 μm, it will first grow vertically probably sloping deeper until reaching the depth of nearly 100 μm, which is the location of the maximum shear stress calculated by Hertz contact theory. The crack then starts to grow horizontally and the material breaks off to form the spall. Again, to validate this assumption, more balls are needed to be sectioned at different RCF test stages.

5.4 The Effects of Finishing Rate on RCF Performance

In the finishing process of HIPed Si_3N_4 rolling elements, maximum material removal rate (finishing rate) is desirable. The goal in finishing is to achieve maximum material removal while maintaining satisfactory surface quality to ensure long RCF life. It was found the lapping load is the most influential parameter on the finishing rate (see Section 4.2), and a maximum finishing rate of 68 μm/hour was achieved under an average lapping load of 42.87 N/ball (see Section 4.3). Whether this accelerated eccentric lapping process, high lapping load and high finishing rate will affect the rolling contact fatigue life or not is a concern of this study.

In Section 5.1, three balls self-finished by this eccentric lapping process with different surface roughness (samples E, F and G), were tested by 4-ball rolling for over 100 hours, and no fatigue spall was found. These balls were finished at an average lapping load of 18.13 N/ball. In this Section, RCF tests were conducted on two balls finished from BBA. One was finished at the highest lapping load — 106.63 N/ball and the other was finished at the highest finishing rate — 68 μm/hour. No further polishing process was applied to these two balls, i. e., they were both rough-

lapped only. The test condition was the typical 4-ball rolling test condition employed throughout this thesis (Plint Machine load 1.96kN, max. compressive stress 6.58 GPa, 10,000 rpm, fully lubricated with Talpa 20, etc.) as described in Section 3.4.1 and Section 3.4.2.

Some surface and subsurface damage occurred under the highest lapping load (see Section 4.3.3). However, this test was arranged so that there was no visible surface or subsurface damage on the rolling track, either under white light or UV light microscopy observation. This ball failed after 9 hours 51 minutes (13.3 million stress cycles). Fig. 5-33 shows the failure after RCF testing ((a) bright field, (b) dark field). The failure was a spall with a diameter of 320 μm, and the depth was 65 μm measured by microscopy focus method. Compared with other fatigue spalls in Fig 5-32 (c), Fig 5-29 (b), Fig 5-27 (d) and Fig 5-36 (a), this spall was shallow and very flat at the bottom (Fig 5-33 (b)). There is one possibility, which is that under such high lapping load the surface damage zone reached about 65 μm and the spall was initiated from the interface of this damage zone and bulk material. To validate this, the ball needs to be sectioned and etching technology used to obtain the grain morphology.

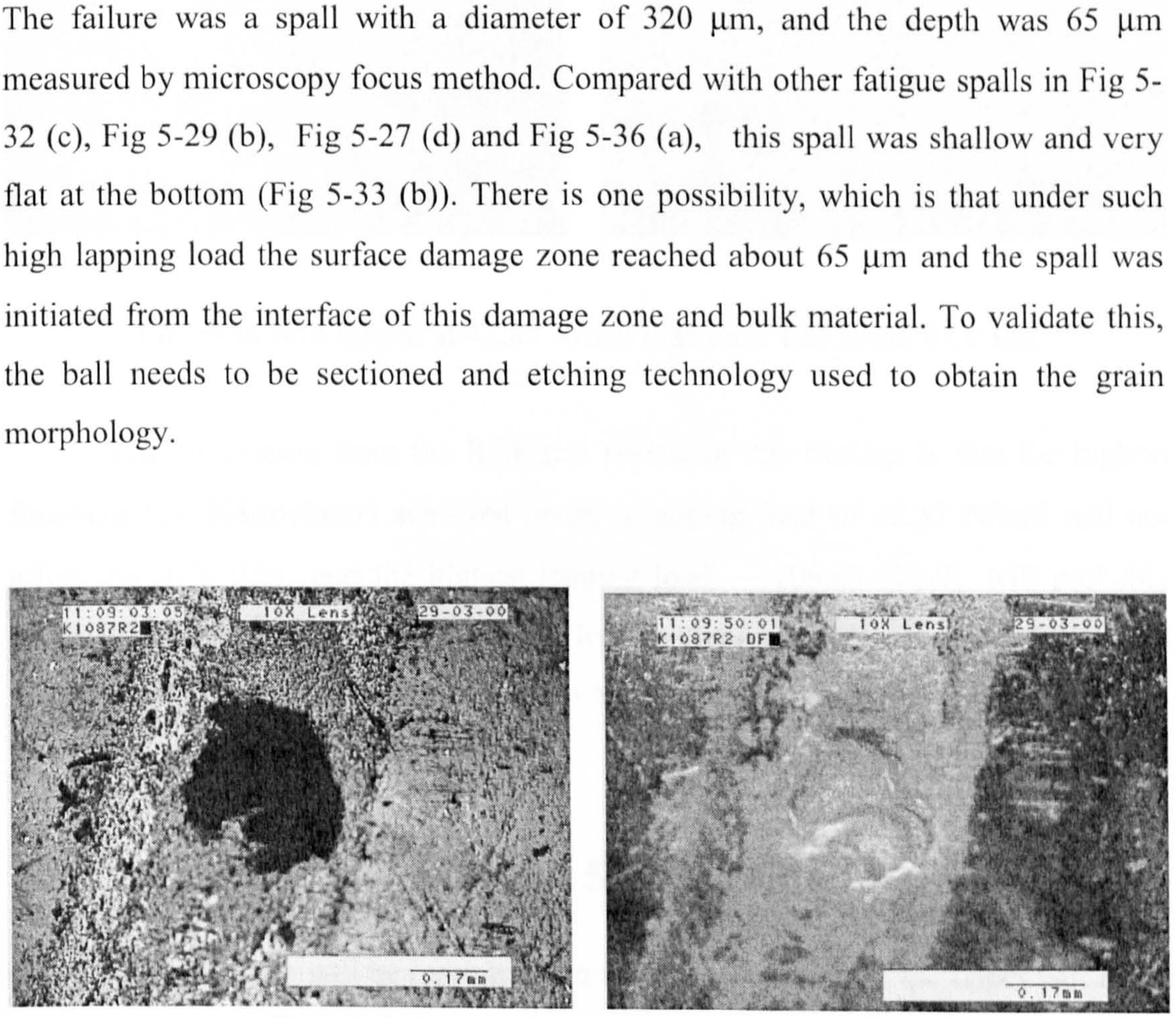

(a) (b)

Fig. 5-33 Ball lapped at 106.63 N/ball load failed after RCF test

The RCF test conducted on a ball lapped from BBA at the highest finishing rate (68μm/hour) (at lapping load 42.87 N/ball) for 102.2 hours (138 million stress cycles), showed no failure occurring on the rolling track, only small pittings and further developed scratch marks as with Sample F in Section 5.1. Fig. 5-34 shows the appearance of the rolling track of this ball after 102 hours RCF testing.

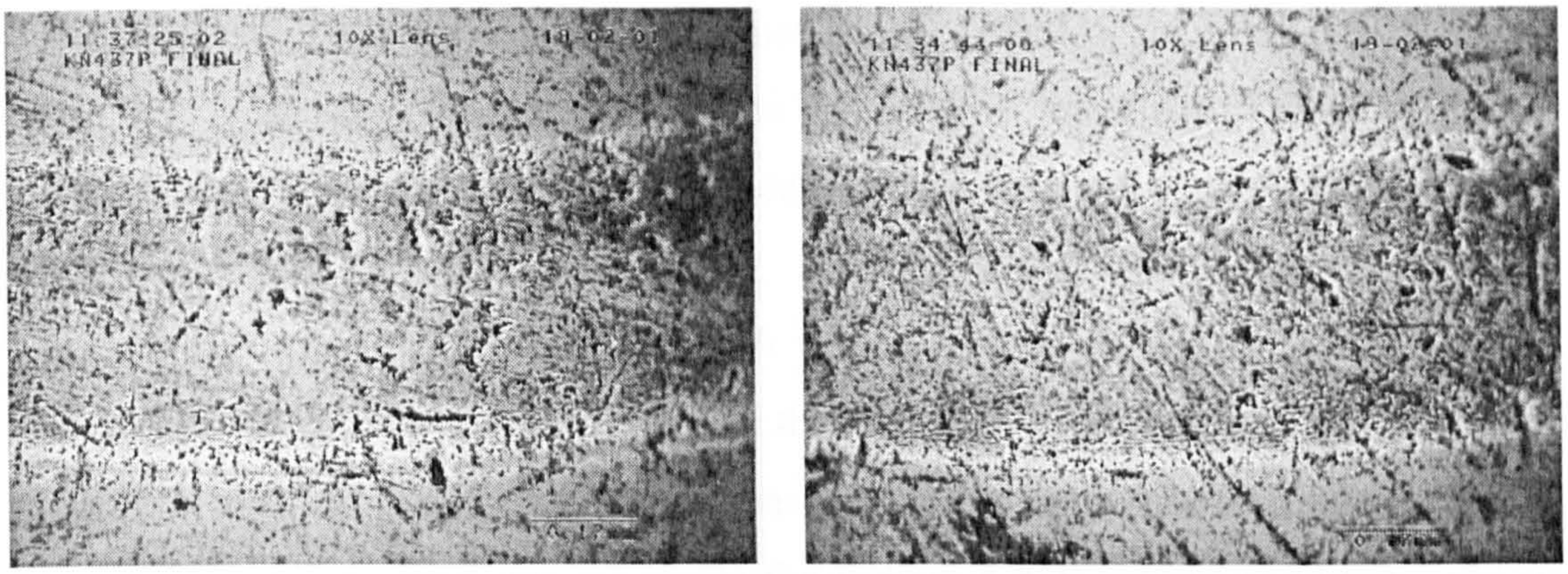

Fig. 5-34 Ball lapped at 42.87 N/ball load after 102 hours RCF test

The conclusion from the RCF test results in this Section is that the highest finishing rate (68μm/hour) achieved under a lapping load of 42.87 N/ball will not affect the RCF life; and the highest lapping load — 106.63 N/ball, will probably cause RCF failure. The highest lapping load is definitely not acceptable, as it had already caused surface and subsurface damage and the finishing rate was not high.

5.5 Comparison of 4-Ball and 5-Ball Rolling Tests

It is anticipated there will be more traction in the contact zone of the upper ball in the 5-ball rolling test. The word "traction" here means the frictional force in the Hertzian contact ellipse at upper ball and lower ball contact point, which drives the lower ball to spin and roll. The lubricant viscosity, film thickness and ball kinematics must be taken into account. The source of friction may include elastic hysteresis in rolling, sliding in rolling element due to contact geometry, sliding due to deformation of

contacting elements and viscous drag of the lubricant on the rolling element, etc. (Harris, 1991). Rolling with traction and spin of three-dimensional bodies was classified as three categories: (a) vanishing slip: linear creep theory; (b) complete slip; (c) partial slip: nonlinear creep theory (Johnson, 1985). Although the theoretical calculation of the "traction" in 5-ball rolling is possible by making reference to (Harris, 1991) (Johnson, 1985) (Yu 1999), it is very intricate and beyond the scope of this PhD thesis. The experimental assessment of the "traction" in 5-ball rolling can be made by measuring the torque on the spindle of the Plint TE92/HS Rotary Tribometer. Unfortunately, the torque measurement function of this machine is not working properly.

Self rough-lapped balls from BBA were chosen to run the 5-ball rolling test. These balls were from the same batch as the sample F described in Section 5.1. The purpose of this test was to make a comparison with sample F, which had run 136.4 hours (184 million stress cycles) under the typical 4-ball rolling condition, and no failure occurred except occasional surface pittings (Fig 5-1 F in Section 5.1). The 5-ball rolling test was set up as described in Section 3.4.3, to ensure that the contact load and unit time stress cycles were the same as for the 4-ball rolling test in order to see the effect of traction.

5-ball rolling tests were conducted on four balls. The first ball—No. 1, after running 6 hours and 56 minutes, suffered traction cracks all over the rolling track, more obvious on the outer side of the track. Fig. 5-35 shows the microscopy appearance, (a) and (b) with 5× object lens, (c) and (d) with 10× object lens, (e) and (f) with 20× object lens. After another 5 hours and 1 minute (total 11 hour 57 minutes), this ball failed with a big spall. The diameter of this spall is about 500 μm and the depth is about 100 μm measured by microscopy focus method. It is likely this spall was initiated by two traction cracks (Fig. 5-36 (b)). Delamination also occurred on the track (Fig. 5-36 (f)). The traction cracks are now clearly on both sides of the track, but the crack orientations are opposite at two sides of the track (Fig. 5-36 (e) and (f)). This is illustrated in Fig 5-37.

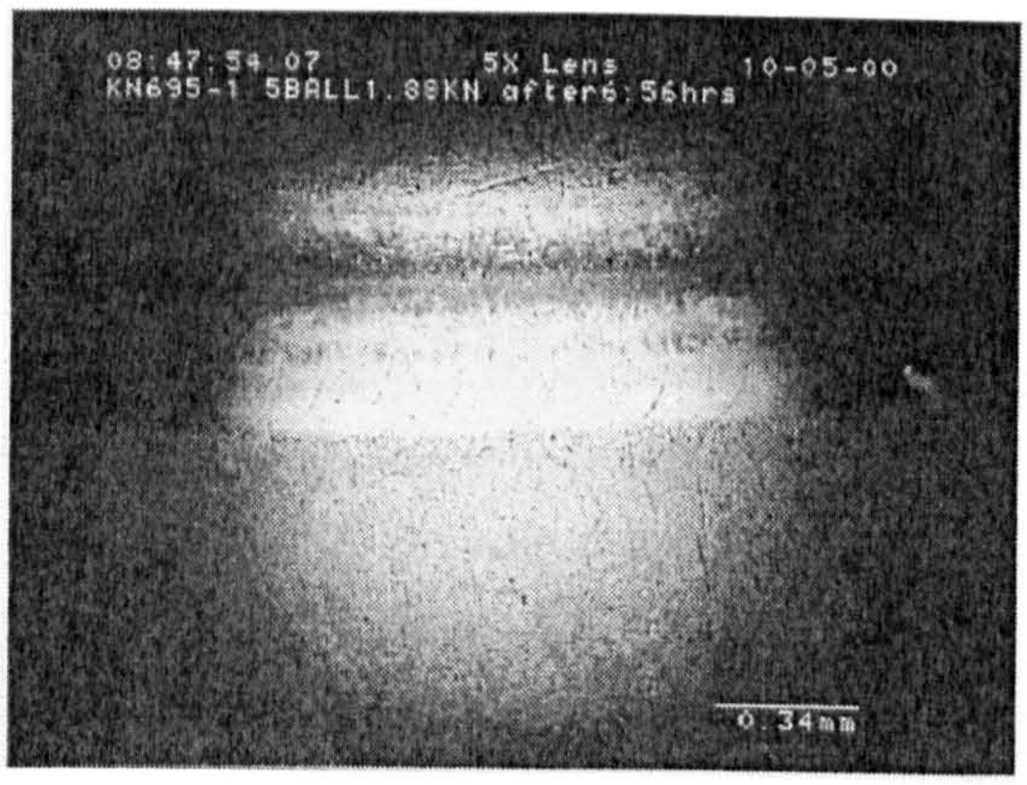

(a)

(b)

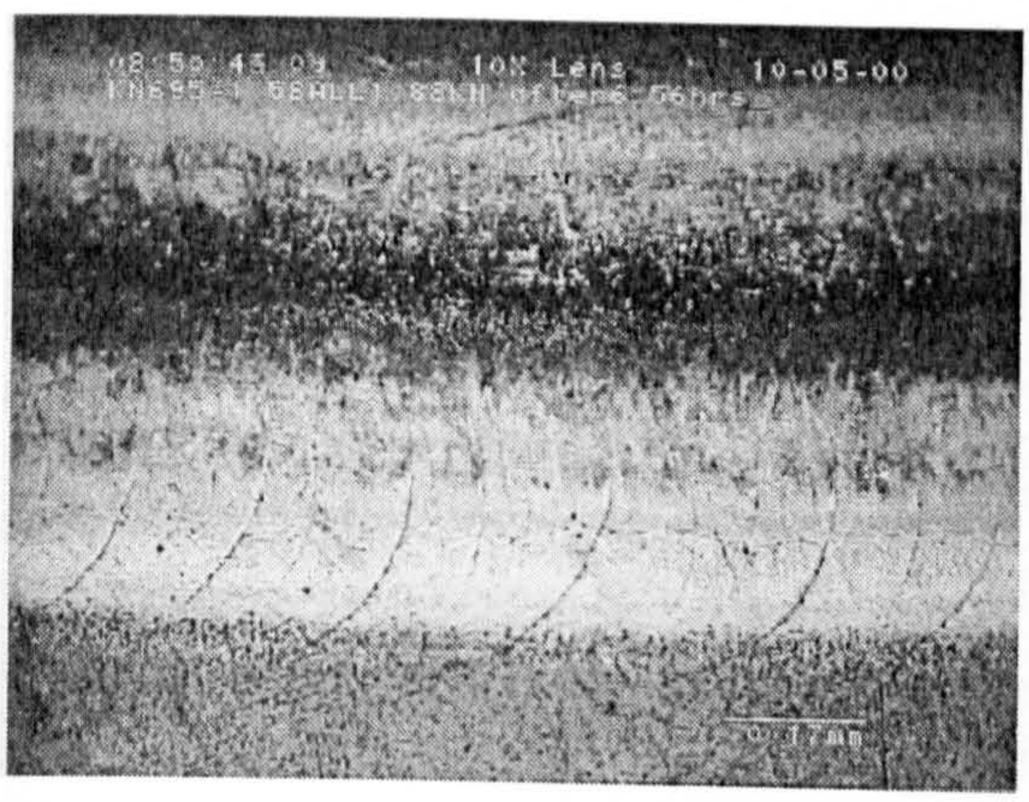

(c)

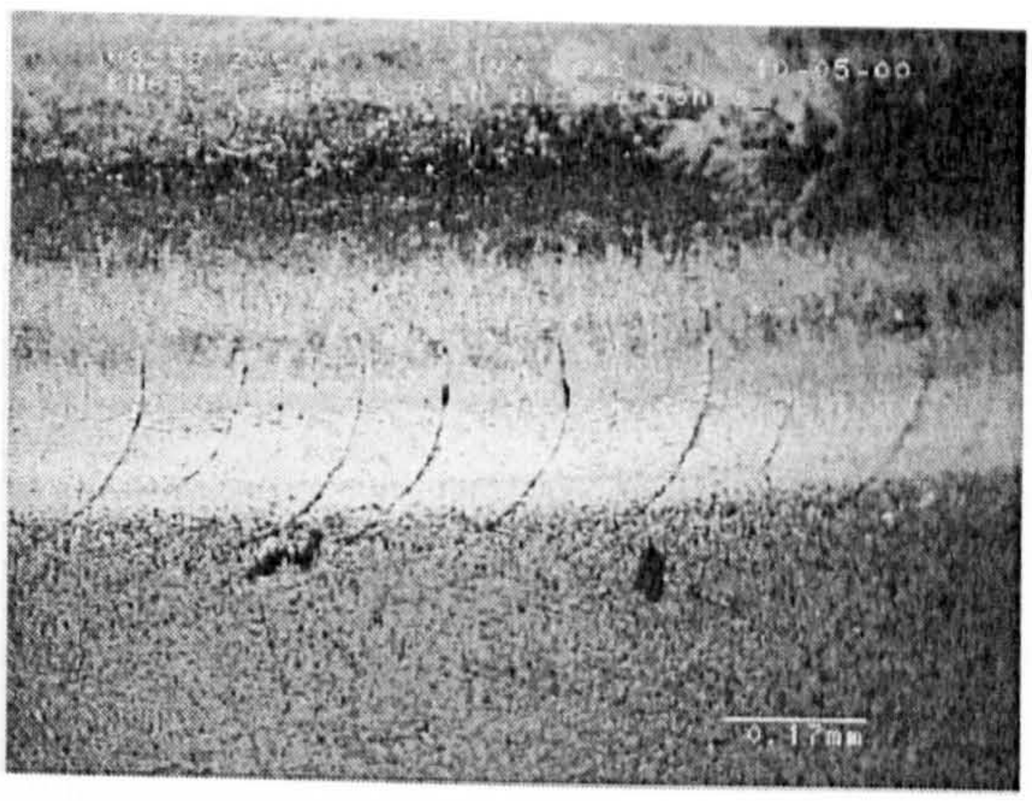

(d)

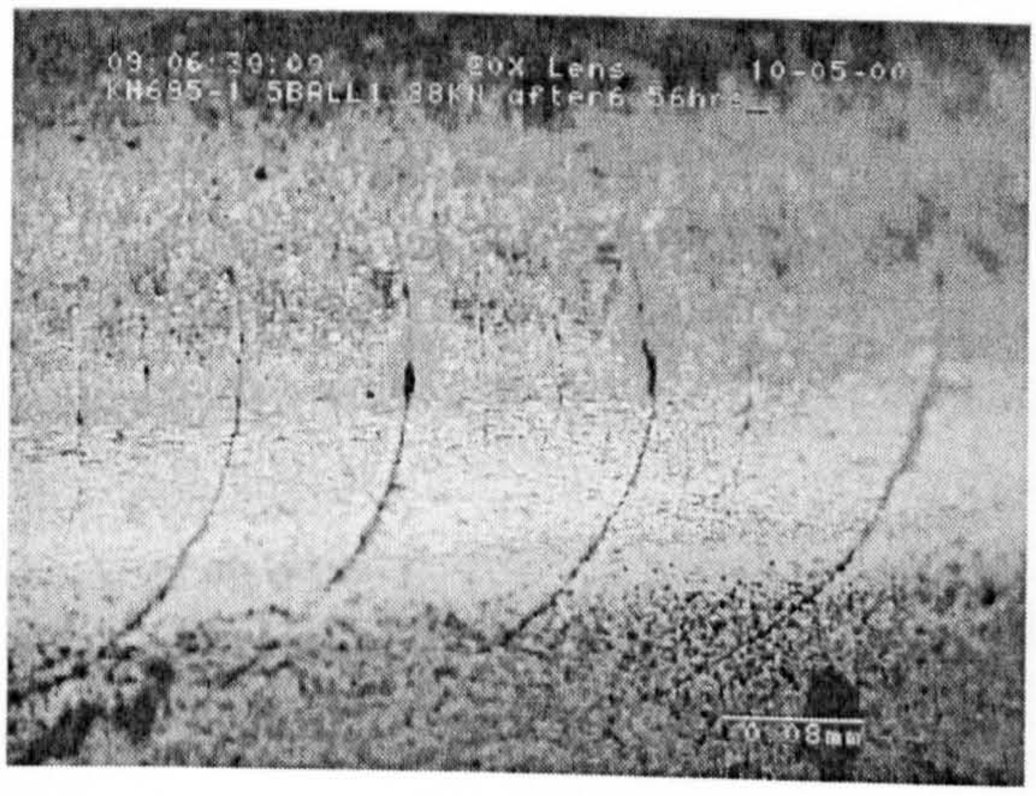

(e)

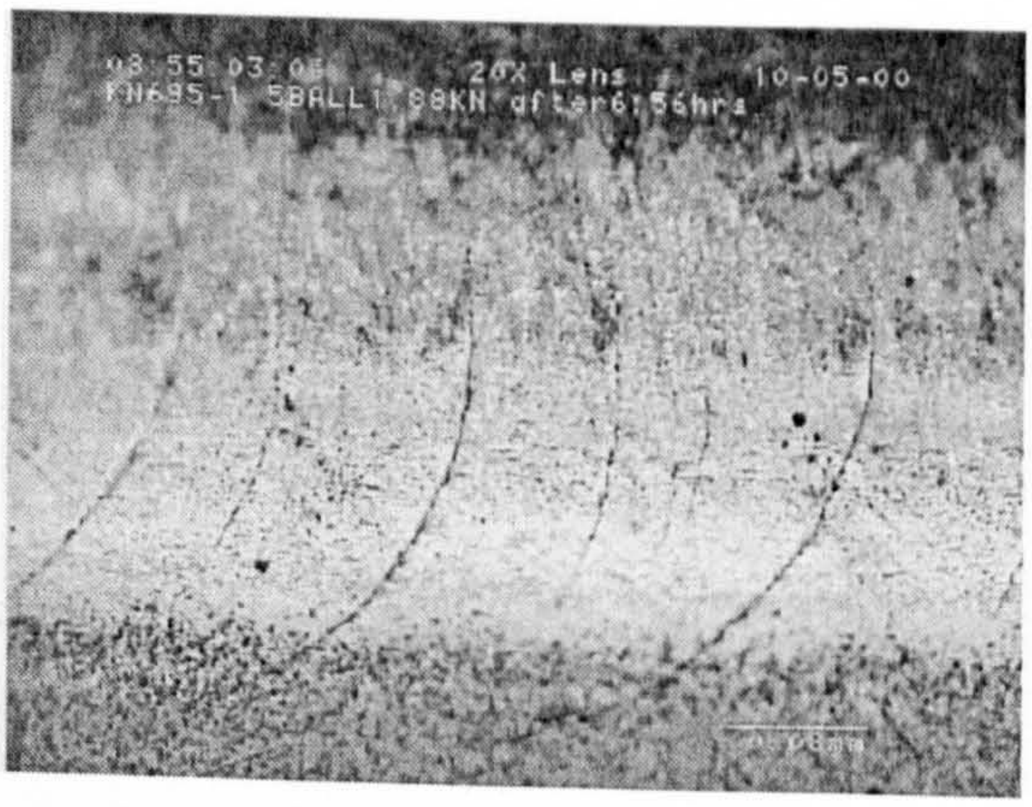

(f)

Fig. 5-35 Traction cracks on No.1 ball after 6 hours and 56 minutes

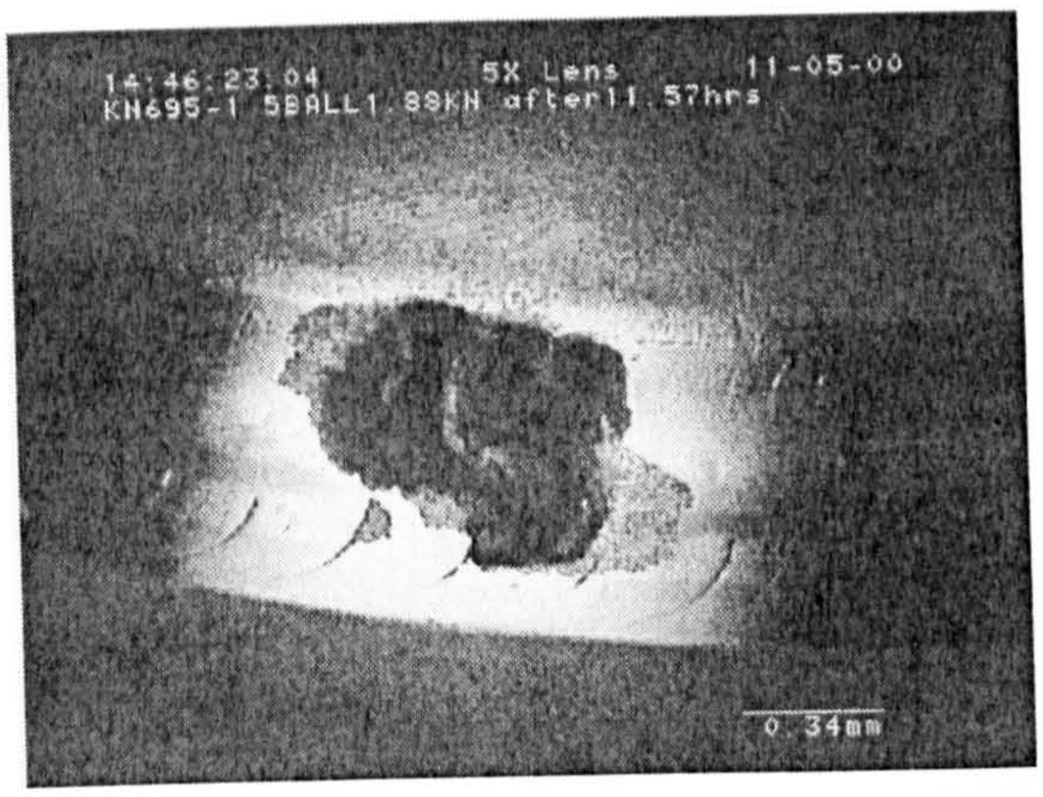

(a)

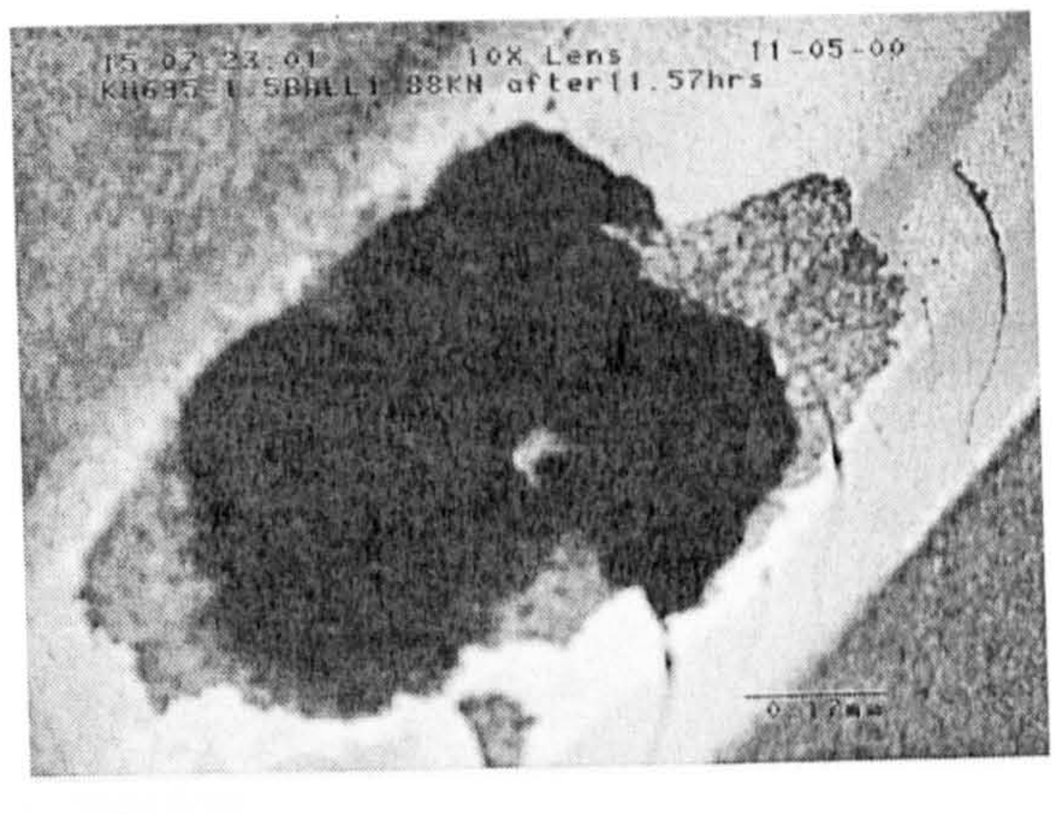

(b)

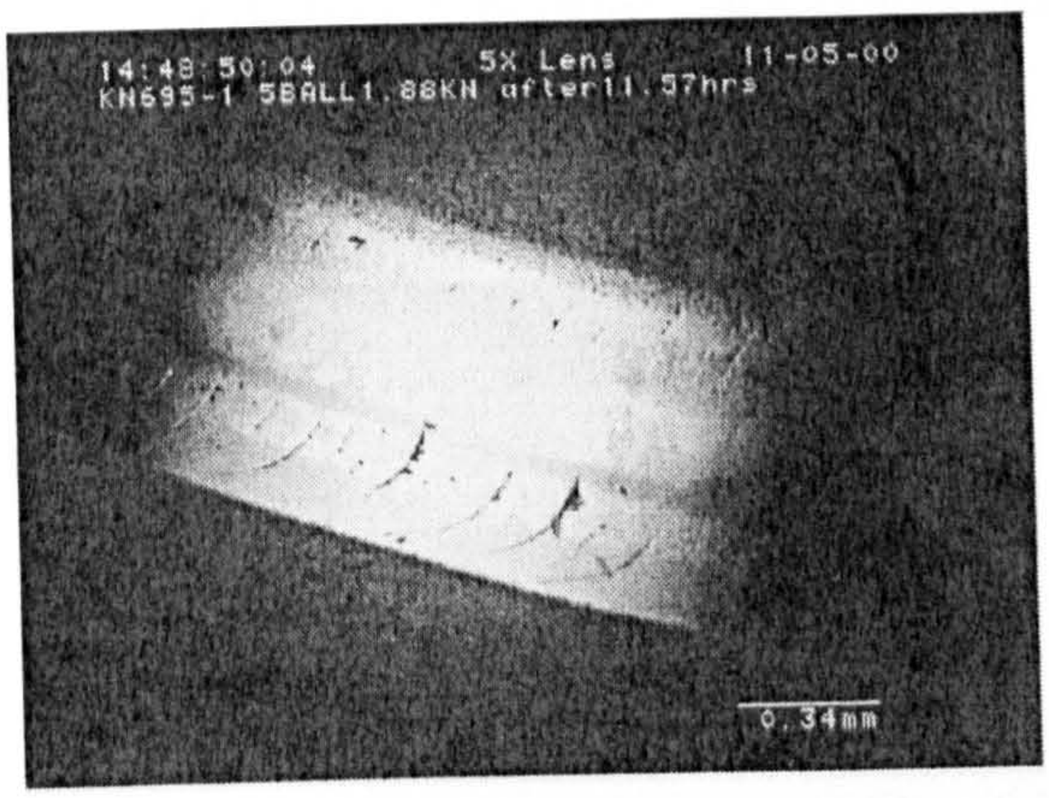

(c)

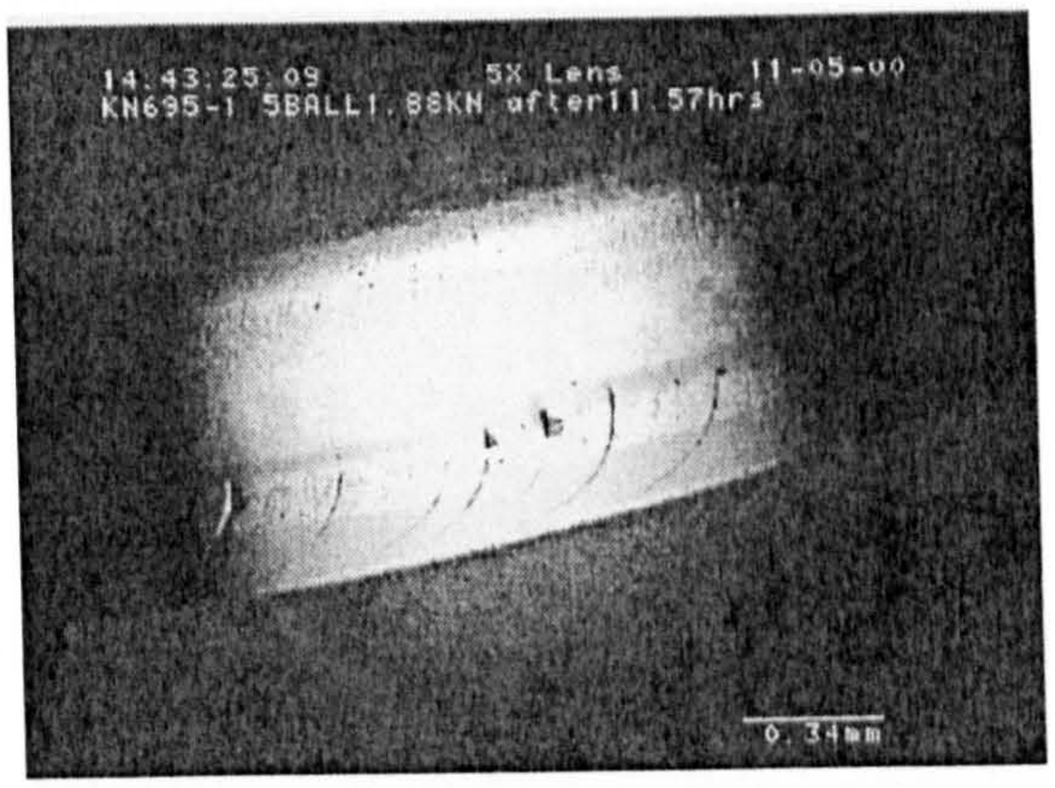

(d)

(e)

(f)

Fig 5-36 No.1 ball after 11 hours and 57 minutes

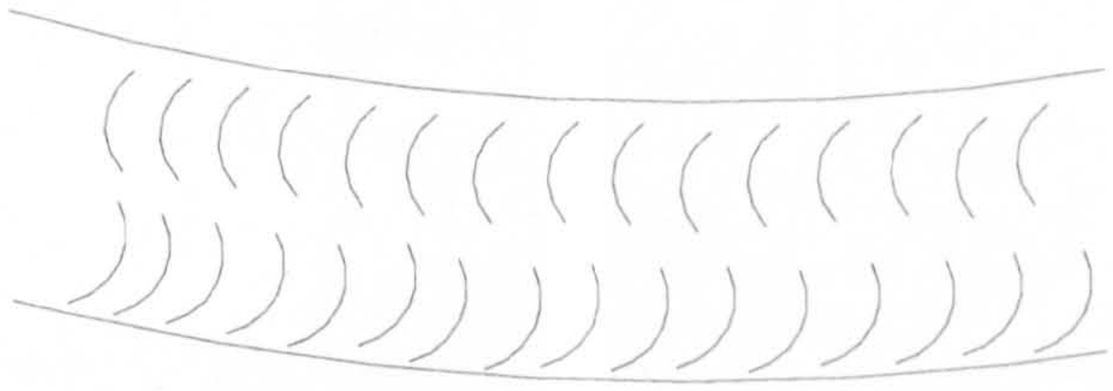

→ rolling direction

Fig 5-37 Opposite crack orientations on two sides of the rolling track

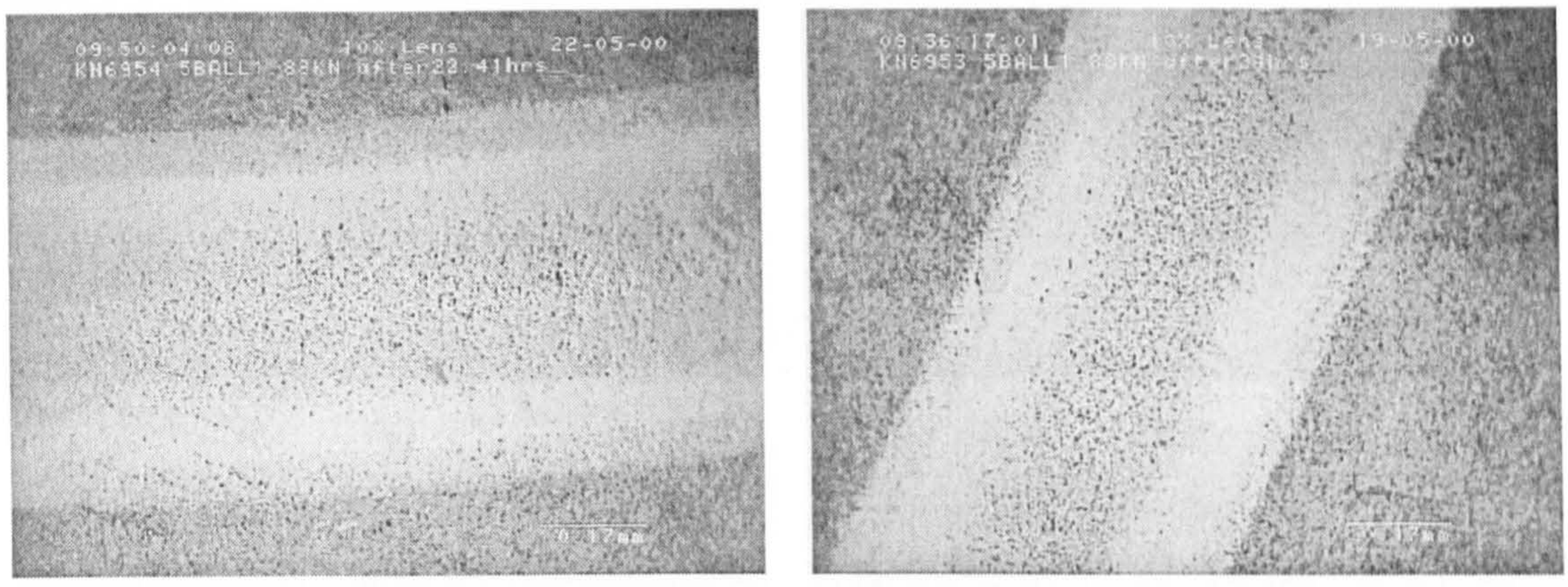

(a) (b)

Fig 5-38 No. 2 ball after 22 hours 41 minutes (a), and No. 3 ball after 24 hours (b)

To see if these traction cracks are inevitable, 5-ball rolling tests were conducted on another two balls (No. 2 and No. 3) from the same batch as sample F. After 22 hours 41 minutes (Fig. 5-38 (a)), and after 24 hours (Fig 5-38 (b)) respectively, no traction cracks occurred on these two balls. The appearance of these two tracks, however, is very different from sample F in Section 5.1 (Fig. 5-1 F), featuring a 0.05~0.1mm smooth zone 0.05mm from the track edge on both sides of the track.

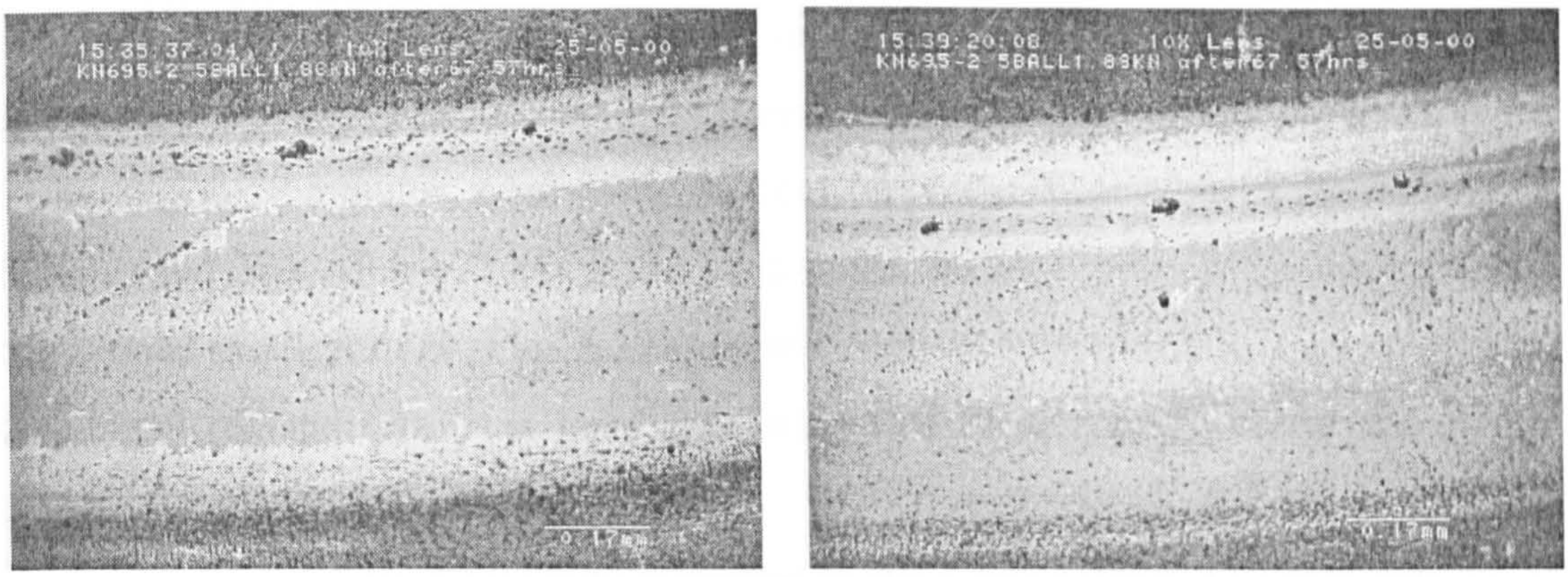

(a) (b)

(c) (d)

(e) (f)

Fig 5-39 No 4 ball, (a) and (b) after 67 hours 57minutes;
(c), (d), (e), (f) after 102 hours 19 minutes

A 5-ball rolling test was conducted on another ball, No. 4 from the same batch as sample F, for 102 hours and 19 minutes. No traction cracks occurred. After 67 hours and 57 minutes, some pittings occurred on the inner edge of the track (Fig. 5-39 (a) and (b)). After 102 hours and 19 minutes, the inner edge of the track showed continuous small pittings (Fig. 5-39 (c)), and some evenly distributed round pittings (Fig. 5-39 (e) and (f)). It is very interesting that these round pittings are almost exactly evenly spaced.

Further experimental study is needed on the 5-ball rolling. The performance of 5-ball rolling test is definitely different from the 4-ball rolling test, which implies that the traction in rolling contact fatigue does play an important part.

5.6 The Change of Residual Stresses Distribution during RCF Test

The residual stress change occuring during the RCF test is of much concern, since this change may be related to the fatigue life and performance. Four kinds of commercially finished balls before and after RCF tests were investigated. The measurement procedure is described in Section 3.7.

Description of the ball before RCF test	Abbreviation in Section 3.1.2	Residual stress value (MPa)
From Manufacturer A1	A	-132.857(±)30.17
From Manufacturer B1	B	-76.742(±)15.56
From Manufacturer C1	C	-81.465(±)34.57
From Manufacturer D1	D	-21.276(±)10.50

Table 5-5 Residual stress measurement results before RCF test

The surface and subsurface residual stress values (from top surface to 30 μm underneath the surface on an average base) for these four kinds of balls before RCF tests are listed in Table 5-5. The characteristics of these balls are listed in Table 3-2, whilst their 3-D topographic details and microscopy images are shown in Fig 3-2 and

Fig 3-3 respectively.. The residual stress values for these balls are all compressive before RCF test ranging from -132.857 MPa to -21.276 MPa.

The surface and subsuface residual stress values (from top surface to 30 μm underneath the surface on an average base) for these four kinds of balls after RCF test were measured at two points on each sample, with one point on the rolling track and another point at the centre of the rolling track circle as shown in Fig 3-8. The measurement results are listed in Table 5-6. Samples A, B, C and D were subjected to RCF tests for over 100 hours. Detailed surface examination after RCF tests is described in Section 5.1. Another two samples, one from the same batch as sample B and one from the same batch as sample C, were subjected to RCF tests for 67 hours and 44 hours in order to see the residual stress change during RCF test.

Description of the ball after RCF test	**Abbreviation in Section 5.1**	**Residual stress value (MPa)**
A1 ball after 134 hours, On the track	A	119.034(±)34.40
A1 ball after 134 hours, At the centre	A	32.106(±)23.94
B1 ball after 100 hours, On the track	B	174.208(±)34.46
B1 ball after 100 hours, At the centre	B	23.674(±)24.94
B1 ball after 67 hours, On the track		-269.925(±)56.01
B1 ball after 67 hours, On the track another measurement		-277.054(±)58.42
B1 ball after 67 hours, At the centre		57.699(±)30.18
C1 ball after 110 hours, On the track	C	133.959(±)37.94
C1 ball after 110 hours, At the centre	C	63.965(±)25.93
C1 ball after 44 hours, On the track		-45.543(±)14.50
C1 ball after 44 hours, At the centre		36.224(±)18.86
D1 ball after 132 hours, On the track	D	110.326(±)38.46
D1 ball after 132 hours, At the centre	D	78.199(±)22.01

Table 5-6 Residual stress measurement results after RCF test

It was found from Table 5-6 that the residual stress at the rolling track will change greatly during the RCF test process. The residual stress at the rolling track for the B1 ball after 67 hours RCF test is -269.925 MPa and after 100 hours RCF test it becomes 174.208 MPa, an absolute value change of nearly 450 MPa. To verify this, another point was measured on the rolling track for the B1 ball after 67 hours RCF

test, and the result was very close (-277.054 MPa). The residual stress at the rolling track for C1 ball after 44 hours RCF test is -45.543 MPa and after 110 hours RCF test it becomes 133.959 MPa.

The assumption here is: during the RCF test, the residual stress on the rolling track will first become compressive, then change to tensile. When the tensile residual stress is high, it is near failure. The time period for this change of residual stress is different for different kinds of HIPed Si_3N_4 rolling elements, depending on the material properties, applied load etc.. If this phenomenon does exist, the residual stress measurement could be used to predict the failure.

Another finding from the measurement results is that the residual stress change zone during RCF test is far beyond the rolling track. It was anticipated in Section 3.7 that the point at the centre of the rolling track circle (Fig 3-8 (b)) had endured least stress during RCF test. This point is 4 mm away from the rolling track. After RCF tests, the residual stress values at this point in all of the six samples have become tensile, and the absolute residual stress value change is around 100 MPa for each sample no matter whether the RCF test is 44 hour or over 100 hours. It is likely that during RCF test, the rolling track surface and subsurface become compressive thus causing nearby tensile residual stress. The residual stress on the rolling track will change greatly during RCF test. In contrast, the residual stress at the nearby area will probably not change very much: for the B1 ball from 57.699 MPa at 67 hours to 23.674 MPa at 100 hours and for the C1 ball from 36.224 MPa at 44 hours to 63.965 MPa at 110 hours, as shown in Table 5-6.

In order to prove the first assumption, more residual stress measurements on a single ball at regular intervals during RCF test are needed to trace the residual stress change.

6.0 CONCLUDING REMARKS, CONCLUSIONS AND FUTURE WORK

6.1 Concluding Remarks

As illustrated in Fig 1-6, The scope of this PhD thesis is to investigate experimentally the relationships between finishing parameters and surface quality, between surface quality and RCF performance, between finishing parameters and RCF performance.

In order to investigate the finishing process, a novel eccentric lapping machine was designed and manufactured to serve as a test bench. A finishing rate of 68 μm/hour was achieved which is 15 times higher than the conventional concentric lapping (normally 3~4μm/hour). The polished ball surface roughness value R_a was 0.003 μm and ball roundness was 0.08~0.09μm which were above grade 5, close to grade 3 precision bearing ball specification. The kinematics of eccentric lapping has been analysed. Equations have been derived for ball spin angular speed ω_b, ball spin angle β and ball circulation angular speed ω_c at different contact points on the V-groove as functions of eccentricity E, V-groove half-angle θ, circular V-groove radius R_g and lapping speed Ω_p. This eccentric lapping machine can be further developed for industrial application and the kinematics analysis can be used as guidelines to design large-scale eccentric lapping machine.

The finishing process of HIPed Si_3N_4 rolling elements can be divided into two steps: first step lapping and second step polishing. Experiment results showed that it is feasible to accelerate the finishing process without affecting the surface quality. The maximum material removal rate can be achieved under the average lapping load to 43 N/ball, lapping speed 169~270 rpm (linear speed at ball/V-groove contact

points 0.7 m/s ~ 1.1 m/s), diamond particle size 45μm ~60 μm and diamond paste concentration 1g:30ml. In the first step of finishing, the upper limits for lapping load and lapping speed are 43 N/ball and 270 rpm. Excessive high lapping load and speed will cause surface damage. Also the diamond particle size should be gradually reduced in the first step of finishing when nearly reaching the final dimension in order to avoid leaving scratch marks on the surface. The surface roughness and roundness specification of HIPed Si_3N_4 rolling elements can be achieved in the polishing stage. In this stage, the speed should be under 94 rpm (linear speed 0.4 m/s) to avoid possible C-crack formation.

Rolling contact fatigue tests were concentrated on ceramic/steel contact at a load of 6.58 GPa, and at a speed of 10,000rpm using Shell Talpa 20 oil as lubricant under 4-ball rolling configuration. The relationship between surface quality and rolling contact fatigue performance was explored by 4-ball RCF tests on commercially finished and self finished HIPed silicon nitride balls with different surface roughness values; on commercially-finished balls with heterogeneous porosity and star defects; on self-finished balls with C-crack defects and on balls with grinding defects introduced by an aggressive grinding process. The effects of the finishing rate on rolling contact fatigue life were assessed by RCF tests on self-finished balls under different loads and speeds.

Experimental results showed that different surface roughness value R_a on HIPed Si_3N_4 rolling elements did not cause surface spall failure under accelerated 4-ball rolling test for over 135 million stress cycles. With a surface roughness value R_a from 0.016 to 0.094 μm, it is more likely for the surface to become smoother due to polishing wear, and surface pitting in the sizes between 10~20 μm may occur. With a surface roughness value R_a from 0.002 to 0.008 μm, it is more likely for the surface to become rougher, lubricant oil may be deposited at the edges of the rolling track, small and shallow surface pitting in the size of about 2μm may occur. Scratch marks left on surface by previous lapping processes can be further extended during RCF, although no failure caused by this has yet been observed. R_a and R_q (RMS, rms) are still the most important roughness parameters in relation to RCF life. The effects of other surface roughness parameters, like the shape of the valley, R_{sk} and R_{ku} are not

obvious. In contrast, surface defects are potentials for fatigue failure. Severe fatigue wear will occur on the heterogeneous porosity surface if the diameter of the pore in excess of 4 μm although it performed slightly better under high viscosity lubricant. Different surface or subsurface crack type defects could cause fatigue spall failure.

In view of the relationship between finishing process and the RCF life and performance of HIPed Si_3N_4 rolling elements, experiment results showed that the most influential parameter was lapping load. Extreme high lapping load can cause surface spall and surface or subsurface cracks, which could lead to fatigue failure. Even on the surface without detectable spall or cracks, the fatigue life could be much shortened.

The second influential finishing parameter in relation to RCF life is the final finishing speed. Surface C-cracks seem to be related to the final finishing speed: under a certain speed range C-cracks are more likely to be formed, although more theoretical and experimental studies are needed to confirm this. Each C-crack could be a potential for a fatigue spall failure. The previous lapping speed in the finishing process is less relevant in relation to RCF life, apart from the fact that extreme high speed could cause various sizes of surface spall.

Large diamond particles could leave scratch marks on the ball surface which could be difficult to remove during polishing. But no fatigue failure caused by scratch marks has yet been observed. The paste concentration parameter also has less effect on RCF life.

Residual stress induced by the finishing process is within 130 MPa even under high lapping load. It will not affect the contact stress distribution greatly during RCF test according to FEA modelling.

6.2 Conclusions

(1) A novel eccentric lapping machine designed by the author is very promising in finishing HIPed silicon nitride bearing balls.

(2) The lapping load is the most influential parameter to the finishing rate in this eccentric lapping machine. The finishing rate is almost proportional to the lapping load when the lapping load is under 4.37 kgf/ball. The maximum finishing rate is achieved at lapping load 4.37 kgf/ball with no substantial surface or subsurface damage or residual stress change, and still maintaining satisfactory RCF performance. When the lapping load is higher than 4.37kg/ball, the finishing rate starts to drop. Poor ball roundness, surface and subsurface damage occur.

(3) Increasing the lapping speed to 270 rpm or 500 rpm will not increase the finishing rate in this eccentric lapping machine. Surface spalls in various sizes were found on the balls lapped at 500 rpm. No substantial surface or subsurface damage was found apart from C-cracks under the speed of 270 rpm, and the C-cracks seem to be related to the final finishing speed.

(4) The previous manufacturing processes left a high compressive residual stress on the surface and subsurface of HIPed Si_3N_4 ball blanks. This high compressive residual stress layer is mostly removed during the finishing process. The finishing process itself is unlikely to introduce high residual stress.

(5) Different surface roughness value on HIPed Si_3N_4 rolling elements will not cause surface fatigue spall failure.

(6) The influence of surface heterogeneous porosity in HIPed Si_3N_4 rolling elements on RCF life is dependent on the diameter of the pore. If the diameter of the pore is 2 μm or under, it will not affect the RCF performance, but if the diameter of the pore is 4 μm or above, severe wear will occur.

(7) The surface and subsurface crack type defects (star defects, grinding defects and C-crack defects) on HIPed Si_3N_4 rolling elements could cause surface spall failure in RCF test, and the failure time may be related to the depth of the initial crack.

(8) The rolling track appearance and RCF performance of HIPed Si_3N_4 rolling elements under 5-ball rolling test are different from that under 4-ball rolling test.

6.3 Future Work

A theoretical model on the mechanics of eccentric lapping which involves both kinematics and dynamics, including lapping pressure, friction force, centrifugal force, lapping fluid drag force, etc., making use of the existing three-body abrasion lapping model on a flat surface, is needed.

The grain morphology study in the near surface region is needed in the future in order to quantify the near surface dislocation and microcracking in relation to lapping parameters. This information is useful in determining the thickness of the layer to be removed in the polishing stage. To fulfil this, balls under different lapping parameters need to be sectioned and then etched.

Quantitative analysis on the surface crack type defects formation and propagation under RCF is needed. Although this is a huge task it is valuable because this is the only defect that could be introduced in the finishing process and proved to be detrimental in RCF life. To fulfil this, more balls under different finishing parameters and more balls with different surface crack defects at different RCF test stages need to be sectioned and then dye- penetrant treated to observe the crack under UV light microscope. This investigation should be based on fairly large number of samples and statistic analysis should be conducted in order to draw any conclusions.

Both theoretical and experimental studies are needed to distinguish the traction effect between 5-ball rolling test and 4-ball rolling test. The experimental study can be accomplished by design a rig to measure the frictional torque on the 4-ball and 5-ball cup, and then compare the differences. The theoretical study can be achieved by comparing the difference of friction involved in 4-ball rolling and 5-ball rolling (refer to Section 5.5).

The residual stress change during RCF test is of great interest. To verify the assumption proposed in Section 5.6, more experiments on residual stress measurement at regular intervals during RCF test are needed to monitor the residual stress change.

APPENDICES

Appendix 1

TECHNICAL DRAWINGS FOR ECCENTRIC LAPPING MACHINE

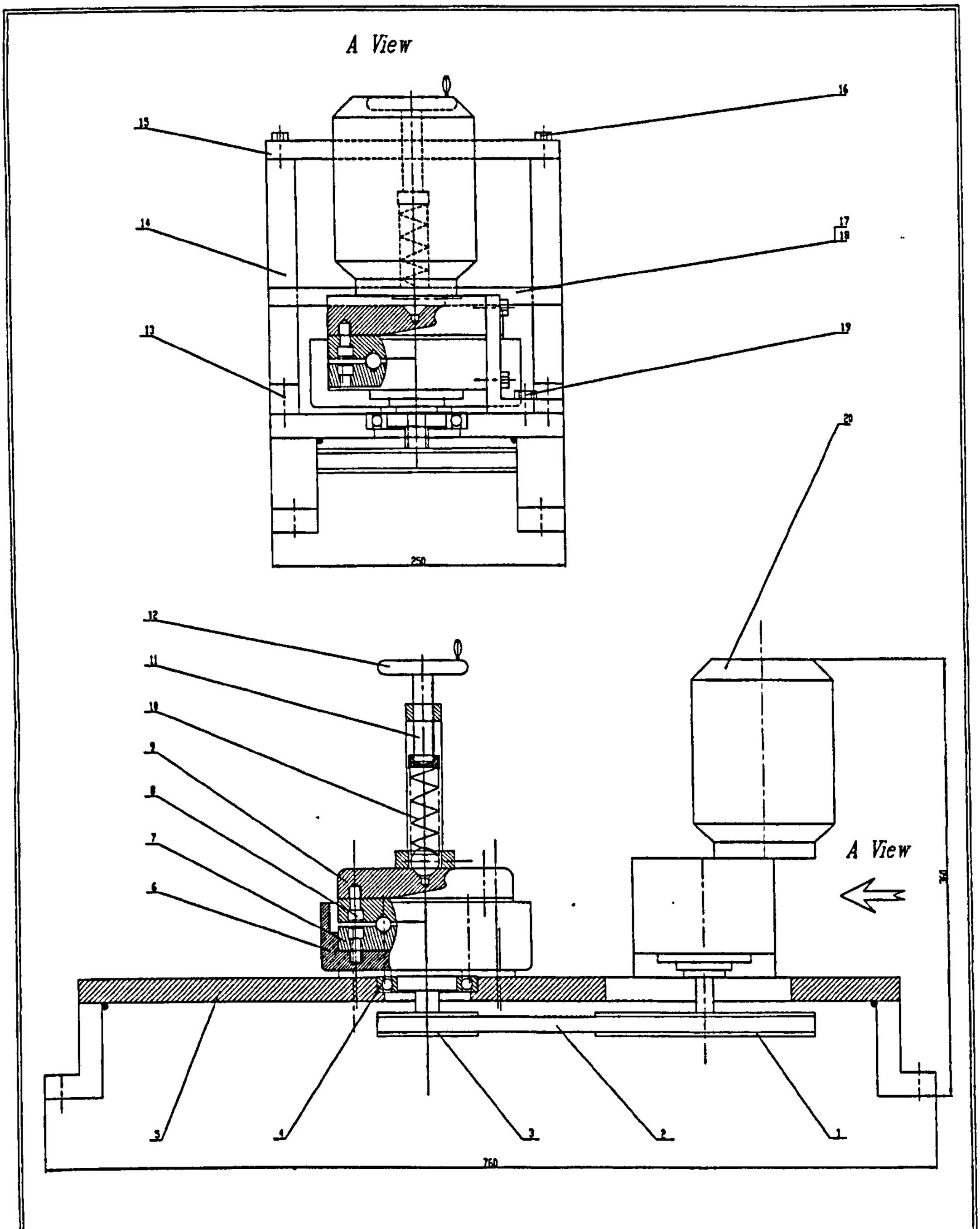

NOTE

1. *Unspecified Dia, tolerance and surface roughness of parts can be decided by manufacturer provided that the final assembly accuracy be insured.*
2. *Unspecified fillet/chamfer is 3 mm.*
3. *Taper pins will be applied to fix the locations of two V-Groove Plates, Bracket and Frame after all bolts be fastened.*
4. *To check the accuracy of assembly, put dial indicator on the Ram, plunger pointed to two v-groove surfaces, rotate the Lower Plate, the readings should be within 0.02 mm.*
   Put dial indicator on top of Lower Plate, plunger pointed to Spring Assembly, rotate the Lower plate, the readings should be within 0.2 mm.

NO.	DESCRIPTION	QTY. TOL.	DWG. No.	NO.	DESCRIPTION	QTY. TOL.	DWG. No.	NO.	DESCRIPTION	QTY. TOL.	DWG. No.	NO.	DESCRIPTION	QTY. TOL.	DWG. No.	NO.	DESCRIPTION	QTY. TOL.	DWG. No.	TITLE: Grinding Machine General Assembly	
17	HP BAR	1	88007	13	M8 SOCKET HEAD BOLT	4		9	UPPER PLATE	1	88002	5	BASE	1	88006	1	PULLEY M8 & BUSH	1			
16	OIL PIN	2		14	BRACKET	2	88008	10	SPRING ASSEMBLY	1	88003	6	LOWER PLATE	1	88004	2	V BELT A800	1		DRAWN BY: X. XIANG	DRG NO. 1
15	M10 HEX BOLT & NUT	2		15	FRAME	1	88005	11	SCREW BAR	1	88007	7	V-GROOVE PLATE	2	88001	3	PULLEY M8 & BUSH	1		DATE: May 28, 98	SCALE
20	STAR 1/4 MOTOR	1		16	M8 HEX HEAD BOLT	8		12	HAND WHEEL	1		8	M8 SOCKET HEAD BOLT	8		4	BEARING 7200B	1		MEASUREMENT IN MM	DWG No. 88001

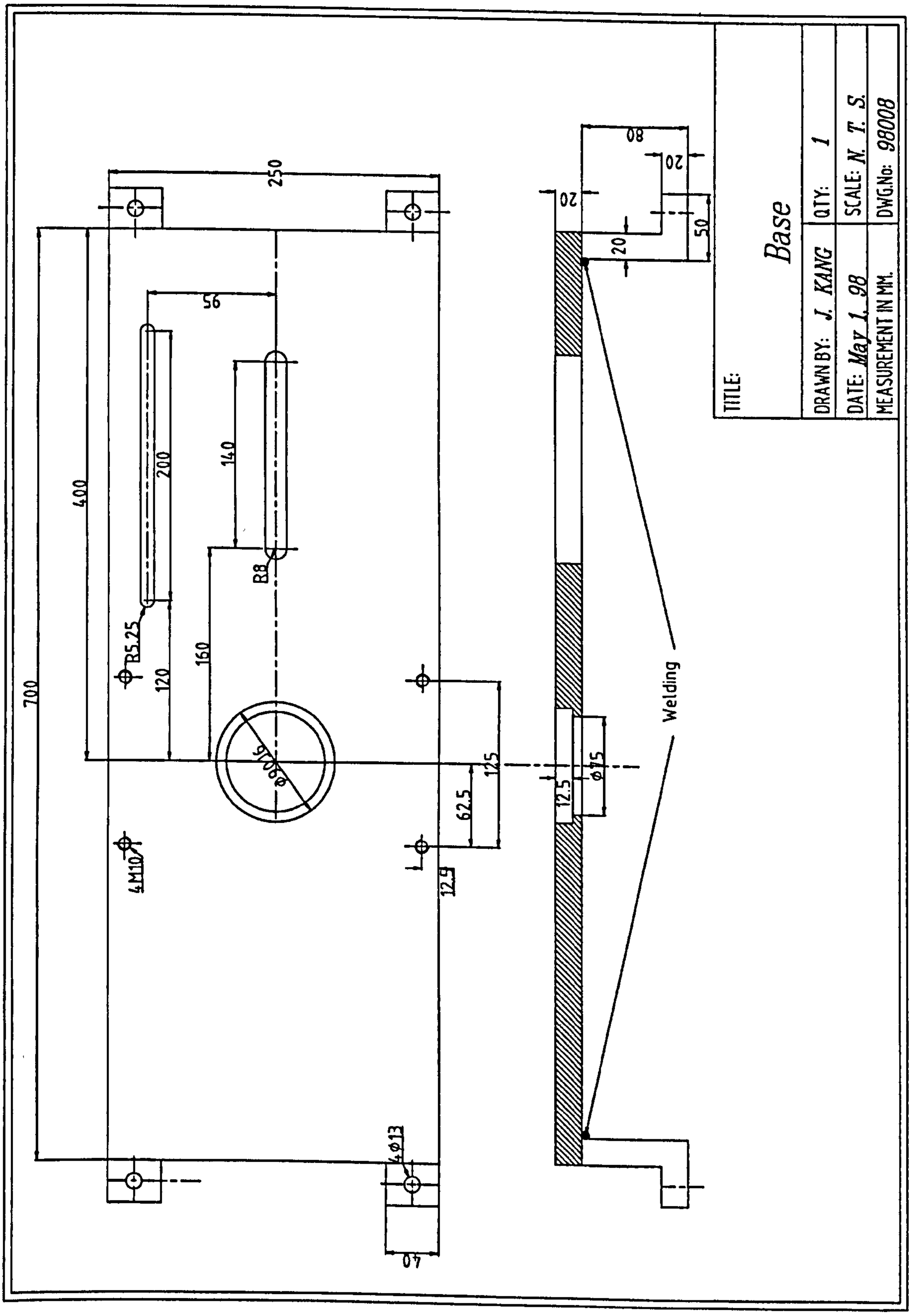
250
56
400
200
140
R8
R5.25
120
160
700
Ø100
4M10
12.5
62.5
125
4-Ø13
40
Ø8
20
20
20
50
Welding
Ø15
12.5
TITLE:
Base
DRAWN BY: J. KANG
QTY: 1
DATE: May 1 98
SCALE: N. T. S.
MEASUREMENT IN MM.
DWG.No: 98008

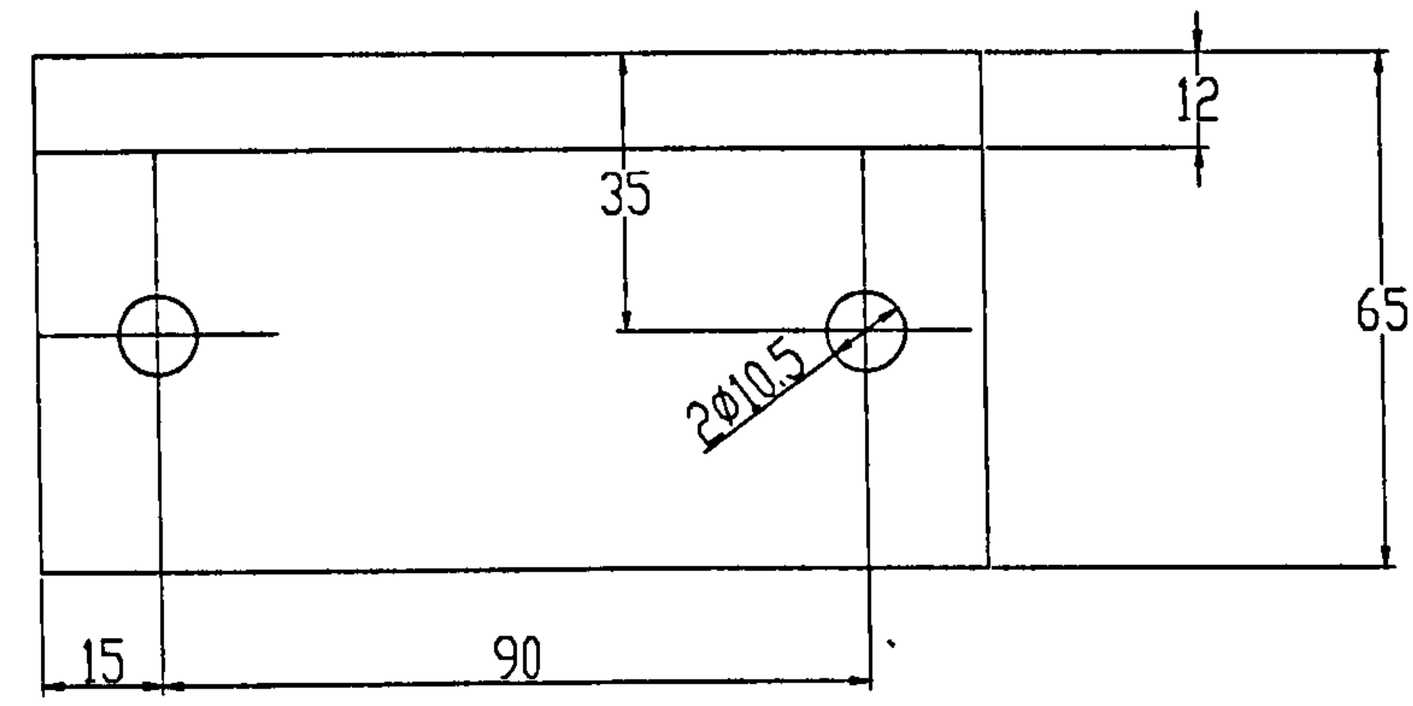

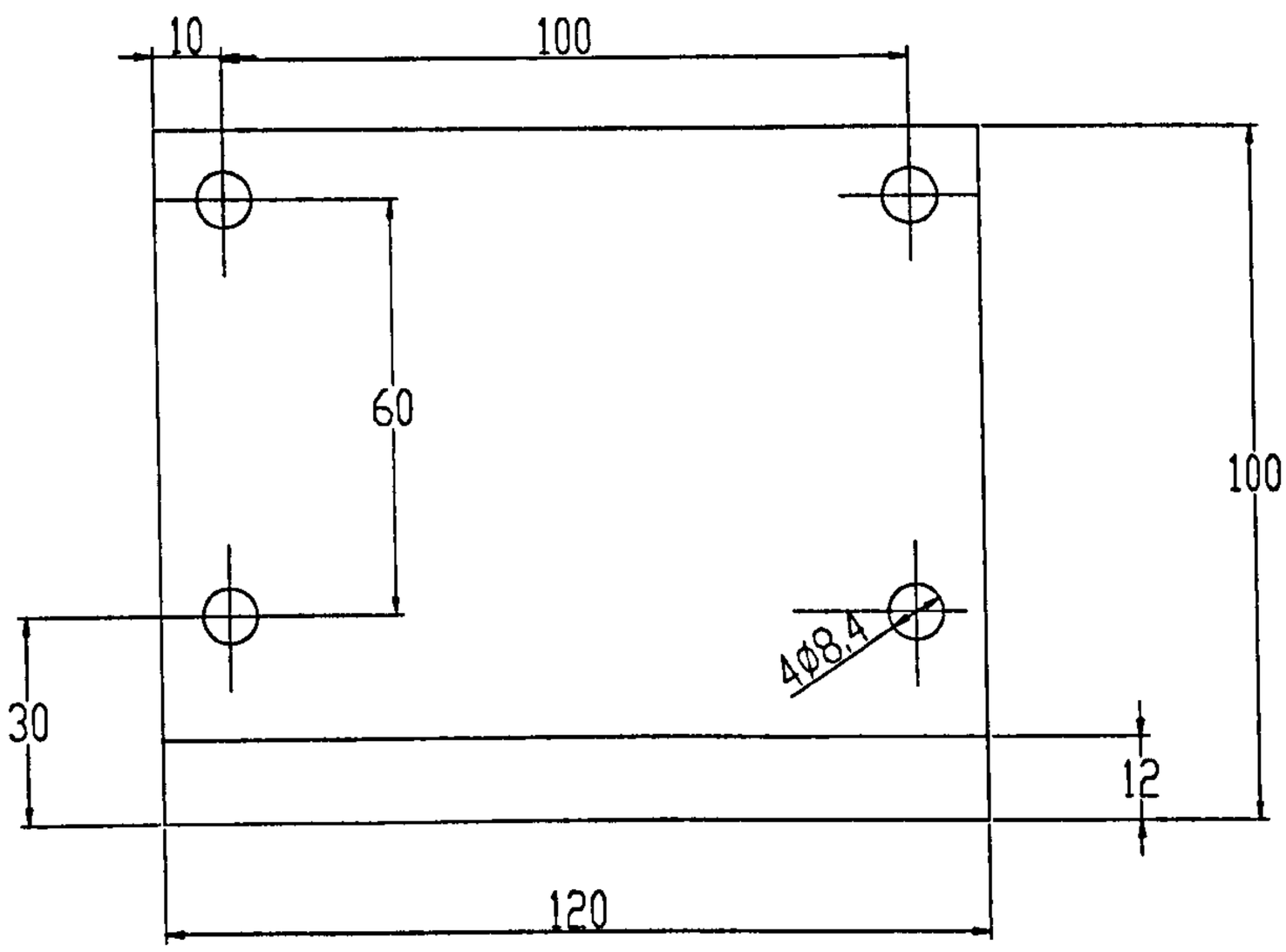

TITLE: *Supporting*	
DRAWN BY: *J. KANG*	QTY: *1*
DATE: *May 1, 98*	SCALE: *N. T. S.*
MEASUREMENT IN MM.	DWG.No: *98009*

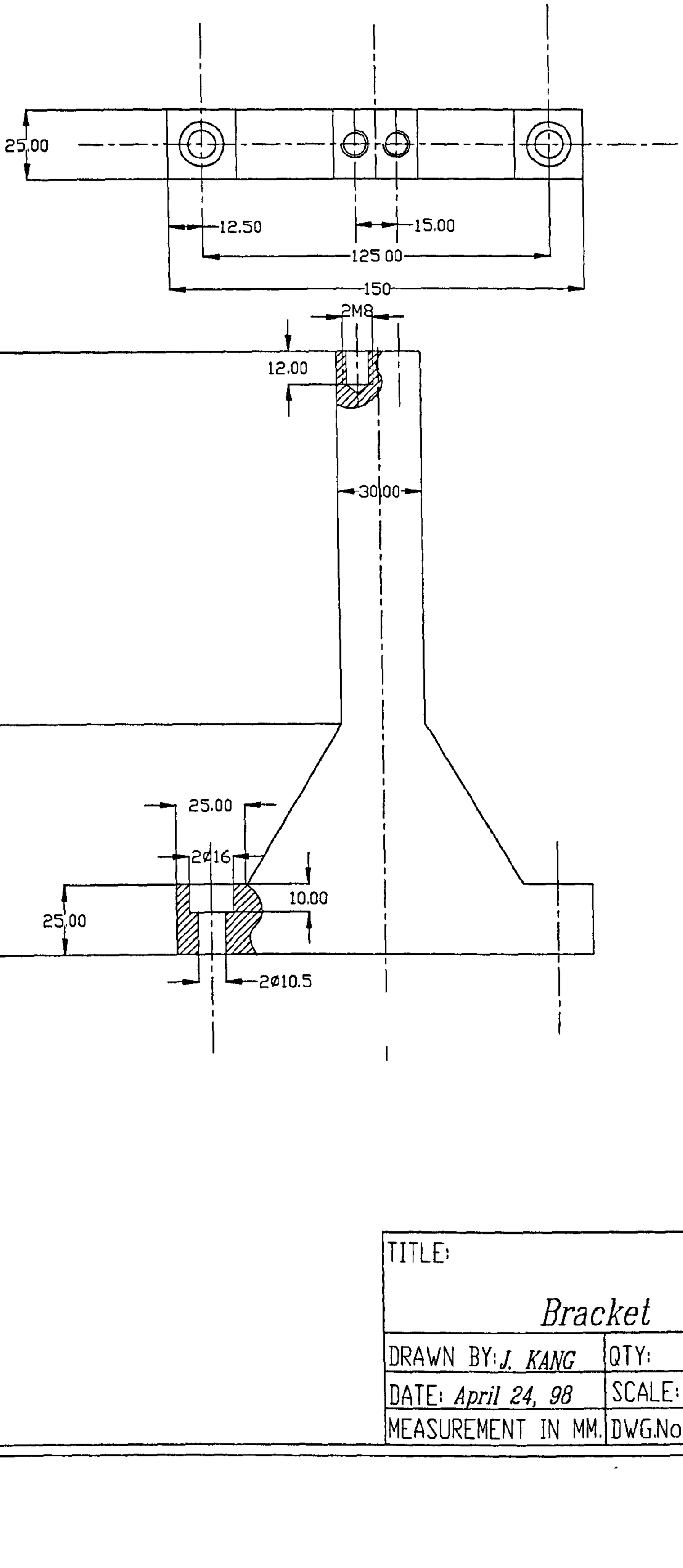

TITLE: *Bracket*	
DRAWN BY: *J. KANG*	QTY: *2*
DATE: *April 24, 98*	SCALE: *N. T. S.*
MEASUREMENT IN MM.	DWG.No: *98005*

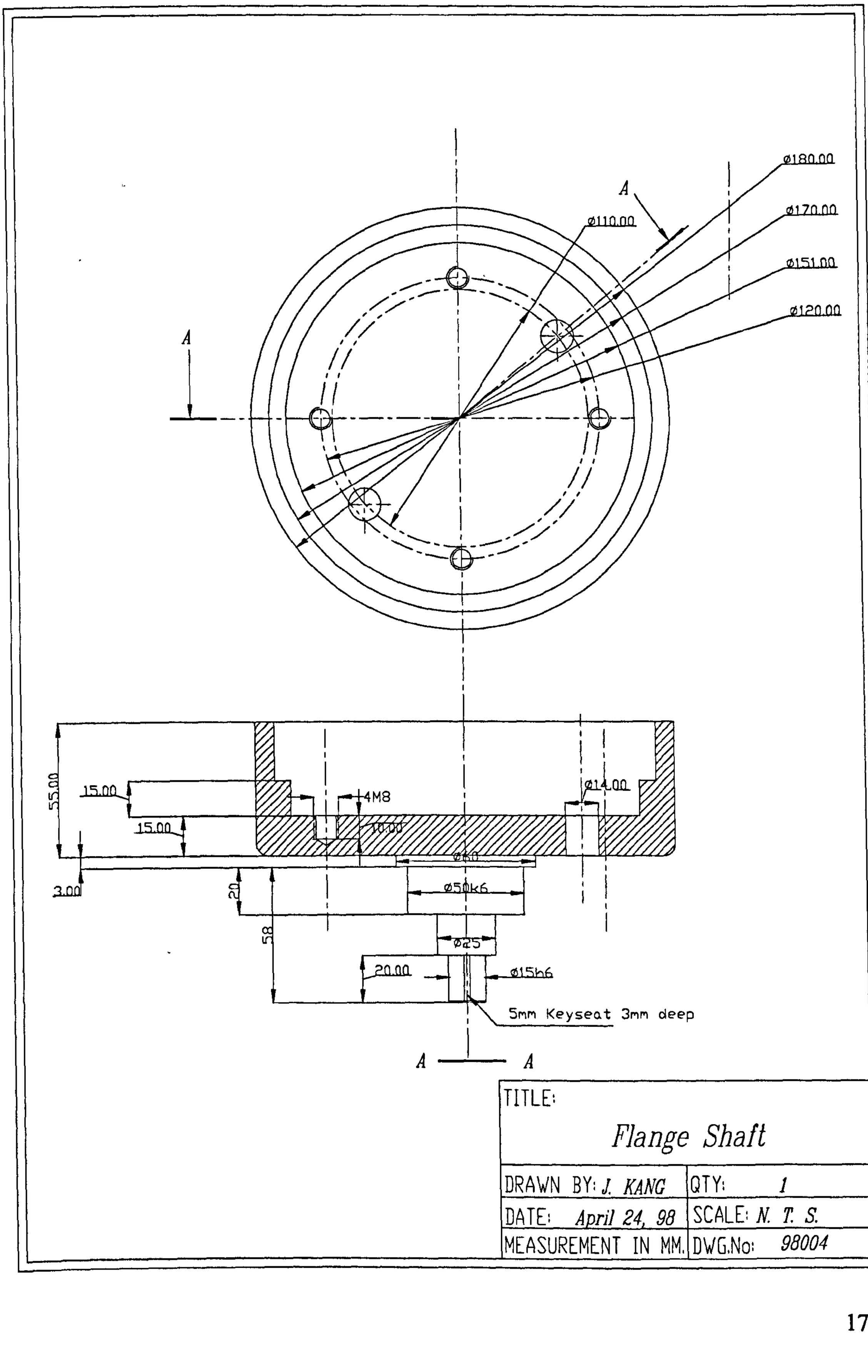

TITLE: *Flange Shaft*	
DRAWN BY: *J. KANG*	QTY: *1*
DATE: *April 24, 98*	SCALE: *N. T. S.*
MEASUREMENT IN MM.	DWG.No: *98004*

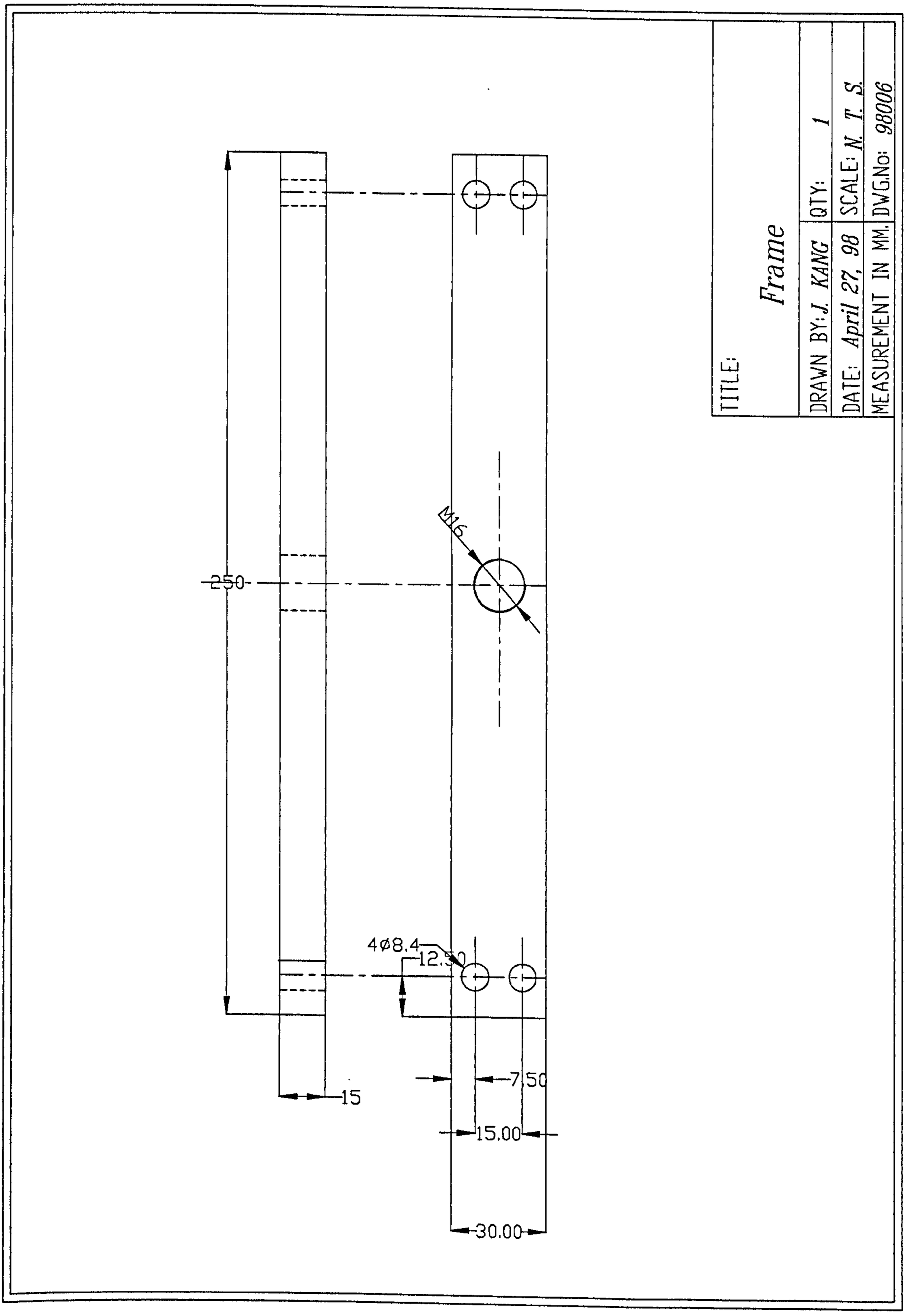
250
M16
4ø8.4
12.50
15
7.50
15.00
30.00
TITLE:
Frame
QTY: 1
SCALE: N. T. S.
DWG.No: 98006
DRAWN BY: J. KANG
DATE: April 27, 98
MEASUREMENT IN MM.

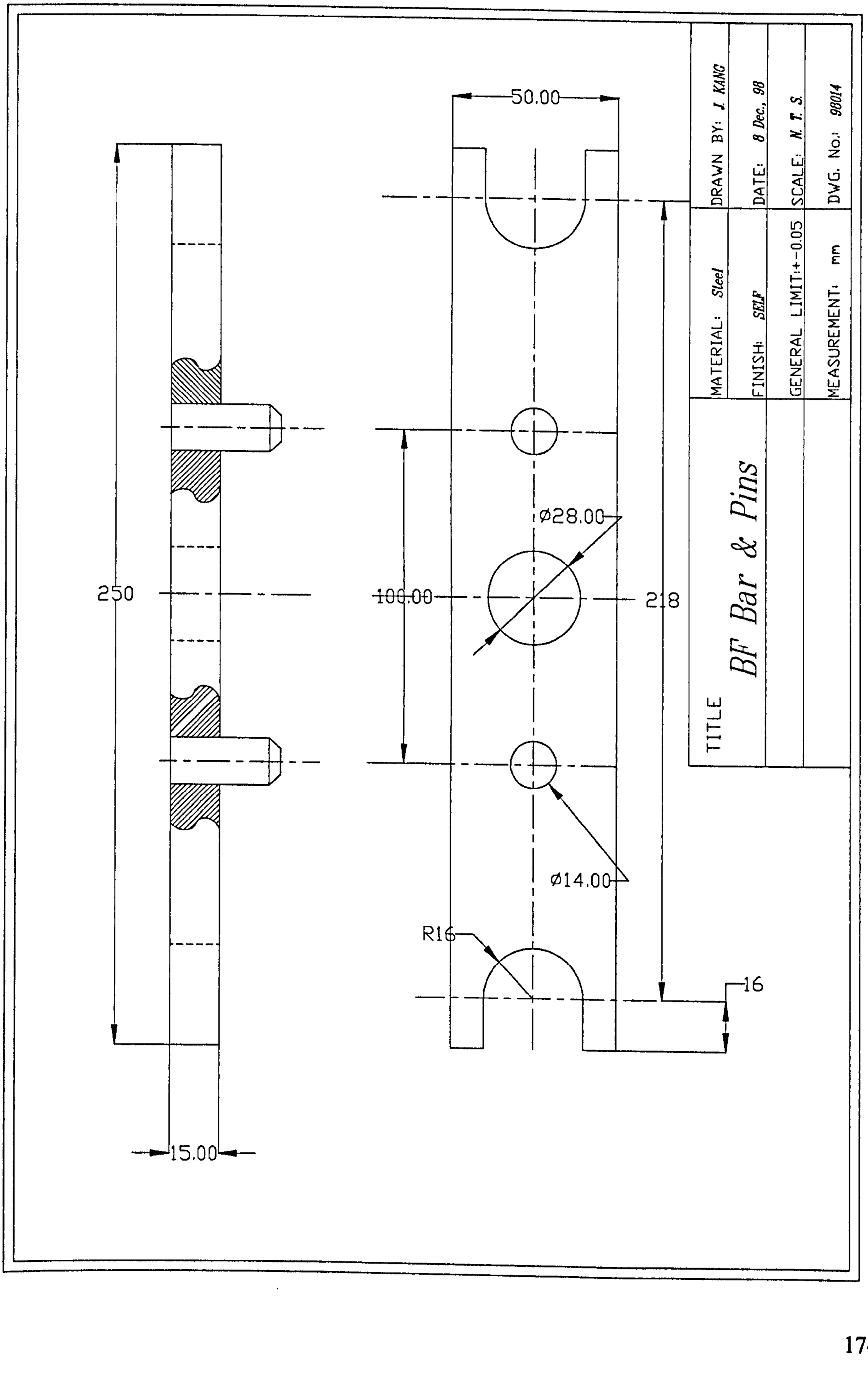
50.00
250
100.00
218
Ø28.00
Ø14.00
R16
16
15.00
DRAWN BY: J. KANG
DATE: 8 Dec., 98
SCALE: N. T. S.
DWG. No.: 98014
MATERIAL: Steel
FINISH: SELF
GENERAL LIMIT:+-0.05
MEASUREMENT: mm
TITLE
BF Bar & Pins

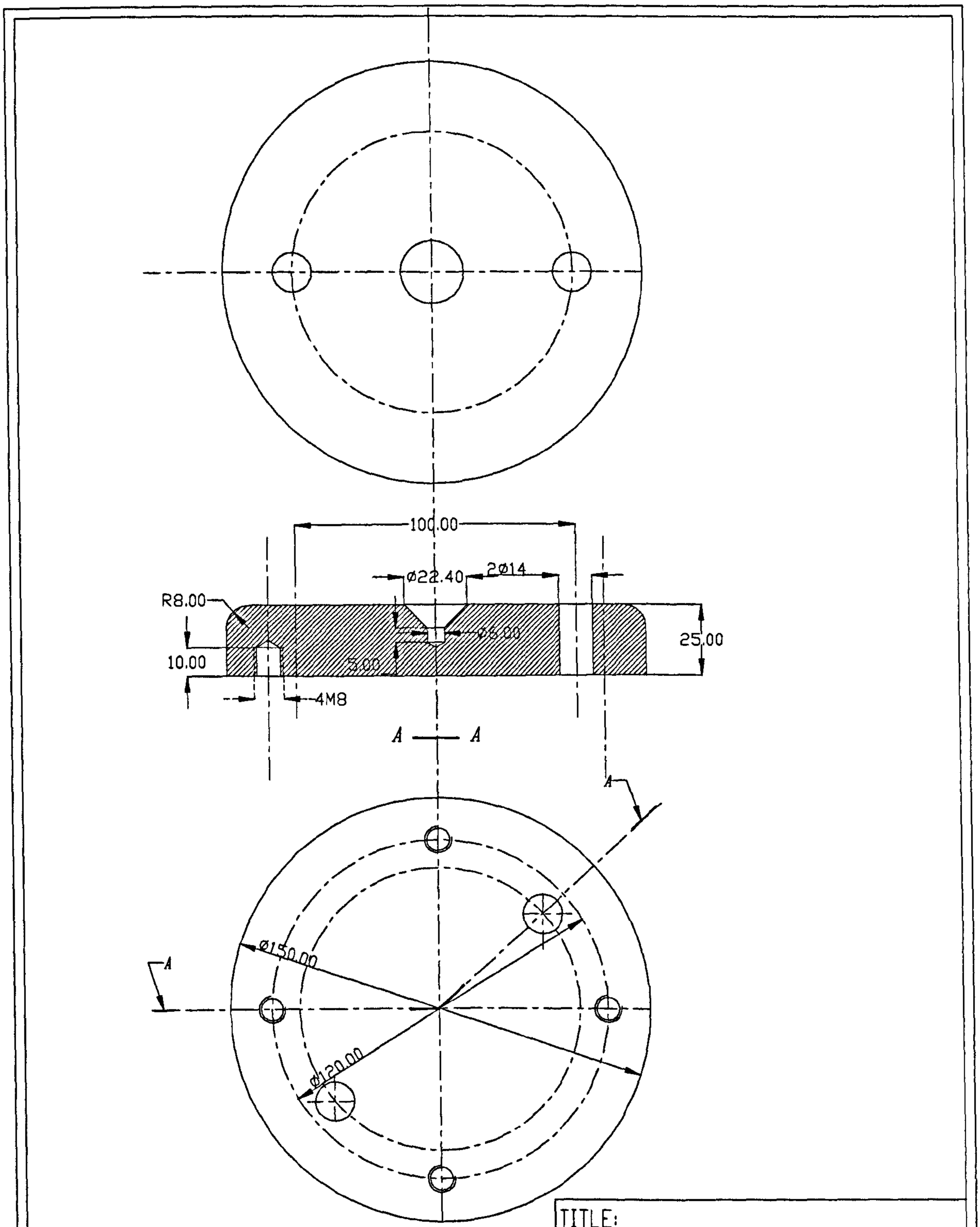

TITLE: *Backing Plate*	
DRAWN BY: *J. KANG*	QTY: *1*
DATE: *April 23, 98*	SCALE: *N. T. S.*
MEASUREMENT IN MM.	DWG.No: *98002*

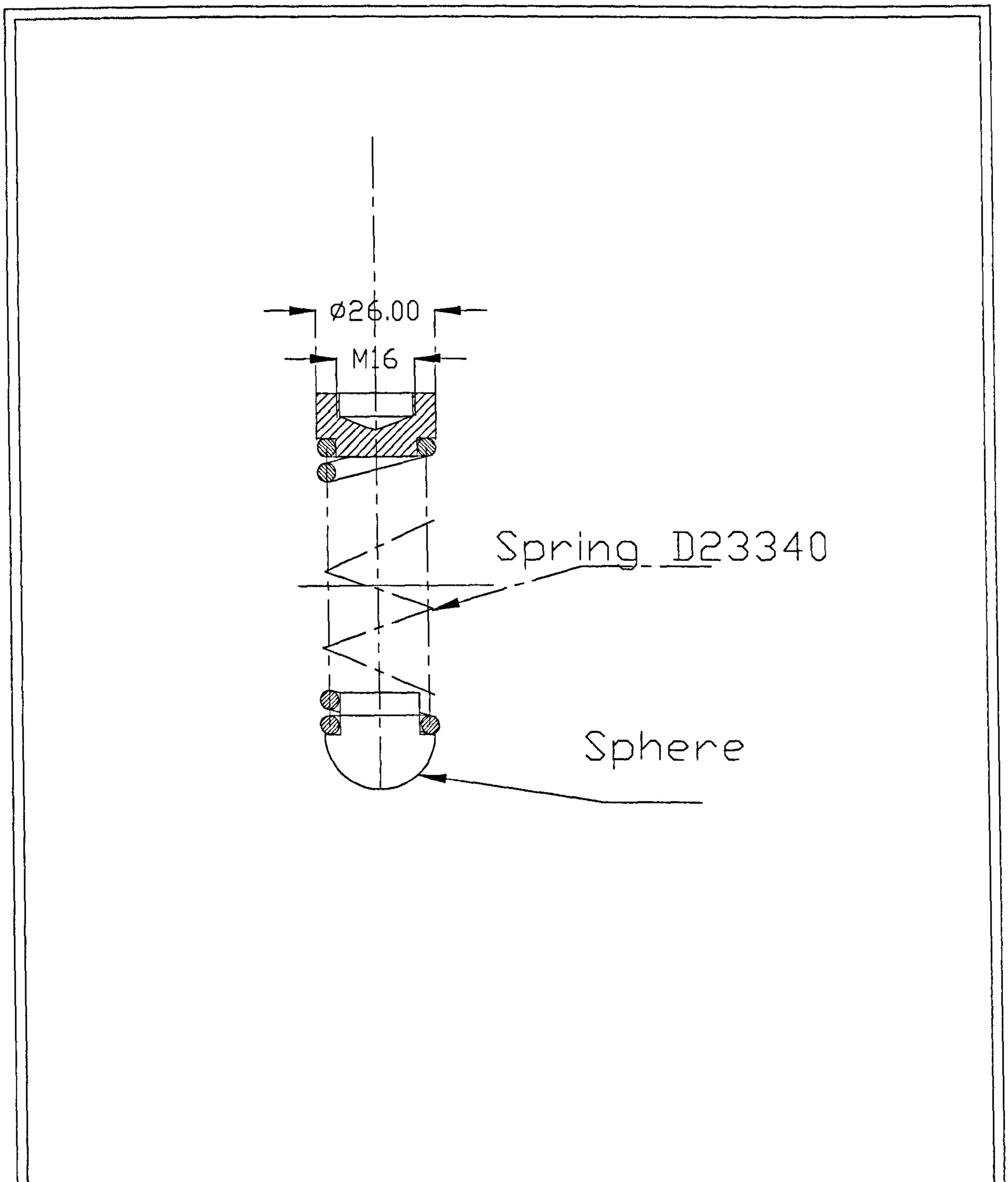
ø26.00
M16
Spring D23340
Sphere
TITLE:
Spring Assembly
DRAWN BY: J. KANG
QTY: 1
DATE: April 24, 98
SCALE: N.T.S.
MEASUREMENT IN MM.
DWG.No: 98003

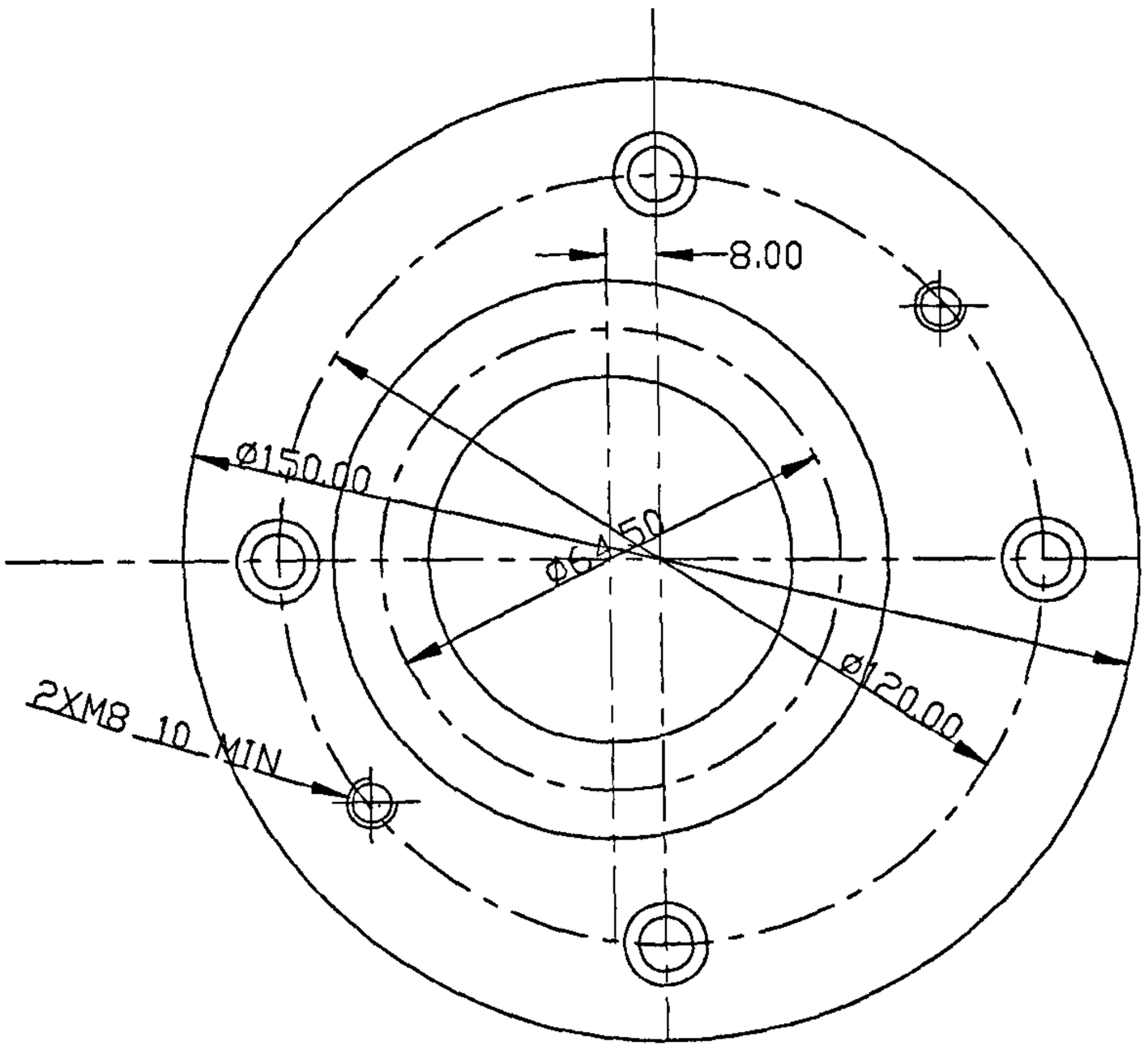

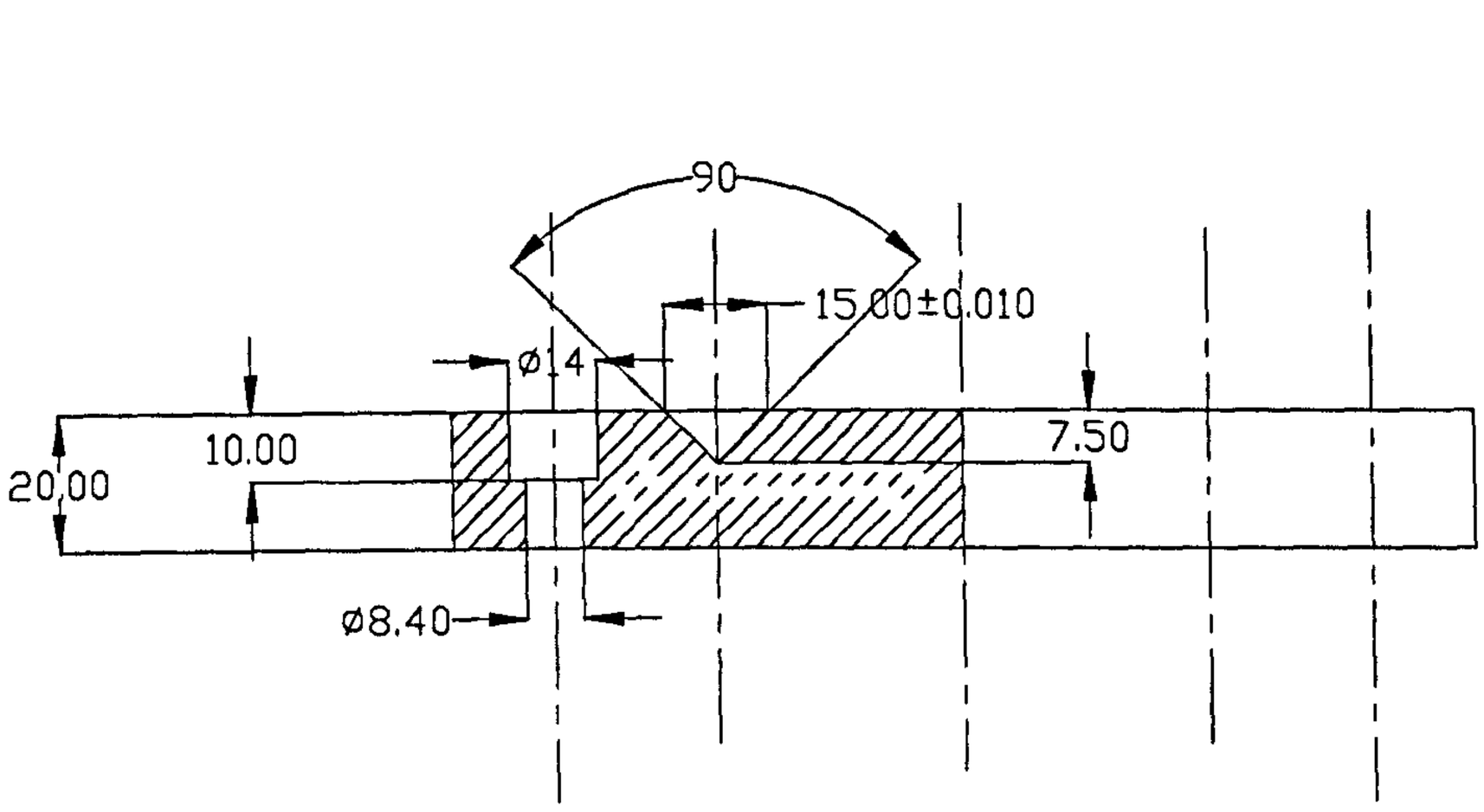

TITLE: *Lower Lapping Plate (Cast Iron)*	
DRAWN BY: *J. KANG*	QTY: *1*
DATE: *8 Dec., 98*	SCALE: *N. T. S.*
MEASUREMENT IN MM.	DWG.No: *98016*

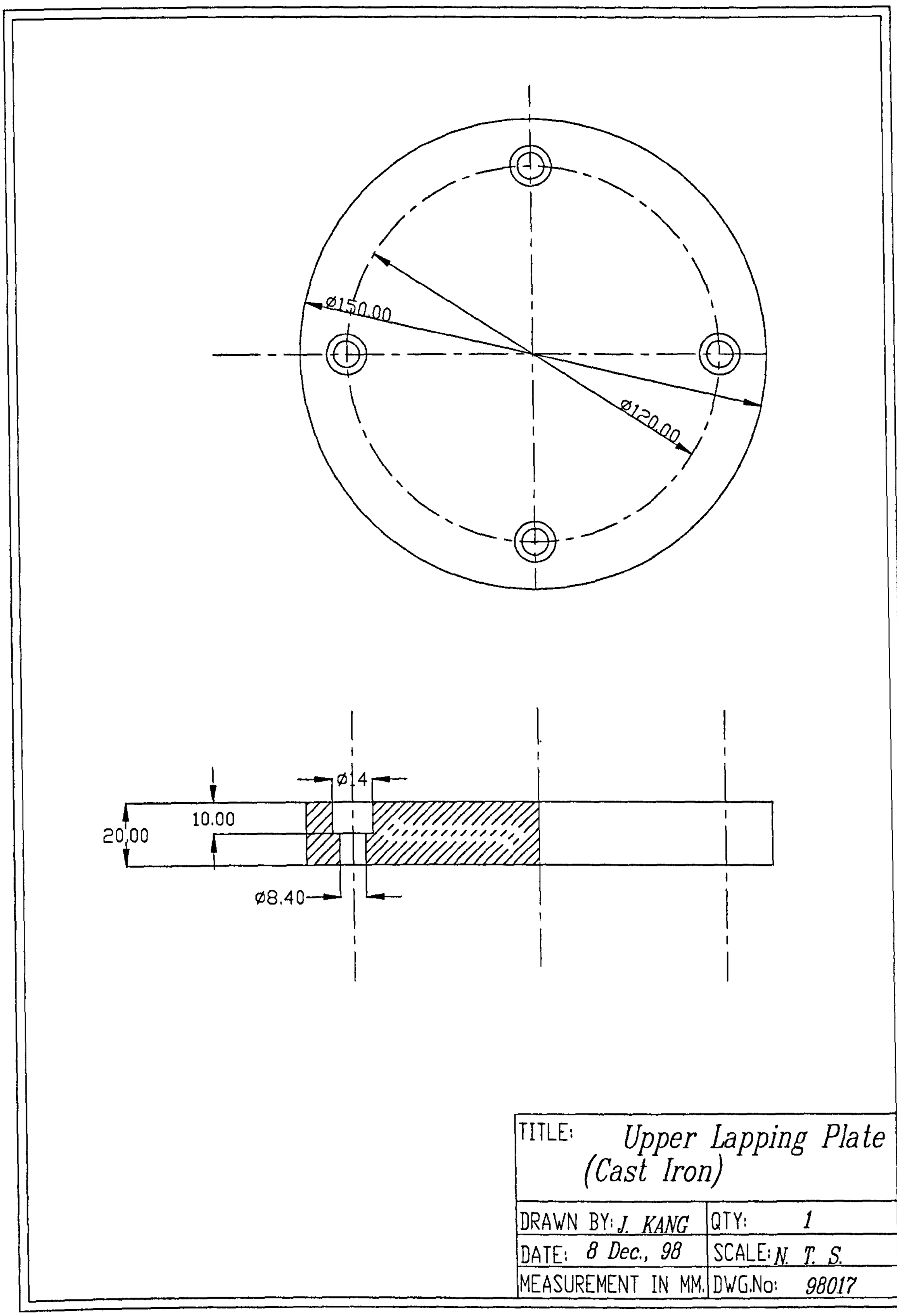

TITLE: *Upper Lapping Plate (Cast Iron)*	
DRAWN BY: *J. KANG*	QTY: *1*
DATE: *8 Dec., 98*	SCALE: *N. T. S.*
MEASUREMENT IN MM.	DWG.No: *98017*

Appendix 2

TECHNICAL DRAWINGS FOR 5-BALL ROLLING CONTACT FATIGUE TEST

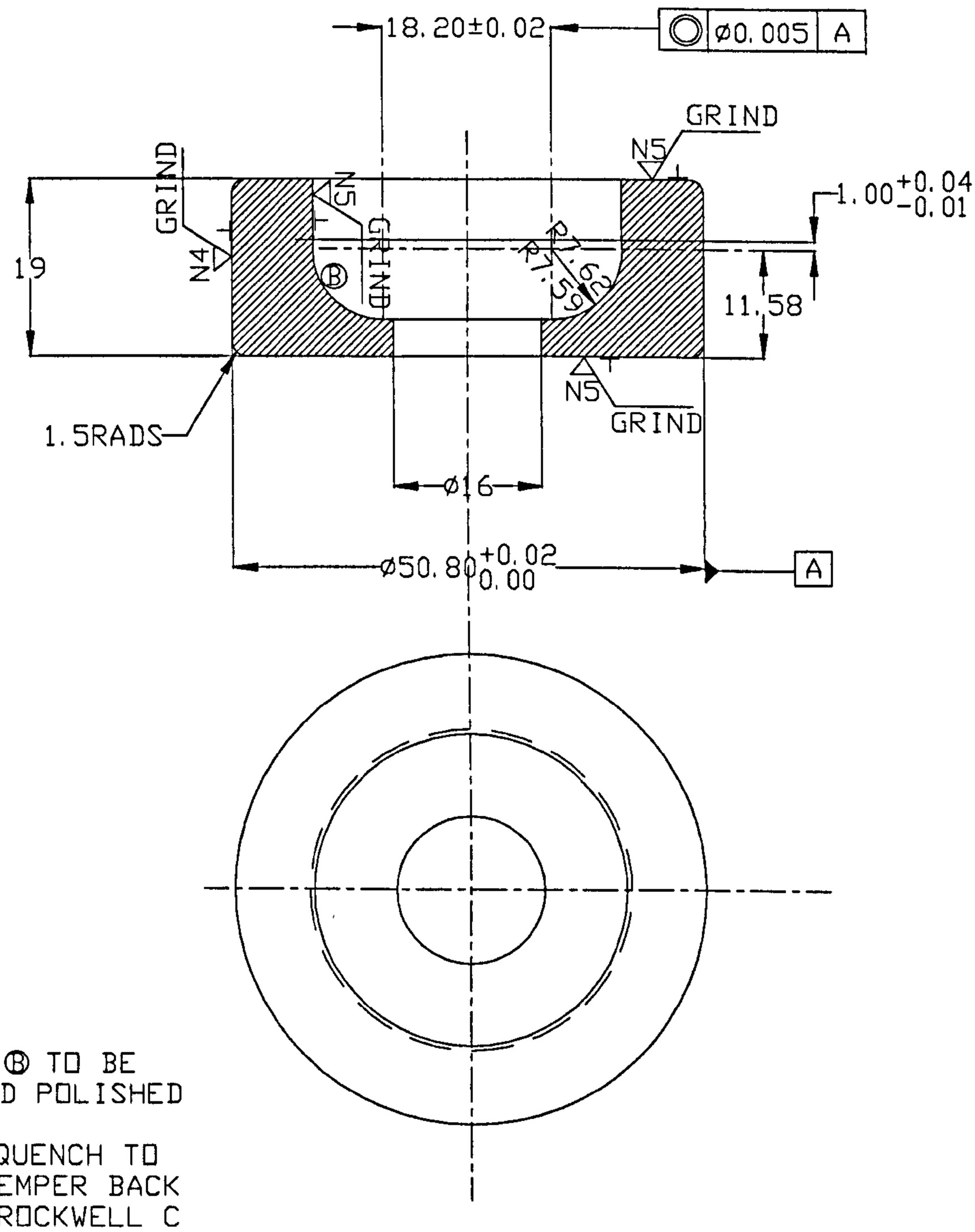

NOTE:

1. RADIUS Ⓑ TO BE GROUND AND POLISHED TO N1
2. WATER QUENCH TO HARDEN, TEMPER BACK TO 60~62 ROCKWELL C SCALE

TITLE *5 Ball Cup*	MATERIAL: *EN31(534A99)*	DRAWN BY: *J. KANG*
	FINISH: *SELF*	DATE: *1 Dec., 99*
	GENERAL LIMIT: +-0.1	SCALE: *N. T. S.*
	MEASUREMENT: mm	DWG. No.: *990101*

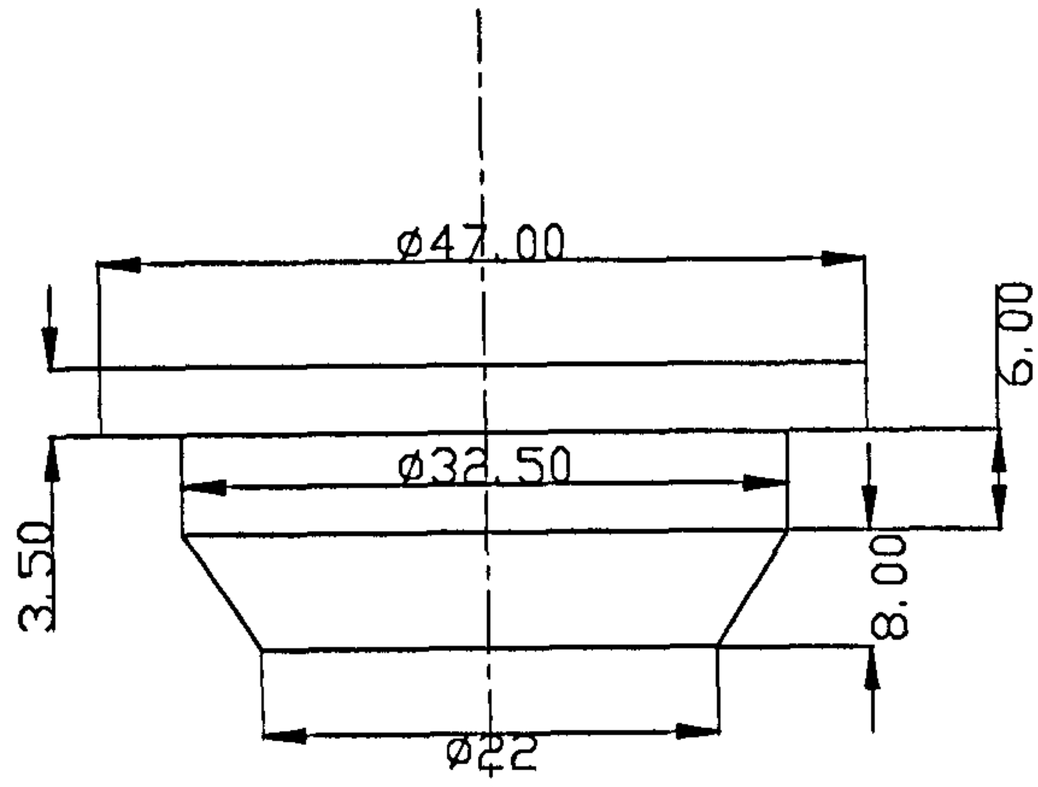

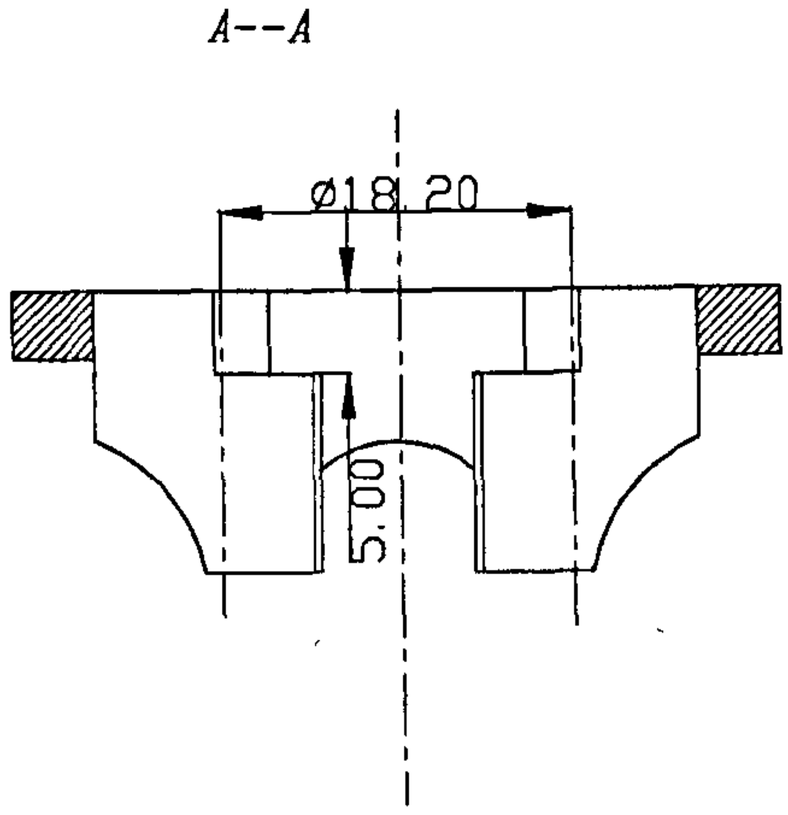

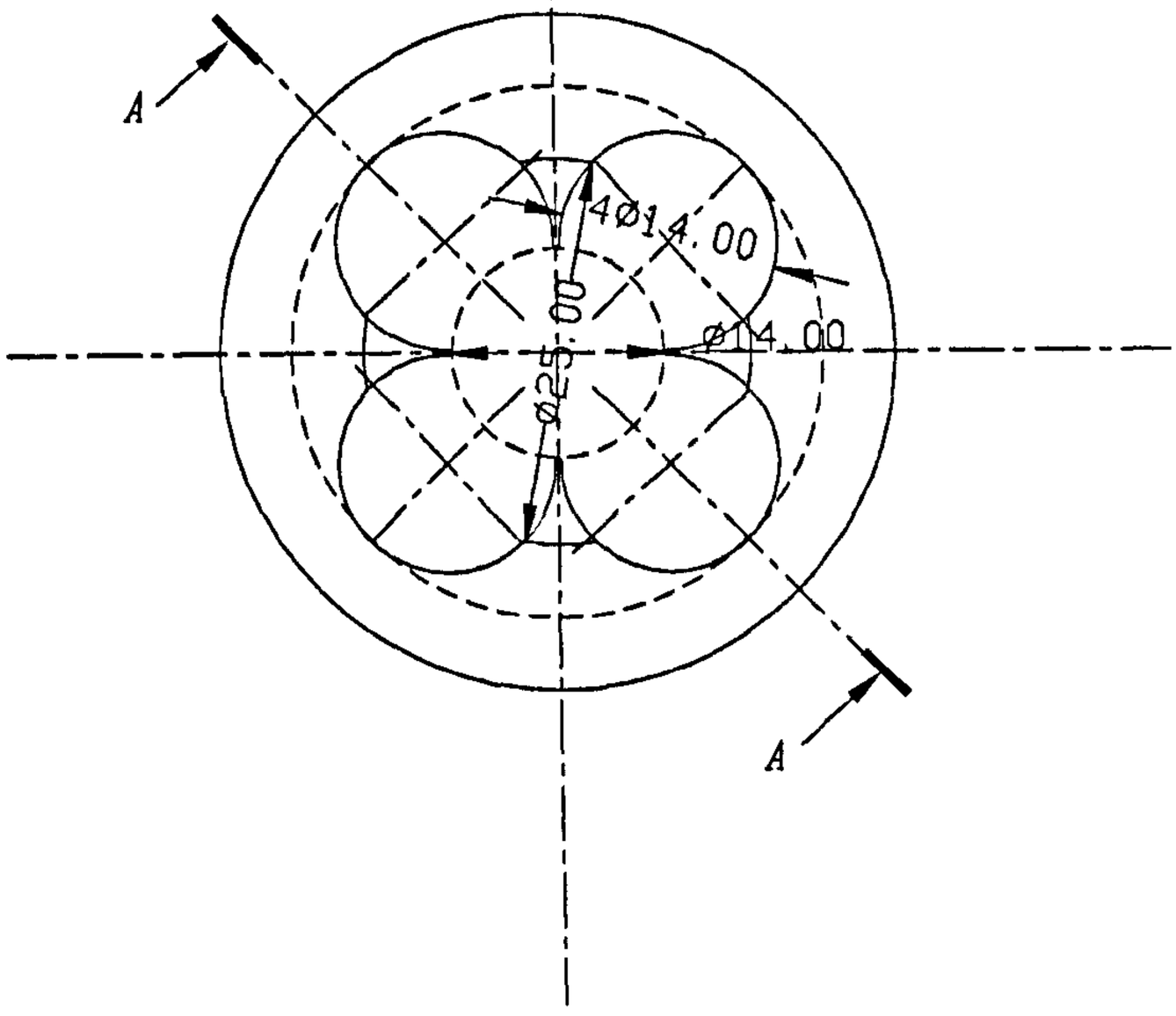

TITLE *Cage*	MATERIAL: *reinforced phenolic resin*	DRAWN BY: *J. KANG*
	FINISH: *SELF*	DATE: *1 Dec., 99*
	GENERAL LIMIT: +-0.1	SCALE: *1:1*
	MEASUREMENT: mm	DWG. No.: *990102*

Appendix 3

EXPERIMENTAL EQUIPMENT FOR SURFACE ANALYSIS AND TYPICAL OUTPUTS

A3.1 OLYMPUS BX60 Microscope

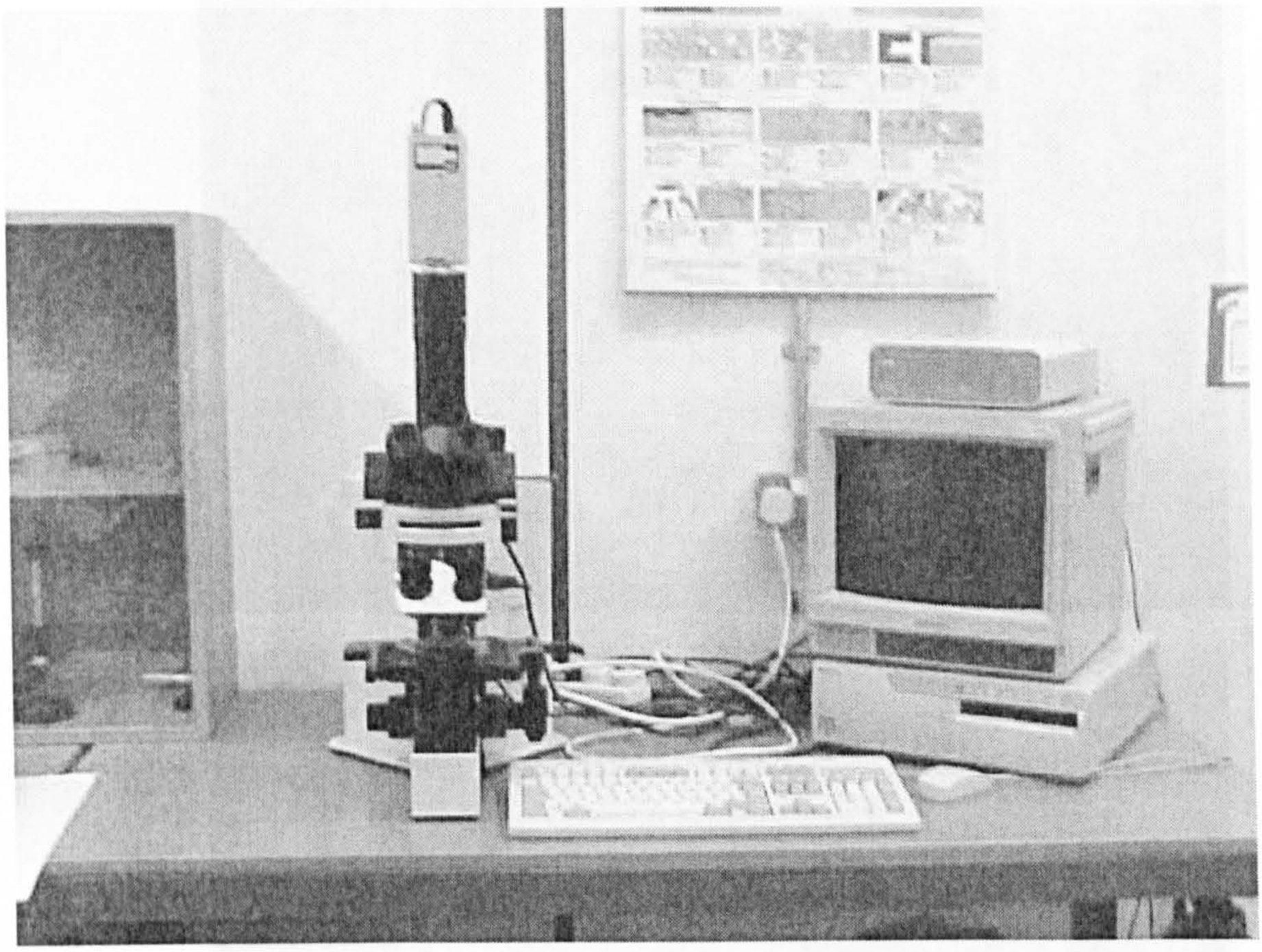

A3.2 PHILIPS SEM 505 Scanning Electron Microscope with EDX

A3.3 Atomic Force Microscope & a typical output

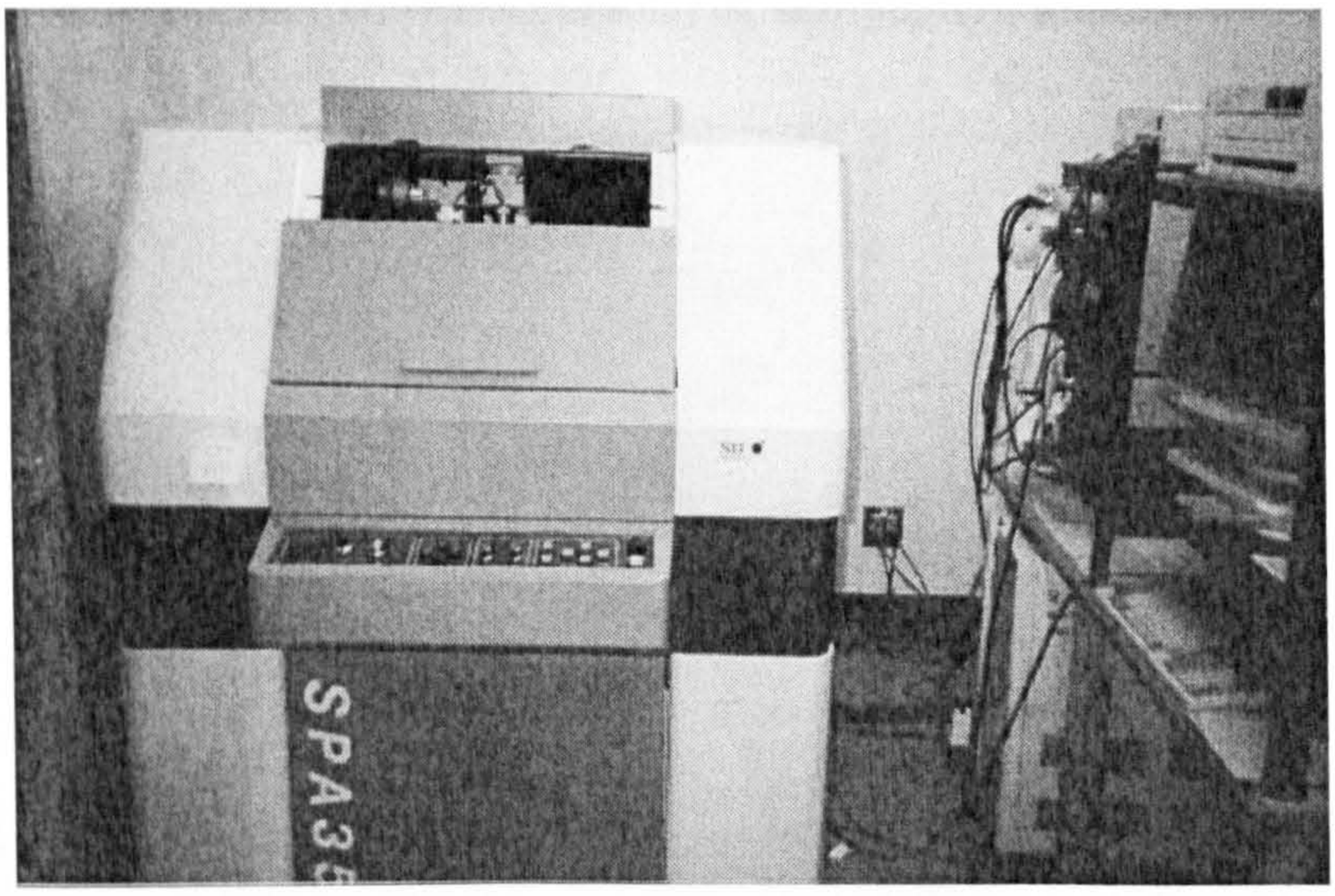

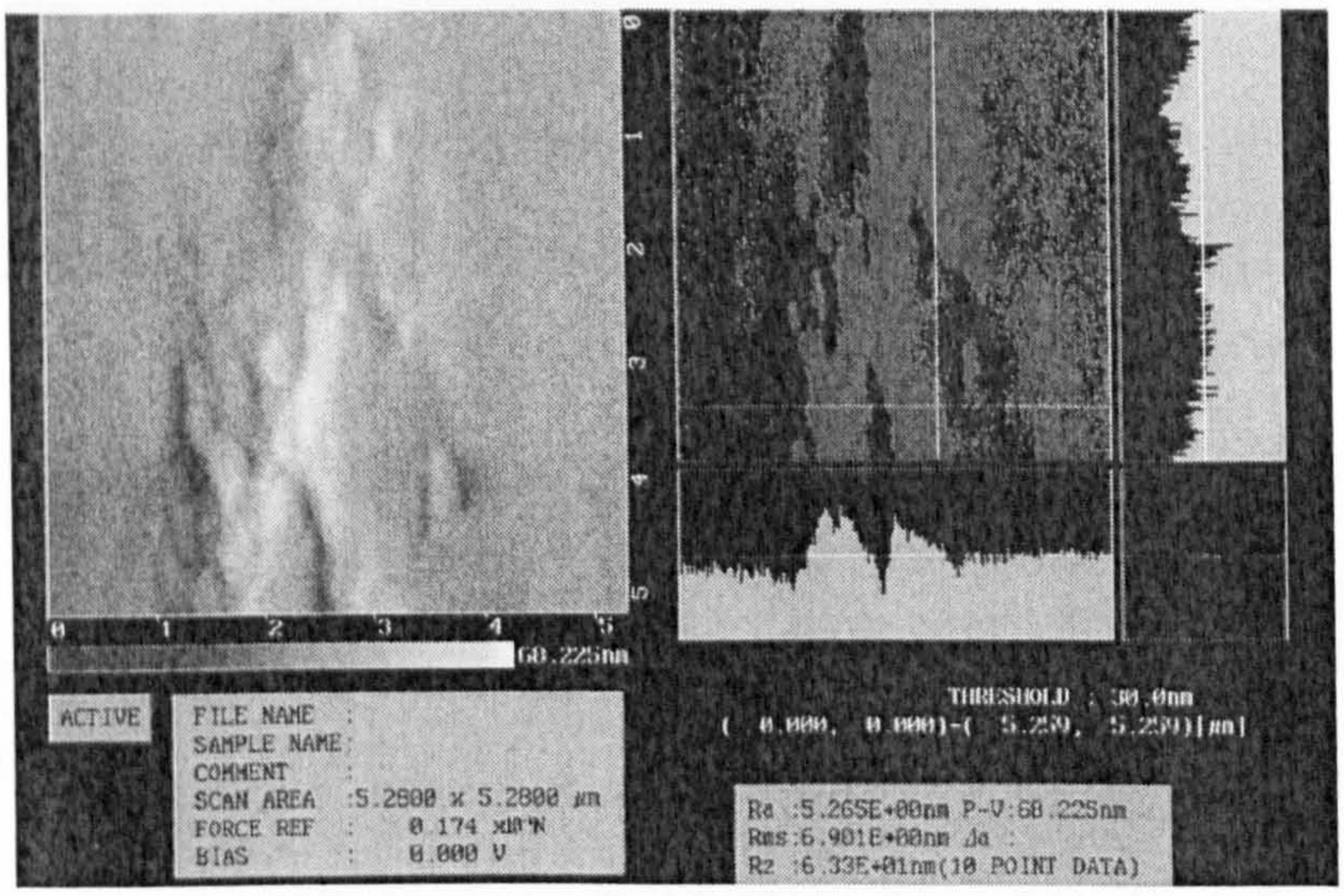

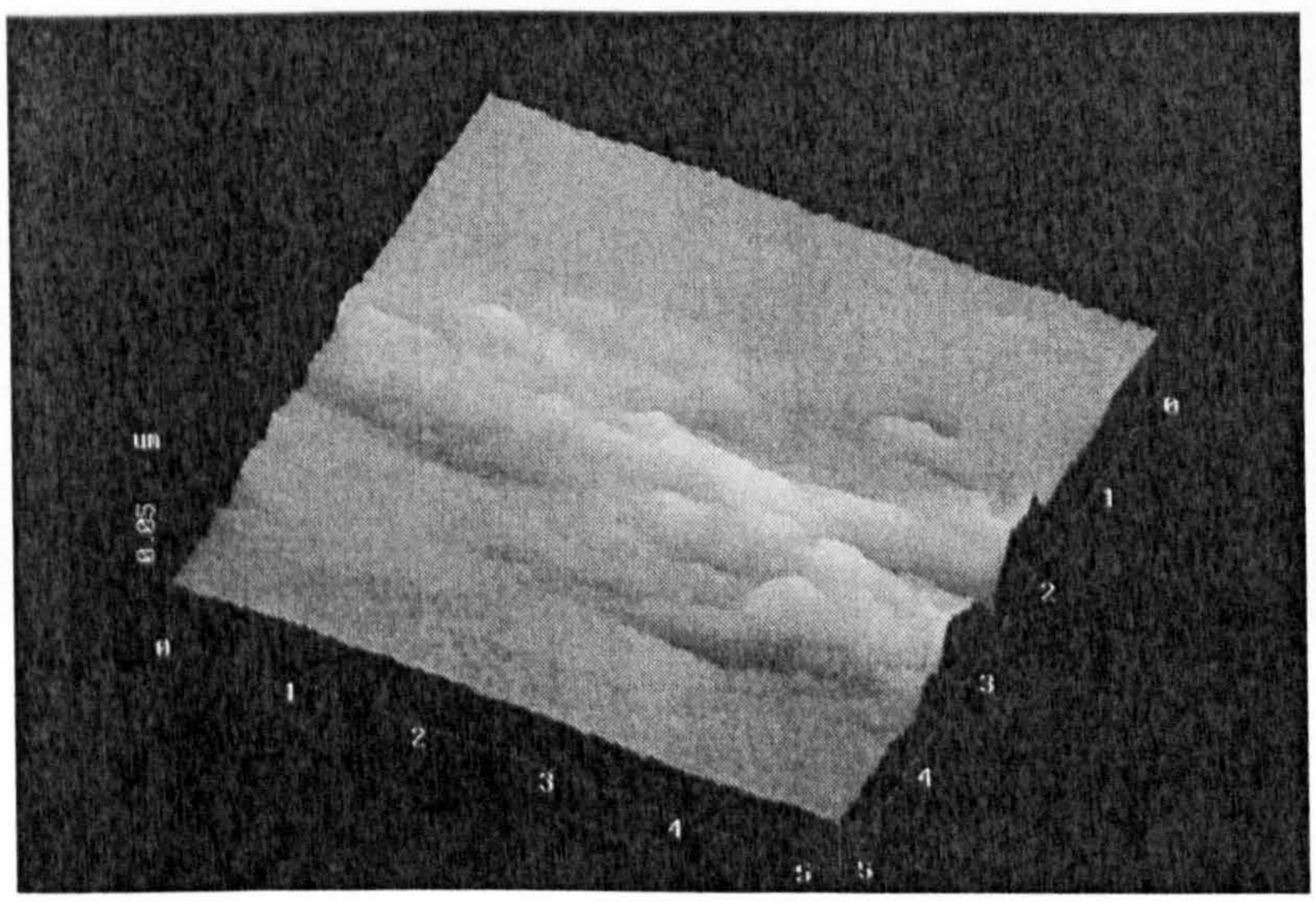

A3.4 Buehler Harness Indenter & sample ball holder

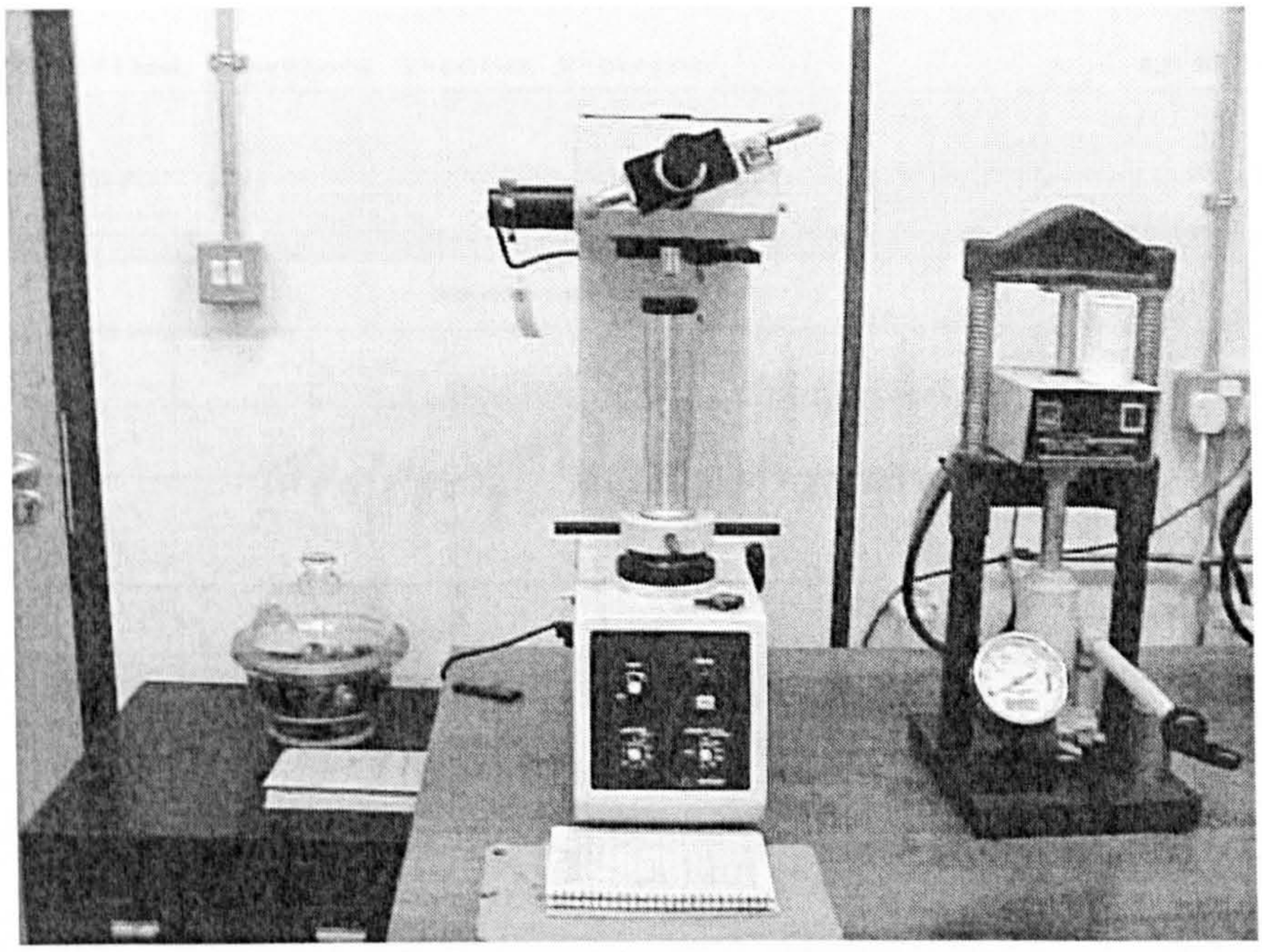

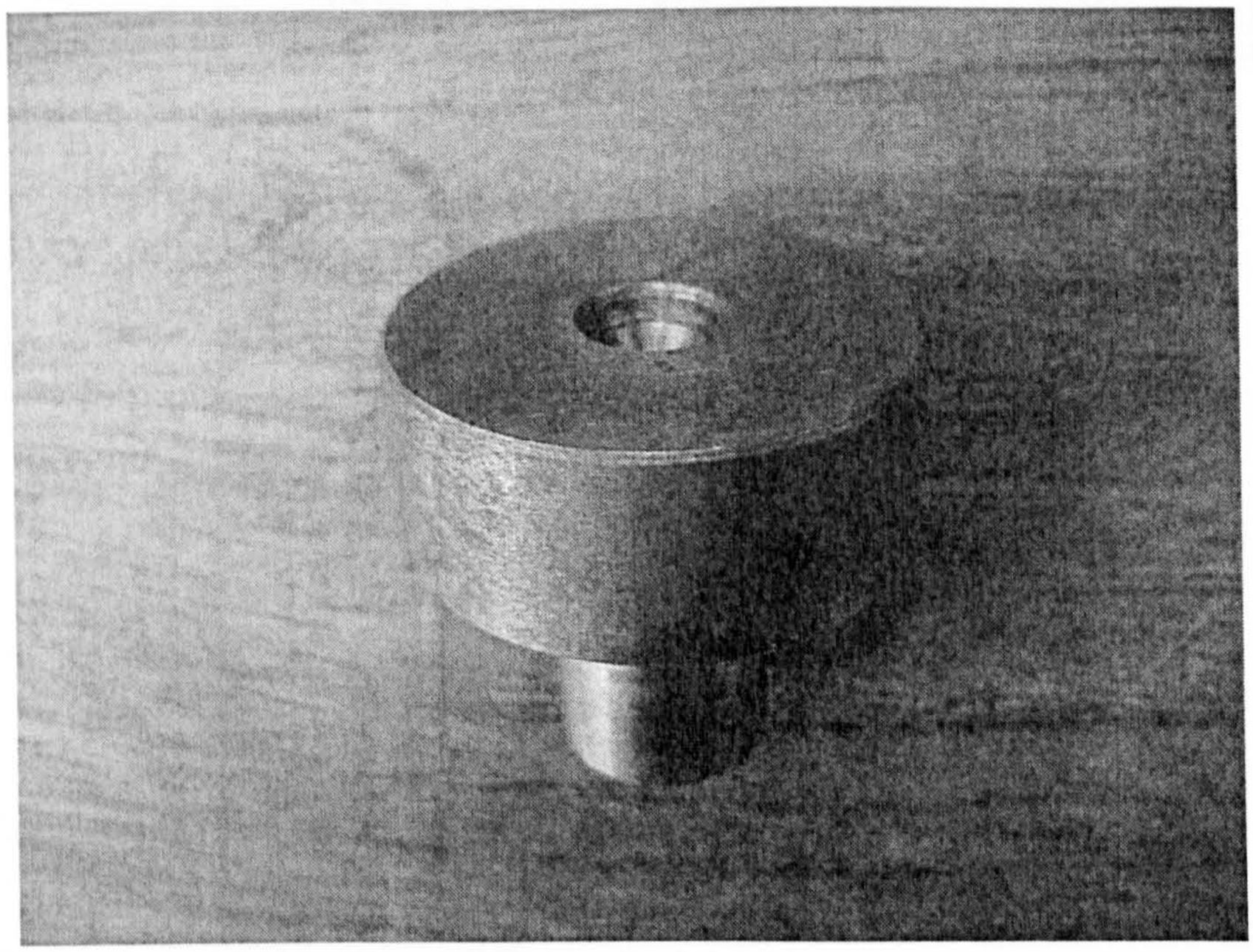

A3.5 Typical outputs from the Talysurf 2D surface profiler

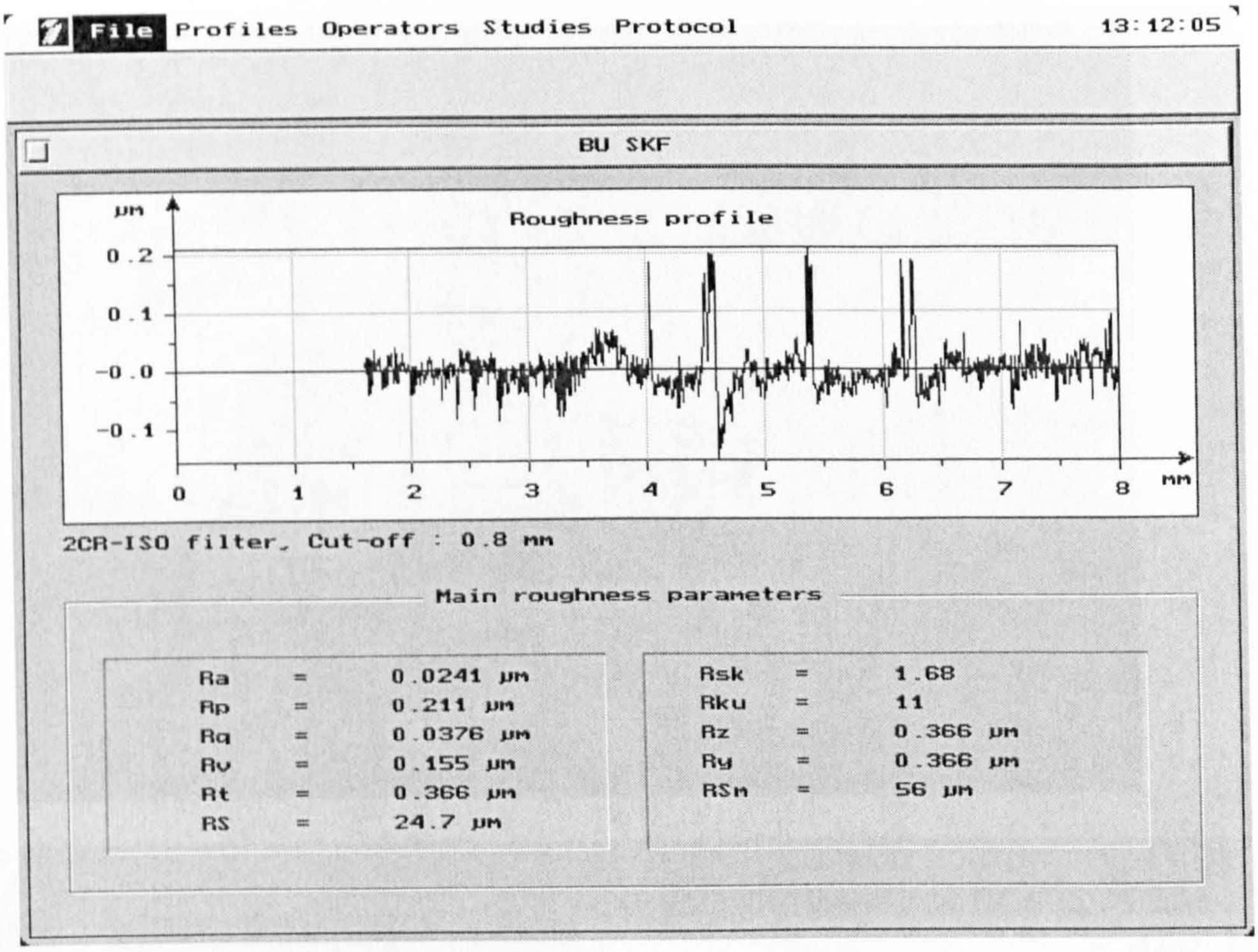

ROUGHNESS - ISO

STATISTICAL ANALYSIS

4

		S	$\bar{X}$	X MAX	X MIN	LAST X
Ra	µm	0.000	0.002	0.002	0.002	0.002
Rq	µm	0.000	0.003	0.003	0.003	0.003
Ry	µm	0.016	0.047	0.065	0.036	0.041
Rtm	µm	0.001	0.027	0.028	0.026	0.028
Rv	µm	0.004	0.027	0.030	0.022	0.030
Rp	µm	0.023	0.028	0.054	0.012	0.012
Sm	µm	5	29	34	25	25
λq	µm	2	27	28	25	25
Δq	°	0.0	0.0	0.0	0.0	0.0
Rsk		2.7	0.2	3.2	-1.7	-1.7
Rku		30.2	29.4	64.1	9.6	14.5
S	µm	1	14	15	13	13
R3z	µm	0.002	0.014	0.016	0.013	0.016
Rpm	µm	0.004	0.011	0.016	0.008	0.008
R3y	µm	0.004	0.018	0.023	0.014	0.023

0-EXCLUDE LAST X N= 3 OF 3

ID: 11 CFI-BU 23-JUN-98 1/2" R^{T}H

A3.6 Zygo New View 3-dimensional imaging surface structure analyser & a typical output

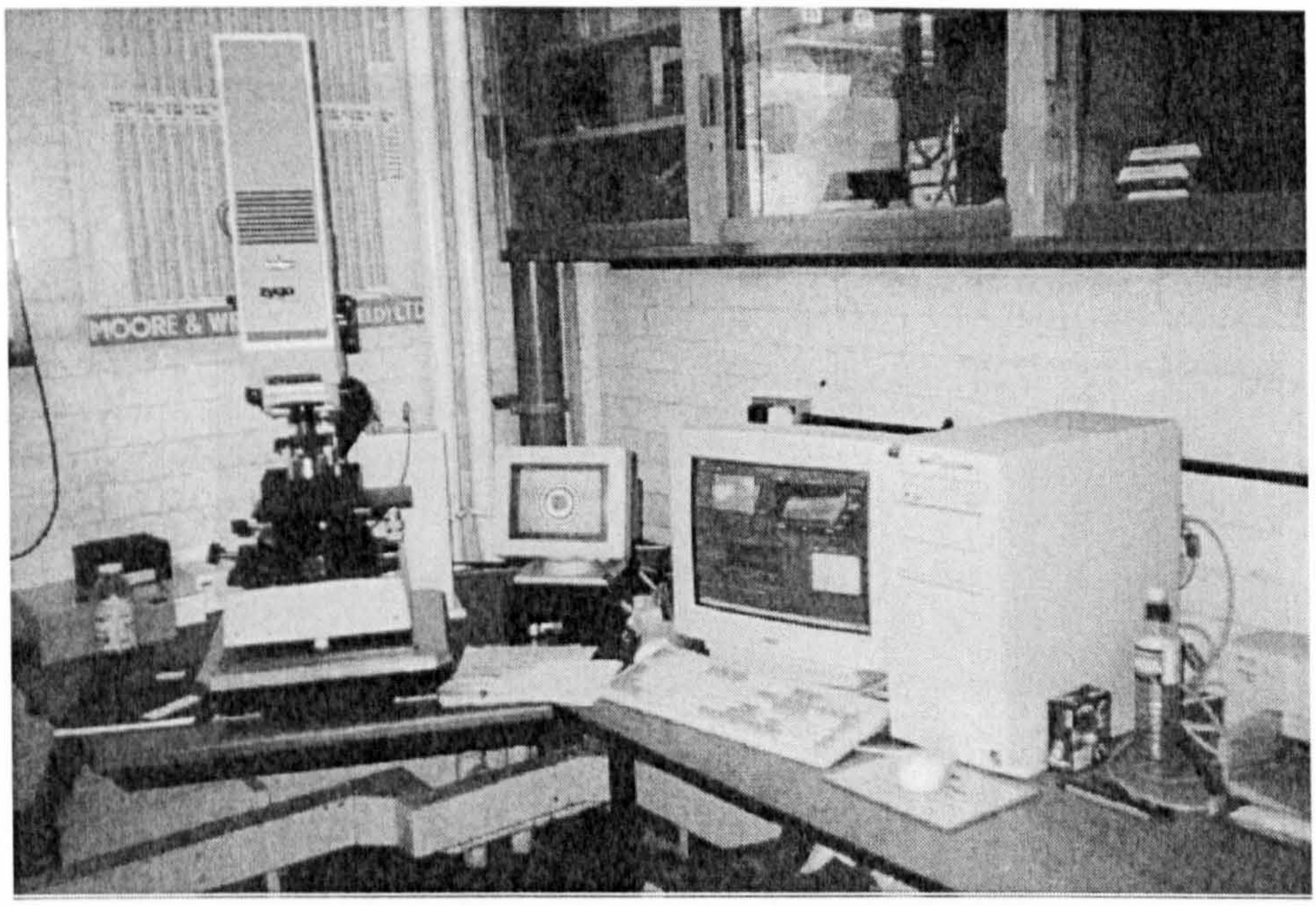

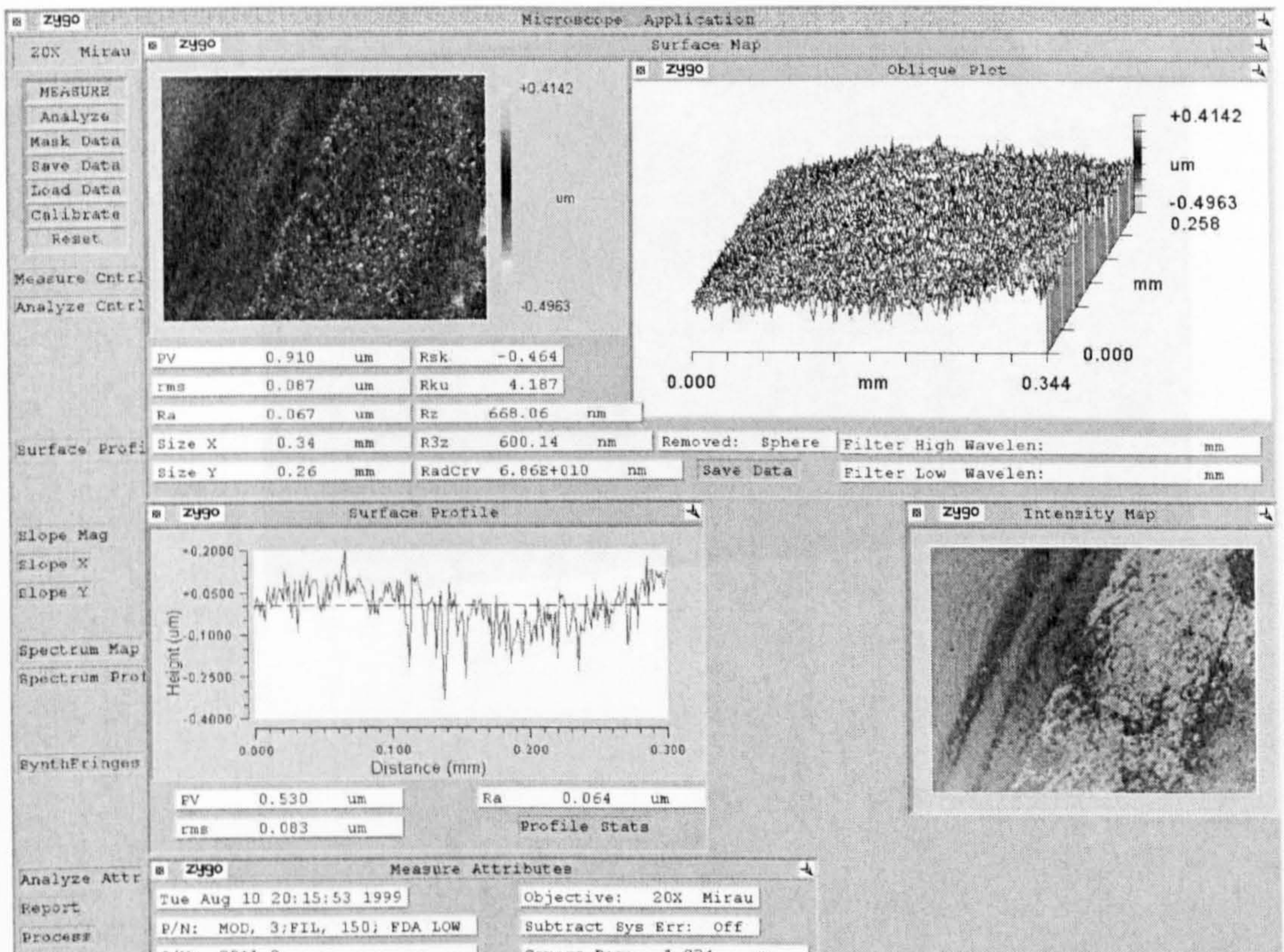

A3.7 Typical outputs from Interference Profilometer (WYKO image)

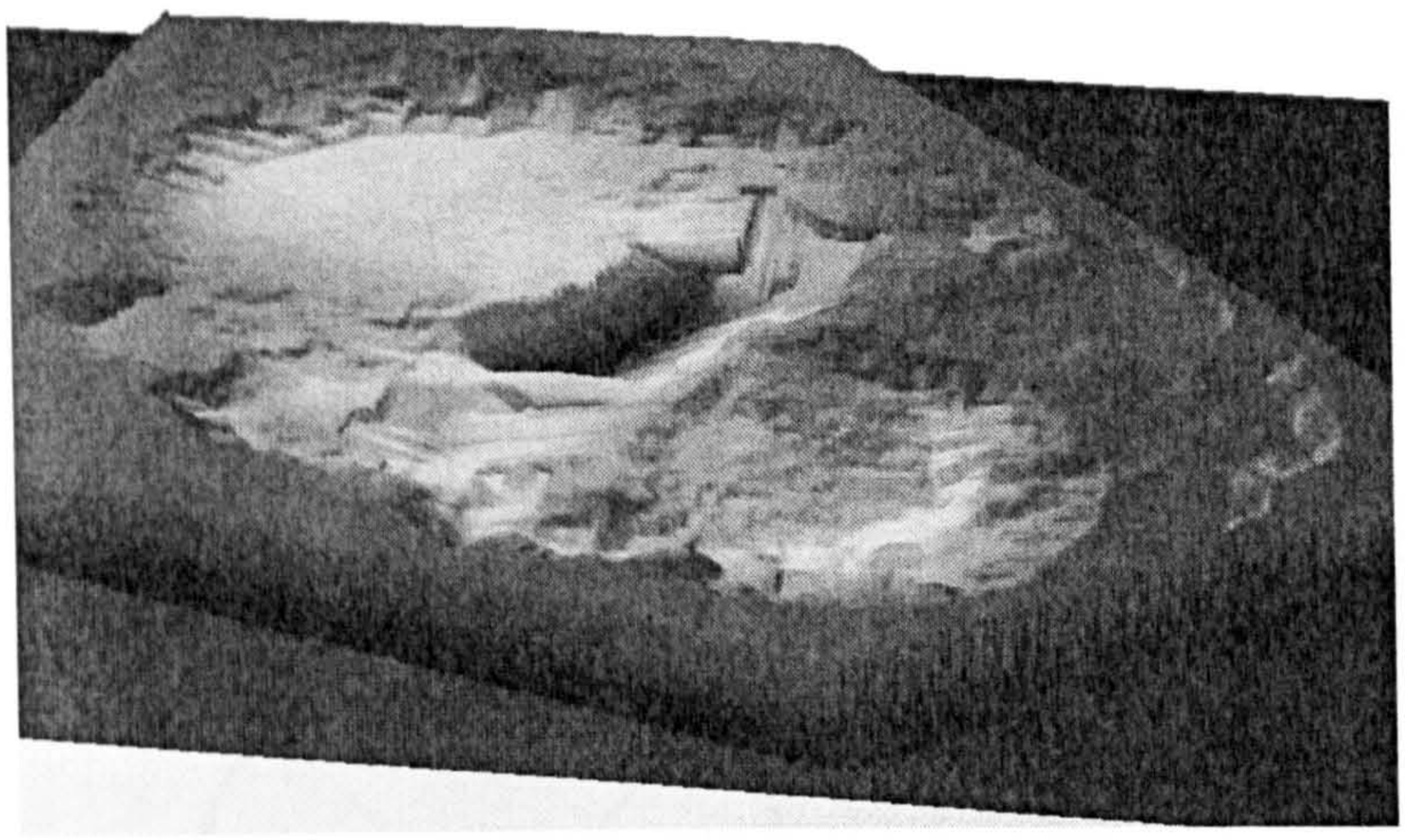

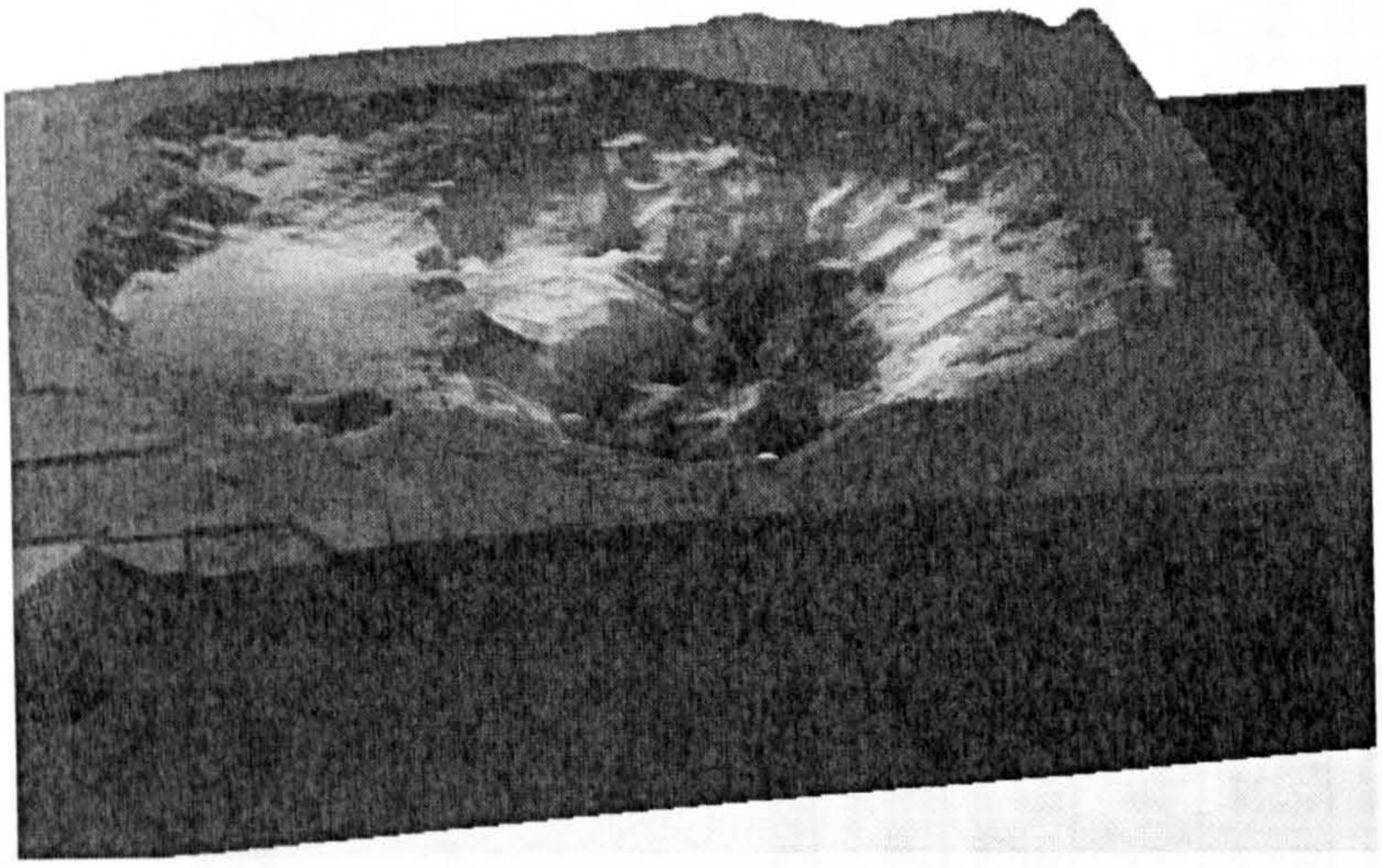

A3.8 Outputs from Ball Roundness Measurement

A3.8.a Outputs from MWA 1605B Roundness machine

Factory:
Type: Sample 2
Operation: Waviness

Machine: MWA 160B - NR. 6165
Operator: W.de Ronde
Shift:

SKF

UNFILTERED POLAR DIAGRAM

Note:

MS02

0.5 µm / Unit (20000)

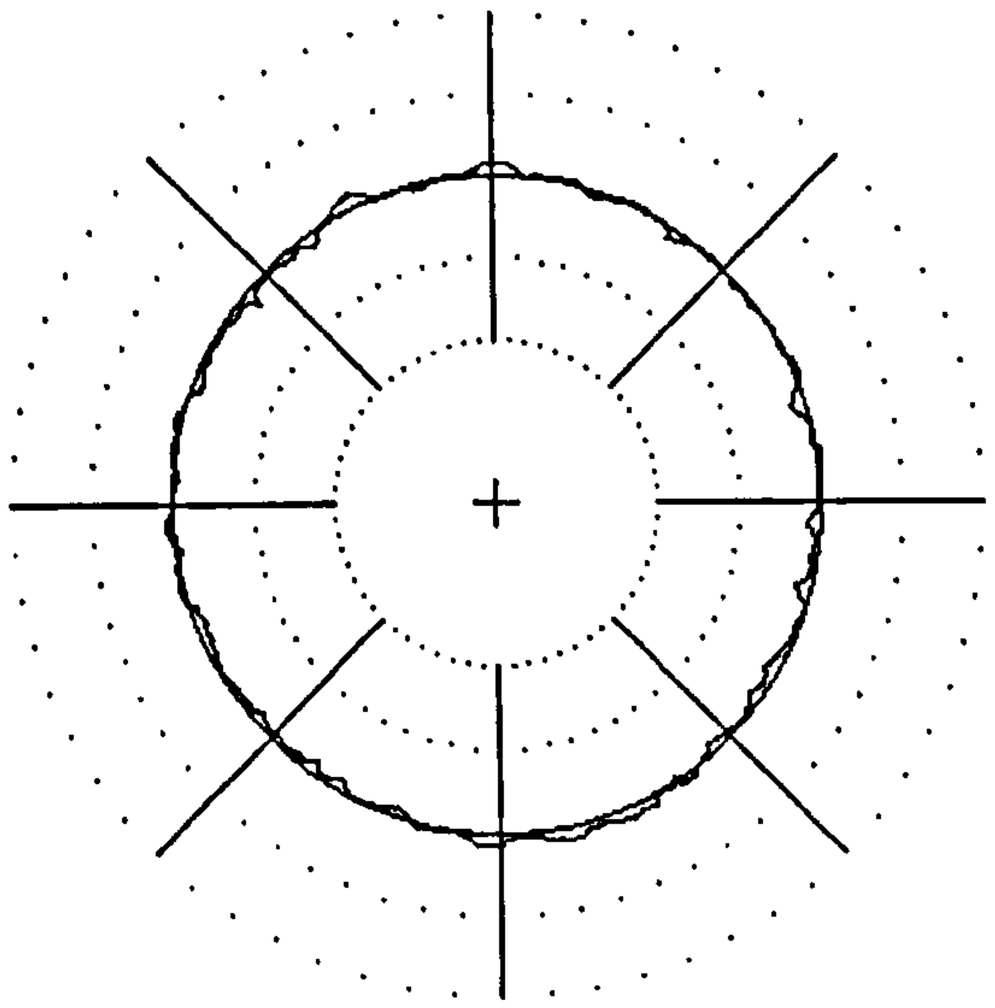

NMP = 1024 4.023 rpm 06/24/99 09:04:18

Change MS with +/-
Screen - Configuration
Measuring range

LSC

Δr	=	0.2091 µm
Xm	=	-0.1160 µm
Ym	=	-0.3915 µm

MDw

L	= 6.6029 µm/s
M	=23.0797 µm/s
M1	= 2.9812 µm/s
M2	=22.8864 µm/s
H	=57.9156 µm/s
max1	=11.5574 µm/s
max2	=11.2875 µm/s

A3.8.b Outputs from Taylor-Hobson Talyrond 73 Roundness Profiler

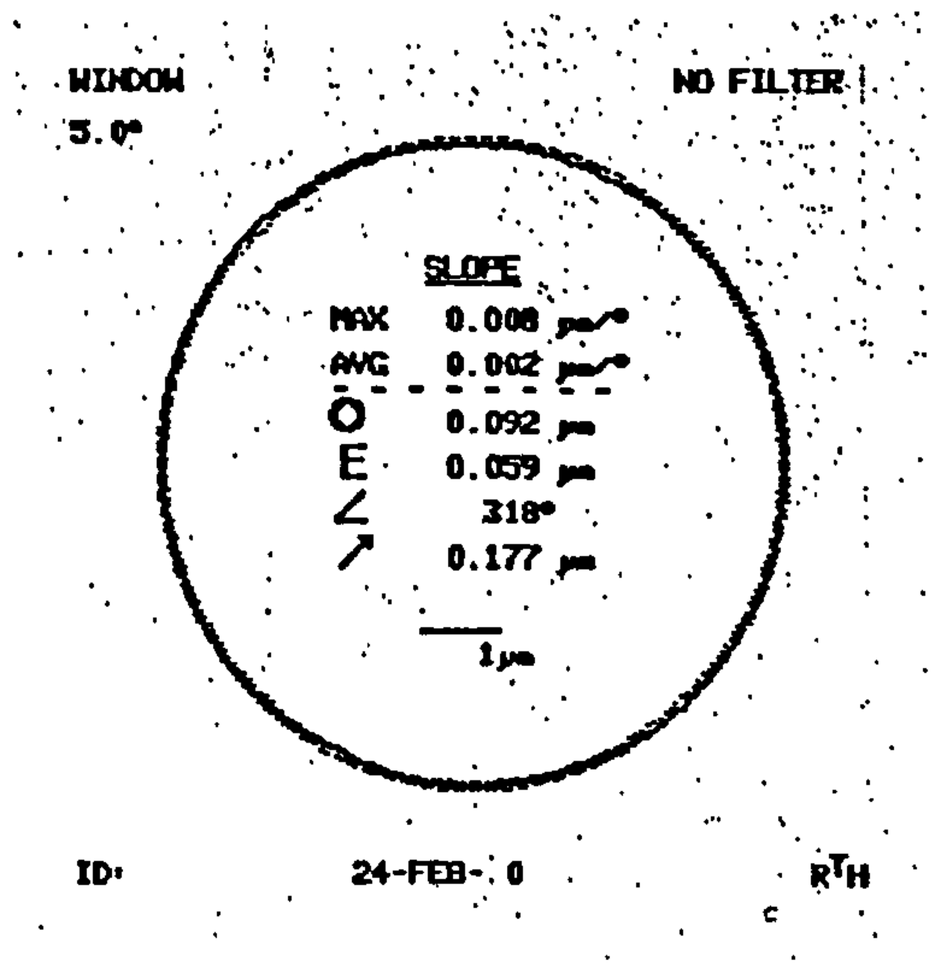

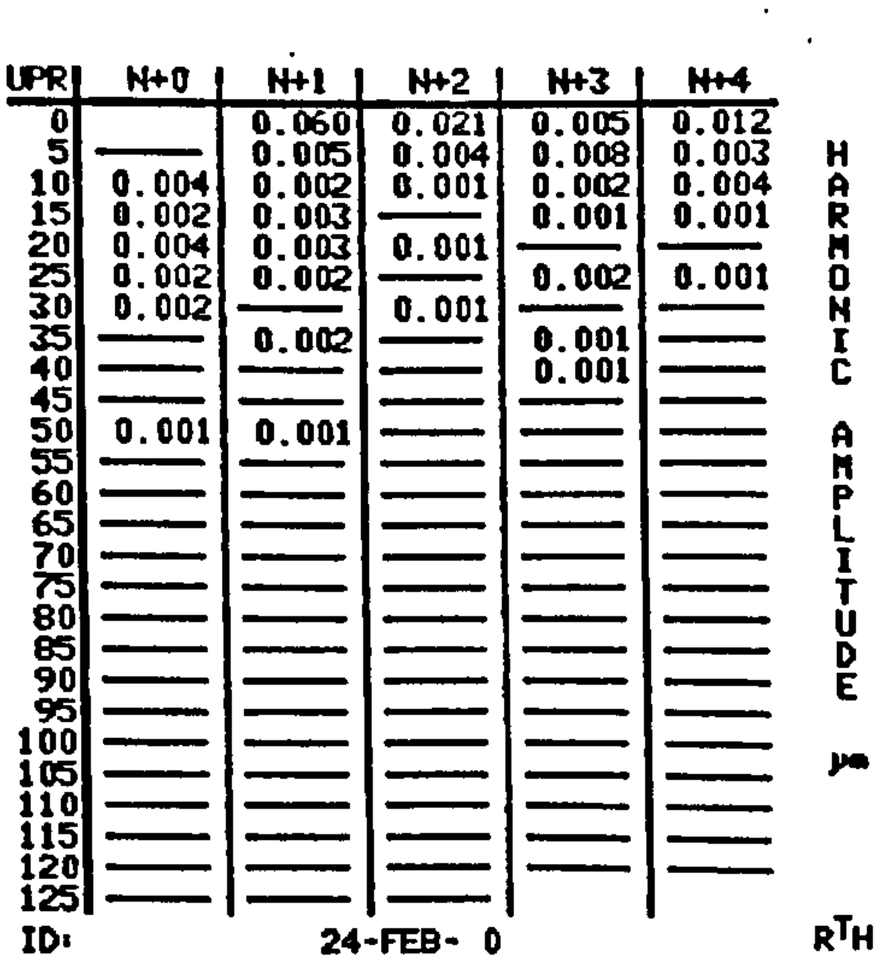

A3.9 RIGAKU RINT 2000 X-Ray diffractormeter & a typical output

A3.9a Outside appearance of the machine

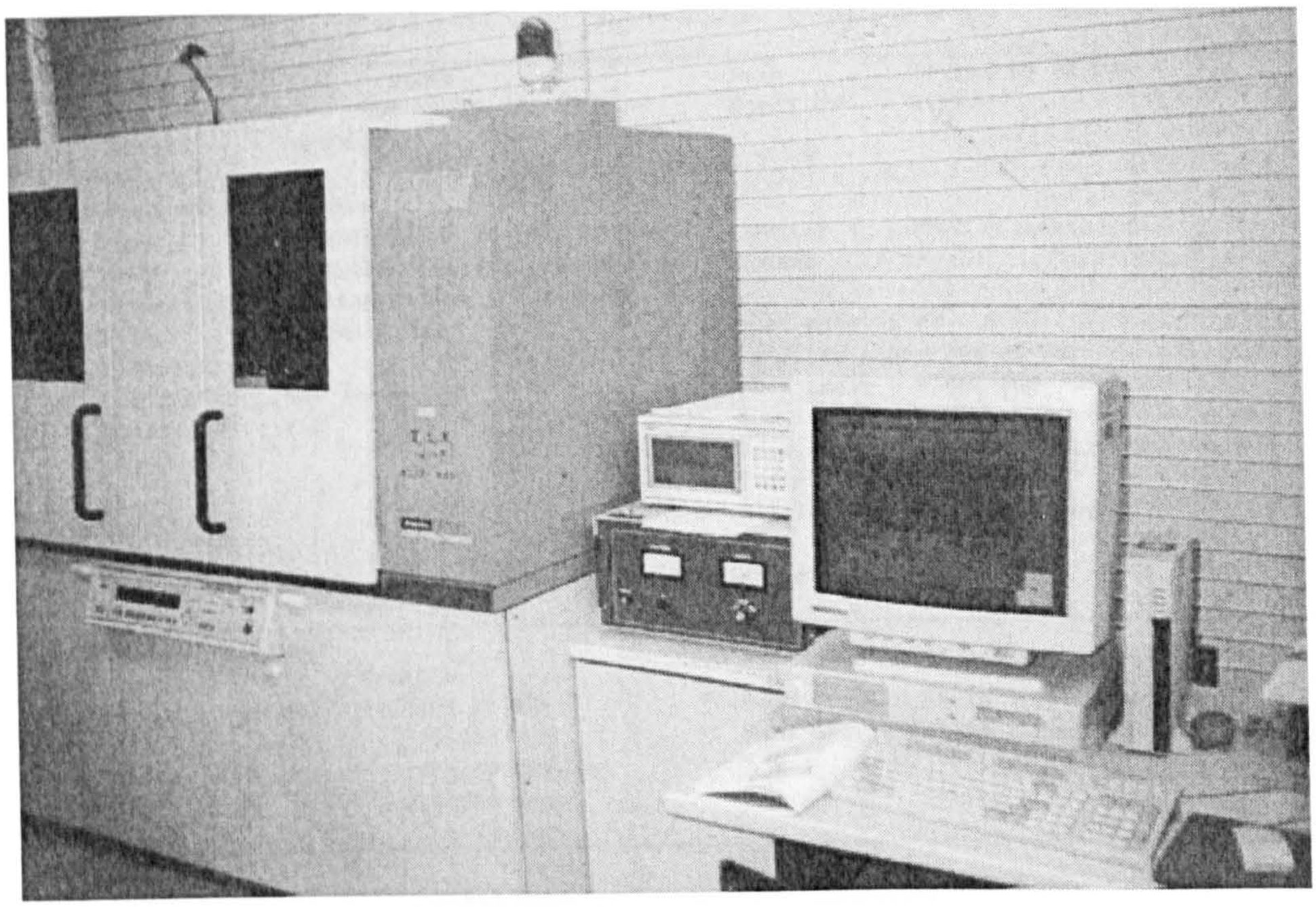

A3.9b Inside measuring chamber

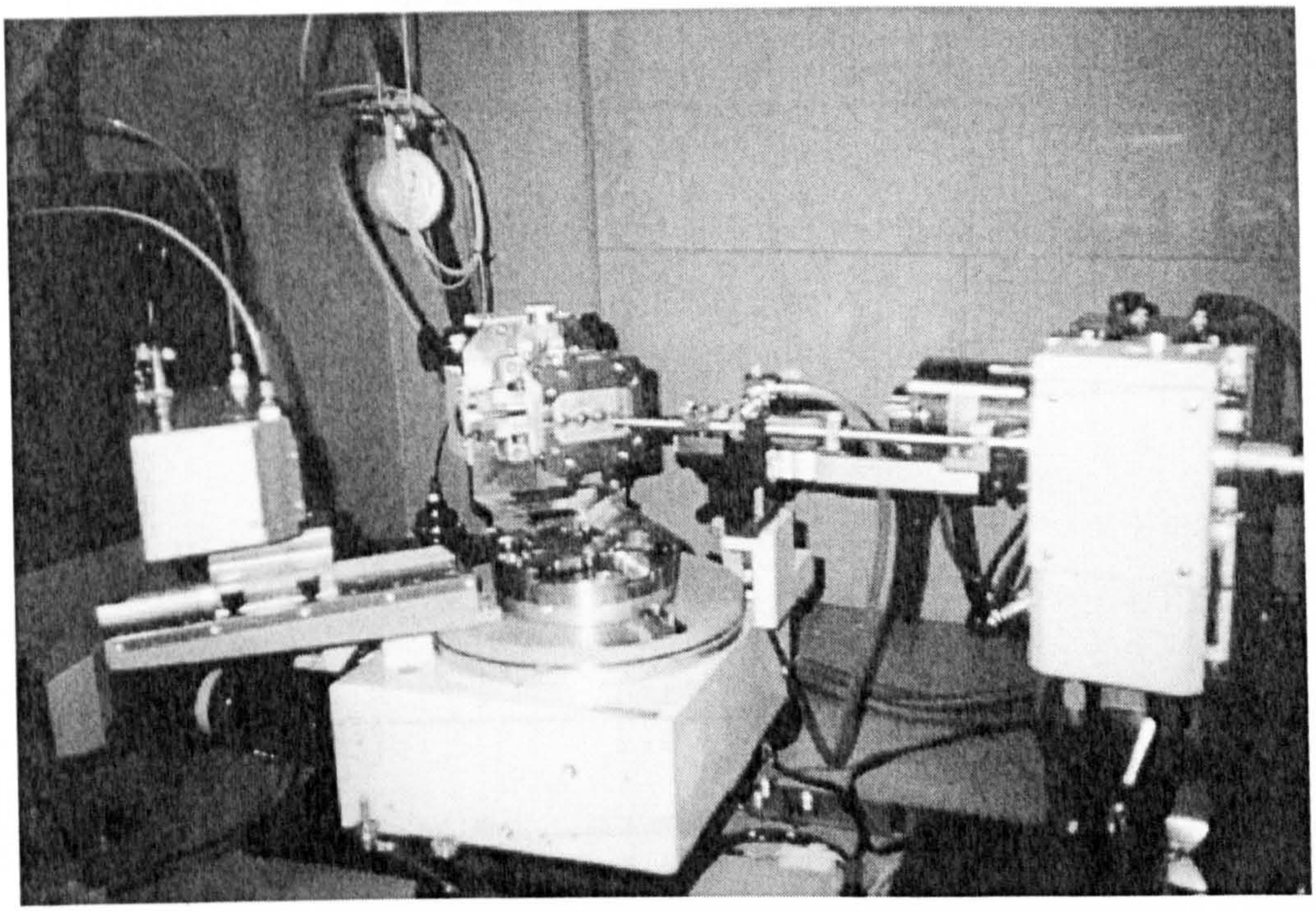

A3.9c A typical measurement output

Residual Stress (stress)

```
Sample      :          blank                    Date       : 12-Jul-00 19:27
File        : 12-7-2000.1373                    Operator   : RINT
Comment     : left0000
Memo        :
Measurement condition
X-ray       : Cr K-ALPHA1 / 40 kV / 250 mA      Counter    : PSPC (Linear)
Gonio       : RINT2000 Wide angle goniometer (Stress)
Attachment  : Special Stress attachment
Filter      : K-beta filter                     Scan mode  : FT
I.Monochro  :                                   Sampling time: 100.00 sec.
C.Monochro  : Not installed                     Step angle : 0.002 deg.
Collimator  : 1.0                               Scan axis  : 2 Theta
                                                Scan range : 123.000 -> 127.000 deg.
                                                Theta      : 62.702 deg.
                                                Sample rotation: 0.000 deg.

method      :Fixed psi0 (input psi)   Iso-Inclination  Pai axis angle :  0.000 deg.
```

```
Physical constant
Sample           : Si3N4-b
Young's modulus  :  310000.00 MPa               Peak 2 theta angle : 125.40300 deg.
Poisson's ratio  :       0.260                  Peak search method : Peak top
Stress constant  :    -953.50 MPa/deg.          h k l              :   0   0   0
Wave length      :  2.2897000 Ang
```

```
Results
Slope(+)         :      0.843 deg.
Stress(+)        :   -803.699 MPa
Reliability(+)   :   (+-)   58.28 MPa
Ave.2T(+)        :    125.476 deg.
2T(psi=0)(+)     :    125.281 deg.
Psi=0 FWHM       :     2.2012 deg.
```

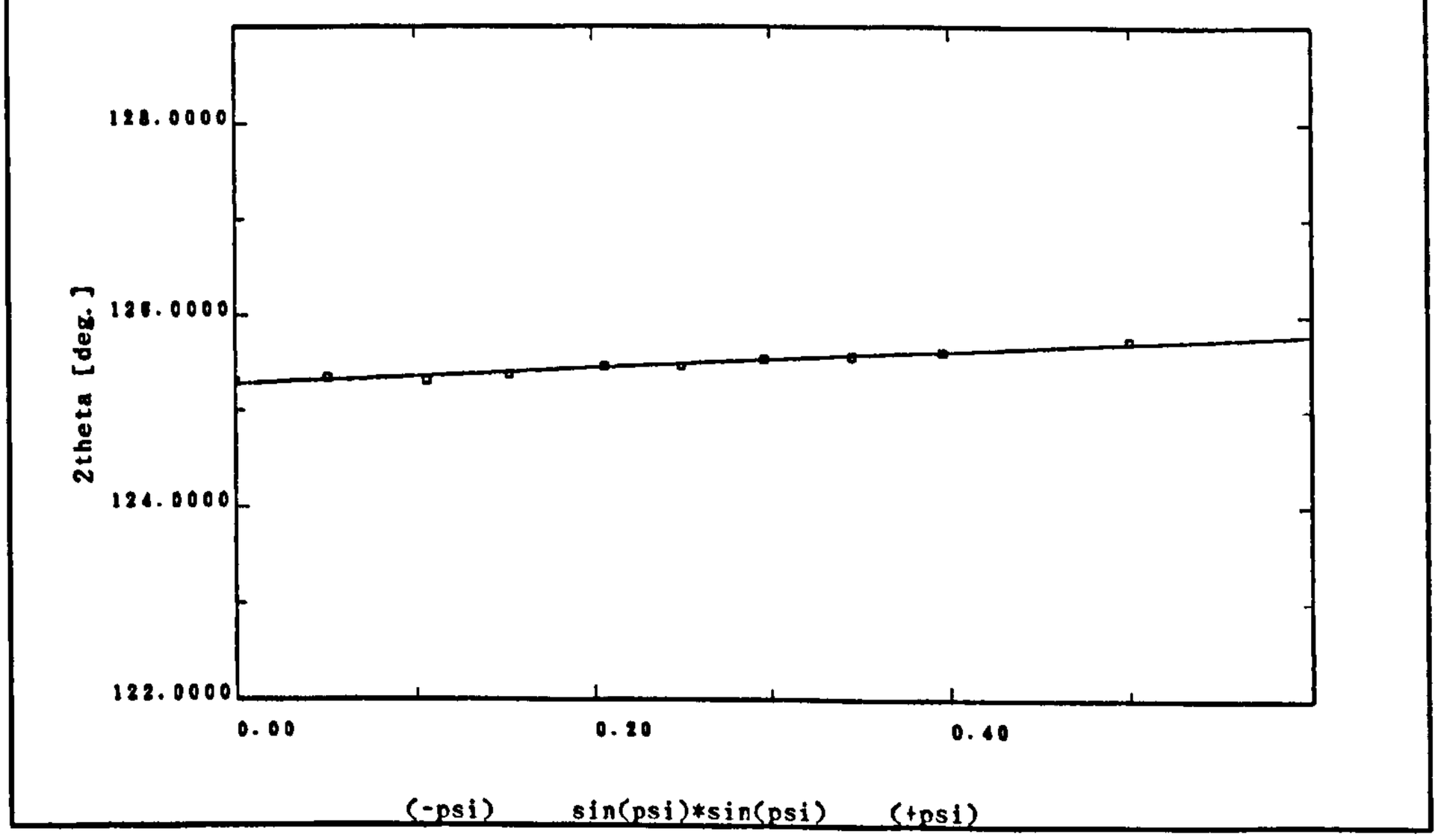

2000-Jul-12 19:30:59 Page-1

Residual Stress (peak search)

Sample : blank
File : 12-7-2000.1373
Comment : left0000
Memo :

Date : 12-Jul-00 19:27
Operator : RINT

[Smoothing]
[L.P. correction]

[Abs. correction]

[Normalization]
[B.G. elimination]

[Ka2 elimination]

Measurement condition
Scan area : 123.000 -> 127.000 deg.

No.	Psi	Peak top	FWHM MPM	FW2/3M MPM	Gravity	Intensity	FWHM
1	0.00	125.3128	125.3128	125.2770	125.0456	2051	2.2012
2	13.00	125.3507	125.3507	125.2743	125.0560	1819	2.3348
3	19.00	125.3271	125.3271	125.3337	125.0602	1696	2.3934
4	23.00	125.3905	125.3905	125.3096	125.0722	1585	2.5907
5	27.00	125.4693	125.2901	125.3971	125.0900	1525	2.8421
6	30.00	125.4648	125.4648	125.3752	125.0885	1412	2.6869
7	33.00	125.5371	125.0311	125.4191	125.1078	1344	3.7009
8	36.00	125.5618	125.5618	125.4244	125.1071	1258	2.6502
9	39.00	125.6101	125.0020	125.5197	125.1261	1190	3.9731
10	45.00	125.7313	125.7313	125.4024	125.1356	965	3.5451

2000-Jul-12 19:30:59 Page-2

Appendix 4

CONTACT MECHANICS ANALYSIS

A4.1 Ball/Ball Contact Stress Analysis

Ball/ball contact resembles the situation in the 4-ball or 5-ball rolling test: one upper ceramic ball in contact with 3 or 4 lower steel balls. Contact stresses were calculated using classical Hertz elastic contact stress formulae (circular point contacts) from reference (Johnson 1985).

The maximum compressive stress, P_o, is:

$$P_0 = \left[\frac{6PE_1^2}{\pi^3 R_1^2}\right]^{\frac{1}{3}} \qquad \text{(A4-1)}$$

Where P is the contact load, under 4-ball rolling condition it is $P_{contact4}$ in equation (3-2) in Chapter 3, and under 5-ball rolling condition it is $P_{contact5}$ in equation (3-3) in Chapter 3. E_1 is effective elasticity modulus with relation:

$$\frac{1}{E_1} = \frac{1-\nu_a^2}{E_a} + \frac{1-\nu_b^2}{E_b} \qquad \text{(A4-2)}$$

Where ν_a and E_a are Poisson's ratio and Young's modulus for ceramic ball, ν_a =0.27 and E_a= 315 GPa. While ν_b and E_b are Poisson's ratio and Young's modulus for steel ball, ν_a =0.3 and E_a= 207 GPa.

In equation (A4-1), R_1 is effective geometric radius,

$$\frac{1}{R_1} = \frac{1}{R_a} + \frac{1}{R_b} \qquad \text{(A4-3)}$$

Where R_a is the radius for ceramic ball and R_b is the radius for steel ball, R_a = R_b = 6.35 mm = 0.00635 m.

Radius of contact circle, a, is:

$$a=\left[\frac{3PR_1}{4E_1}\right]^{\frac{1}{3}} \qquad \text{(A4-4)}$$

Max. shear stress, τ_1, is:

$$\tau_1=0.31P_0 \quad at\ r=0,\ z=0.48a \qquad \text{(A4-5)}$$

Max. tensile stress, σ_r, is:

$$\sigma_r=(1-2\nu)P_0/3 \quad at\ r=a,\ z=0 \qquad \text{(A4-6)}$$

Where take $\nu=\nu_a=0.27$, the Poisson's Ratio for ceramic ball.

The calculation is carried out on Microsoft Excel 97. Table A4-1 is the calculated Hertz contact stresses on 0.5" (12.7mm) balls ceramic/steel contact under Plint 4-ball rolling test configuration.

Plint Machine Load (kN)	Contact Load $P_{contact4}$ (N)	Max. Compressive Stress (GPa)	Radius of Contact circle (m)	Max. Shear Stress (GPa)	Max. Tensile Stress (GPa)
0.1962	80	3.057	0.000112	0.948	0.4687
0.3924	160	3.851	0.000141	1.194	0.5905
0.5886	240	4.408	0.000161	1.367	0.6760
0.7848	320	4.852	0.000178	1.504	0.7440
0.981	400	5.227	0.000191	1.620	0.8014
1.177	480	5.554	0.000203	1.722	0.8516
1.373	561	5.847	0.000214	1.813	0.8966
1.570	641	6.113	0.000224	1.895	0.9374
1.766	721	6.358	0.000233	1.971	0.9749
1.962	801	6.585	0.000241	2.041	1.010
2.158	881	6.798	0.000249	2.107	1.042
2.354	961	6.998	0.000256	2.169	1.073
2.551	1041	7.187	0.000263	2.228	1.102
2.747	1121	7.367	0.000270	2.284	1.130
2.943	1202	7.538	0.000276	2.337	1.156
3.139	1282	7.702	0.000282	2.388	1.181
3.335	1362	7.859	0.000288	2.436	1.205
3.531	1442	8.011	0.000293	2.483	1.228
3.728	1522	8.156	0.000299	2.528	1.251
3.924	1602	8.297	0.000304	2.572	1.272
4.120	1682	8.433	0.000309	2.614	1.293

Table A4-1 Calculated Hertz contact stresses
for ceramic ball/steel ball contact

A4.2 Ball/Flat Surface Contact Stress Analysis

Ball/flat surface contact is reproduced in the lapping test: ceramic balls being lapped in contact with upper flat lapping plate (steel or cast iron). The calculation is very similar to A4.1, apart from the contact load P and the effective geometric radius R_1. In this case the contact load P is P_{flat}. P_{flat} is the contact load between the flat upper lapping plate and the ceramic ball being lapped. According to Section 2.1.3 Lapping Load, P_{flat} can be three very different values: nominal contact load $P_{flat\ nominal}$, eccentric contact load $P_{flat\ eccentric}$ and contact load under extreme condition $P_{flat\ extreme}$.

Lapping Load	Contact Load	Max. Compressive Stress (GPa)	Radius of Contact Circle (m)	Max. Shear Stress (GPa)	Max. Tensile Stress (GPa)
8.829N/ball	$P_{flat\ nominal}$ 8.829 N	0.923	0.000068	0.286	0.142
	$P_{flat\ eccentric}$ 11.478 N	1.007	0.000074	0.312	0.154
	$P_{flat\ extreme}$ 56.506 N	1.714	0.000125	0.531	0.263
12.753N/ball	$P_{flat\ nominal}$ 12.753 N	1.043	0.000076	0.323	0.160
	$P_{flat\ eccentric}$ 16.579 N	1.139	0.000083	0.353	0.175
	$P_{flat\ extreme}$ 81.619 N	1.937	0.000142	0.601	0.297
18.149N/ball	$P_{flat\ nominal}$ 18.149 N	1.174	0.000086	0.364	0.180
	$P_{flat\ eccentric}$ 23.593 N	1.281	0.000094	0.397	0.196
	$P_{flat\ extreme}$ 116.15 N	2.179	0.00016	0.676	0.334
42.87N/ball	$P_{flat\ nominal}$ 42.87 N	1.563	0.000114	0.485	0.240
	$P_{flat\ eccentric}$ 55.73 N	1.706	0.000125	0.529	0.262
	$P_{flat\ extreme}$ 274.37 N	2.902	0.000212	0.900	0.445
106.63N/ball	$P_{flat\ nominal}$ 106.63 N	2.118	0.000155	0.657	0.325
	$P_{flat\ eccentric}$ 138.63 N	2.312	0.000169	0.717	0.354
	$P_{flat\ extreme}$ 682.46 N	3.932	0.000288	1.219	0.603

Table A4-2 Calculated Hertz contact stresses
for ceramic ball/upper steel lapping plate contact

$P_{flat\ nominal}$ is simply the entire lapping load divided by 15 which is the lapping load denoted throughout this thesis. While $P_{flat\ eccentric}$ is $P_{flat\ nominal}$ multiplied by 1.3 (suppose the eccentric loading effect introduces a 30% higher contact load), and $P_{flat\ extreme}$ is $P_{flat\ nominal}$ multiplied by 6.4.

The effective geometric radius, R_1, in this case is still calculated with (A4-3), but with $R_a = 0.00635$ and $R_b = \propto$ (infinite).

Table A4-2 shows the calculated Hertz contact stresses on ceramic ball/upper steel flat lapping plate contact.

A4.3 Ball/Conformed Curved Surface Contact Stress Analysis

Ball/conformed curved surface contact is presented in the lapping test, when the V-groove is worn and conformed to ceramic balls being lapped.

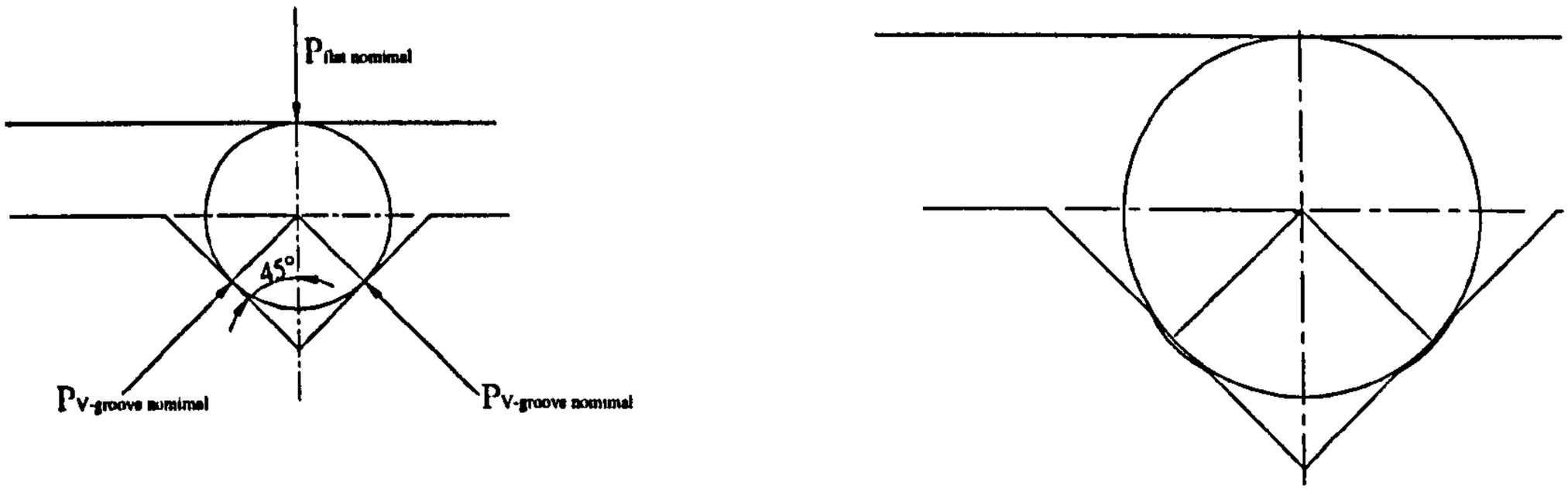

(a) (b)

Fig A4-1 Ball/V-groove contact

Fig A4-1 (a) shows the Ball/V-groove contact under the condition that there is no wear on the V-groove. The contact load between the ball and each side of the V-groove, $P_{V\text{-}groove\ nominal}$, is:

$$P_{flat\ nominal} = 2\, P_{V\text{-}groove\ nominal} \cos(45°)$$

$$P_{V\text{-}groove\ nominal} = \frac{P_{flat\ nominal}}{2\cos(45°)} \qquad \text{(A4-7)}$$

While $P_{V\text{-groove eccentric}}$ is $P_{V\text{-groove nominal}}$ multiplied by 1.3, and $P_{V\text{-groove extreme}}$ is $P_{V\text{-groove nominal}}$ multiplied by 6.4, the same as in A4.2.

Fig A4-1 (b) shows the Ball/V-groove contact under the condition that there are wear tracks on each side of the V-groove. The shape of wear track is conforming to the ball. Assuming the radius of the wear track is 0.008 m, slightly bigger than the ball. In this case, the effective geometric radius, R_1, is still calculated with equation (A4-3), but with $R_a = 0.00635$ m and $R_b = -0.008$ m.

The calculated Hertz contact stresses on ceramic ball/conformed steel V-groove contact is shown in Table A4-3.

Lapping Load	Contact Load	Max. Compressive Stress (GPa)	Radius of Contact circle (m)	Max. Shear Stress (GPa)	Max. Tensile Stress (GPa)
8.829N/ball	$P_{V\text{-groove nominal}}$ 6.242 N	0.287	0.000102	0.089	0.044
	$P_{V\text{-groove eccentric}}$ 8.114 N	0.313	0.000111	0.097	0.048
	$P_{V\text{-groove extreme}}$ 39.949 N	0.533	0.000189	0.165	0.082
12.753N/ball	$P_{V\text{-groove nominal}}$ 9.016 N	0.325	0.000115	0.101	0.050
	$P_{V\text{-groove eccentric}}$ 11.721 N	0.354	0.000126	0.110	0.054
	$P_{V\text{-groove extreme}}$ 57.705 N	0.602	0.000214	0.187	0.092
18.149N/ball	$P_{V\text{-groove nominal}}$ 12.831 N	0.365	0.00013	0.113	0.056
	$P_{V\text{-groove eccentric}}$ 16.680 N	0.398	0.000141	0.123	0.061
	$P_{V\text{-groove extreme}}$ 82.118 N	0.678	0.000241	0.210	0.104
42.87N/ball	$P_{V\text{-groove nominal}}$ 30.309 N	0.486	0.000173	0.151	0.075
	$P_{V\text{-groove eccentric}}$ 39.402 N	0.531	0.000188	0.164	0.081
	$P_{V\text{-groove extreme}}$ 193.977 N	0.903	0.00032	0.280	0.138
106.63N/ball	$P_{V\text{-groove nominal}}$ 75.391 N	0.659	0.000234	0.204	0.101
	$P_{V\text{-groove eccentric}}$ 98.008 N	0.719	0.000255	0.223	0.110
	$P_{V\text{-groove extreme}}$ 482.501 N	1.223	0.000434	0.379	0.188

Table A4-3 Calculated Hertz contact stresses
for ceramic ball/conformed steel V-groove contact

Appendix 5

THE FILM THICKNESS AND THE LUBRICATION REGIME ANALYSIS

The film thickness between the contact surfaces and the lubrication regime are calculated using the classical Elastohydrodynamic (EHD) equations developed by Dowson and Higginson (1966).

$$H_{\min} = 3.63U^{0.68} G^{0.49} W^{-0.073} (1 - e^{-0.68k}) \quad \text{(A5-1)}$$

Here U, G, W and k are dimensionless parameters for speed, materials, load and ellipticity respectively.

$$U = \frac{\eta_0 u}{\Delta R_x} \quad \text{(A5-2)}$$

Where η_0 is dynamic viscosity in the unit of N s/m^2 (pascal second). The SI unit for kinematic viscosity is m^2/s, which is dynamic viscosity divided by density.

The lubricant oil for all tests was Shell Talpa 20 with a kinematic viscosity 94.6 cSt (centistokes) at 40 °C, 8.8 cSt at 100 °C and 66 cSt at 60 °C respectively.

$$66(10^{-6} m^2/s)(900 kg/m^3) = 0.06 Ns/m^2$$

Here 1 cSt = 10^{-6} m^2/s and the density value 900 kg/m^3 is from reference (Moller and Boor 1996), so the calculated dynamic viscosity η_0 at 60 °C is 0.06 Ns/m^2. The actual temperature in the contact region is higher than 60 °C, so take dynamic viscosity η_0 as 0.03 Ns/m^2 for calculation.

In equation (A5-2), u is mean surface velocity in x (motion) direction in the unit of m/s. For pure rolling, the surface velocity u, is

$$u = |\omega_i - \omega_o| \frac{(d_e^2 - d^2)}{4d_e} \quad \text{(A5-3)}$$

Here ω_i is inner contact angular velocity,

$$\omega_i = 2\pi n/60 = 2\pi(10000)/60 = 62800/60 = 1047$$

ω_o is outer contact angular velocity,

$\omega_o = 0.$

d_e is pitch diameter, d is roller contact diameter which is d_o.

$$d_e=(d_o+d_i)/2=(0.0074+2(0.0115)+0.0074)/2=0.0189$$

d_o is the lower ball contact track circle diameter and measured as 0.0115 m. d_i is the upper ball contact track circle diameter and measured as 0.0074 m.

Substitute these values into equation (A5-3),

$$u=1047(0.01189^2 - 0.0115^2)/(4(0.0189)= 3.11 \text{ m/s}$$

In equation (A5-2), Δ is effective elastic modulus,

$$\Delta = \frac{2}{\frac{1-\nu_a^2}{E_a}+\frac{1-\nu_b^2}{E_b}} \qquad \text{(A5-4)}$$

Where ν_a and E_a are Poisson's ratio and Young's modulus for ceramic ball, ν_a =0.27 and E_a= 315 GPa. While ν_b and E_b are Poisson's ratio and Young's modulus for steel ball, ν_a =0.3 and E_a= 207 GPa.

$$\Delta = 2/((1-0.27^2)/315+(1-0.3^2)/207))=272.5 \text{ Gpa}$$

R_x is effective radius,

$$\frac{1}{R_x}=\frac{1}{R_{ax}}+\frac{1}{R_{bx}}=\frac{1}{0.00635}+\frac{1}{0.00635} \quad =0.003175$$

So, equation (A5-2) becomes,

$$U=\frac{\eta_0 u}{\Delta R_x} \quad =(0.03)(3.11)/((2.72\times10^{11})(0.003175))=1.08\times10^{-10}$$

In equation (A5-1), G is dimensionless materials parameter,

$$G=\xi\Delta \qquad \text{(A5-5)}$$

Here ξ is pressure-viscosity coefficient, $\xi=2.3\times10^{-8}$ m^2/N (Hadfield 1992)

In equation (A5-1), W is dimensionless load parameter,

$$W=\frac{P_{contact}}{\Delta(R_x)^2} \qquad \text{(A5-6)}$$

Where $P_{contact}$ is the contact load, in this case, $P_{contact}$= 801 N.

In equation (A5-1), k is dimensionless ellipticity parameter,

$$k = \left(\frac{R_y}{R_x}\right)^{\frac{2}{\pi}} \qquad \text{(A5-7)}$$

Where R_x is effective radius in x direction, and R_y effective radius in y direction, R_x= R_y=0.003175. So, k=1, in this case.

Substitute all these values into equation (A5-1), the dimensionless minimum film thickness parameter (H_{min}) can be calculated. The minimum film thickness (h_{min}) is found from the product of the dimensionless minimum film thickness parameter (H_{min}) and effective radius.

$$h_{min}=H_{min}R_x \qquad \text{(A5-8)}$$

The lubrication regime (lambda) is found from the ratio of minimum film thickness to composite surface roughness,

$$\lambda= h_{min}/\sigma \qquad \text{(A5-9)}$$

where σ is composite surface roughness,

$$\sigma = \sqrt{\left(R_{q1}^2 + R_{q2}^2\right)} \qquad \text{(A5-10)}$$

R_{q1} and R_{q2} are the rms roughness values for the two contacting surfaces. According to Elastohydrodynamic Lubrication theory, if $\lambda>3$, a full fluid film will separate the two surfaces, if $1<\lambda<3$, some asperities contact will occur.

The calculation is carried out on Microsoft Excel 97. Table A5-1 is the calculated minimum film thickness and lambda ratio on 0.5" (12.7mm) ceramic balls with different surface roughness values (as described in Section 3.1.2) in contact with steel balls under 4-ball rolling test configuration, $P_{contact}$=800 N, spindle speed 10,000rpm.

Sample	R_{q1} (m) ceramic	R_{q2} (m) steel	h_{min} (m)	λ
A	0.7×10^{-8}	3.76×10^{-8}	1.2467×10^{-7}	3.2597
B	2.1×10^{-8}	3.76×10^{-8}	1.2467×10^{-7}	2.8948
C	0.4×10^{-8}	3.76×10^{-8}	1.2467×10^{-7}	3.2971
D	0.3×10^{-8}	3.76×10^{-8}	1.2467×10^{-7}	3.3052
E	13.2×10^{-8}	3.76×10^{-8}	1.2467×10^{-7}	0.9083
F	11.8×10^{-8}	3.76×10^{-8}	1.2467×10^{-7}	1.0007
G	1.0×10^{-8}	3.76×10^{-8}	1.2467×10^{-7}	3.2043

Table A5-1 Calculated minimum film thickness and lambda ratio

Appendix 6

FEA MODELLING RESULTS

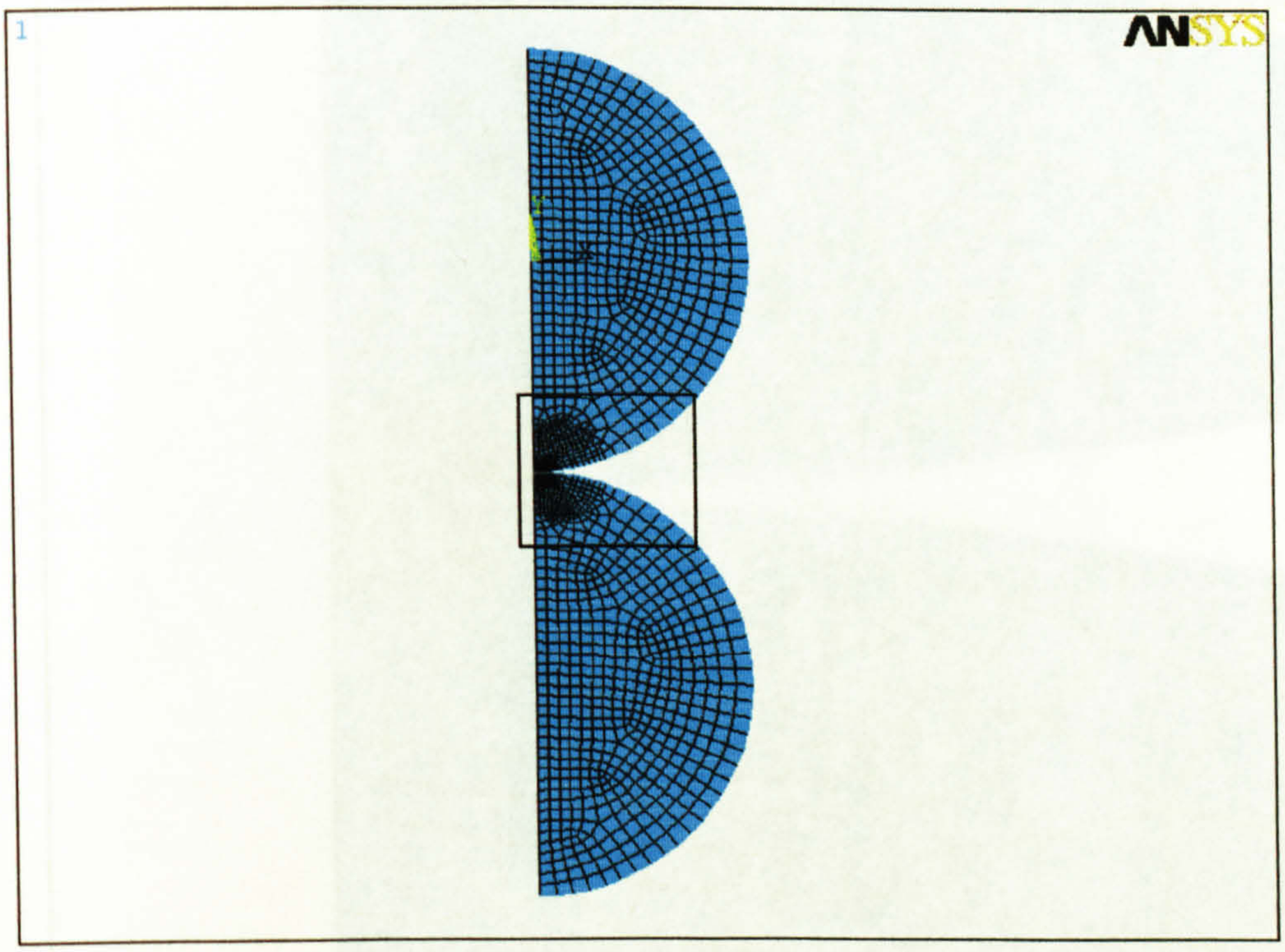

A6.1 Overall mesh distribution

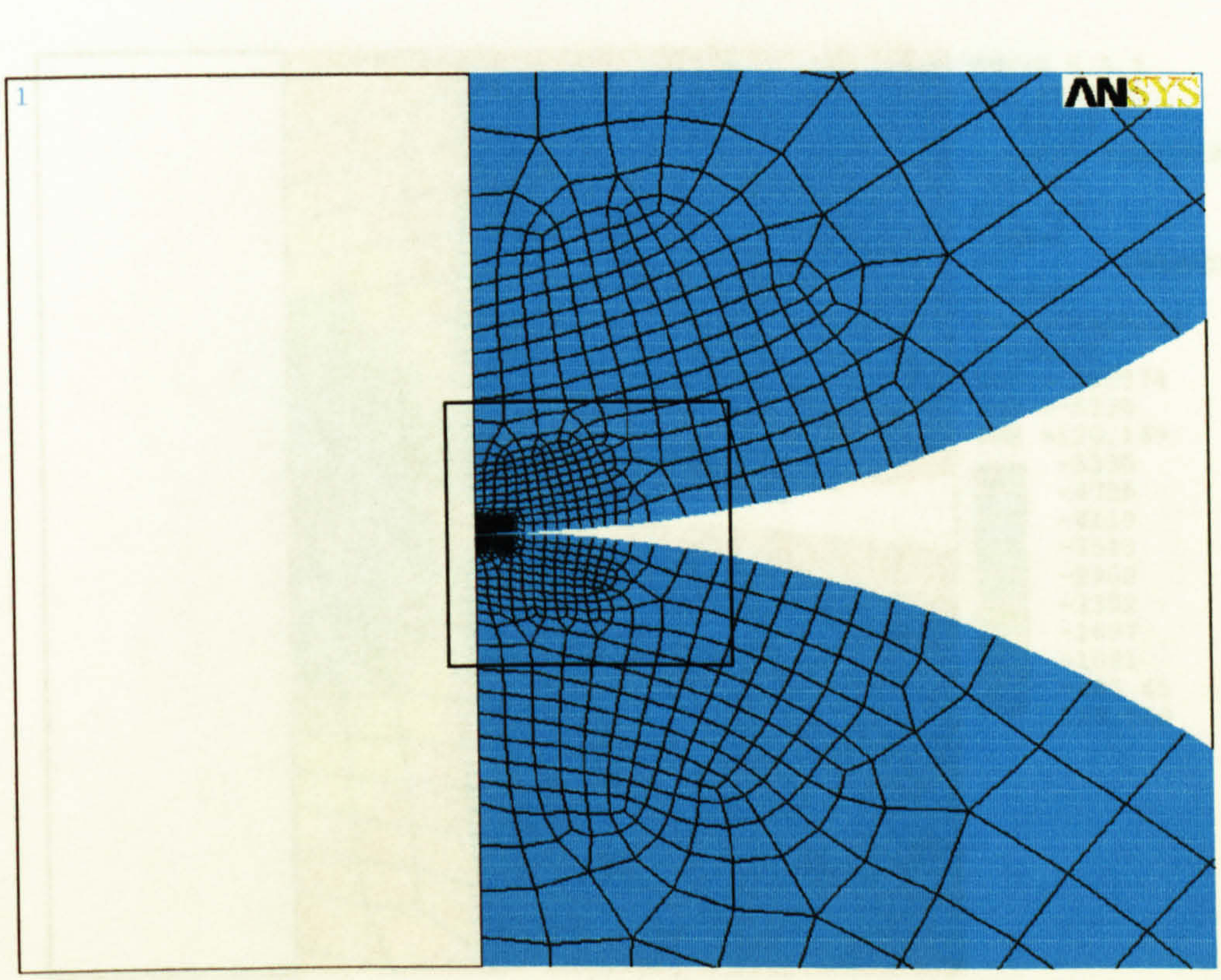

A6.2 Local meshes within contact region at low magnification.

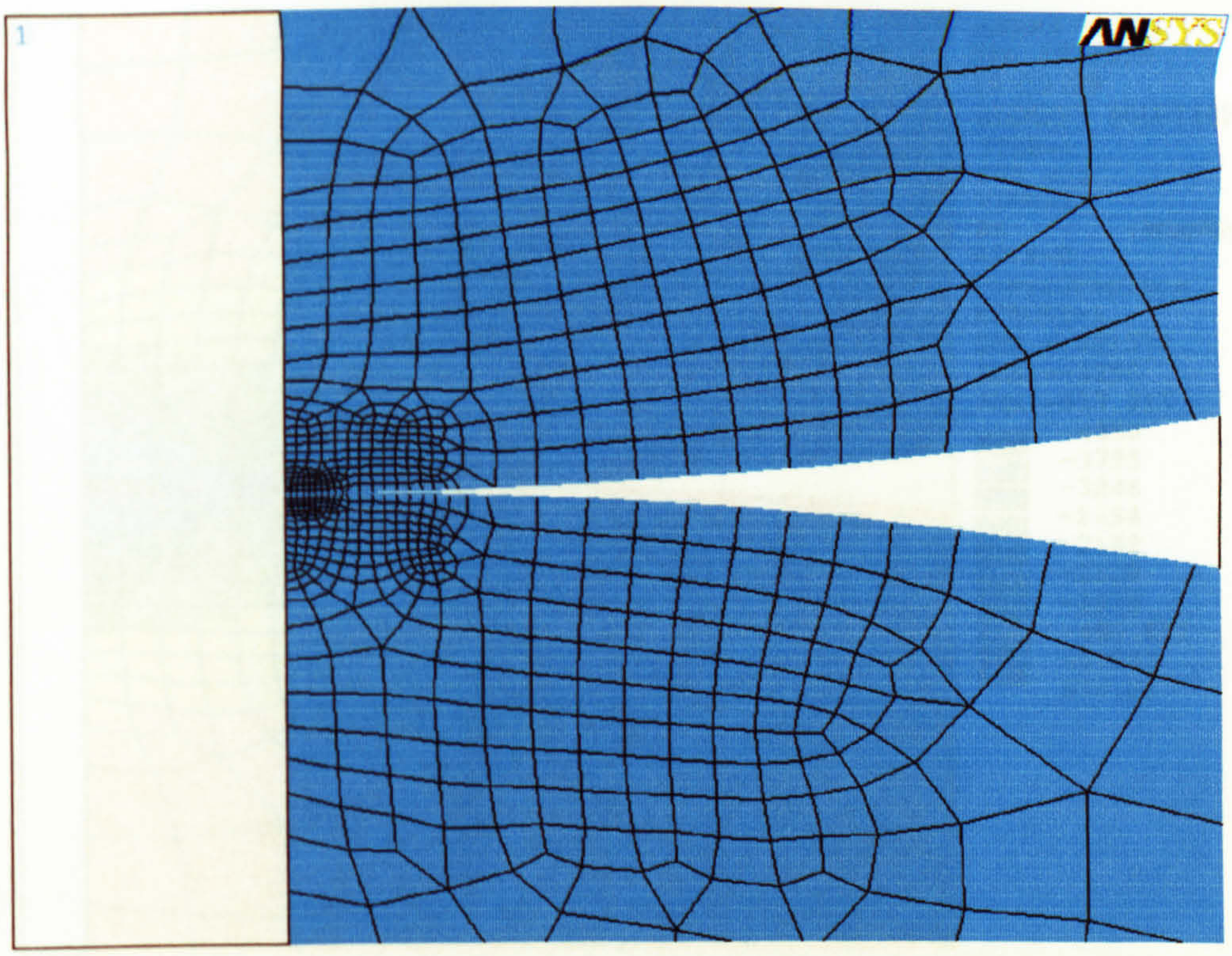

A6.3 Local meshes within contact region at high magnification.

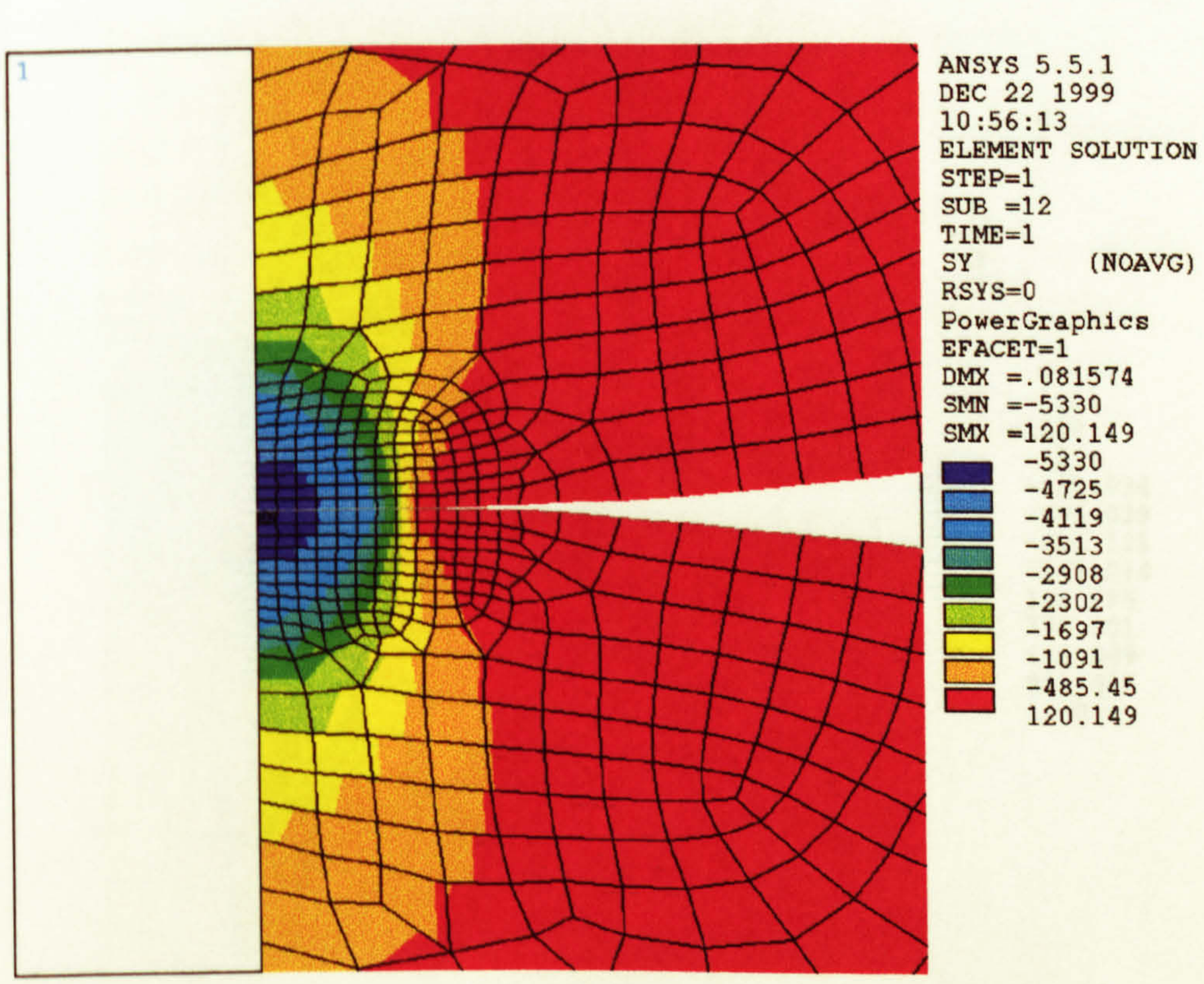

A6.4 Stress contour of Y stress (along axisymmetric axis)
Ceramic/Steel 400 N

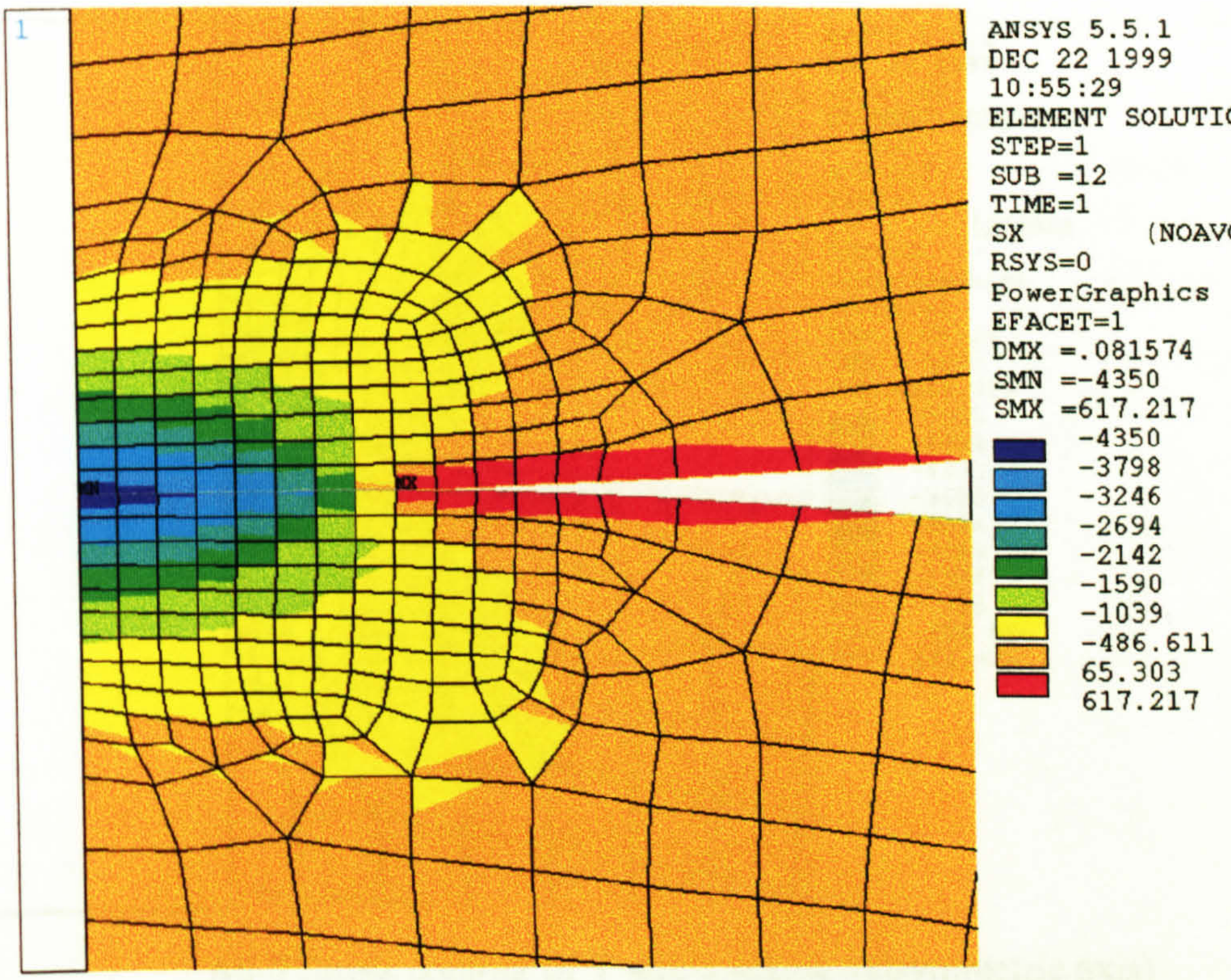

A6-5 Stress contour of X stress (perpendicular to axisymmetric axis)
Ceramic/Steel 400 N

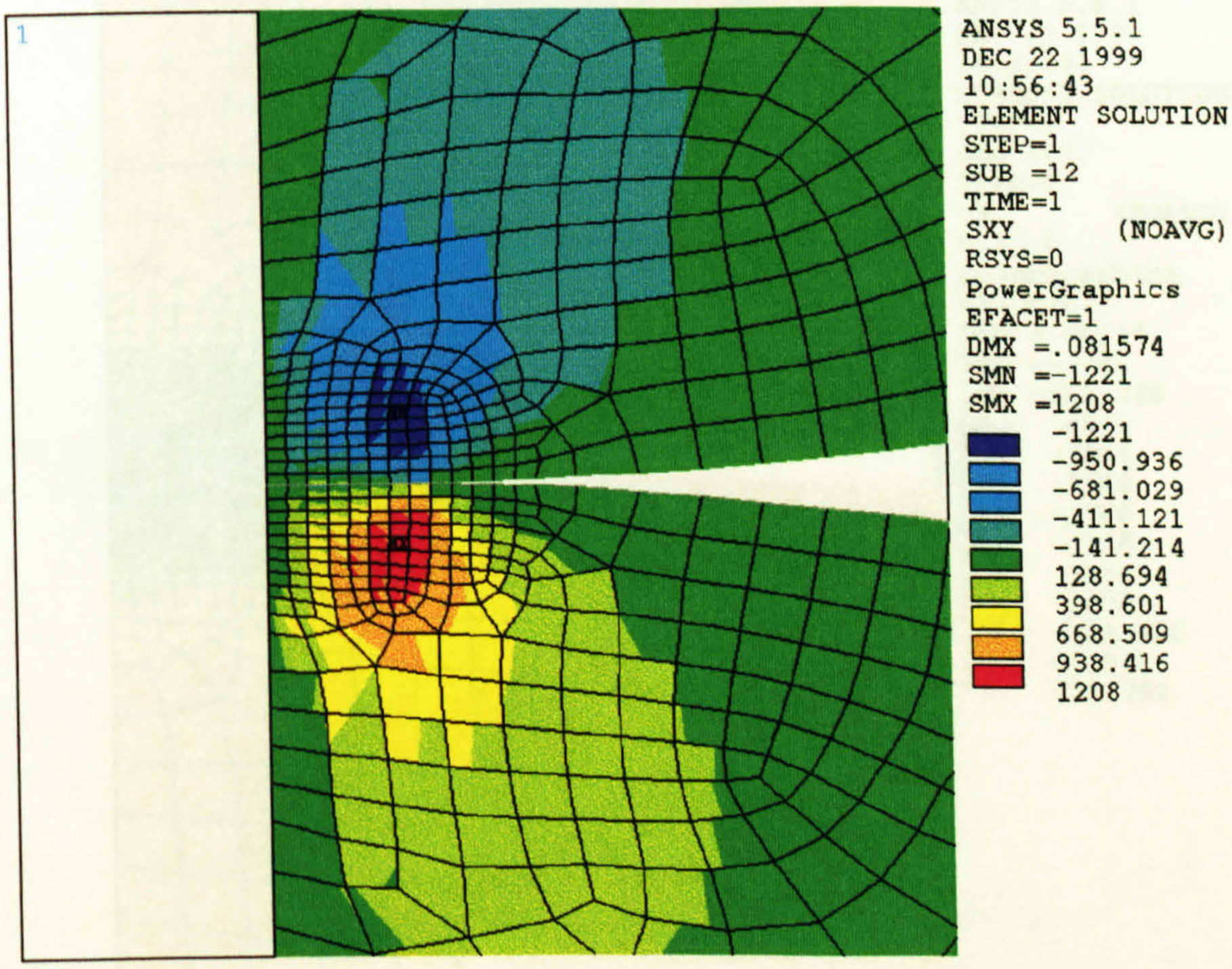

A6.6 Stress contour of XY shear stress
Ceramic/Steel 400 N

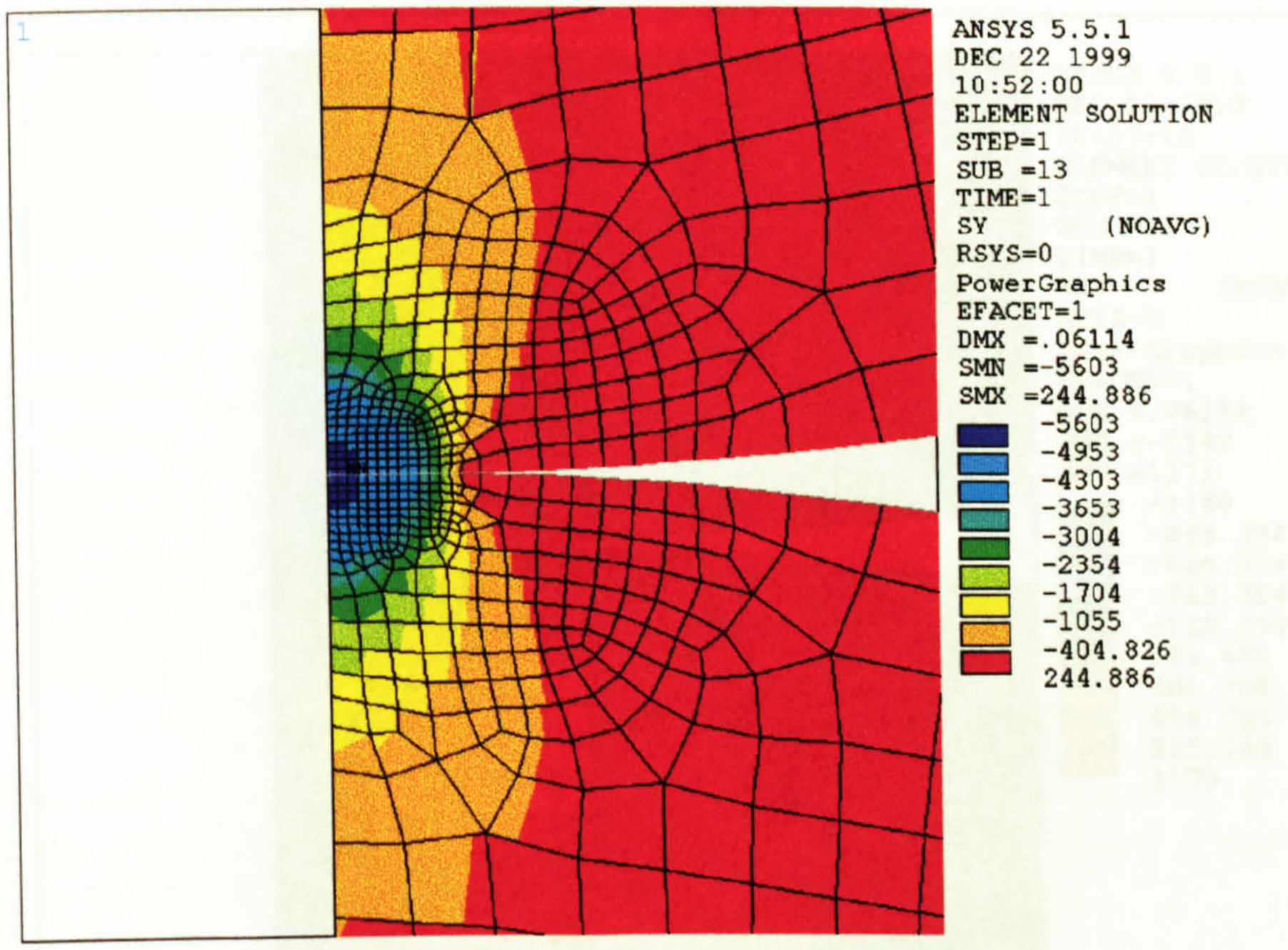

A6-7 Stress contour of Y stress (along axisymmetric axis)
Ceramic/Steel 400 N with imposed residual stresses

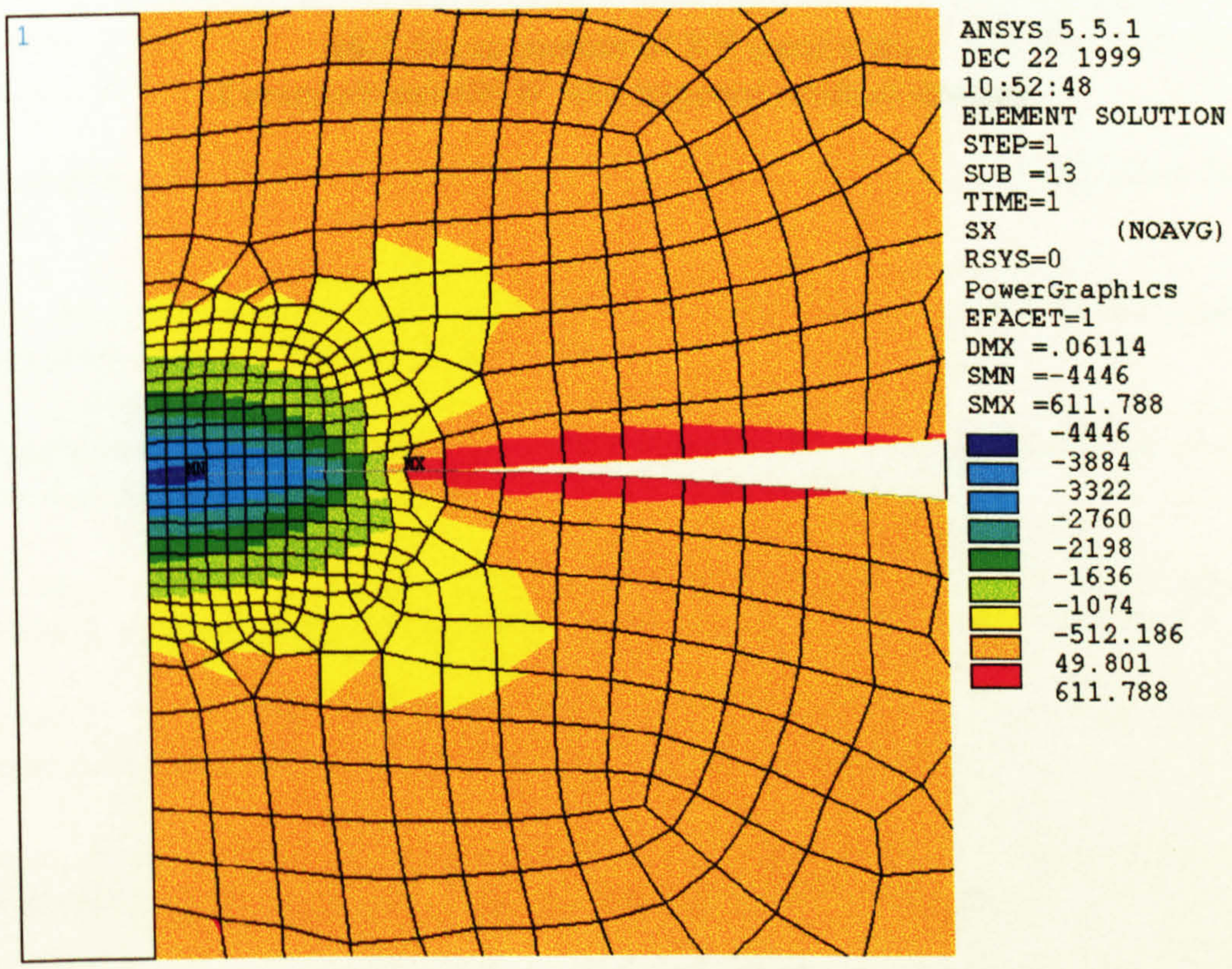

A6-8 Stress contour of X stress (perpendicular to axisymmetric axis)
Ceramic/Steel 400 N with imposed residual stresses

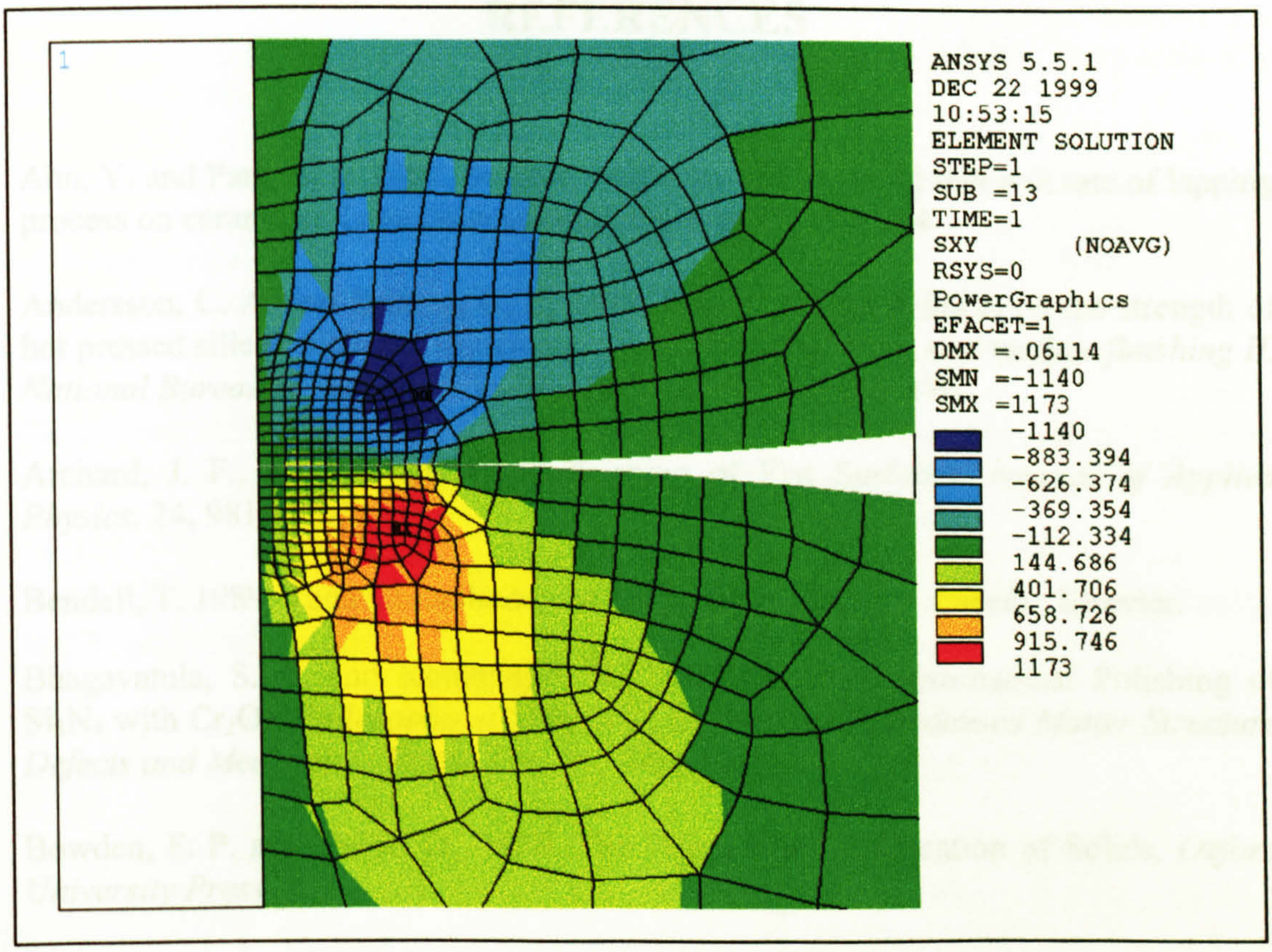

A6-9 Stress contour of XY shear stress
Ceramic/Steel 400 N with imposed residual stresses

REFERENCES

Ahn, Y. and Park, S. S. 1997. Surface roughness and material removal rate of lapping process on ceramics. *Ksme International Journal,* 11, 494-504.

Andersson, C. A. and Bratton, R. J., 1979. Effect of surface finish on the strength of hot pressed silicon nitride. *The science of ceramic machining and surface finishing II, National Bureau of Standards Special Publication 562,* 463-476.

Archard, J. F., 1953. Contact and Rubbing of Flat Surfaces. *Journal of Applied Physics,* 24, 981-988.

Bendell, T. 1989. Taguchi methods, 1st European conference Papers. Elsevier.

Bhagavatula, S. R. and Komanduri, R. 1996. On Chemomechanical Polishing of Si_3N_4 with Cr_2O_3. *Philosophical Magazine A: Physics of Condensed Matter Structure Defects and Mechanical Properties*, 74, 1003-1017.

Bowden, F. P. and Tabor, D., 1950. The Friction and Lubrication of Solids. *Oxford University Press.*

Braza, J. F., Cheng, H. S., Fine, M. E., Gangopadhyay, A. K., Keer, L. M. and Worden, R. E., 1989. Mechanical failure mechanisms in ceramic sliding and rolling contacts. *Tribology Transactions,* 32, 1-8.

Buckingham, E. 1915. Model experimnets and the form of empirical equations *Trans ASME*, 37.

Buijs, M. and Korpelvanhouten, K., 1993a. 3-Body Abrasion of Brittle Materials as Studied by Lapping. *Wear,* 166, 237-245.

Buijs, M. and Korpelvanhouten, K., 1993b. A Model for Lapping of Glass. *Journal of Materials Science,* 28, 3014-3020.

Bulsara, V. H., Ahn, Y., Chandrasekar, S. and Farris, T. N., 1998. Mechanics of polishing. *Journal of Applied Mechanics-Transactions of the ASME,* 65, 410-416.

Burke, J. J., Gorum, A. E. and Katz, R. N. (Eds.). 1974. *Ceramics for high performance application Vol. I,* Brook Hill Publishing, Chestnut, MA.

Burke, J. J., Gorum, A. E. and Katz, R. N. (Eds.). 1978. *Ceramics for high performance application Vol. II,* Brook Hill Publishing, Chestnut, MA.

Burrier, H. I., 1996. Optimizing the structure and properties of silicon nitride for rolling contact bearing performance. *Tribology Transactions,* 39, 276-285.

Chandrasekar, S., Shaw, M. C. and Bhushan, B., 1987. Comparison of Grinding and Lapping of Ferrites and Metals. *Journal of Engineering for Industry-Transactions of the ASME,* 109, 76-82.

Chandrasekar, S., Kokini, K. and Bhushan, B., 1988. Effect of abrasive properties on surface finishing damage in ceramics. In: *Intersociety Symposium on Machining of Advanced Ceramic Materials and Components Presented at the Winter Annual Meeting of the American Society of Mechanical Engineers,* Chicago, IL, USA, 27 Nov - 02 Dec 1988, 33-46.

Chandrasekar, S., Kokini, K. and Bhushan, B., 1990. Influence of abrasive properties on residual stresses in lapped ferrite and alumina. *Journal of the American Ceramic Society,* 73, 1907-1911.

Chandrasekar, S. and Farris, T. N., 1997. Machining and surface finishing of brittle solids. *Sadhana - Academy Proceedings in Engineering Sciences,* 22, 473-481.

Chao, L. Y., 1995. Development of Silicon Nitride for Rolling-Contact Bearing application: A Review. *Journal of Materials Education,* 17, 245-303.

Chao, L. Y., Lakshminarayanan, R., Iyer, N., Lin, G. Y. and Shetty, D. K., 1998. Transient wear of silicon nitride in lubricated rolling contact. *Wear,* 223(1-2), 58-65.

Chen, C. and Inasaki, I., 1991. Optimization of Ceramics Lapping. *Transactions of the North American Manufacturing Research Institution of SME*, 108-112.

Childs, T. H. C., Jones, D. A., Mahmood, S., Zhang, B., Kato, K. and Umehara, N., 1994. Magnetic Fluid Grinding Mechanics. *Wear,* 175, 189-198.

Childs, T. H. C., Mahmood, S. and Yoon, H. J., 1995. Magnetic fluid grinding of ceramic balls. *Tribology International,* 28, 341-348.

Cochran, W. G. and Cox, G. M., 1968. Experimental designs (2nd edition). Wiley, New York

Cundill, R. T., 1983. Light-weight material for the rolling elements of aircraft bearings. *Ball Bearing Journal,* 216, 33-36.

Cundill, R. T., 1992a. High-precision silicon nitride balls for bearings, *Commercial Applications of Precision Manufacturing at the Sub-Micro Level, SPIE Vol. 1573*, 75-86

Cundill, R. T., 1992b. Material Selection and Quality for Ceramic Rolling Elements. In: *4th International Symposium on Ceramic Materials and Components for Engines,* 905-912.

Cundill, R. T., 1997. Impact Resistance of Silicon Nitride Balls. In: *6th international symposium on ceramic materials & components for engines,* Arita, Japan.

Cullty, B. D. 1996. Elements of X-ray diffraction (Second Edition). Addison-Wesley Publishing Company

Dill, J. F., Gardos, M. N. and Hardisty, R. G. 1997. An evaluation of indentation and finishing properties of bearing grade silicon nitrides. *Journal of Engineering for Gas Turbines and Power-Transactions of the ASME,* 119, 196-199.

Divakar, R., 1994. Sintered silicon carbides with controlled porosity for mechanical face seal applications. *Lubrication Engineering,* 50, 75-80.

Dowson, D. and Higginson, G. R., Elasto-Hydrodynamic Lubrication, Pergamon Press, 1966.

Effner, U. and Woydt, M., 1995. Economical Machining and Tribological Rolling Wear of Ceramics. *Proc. Int. Tribology Conference,* I, 503-508.

Effner, U. and Woydt, M., 1998. Importance of machining on tribology of lubricated slip-rolling contacts of Si_3N_4, SiC, Si_3N_4-TiN and ZrO_2. *Wear,* 216, 123-130.

Evans, A. G., 1980. Fatigue in Ceramics. *International Journal of Fracture,* December, 485-498.

Feng, G., 1993. Surface Grinding Induced Phase Transformation and Residual Stresses in Al_2O_3-ZrO_2 Composites (PhD Thesis). *University Microfilms International,* Ann Arbor, MI, USA.

Field, M. and Kahles, J. F., 1971. Review of Surface Integrity of Machined Components. *Annals of CIRP,* 2, 153-163.

Firestone, R. F., 1978. Abrasionless Machining Methods for Ceramics. In: *The science of ceramic machining and surface finishing II : proceedings of a symposium held at the National Bureau of Standards, Gaithersburg, Maryland,* 261-281.

Fowlkes, W. Y. and Creveling, C. M., 1995. Engineering methods for robust product design, Using Taguchi Methods in technology and product development. Addison-Wesley Publishing Company.

Gardos, M. N. and Hardisty, R. G., 1993. Fracture Toughness-Dependent and Hardness-Dependent Polishing Wear of Silicon-Nitride Ceramics. *Tribology Transactions,* 36, 652-660.

Gazza, G. E., Kats R. N. and Knoch H., 1979. Factors influencing the quality of fully dense silicon nitride. In: *Proceedings of the 6th Army Materials Technology Conference, Ceramics for High-performance Applications, Reliability.* 335 –345.

Gee, M. G. and McCormick, N. J. 1996. 3D Topography Measurement of Ceramics. The National Physical Laboratory, London.

Gent, T. and Tucker, D., 1995. Lifetime Predictions of a Glass-Ceramic With Machined Flaws. *Journal of Materials Science,* 30, 1535-1538.

Guha, S. K. and Chatterjee, S., 1980. Effect of Lapping and Polishing on the Strength of Alumina Ceramics. *Transactions of the Indian Ceramic Society,* 39, 127-130.

Hadfield, M., 1992. Rolling contact fatigue of ceramics (PhD Thesis). *University Microfilms International,* Ann Arbor, MI, USA.

Hadfield, M., Stolarski, T. A. and Cundill, R. T., 1993a. Failure Modes of Ceramics in Rolling-Contact. *Proceedings of the Royal Society of London, Series A: Mathematical and Physical Sciences,* 443, 607-621.

Hadfield, M., Fujinawa, G., Stolarski, T. A. and Tobe, S., 1993b. Residual-Stresses in Failed Ceramic Rolling-Contact Balls. *Ceramics International,* 19, 307-313.

Hadfield, M., Stolarski, T. A., Cundill, R. T. and Horton, S., 1993c. Failure Modes of Ceramic Elements with Ring-Crack Defects. *Tribology International,* 26, 157-164.

Hadfield, M., and Stolarski, T. A., et al., 1993d. Delamination of ceramic balls in rolling contact, *Ceramics International,* 19, 151-158.

Hadfield, M. and Stolarski, T. A., 1995a. Observations of Delamination Fatigue On Precracked Ceramic Elements in Rolling-Contact. *Ceramics International,* 21, 125-130.

Hadfield, M. and Stolarski, T. A., 1995b. Observations of Lubricated Rolling-Contact Fatigue on Silicon-Nitride Rods. *Ceramics International,* 21, 13-19.

Hadfield, M. and Tobe, S., 1998. Residual stress measurements of hot isostatically pressed silicon nitride rolling elements. *Ceramics International,* 24, 387-392.

Hah, S. R. and Fischer, T. E., 1998. Tribochemical polishing of silicon nitride. *Journal of the Electrochemical Society,* 145, 1708-1714.

Harris, T. A. 1990. Rolling Bearing Analysis (Third Edition). New York, John Wiley & Sons Inc.

Hasselt, R. V., 1969. The Functional Behaviour of Surfaces. Some Mechanical Function. *Annals of the CIRP,* XVII, 217-224.

He, Y. and Winnubst, L.1997. Influence of porosity on friction and wear of tetragonal zirconia polycrystal. *Journal of the American Ceramic society*, 80, 2, 377 –380.

Hockey, B. J., and Rice, R. W., 1979. *The science of ceramic machining and surface finishing II : proceedings of a symposium held at the National Bureau of Standards, Gaithersburg, Maryland, November 13-15, 1978,* Gaithersburg, MD.

Holm, R., 1946. Electrical Contact. *H. Gerbers, Stockholm,*

ISO 4505-1978(E) 1978. International Standards Hardmetals—Metallographic Determination of Porosity and Uncombined Carbon, International Organization for Standardization

Ichikawa, S., Ona, H., Yoshimoto, I. and Kobayashi, A., 1993. Proposal of new lapping method for ceramic balls. *CIRP Annals,* 42, 421-424.

Imanaka, O. and Okutomi, M., New Concepts on Surface Finishing and its Application to Ceramics -- Recent Progress in Ultra-Fine Finishing in Japan. In: *The science of ceramic machining and surface finishing II : proceedings of a symposium held at the National Bureau of Standards, Gaithersburg, Maryland, November 13-15, 1978,* , 157-169.

Jiang, M. and Komanduri, R., 1998. On the finishing of Si3N4 balls for bearing applications. *Wear,* 215, 267-278.

Jisheng, E., Stolarski, T. A. and Gawne, D. T., 1996. Tribochemically assisted wear of silicon nitride ball. *Journal of the European Ceramic Society,* 16, 25-34.

Johnson, K. L., 1985. Contact Mechanics. Cambridge University Press.

Kurobe, T., Kakuta, H. and Onoda, M., 1996. Spin angle control lapping of balls (1st report) - theoretical analysis of lapping mechanism. *Seimitsu Kogaku Kaishi/Journal of the Japan Society for Precision Engineering,* 62, 1773-1777.

Kurobe, T., Kakuta, H. and Onoda, M., 1997. Spin angle control lapping of balls (2nd report) - lapping of silicon nitride ball. *Seimitsu Kogaku Kaishi/Journal of the Japan Society for Precision Engineering,* 63, 726-730

Lawn, B. and Wilshaw, R. 1975 Indentation fracture: Principles and applications. *J of Mat. Sci.* 10. 1049-1081.

Lakshminarayanan, R., Chao, L. Y., Iyer, N. and Shetty, D. K., 1997. Wear of steel in rolling contact with silicon nitride. *Wear,* 210, 278-286.

Latella, B. A., O'connor, B. H., Padture, N. P. and Lawn, B. R. 1997. Hertzian contact damage in porous alumina ceramics, *Journal of American Ceramics Society,* 80, 4, 1027-1031.

Liu, Y. P., 1994. The Dependence of Roller Bearing Surface Fatigue on Lambda Ratio and Other Variables. *SEA Technical Paper Series 941788.*

Marinescu, I., Tonshoff, H. and Inasaki, I. 2000, Handbook of ceramic grinding and polishing, New York, Noyes Publications/William Andrew Publishing, LLC.

Marshall, D. B., Evans, A. G., KhuriYakub, B. T., Tien, J. W. and Kino, G. S., 1983. Nature of Machining Damage in Brittle Materials. *Proceedings of The Royal Society of London, Series A: Mathematical and Physical Sciences,* 385, 461-475.

McColm, I. J. and Clark, N. J., 1988. Forming, shaping, and working of high performance ceramics. Blackie and Son Ltd., Glasgow, New York.

Moller, U. J. and Boor, U., 1996. Lubrications in operation, Mechanical Engineering Publication Ltd.

Murakami, Y., Kaneta, M. and Yatsuzuka,H., 1985. Analysis of surface crack-propagation in lubricated rolling-contact, *ASLE Transactions,* 28 (1), 60-68.

NLG, 4776 D, 1990. Parameters R_K, R_{PK}, R_{VK}, M_{r1}, M_{r2} for the Description of the Material Portion (Profile Bearing Length Ratio) in the Roughness Profile. *Normenausschuß Länge und Gestalt (NLG) im Deutsches Institut füNormung, Berlin, Germany.*

Ovri, J. E. O. and Davies, T. J., 1987. Effect of Surface Condition on the Flexural Strength of Sintered Silicon Nitride. *Journal of Materials Science Letters,* 6, 849-850.

Parker, R. J. and Zaretsky, E. V., 1975. Fatigue life of high-speed bearing with silicon nitride balls. *Journal of Lubrication Technology, Transactions of the ASME,* JULY, 350-357.

Pfeiffer, W. and Hollstein, T., 1997. Influence of grinding parameters on strength-dominating near-surface characteristics of silicon nitride ceramics. *Journal of the European Ceramic Society,* 17, 487-494.

PowellDogan, C. A., Heuer, A. H., Ready, M. J. and Merriam, K., 1991. Residual-stress-induced grain pullout in a 96% alumina. *Journal of the American Ceramic Society,* 74, 646-649.

Pruitt, L. and Suresh, S., 1993. Cyclic Stress-Fields for Fatigue Cracks in Amorphous Solids Experimental Measurements and Their Implications. *Philosophical Magazine A: Physics of Condensed Matter Structure Defects and Mechanical Properties,* 67, 1219-1245.

Rice, R. W. and Schneider, S. J., 1972. The science of ceramic machining and surface finishing: proceedings of a symposium held at the National Bureau of Standards. NBS Special Publications.

Rice, R. W., 1998. Porosity of ceramics. Marcel Dekker Inc., New York.

Sarkar, B. K., 1995. Fatigue of brittle materials - A critical appraisal. *Bulletin of Materials Science,* 18, 755-772.

Sornakumar, T., Annamalai, V. E., Krishnamurthy, R. and Gokularathnam, C. V., 1994. Lapping of composite of Y-TZP and Ce-TZP. *Journal of Materials Science Letters,* 13, 187-189.

Stokes, R. J., 1972. The Effect of Surface Finishing on Material and Other Physical Properties of Ceramics. *The science of ceramic machining and surface finishing; proceedings of a symposium held at the National Bureau of Standards, NBS special publication,* , 343-353.

Stolarski, T. A., 1989. Fracture-Mechanics and the Contact Between a Pair of Surface Asperities During Rolling. *International Journal of Engineering Science,* 27, 169-179

Stolarski, T. A. and Tobe, S., 1997. The effect of accelerated material removal on roundness and residual stresses in ceramic balls. *Wear,* 205, 206-213.

Stolarski, T. A. and Jisheng, E., 1998. Effect of water in oil based slurry on wear of silicon nitride. *British Ceramic Transactions,* 97, 61-67.

Taguchi, G., 1992a. Taguchi Methods ---- Research and Development. ASI Press, Dearborn, MI.

Taguchi, G., 1992b. Taguchi on robust technology development, bringing quality engineering upstream. ASME Press, New York.

Tallian, T. E., 1996. A data-fitted rolling bearing life prediction model-Part II: Model fit to the historical experimental database. *Tribology Transactions,* 39, 259-268.

Tani, Y. and Kawata, K., 1984. Development of High-Efficient Fine Finishing Process Using Magnetic Fluid. *CIRP Annals,* 33, 217-220.

Timoshenko, S. and Woinowsky-Krieger, S., 1981. Theory of Plates and Shells. MacGraw-Hill International Book Company

Tomlinson, W. J. and Newton, R. C., 1990. Effect of Grinding, Lapping and Various Surface Treatments On the Strength of Silicon-Nitride. *Ceramics International,* 16, 253-257.

Tourret, R. and Wright, E. P. (Eds.) 1977. Rolling contact fatigue: Performance testing of lubricants. Heyden & Son LTD, London

Umehara, N. and Kato, K., 1988. Study on magnetic fluid grinding (1st report, The effect of the floating pad on removal rate of Si_3N_4 balls). *Nippon Kikai Gakkai Ronbunshu, C Hen/Transactions of the Japan Society of Mechanical Engineers, Part C,* 54, 1599-1604.

Umehara, N. and Kato, K., 1996. Magnetic fluid grinding of advanced ceramic balls. *Wear,* 200, 148-153.

Wachtman, J. B. 1996. Mechanical properties of ceramics. Wiley, New York.

Wang, Y. H., M, 2000a. The influence of ring crack location on the rolling contact fatigue failure of lubricated silicon nitride: experimental studies. *Wear,* 243, 157-166.

Wang, Y. H., M, 2000b. The influence of ring crack location on the rolling contact fatigue failure of lubricated silicon nitride: fracture mechanics analysis. *Wear,* 243, 167-174.

Westkaemper, E. and Hoffmeister, H. W., 1996. Function-oriented lapping and polishing of ceramic rolling elements through characterization of the workpiece surface. *CIRP Annals - Manufacturing Technology,* 45, 529-532.

Westkaemper, E. and Hoffmeister, H. W., 1997. Function-oriented surface characterization of lapped and polished ceramic rolling elements. In: *7th Int. Conf. on Metrology and Properties of Engineering Surfaces,* 432-443.

Woydt, M. and Effner, U., 1996a. Generation of Surface Texture by Machining, the Influence on the Tribological Behaviour and the Characterization by means of Ultrasonics. In: *Por. Material Week Symposium 5,* 153-158.

Woydt, M. and Effner, U., 1996b. Zirkondioxid Ein neuer Wälzlagerwerkstoff?" (Zirconia: A new Rolling Bearing Material?). *Keramische Zeitschrift,* 48, 389-393.

Woydt, M. and Effner, U., 1997. Influence of machining on friction and wear of lubricated ceramics in slip-rolling contacts. *Machining Science and Technology,* 1, 275-287.

Wu, C. C. and McKinney, K. R., 1979. The effect of surface finishing on the strength of commercial hot pressed Si3N4. *The science of ceramic machining and surface finishing II, National Bureau of Standards Special Publicatio*n *562,* , 477-481.

Wu, Y. 1989. Taguchi methods case studies from the US and Europe. ASI Press, Dearborn, MI

Yu, K. W., 1999. A new stress-based fatigue life model for rolling bearings (PhD Thesis). *University Microfilms International,* Ann Arbor, MI, USA.

Zanoria, E. S., 1998. Effect of Machined Surface Condition on the Repeated Impact Behavior of Silicon Nitride. *Wear,* 218, 66-77.

BIBLIOGRAPHY

Adachi, K., Kato, K. and Chen, N., 1997a. Wear map of ceramics. *Wear,* 203-204, 291-301.

Amada, S. and Ichimura, K., 1997. Surface topography and mechanical characteristics of ceramics roughened by erosion. *Nippon Seramikkusu Kyokai Gakujutsu Ronbunshi/Journal of the Ceramic Society of Japan,* 105, 141-146.

Asada, S., Fukuda, K. and Ueki, M., 1997. Surface damage of engineering ceramics in rolling contact. *Journal of the Ceramic Society of Japan,* 105, 238-240.

Babini, G. N., Haviar, M. and Šajgalík, P., 1997. *Engineering ceramics '96 : higher reliability through processing,* Dordrecht, Boston.

Barsoum, M. W., 1997. *Fundamentals of ceramics,* McGraw Hill, New York.

Becker, A. and Seifert, B., 1997. Simulation of wear with a FE type model using a steady state rolling formulation. *International Conference on Contact Mechanics, Proceedings,* 119-128.

Blau, P. J., Martin, R. L. and Zanoria, E. S., 1997. Effects of surface grinding conditions on the reciprocating friction and wear behavior of silicon nitride. *Wear,* 203-204, 648-657.

Fleming, J. R. and Suh, N. P., 1977a. Mechanics of Crack Propagation in Delamination Wear. *Wear,* 44, 39-56.

Fleming, J. R. and Suh, N. P., 1977b. Relationship Between Crack Propagation Rates and Wear Rates. *Wear,* 44, 57-64.

Gatzen, H. H. and Maetzig, J. C., 1997. Nanogrinding. *Precision Engineering,* 21, 134-139.

Geiger, M., Roth, S. and Becker, W., 1998. Influence of laser-produced microstructures on the tribological behaviour of ceramics. *Surface & Coatings Technology,* 100-101, 17-22.

Hadfield, M., 1998. Failure of silicon nitride rolling elements with ring crack defects. *Ceramics International,* 24, 379-386.

Jisheng, E., Stolarski, T. A. and Gawne, D. T., 1997. Mechanical and tribochemical effects during accelerated wear of silicon nitride in diamond slurries. *Tribology Transactions,* 40, 597-604.

Kahlman, L., 1997. *Engineering ceramics for tribological systems manufacture, properties and testing,*, Göteborg Chalmers University of Technology, Department of Ceramic Technology.

Kalin, M., Vizintin, J., Novak, S. and Drazic, G., 1997. Wear mechanisms in oil-lubricated and dry fretting of silicon nitride against bearing steel contacts. *Wear,* 210, 27-38.

Khurshudov, A. and Kato, K., 1997. Wear mechanisms in reciprocal scratching of polycarbonate, studied by atomic force microscopy. *Wear,* 205, 1-10.

Komanduri, R. and Ramamohan, T. R., 1994. On the Mechanisms of Material Removal in Fine Grinding and Polishing of Advanced Ceramics and Glasses. , K 38-K 51.

Kumar, A. M., Hahn, G. T. and Rubin, C. A., 1993. A Study of Subsurface Crack Initiation Produced By Rolling-Contact Fatigue. *Metallurgical Transactions a-Physical Metallurgy and Materials Science,* 24, 351-359

Kunz, R. R., Clark, H. R., Nitishin, P. M., Rothschild, M. and Ahern, B. S., 1996. High resolution studies of crystalline damage induced by lapping and single-point diamond machining of Si(100). *Journal of Materials Research,* 11, 1228-1237.

Melander, A., 1997. A finite element study of short cracks with different inclusion types under rolling contact fatigue load. *International Journal of Fatigue,* 19, 13-24.

Melander, A., 1998. Simulation of the behaviour of short cracks at inclusions under rolling contact fatigue loading - specially the effect of plasticity. *ASTM Special Technical Publication,* 1327, 70-86.

Mitchell, D. J., Sabia, R., Whitney, E. D. and Adair, J. H., 1997. Characterizing the performance of advanced rolling element materials. *Ceramic Engineering and Science Proceedings,* 18, 85-92.

Niezgoda, T., Malachowski, J. and Boniecki, M., 1998. Finite element simulation of vickers microindentation on alumina ceramics. *Ceramics International,* 24, 359-364.

Niizeki, S. and Matsunaga, S., 1998. Trends of research and development in rolling bearings for special environments. *Journal of Japanese Society of Tribologists,* 43, 450-455.

Nishioka, T., Mochida, Y., Yamamoto, T. and Yamakawa, A., 1998. Effects of grinding conditions and grinding wheel structure on the grinding mechanism of fine ceramics. *SEI Technical Review,* , 130-136.

Nosaka, M., Oike, M., Kikuchi, N. and Mayumi, T., 1997. Tribo-characteristics of cryogenic hybrid ceramic ball bearings for rocket turbopumps: Self-lubricating performance. *Tribology Transactions,* 40, 21-30.

Obara, S. and Suzuki, M., 1997. Long-term operation of Si_3N_4 ball bearings at temperatures up to 650 degrees C in ultra-high vacuum. *Tribology Transactions,* 40, 31-40.

Parthasarathy, T. A. and Kerans, R. J., 1997. Predicted effects of interfacial roughness on the behavior of selected ceramic composites. *Journal of the American Ceramic Society,* 80, 2043-2055.

Pfeiffer, W. and Hollstein, T., 1997. Influence of grinding parameters on strength-dominating near-surface characteristics of silicon nitride ceramics. *Journal of the European Ceramic Society,* 17, 487-494.

Piskunov, E. G. and Korolev, D. I., 1994. Polish of ceramic part working surface. *Ogneupory,* , 29-30.

Poon, C. Y. and Bhushan, B., 1996. Nano-asperity contact analysis and surface optimization for magnetic head slider/disk contact. *Wear,* 202, 83-98.

Raghunandan, M. and Komanduri, R., 1998. Finishing of silicon nitride balls for high-speed bearing applications. *Journal of Manufacturing Science and Engineering, Transactions of the ASME,* 120, 376-386.

Raghunandan, M., Umehara, N., NooriKhajavi, A. and Komanduri, R., 1997. Magnetic float polishing of ceramics. *Journal of Manufacturing Science and Engineering, Transactions of the ASME,* 119, 520-528.

Rutherford, K. L. and Hutchings, I. M., 1997. Theory and application of a micro-scale abrasive wear test. *Journal of Testing & Evaluation,* 25, 250-260.

Saunders, C. R. and Kusy, R. P., 1994. Surface-Topography and Frictional Characteristics of Ceramic Brackets. *American Journal of Orthodontics and Dentofacial Orthopedics,* 106, 76-87.

Schwartz, M. M., 1992. *Handbook of structural ceramics,* New York, McGraw-Hill, New York.

Spur, G. and Holl, S. E., 1996. Ultrasonic assisted grinding of ceramics. *Journal of Materials Processing Technology,* 62, 287-293.

Swab, J. J. and Sweeney, M. P., 1995. Fracture-Analysis of an All-Ceramic Bearing System. *Engineering Failure Analysis,* 2, 175-190.

Thomsen, N. B., Stump, D. M. and Keer, L. M., 1996. Surface uplift and wear implications of zirconia toughened ceramics. *International Journal of Mechanical Sciences,* 38, 233-245.

Tonshoff, H. K., Egger, R., Longerich, W. and Preising, D., 1998. Superfinishing ceramics. *Manufacturing Engineering,* 120, 5p.

Xu, J. and Kato, K., 1996. Microwear mechanisms of silicon sliding against diamond in water vapor. *Tribology Transactions,* 39, 621-626.

Yasui, H., Arino, Y. and Matsunaga, K., 1997. Ductile-mode high smoothness grinding of fine ceramics by diamond wheel of coarse grain size (1st Report) - ductile-mode grinding of fine ceramics by metal bond diamond wheel of grain size of #140. *Seimitsu Kogaku Kaishi/Journal of the Japan Society for Precision Engineering,* 63, 1270-1274.

Yoshioka, T., 1998. Present situation and research subjects of diagnosis techniques for rolling bearing and evaluation techniques for rolling bearing material. *Journal of Japanese Society of Tribologists,* 43, 445-449.

Yu, M. M. H., Moran, B. and Keer, L. M., 1995. A Direct Analysis of 3-Dimensional Elastic-Plastic Rolling-Contact. *Journal of Tribology-Transactions of the ASME,* 117, 234-243.

Zarudi, I., Zhang, L. C. and Cockayne, D., 1998. Subsurface structure of alumina associated with single-point scratching. *Journal of Materials Science,* 33, 1639-1645.

Zastrau, B., Nackenhorst, U. and Jarewski, J., 1997. On the computation of elastic-elastic rolling contact using adaptive finite element techniques. *International Conference on Contact Mechanics, Proceedings,* , 129-138.

Zhang, B., Umehara, N. and Kato, K., 1995. Effect of the eccentricity between the driving shaft and the guide ring on the behavior of magnetic fluid grinding of ceramic balls. *Seimitsu Kogaku Kaishi/Journal of the Japan Society for Precision Engineering,* 61, 586-590.

Zhang, G. M., Anand, D. K., Ghosh, S. and Ko, W. F., 1993. Study of the formation of macro- and micro-cracks during machining of ceramics. *NIST Special Publication,* 465-478.

Zouaghi, N. and Ichida, Y., 1996. Grinding Mode-Identification and Surface Quality Prediction Using Neural-Network in Grinding of Silicon-Nitride. *International Journal of the Japan Society for Precision Engineering,* 30, 35-40.